Numerical Simulations of High Temperature and Pressure Diesel Spray Injection and Combustion

Sean Louis Francis Nicholson

Pembroke College

University of Oxford

A thesis submitted in partial fulfilment of the requirements for the degree of Doctor of Philosophy

Hilary 2020

This thesis is dedicated to
my parents, Lynne and Wilf,
for their endless support, love,
and sarcasm.

Acknowledgements

Firstly, I'd like to thank my supervisor, Professor Martin Davy, for his support throughout my studies and giving me the opportunity to work on this project. Your support through the harder times of my PhD has ensured I've come out of this a more confident person in both my work and myself. My thanks also go to Professor Richard Stone, Professor Ben Williams, Dr Felix Leach, Dr Joe Camm and Dr Chris Willman for their support throughout my time and advice on various parts of this work.

Special thanks also have to go out to everyone in the Oxford Thermal Propulsion Systems Research Group, especially Dr Blane Scott, Dr Leo Fang, Dr Riyaz Ismail and Dr Nick Papaioannou for making me feel so welcome to begin with and helping me out when times were a little tougher. You've all made my time better here and I'm very thankful for that.

I'm incredibly appreciative of the financial support provided by the EPSRC to allow me to undertake this work, and for Jaguar Land Rover for their additional support, with special thanks going to Dave Richardson, Dr. Sridhar Ayyapureddi and Dr. Steven Pierson for their support and suggestions for work for this thesis. My thanks also go to Siemens and Rickard Solsjo for their software support and in ensuring things went as smoothly as possible with my work.

To my friends in Pembroke and beyond, you've provided me with some of the best memories anyone could ask for. I feel so honoured to call you all my friends as you've all given me so much stability and warmth over my time here that I sometimes so badly needed. To Chris, Scarlett, Livvy, Patrick, Britt, Katie, Hannah, Gus, Zana, Simon, Constantin, Cillian, Ella, Kathryn, Allie, Ari, Lisanne, Ben, Alice, Til, Beth, Josh, Mira, Mirela, Hanna, Louis, Denise and Corina, from the bottom of my heart, thank you for everything and I love you all.

Last but by no means least, to my parents Lynne and Wilf. You are my rocks. I couldn't imagine anyone better in the entire world for support and love as you two. You have provided me with my inspiration for life, and without you I would be an infinitely worse person. I know I would not have got this far without you and I will be eternally grateful for every sacrifice you've made to help me be better. I love you more than anything in the world and can only hope this makes up for me not being an artist!

Abstract

Compression Ignition (CI) engines are state of the art power generating machines, and as such have found widespread use in a variety of implementations due to their high thermal efficiency, fuel efficiency, durability, reliability, and low carbon dioxide (CO_2) emissions. These include power generation, marine propulsion, light and heavy duty road vehicles, and off-road applications. However, due to the nature of a CI engine's combustion process, emissions of other harmful pollutants is increased, such as nitrogen oxides (NO_x) and particulate matter (PM). Multiple injection strategies have been used to combat this rise in emissions; along with low temperature combustion (LTC) methodologies these have been able to reduce both NO_x and PM emissions, and as such this thesis will focus on the modelling of the transient period of the diesel spray and its impact on the combustion of the fuel.

Initially, this thesis will consider the transient period of diesel injection by focusing on the prediction of the early stage of the spray formation at the Engine Combustion Network's (ECN) "Spray A" condition, comprising of a single-hole injection of n-dodecane (diesel surrogate) fuel. This is achieved by comparing two different commercially available Computational Fluid Dynamics (CFD) codes and their predictions of the liquid and vapour lengths, initially with different computational set-ups before these set-ups are converged to being identical with each other. All simulations are undertaken under a Reynolds Averaged Navier Stokes (RANS) framework, in a well characterised domain for both CFD codes. This convergence of set-ups shows that the transient region of the spray is highly dependent on the break-up model, however comparison with experimental data showed a deficiency in the implementation of the break-up model within Star-CD. This was corrected with the inclusion of a novel break-up length criterion, with the corrected model showing good agreement with experimental data, with particular strengths in decoupling the liquid and vapour length predictions.

Following the implementation of the novel break-up length criterion within Star-CD, the performance of this model at a combusting condition is tested. This study was performed under the same framework as previously, however with the implementation of a commonly used chemical mechanism for n-dodecane combustion.

When the novel break-up length criterion is compared to the original baseline case within Star-CD the results match very well to each other, with predicted ignition delays, lift-off-lengths and combustion fields being closely aligned. An over-prediction in lift-off-length to experimental data is noted, however this is commonly seen for the mechanism used.

Finally, by utilising the decoupling of the liquid and vapour penetrations offered through the novel break-up length criterion, the impact of the vaporising match on the combustion criteria detailed previously is investigated. A variety of cases are considered, with high, low and matched variations on both the liquid and vapour lengths compared against each other. The results from these tests show a strong effect of certain model constants on the combusting criteria, with break-up model constants especially having a large impact on the mixture fraction and temperature predictions. In contrast, the turbulence model constants often used when matching simulated tests to experimental results have very minimal impact on either the mixture fraction or temperature fields, with only the position of the combustion field changing, as expected. The effect of the combustion field position on the combustion temperatures is also considered, further reinforcing the break-up model constant's impact on combustion prediction.

Contents

List of Figures

List of Tables

Abbreviations and Nomenclature

Abbreviations

AEOI . . After End of Injection

AMR . . Adaptive Mesh Refinement

ASOI . . After Start of Injection

ATDC . After Top Dead Centre

BTDC . Before Top Dead Centre

CDST . Cold Driven Shock Tube

CI . . . . Compression Ignition

CFD . . Computational Fluid Dynamics

ECN . . Engine Combustion Network

EGR . . Exhaust Gas Recirculation

EOI . . . End of Injection

ES . . . Embed Scale

GCI . . Gasoline Compression Ignition

HCCI . Homogeneous Charge Compression Ignition

KH . . . Kelvin-Helmholtz

LES . . . Large Eddy Simulation

LOL . . Lift-Off-Length

LTC . . Low Temperature Combustion

NWMI . Normalised Weighted Magnitude Index

PM . . . Particulate Matter

PS . . . Parcel Scale

RANS . Reynolds Averaged Navier-Stokes

R-D . . . Reitz-Diwakar

ROI . . . Rate of Injection

RT . . . Rayleigh-Taylor

SMD . . Sauter Mean Diameter

TDC . . Top Dead Centre

TKE . . Turbulent Kinetic Energy

TLS . . . Turbulent Length Scale

UDF . . User Defined Function

WMI . . Weighted Magnitude Index

Nomenclature

Latin:

a	Acceleration
c_d	Discharge Coefficient
C_d	Drag Coefficient
D	Diameter
E	Energy
F	Diffusion Flux Component
k	Turbulent Kinetic Energy
K	Maximum Surface Wave Growth Wavenumber
L	Length
N	Engine Speed
p	Pressure
r	Droplet Radius
R	Ratio
Re	Reynolds Number, $\frac{\rho U L}{\mu}$
S	Source Term, Production Rate
t	Time
T	Taylor Number, $Z_d\sqrt{We_g}$
T	Temperature
$\mathbf{u}$	3-D Droplet Velocity
u	x-Direction Droplet Velocity
U	Relative Droplet Velocity
$\mathbf{U}$	3-D Droplet Velocity
v	y-Direction Droplet Velocity
w	z-Direction Droplet Velocity
We . . .	Weber Number, $\frac{\rho_d U^2 L}{\sigma}$
y	Mass Fraction
Z	Ohnesorge Number, $\frac{\sqrt{We}}{Re}$

Greek:

ε	Turbulent Dissipation Rate
κ	Wavenumber
Λ	Wavelength
μ	Viscosity
ρ	Density
σ	Surface Tension, Turbulent Prandtl-Schmidt Number
τ	Stress, Time Scale
ϑ	Dynamic Viscosity
Φ	Dimensionless Turbulent Energy Spectrum
ω	Surface Wave Growth Rate, Reaction Rate, Angular Velocity
Ω	Maximum Surface Wave Growth Rate

Subscripts:

$_0$	Initial
$_\varepsilon$	Relating to Turbulent Dissipation Rate
$_A$	Atomisation
$_b$	Relating to Bag Break-Up
$_c$	Child
$_{ch}$	Characteristic
$_d$	Droplet
$_g$	Gas, Group Number
$_i$	Internal, Generic Direction, Species
$_{inj}$	Injection
$_j$	Generic Direction
$_k$	Relating to Turbulent Kinetic Energy
$_{KH}$	Relating to KH Break-Up
$_M$	Momentum
$_p$	Parent
$_{RT}$	Relating to RT Break-Up
$_s$	Relating to Strip Break-Up, Swirl
$_{st}$	Surface Tension
$_t$	Relating to Turbulence
$_w$	Wave
$_x$	x-Direction
$_y$	y-Direction
$_z$	z-Direction

Superscripts and Accents:

$'$	Fluctuating Value
^{0}	Initial
$\overline{x}$	Time Averaged value of x, Mean

1 Introduction

1.1 Compression Ignition Engines

Compression Ignition (CI) engines are state of the art power generating machines, building on over a century's work since Rudolf Diesel's initial theory of compressing air and fuel within a piston chamber to spontaneously combust [1]. A common CI engine consists of a standard 4-stroke cycle, with the fuel injected into the cylinder towards the end of the compression stroke where it atomises into small drops due to the high relative velocity. After this, it vaporises and mixes with the surrounding air at high pressure and temperature before autoigniting after a short delay (commonly referred to as the ignition delay) [1, 2]. The fuel burning rate is controlled by the mixing rate within the cylinder, and as such maximising this mixing process is of utmost importance for a controlled combustion. Inducing swirl and tumble motion is often used to maximise mixing [2–4], with these processes being shown in Figure 1.1. Swirl motion is defined as a rotation of the in-cylinder charge around the cylinder axis, with the intake valves inducing the rotational movement of the charge [2]. The swirl ratio commonly used to measure the magnitude of the swirling flow, and is defined as in Equation 1.1 as a ratio of the angular velocity (ω_s) to the engine speed (N).

$$R_s = \frac{\omega_s}{2\pi N} \tag{1.1}$$

Similarly to the swirl motion, tumble motion acts on the in-cylinder charge, however the axis of the tumble motion is perpendicular to the cylinder axis. Given the motion of the piston during engine operation the centre of rotation of tumble flow will change more markedly than swirling flow as the in-cylinder charge is compressed [5].

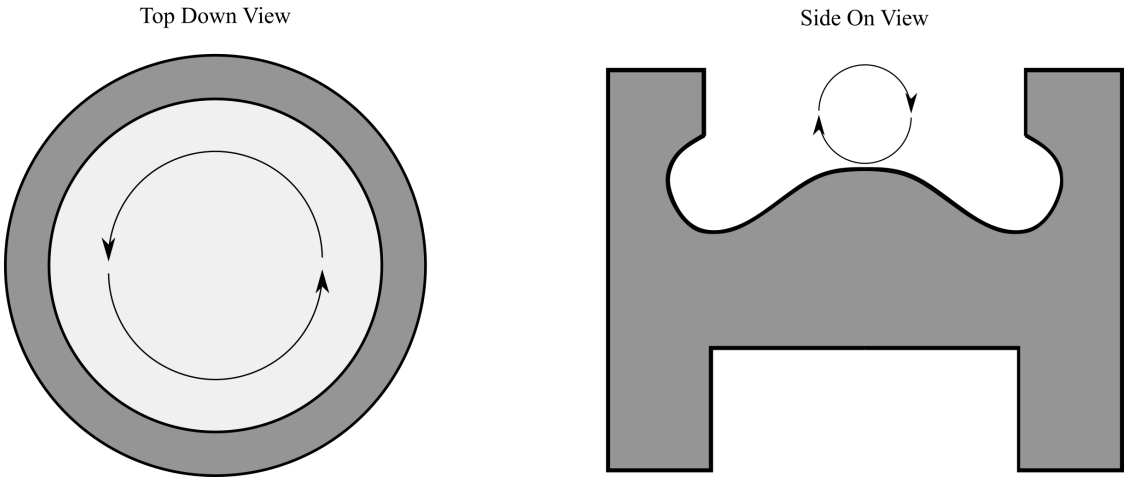

Figure 1.1: Schematic of swirl (top down view) and tumble (side on view) flows within a common CI engine

A bowl-in-piston set-up is particularly important for ensuring compression ratios can stay high within the cylinder whilst ensuring the spray does not impinge on the piston head. This can be achieved by targeting the spray into the bowl, allowing the piston head to be closer to the cylinder head at top dead centre (TDC) to ensure the compression ratio stays high. Increasing the compression ratio at a constant equivalence ratio increases the cycle efficiency and hence brake fuel efficiency [2]. Spray impingement still remains an issue with a bowl-in-piston set-up [6], however the effects of this at lower loads can be reduced by improved spray targeting [7]. The injection timing is also important in reducing spray impingement, however a compromise between injecting early enough to avoid impingement on the piston and injecting late enough to reduce the ignition delay by injecting into a hotter, higher pressure cylinder needs to be found. A common compromise is approximately 20° before top dead centre (BTDC) [2, 8], with this timing advanced with increased engine speed to account for the ignition delay remaining nearly constant throughout the injection cycle [1].

CI engines have found widespread use in a variety of implementations due to their high thermal efficiency, fuel efficiency, durability, reliability, and low carbon dioxide (CO_2) emissions. These include power generation, marine propulsion, light and heavy duty road vehicles, and off-road applications. Many common automotive

engines are powered by diesel fuel, however some research has found improvements in emissions using gasoline within CI engines [9,10], but these engines have only recently made it to a commercial stage and as a result will not be considered within this thesis. CI engines offer a number of improvements over their gasoline counterparts, with an increased fuel efficiency due to their generally leaner combustion as well as the aforementioned low CO_2 emissions [2]. Both these improvements make them highly attractive for medium and heavy duty uses given their savings in fuel cost, which along with the reduction in road tax due to lower CO_2 emissions [11] make them attractive for light duty uses as well.

Within CI engines two injection strategies dominate, Direct Injection (DI) and Indirect Injection (IDI). DI involves injection of the fuel straight into the cylinder, whereas in IDI systems there is a pre-chamber in which the fuel mixes with the air before being introduced into the combustion chamber [1]. DI engines offer improved part-load and full-load fuel efficiency over IDI engines, however IDI engines allow for smaller engines to be run at faster speeds given the reduction in ignition delay caused by the pre-mixing of fuel and air [1]. IDI engines do offer a reduction in combustion noise along with a reduction in smoke values at earlier injection timings [12], however this is at a cost of fuel efficiency. Along with this, DI engines are significantly simpler to design given the lack of a pre-chamber, combined with the improvement of efficiency seen in downsized, turbocharged spark ignition engines IDI engines have become marginalised.

Whilst CI engines offer an improvement in CO_2 emissions over traditional spark-ignition (SI) engines, they also emit other harmful pollutants in greater quantities when compared to SI engines [13]. These primarily comprise of nitrogen oxides (NO_X), a mixture of NO and NO_2, and soot (or particulate matter (PM)). As a result, CI engines are under increasingly stringent emissions legislation, with the most recent Euro 6 emissions standards coming into effect in September 2015 and more stringent CO_2 emissions legislation taking effect within EU countries from the 1st January 2020. A breakdown of the progression of the Euro emissions

standards is shown in Table 1.1, displaying how the maximum permitted NO_X and PM levels have been reduced since 1992.

Table 1.1: Euro 1 to 6 emissions standards for NO_X and PM for diesel cars

Regulation	**Date Introduced**	**NO_X (g/km)**	**PM (g/km)**
Euro 1	Dec 1992	0.97	0.14
Euro 2	Jan 1997	0.7	0.08
Euro 3	Jan 2001	0.5	0.05
Euro 4	Jan 2006	0.25	0.025
Euro 5	Jan 2011	0.18	0.005
Euro 6	Sep 2015	0.08	0.005

Table 1.1 shows clearly how much progress diesel engines have made in the 28 years since the first set of Euro emissions regulations were implemented, with extremely large reductions in both NO_X and soot seen (12 and 28 fold reductions respectively). This is despite diesel engines suffering from the so-called "NO_X / soot trade-off", where any attempts to reduce either NO_X or soot emissions result in the emissions of the other increasing [6, 7, 14]. The underlying cause of this trade-off is the conditions in which either NO_X or soot are produced; with a hotter, leaner combustion vaporising the soot and hence reducing its emission, with the downside of the hotter conditions allowing reactions leading to NO_X to be formed before the expansion stroke, which acts to "freeze" the concentration of nitrous oxides by rapidly cooling the in-cylinder temperature [2, 15]. The opposite of this is also true, by cooling combustion NO_X emissions are reduced however soot is allowed to form without being vaporised in the combustion chamber.

An example of a classic NO_X / soot trade-off is shown in Figure 1.2, showing clearly the challenge of achieving low emissions of both NO_X and soot at the same time within a traditional CI engine [7]. Methods of reducing both NO_X and soot can be achieved with non-conventional set-ups, including utilising highly oxygenated biofuels with exhaust gas recirculation (EGR) to achieve both low NO_X and soot [16], applying low-temperature combustion (LTC) techniques including

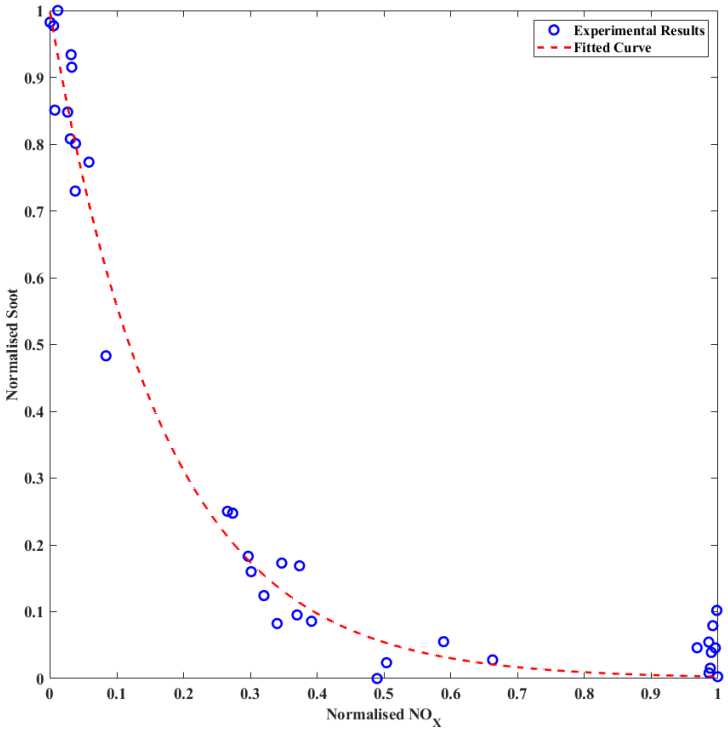

Figure 1.2: Experimental NO_X / soot trade-off, with fitted curve shown. Adapted from [7]

homogeneous charge compression ignition (HCCI) combustion [17], as well as varying the ignition timing whilst also applying EGR [18]. LTC is achieved by keeping the local combustion temperature below 2200 K at low equivalence ratios to minimise nitric oxide production, with this local combustion temperature reducing with an increase in equivalence ratio [19]. HCCI combustion enhances the in-cylinder mixing in the pre-combustion phase, which ensures a reduction in soot and NO_X formation in-cylinder. However, the reduction of soot and NO_X can cause an increase in both CO and unburned hydrocarbon emissions [19, 20], an effect that is enhanced at lower load conditions [21]. Further reductions in emissions from the current pace of research and development have led the UK Government to predict that by 2030 all air quality reporting zones will meet NO_2 limits, without any further legislation on diesel cars [22].

Given the loss in confidence in diesel engines following the Volkswagen "diesel-gate" scandal in 2015 sales of light duty diesel vehicles have dropped. Along with this, car manufacturers are pushing towards increased hybridisation of the power-train.

Also, the corresponding stricter air quality regulations [22] are pushing light duty diesel engine vehicles out of the market. Despite this, diesel engines will continue to find use in the medium and heavy duty sectors (including vans, trucks and marine vehicles), given their increased fuel efficiency, and so research into improving diesel engines is still warranted and required.

Within this thesis, the spray of diesel fuel from the injector will be considered in isolation from in-cylinder effects, with simulations focusing on domains mirroring common combustion bombs [23–25], so as to remove in-cylinder effects and hence focus on the fundamentals of diesel spray phenomena. With this in mind, the following section will consider the issues for future CI engine development and how utilising computational fluid dynamics (CFD) can help develop more efficient engines.

1.2 Current Spray Modelling Methodologies

CFD allows for a level of vision within a cylinder that cannot be provided by standard optical-access engines, allowing researchers to see in-cylinder flows in unparalleled detail. Whereas a common engine is somewhat equivalent to a "black box", where the inputs and outputs from the engine are known but the exact knowledge of what is happening within the cylinder is not, CFD allows for this to be visualised. Along with the increased knowledge of in-cylinder flows CFD provides researchers, it is also extremely useful in engine development due to the relative low cost and small lead time in setting up a CFD simulation in comparison to designing an optical-access engine. Parametric studies of engine components are also much faster to run in a virtual environment, with any changes able to be automated and run simultaneously on clustered computer systems, in comparison to being run sequentially on a real engine. The changeover time for the study would also need to be taken into account; for example the nozzle-tip protrusion study by Leach et al. [7] required only a small change in the CFD simulation, in comparison to requiring a technician to alter the injector position by very small amounts each time a test is required.

Modelling a diesel spray is a computationally expensive process, and as such is commonly split into multiple sub-models to reduce computational cost. A schematic of a common diesel spray is shown in Figure 1.3, with the common spray sub-models shown. The important models for this thesis are discussed in Chapter 2.

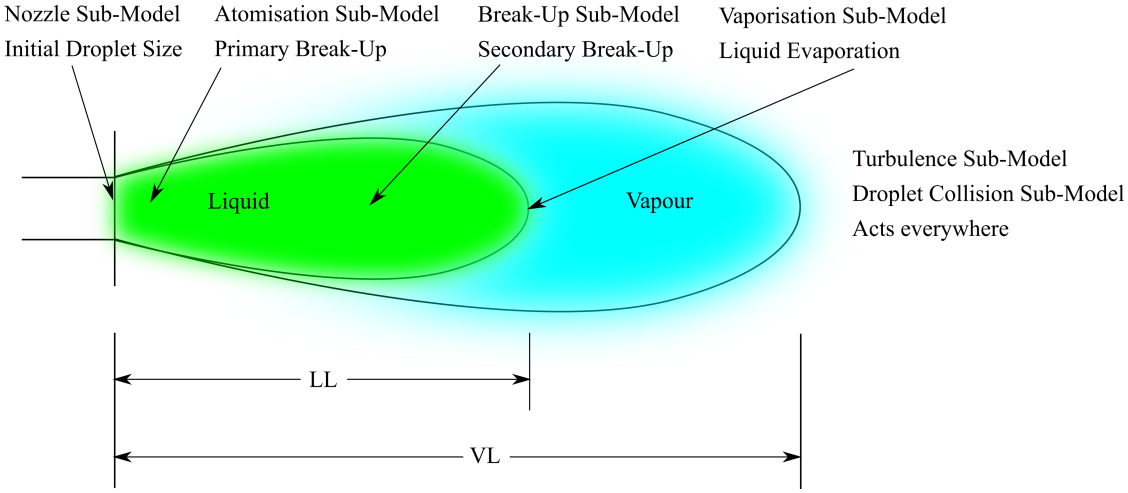

Figure 1.3: Schematic of a common diesel spray, with sub-models noted. LL is the liquid length, VL is the liquid length

To aid modellers in creating new methods for simulating spray injection using CFD, the Engine Combustion Network (ECN) set up a series of baseline spray experiments, mirroring the Turbulent Non-premixed Flame (TNF) workshop's successful standard flame experiments [24, 26]. The ECN have generated a series of test points relevant to engine conditions, with the commonly used "Spray A" test point corresponding to an engine relevant LTC condition using moderate EGR [24]. Along with this a series of injectors were produced to identical specifications by Bosch, allowing for multiple institutions to provide experimental data at nominally identical conditions, ensuring a database of high quality experimental data for modellers to use. This is further aided by a common fuel injection system, ensuring consistent injection strategies and phenomena across institutions. All data produced for the ECN is stored on their database and freely accessible to modellers [27].

One of the key phenomena to model is the reduction in droplet size during the injection of the fuel, called droplet break-up. Accurate modelling of the droplet break-up rate ensures the vaporisation rate of the fuel is well matched,

and as such will feed into better modelling of the combustion. Droplet break-up is commonly split into two modes, primary and secondary break-up. Primary break-up details the disintegration of the liquid jet into droplets as it leaves the injector, with secondary break-up detailing the reduction in diameter of these droplets. Primary droplet break-up can be categorised into multiple regimes, often based on the Ohnesorge and Reynolds numbers. These have been described by Reitz as follows, building on observations from experimental data [28–31]. These four regimes are also shown in Figure 1.4.

I. Rayleigh jet break-up. In this regime break-up is caused by droplet surface oscillation growth, induced by the surface tension of the droplet. The droplet diameter exceeds the jet diameter, and break-up occurs many nozzle diameters downstream of the nozzle.

II. First wind-induced break-up. Within this regime the surface tension effect seen in Rayleigh jet break-up is accelerated by the relative velocity seen between the liquid and gas. Droplet diameters are of the same order as the jet diameter, and break-up occurs closer to the nozzle than Rayleigh jet break-up, but still many nozzle diameters downstream.

III. Second wind-induced break-up. Droplets are produced by unstable surface wave growth caused by the relative velocity between the liquid and gas. This effect is opposed by the surface tension of the liquid. Droplet diameters are much less than the jet diameter, with break-up occurring closer to the nozzle again than the first wind-induced break-up regime.

IV. Atomisation. The jet very quickly disintegrates, usually very close to the nozzle exit. Droplet diameters are much smaller than the jet diameter, often in the order of the nozzle diameter.

Diesel spray injection is a highly pressurised system, with injection pressures of upwards of 1500 bar [24]. As a result, the injection velocity of the fuel is high (usually over 300 m/s). In-cylinder temperatures vary between close to ambient at

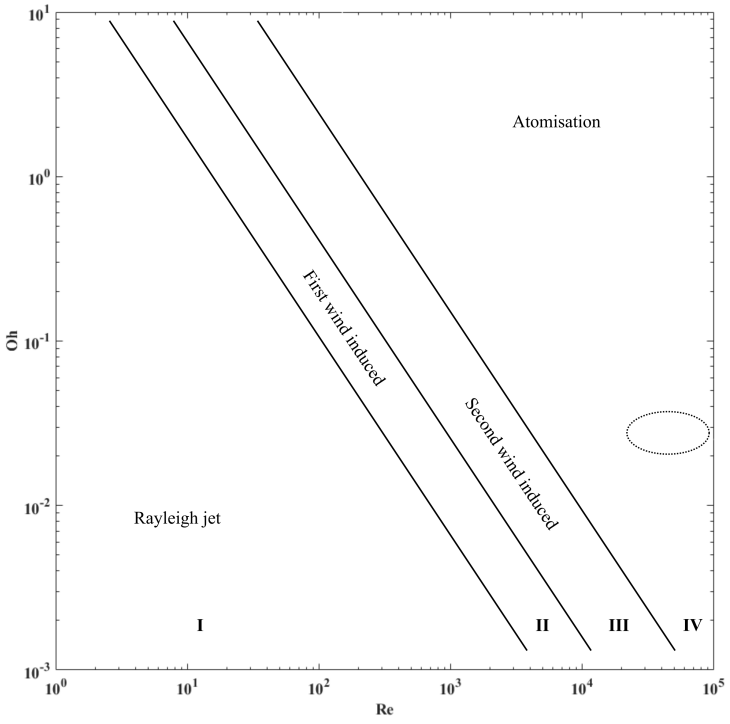

Figure 1.4: Standard Re-Oh graph, showing primary break-up regimes. The dashed ellipse shows common diesel engine operating conditions. Adapted from [28, 29]

start up to above 2500 K at peak temperatures [32]. The fuel properties also vary with the temperature, however at injection diesel fuel has a density in the region of 700 kg/m^3, a surface tension in the region of 0.02 N/m and a viscosity in the region of 5×10^{-4} Pa.s (all values taken from NIST table properties for n-dodecan surrogate diesel fuel). As such, during the injection phase this leads to large Reynolds numbers and a highly turbulent velocity distribution within the liquid jet. This ensures that the spray will be in the atomisation regime, with the primary break-up of the liquid controlled by the turbulence of the spray and not aerodynamic effects [28].

Reitz and Bracco discuss a variety of different processes that cause atomisation, including injector dimensions, cavitation and nozzle geometry [33]. Reitz then used the stability analysis conducted by Reitz and Bracco to define a wave break-up model based on surface wave growth, now commonly known as the Kelvin-Helmholtz model [34], for use within the atomisation regime. Huh and Gosman also derived a model to calculate the atomisation of diesel fuel, based on the assumption of gas inertia and turbulent stresses being the dominant factors in the atomisation

of the liquid [35]. These models are based on various non-dimensional groups, including the Reynolds number, Ohnesorge number, and Weber number. The definitions for these groups are as follows:

- The Reynolds number is the ratio of the inertial forces to the viscous forces in a fluid, and is important in judging if a flow is laminar or turbulent. Within diesel injection flows are often turbulent, however the Reynolds number is still important in computing the intensity of the turbulence seen. The Reynolds number is defined as in Equation 1.2.

$$Re = \frac{\text{inertial forces}}{\text{viscous forces}} = \frac{\rho U L}{\mu} \tag{1.2}$$

- The Weber number is the ratio between the inertial forces and the surface tension of a liquid. It is useful in analysing interfaces between two different fluids, and can be especially important when used to analyse droplet formation. As such, it is commonly used in predicting break-up and child droplet formation. It is as defined in Equation 1.3.

$$We = \frac{\text{inertial forces}}{\text{surface tension}} = \frac{\rho U^2 L}{\sigma} \tag{1.3}$$

- The Ohnesorge number is the ratio between viscous forces and inertial forces with surface tension, comparing the Reynolds number and the Weber number. It is often used in modelling the dispersion of liquids within a gas, and as such is useful for spray modelling. The comparison of the Weber and Reynolds number describes the tendency for the droplet to either stay together or break apart, especially useful for break-up modelling. The Ohnesorge number is defined as in Equation 1.4.

$$Oh = \frac{\text{viscous forces}}{\sqrt{\text{inertia} \times \text{surface tension}}} = \frac{\sqrt{We}}{Re} = \frac{\mu}{\sqrt{\rho \sigma L}} \tag{1.4}$$

Whilst atomisation processes detail the primary break-up of the spray, the secondary break-up is controlled by aerodynamic forces [28]. Pilch and Erdman [36] defined five mechanisms of droplet break-up, based off the initial Weber number of the droplet. These mechanisms also correspond to the break-up modes proposed by Faeth et al. [37], in which the Weber and Ohnesorge numbers are considered, these modes have been implemented in a number of common break-up models [38–41]. Two of the major modes for break-up considered are the bag and strip modes, in which child droplets are created either through a full break-up of the parent droplet (bag) or smaller child droplets being stripped off the parent droplet (strip). Reitz and Diwakar considered these modes as the basis for their Weber based break-up model [42]. Su et al. [43] also developed a stripping based break-up model, utilising surface wave growth caused by aerodynamic forces to determine criteria for break-up to occur. This model was expanded to viscous flows by Joseph et al. [44] and combined with the Kelvin-Helmholtz atomisation model to form a hybrid primary/secondary break-up model [45].

1.2.1 Challenges of Current Spray Modelling for Future Engine Development

In order to improve existing diesel technology, a better understanding of the dominant physical and chemical phenomenon in spray combustion is required. Previous studies have been conducted to observe in-cylinder spray evolution, air-fuel mixing processes, spray auto-ignition and flame developments [23, 46]. However, these studies are commonly performed in rather simplified configurations which allow limited usage in engine design and optimization [24]. Therefore, CFD becomes a more popular and useful tool to integrate experimental studies with physical diesel combustion processes as well as to be part of industrial design and optimization. Among all modelling processes involved in diesel combustion, spray modelling has always been a key component due to its significant impact of fuel injection processes, which greatly affects combustion and emission characteristics. Spray/air mixing involves several different physical processes, for example collision, evaporation and turbulent mixing. Interactions between these processes are extremely non-linear

which makes transient spray modelling really difficult. On this note, it is essential to develop models that could well predict non-reacting spray transient characteristics before reliably implementing these in reacting studies.

In order to derive the models used within a common CFD simulation, various assumptions have to be made about the flow or boundary conditions and as such generating an exact match to a real engine is difficult to obtain. One of the most fundamental assumptions often made within diesel spray modelling is to consider the flow as a Lagrangian-Eulerian flow problem, where the liquid phase is handled as a flow of Lagrangian droplets and the gas phase is modelled in an Eulerian fashion. Applying a Lagrangian solution to the liquid phase allows for droplet break-up and atomisation to be handled easily utilising a discrete droplet method [47]. This splitting of liquid and gas phases helps simplify the liquid phase simulation to work with common CFD setups utilising domains broken down into cells, as the Lagrangian parcels are affected by the conditions of the cell they are in without having to be tied to moving in discrete distances related to the cell size per time-step [48].

Sprays are widely modelled using the Lagrangian-Eulerian approach. The modelling community uses different codes and commercial CFD packages along with various models, model constants, and grid sizes to study spray characteristics. Some early modelling work in diesel spray was performed through KIVA-3V engine simulation code using n-heptane as the surrogate fuel [49]. Senecal et al. were able to accurately obtain liquid length, ignition delay and flame lift-off length under different ambient and injection conditions. Later Lucchini et al. [50] performed a series of non-reacting diesel spray simulations to determine the required grid sizes for fuel-air mixture formation processes. The OpenFOAM code was capable of capturing liquid length, vapour penetration and mixture fraction distributions at different distances from the injector. Adaptive Local Mesh Refinement technique (ALMR) was also implemented to reduce pre-processing and computational time while preserving the simulation accuracy. Som et al. [51] evaluated the Smagorinsky-based Large Eddy Simulation (LES) in n-heptane spray simulation using CFD program CONVERGE. The results were both comparable to a standard Reynolds averaged

(RANS) turbulence model and the ECN data. Some global spray and combustion characteristics were successfully captured by both RANS and LES model with LES being slightly better in predicting the ignition delay. More recently Blomberg et al. [52] investigated n-dodecane split injections using both LES and RANS through Star-CD. The ambient conditions and injection profiles were varied, capturing the combustion recession phenomenon. Both the RANS and LES results showed good agreement with ECN data in terms of vapour penetration, ignition delay and lift-off-length.

Whilst grouping droplets in this method is advantageous for computational speed, ensuring a Lagrangian system correctly captures the experimental set-up is difficult. Under-estimating the number of parcels required can lead to higher than expected void fractions far away from the nozzle, leading to lower predicted drag on the core than expected and hence higher liquid length predictions [46]. Along with this, a Lagrangian-Eulerian system is highly grid-dependent [46, 48, 53–55], and as such ensuring the domain is properly refined to ensure the spray is grid independent is of utmost importance. There is evidence to suggest a move towards an Eulerian-Eulerian flow condition at higher ambient temperatures and pressures is required, as an absence of droplets and ligaments can be seen utilising ballistic imaging [56]. Desantes et al. [57] have compared an Eulerian-Eulerian flow simulation and a classical Lagrangian-Eulerian flow simulation, finding good agreement for both to experimental data, with the Eulerian-Eulerian model predicting the near nozzle field slightly more accurately than the Lagrangian-Eulerian model.

There are few studies concerning comparison of different codes and definitions, as such comparing the implementations of models between codes is of high importance to ensure consistency. Mulemane et al. [58] examined cavitation models using both Fluent and Star-CD. Whereas, Karrholm at al. [59] conducted research on the effect of ambient gas temperature and exhaust gas recirculation on spray as well as combustion characteristics. Two different codes, KIVA-3V and OpenFOAM were implemented, which despite some differences, both successfully captured ignition delay and flame lift-off. Iyenger et al. [60] also compared KIVA-3V with OpenFoam

to study non-reacting spray, where capability of both codes in predicting low and high ambient temperature non-reacting diesel spray is examined. More recently Som et al. [61] did a comprehensive comparison between OpenFOAM and CONVERGE for both reacting and non-reacting spray modelling.

Another common assumption in deriving many break-up models is utilising the Weber number to define criteria for droplet break-up. However, with current CI technology progression this assumption can cause issues when applied to a computational simulation, given the ambient conditions in-cylinder tend towards supercritical conditions for diesel fuel [62, 63]. The issues with this assumption can best be seen by considering the definition of the Weber number, as shown in Equation 1.3. At supercritical conditions the droplet's surface tension tends towards zero [64, 65] and as a result the Weber number will tend towards infinity, making comparisons often used in break-up modelling (as shown in Equations 2.47, 2.50, 2.53 and 2.56) numerically impossible. As a result, care is required when utilising these models at conditions above those of the critical point of the fuel injected.

With greater control over injection timings, and the emissions benefits seen from adopting a multiple injection strategy [66–69] over a single injection strategy means that more, shorter, injections will be used in future. The use of Digital Rate Shaping (DRS) [70, 71] has allowed for very short energising times, and as a result injections that are almost entirely contained within the transient period of the spray (defined as the period of time before the spray settles to its steady state liquid length). These multiple injection studies have been recreated in simulations, with good matches being found [72] at energising times above 0.2 ms. The ability of DRS to reduce the energising times to 0.1 ms and below has been found to cause issues [73], however slightly longer energising times will still result in injections within the transient region of the spray. However, in many cases the transient prediction within simulations is often poorly matched to experimental data [46, 74–76], suggesting this is an area which requires further insight.

1.3 Objectives

The continual exponential rise in computational power over the past decades has allowed higher resolution domains to be created (as can be seen comparing two works of Senecal, both a decade apart from each other [46, 49]), ensuring more complex phenomena can be captured computationally. However, even with this greater computational power available there has been little discussion on the how altering model constants to match experimental data impacts the combustion prediction. Along with this, given the rise of multiple injection strategies to help reduce emissions and the usage of digital rate shaping to facilitate short injection times, computational simulations considering the transient period of diesel injection are required to ensure the models used can match the experimental data correctly.

This thesis sets out to explore the impact of CFD models on the prediction of both the transient period and the combustion of a common diesel spray. All the simulations are carried out in commercially available CFD codes which allow for detailed chemistry integration into the solver. Initially, the impact of the break-up models on the transient spray prediction are examined, with two separate models tested, both of which are commonly used in industry and research settings. By comparison between two commonly used CFD codes deficiencies within each model are identified when compared to experimental data. The combustion performance of the different break-up models is also tested, with results being compared to experimental data for ignition delay, lift-off-length and qualitative comparisons between combustion field positions. The break-up models are compared against each other to identify strengths and weaknesses of each method of modelling break-up when applied to a combusting test point. The impact of the various "tuning" constants within each sub-model on the combustion prediction are also investigated, comparing between matches to determine the influence of each model constant. These combustion studies should help shed light on the importance of the vaporising match to the combustion prediction, an area that is rarely discussed currently and which is important when considering model performance.

1.4 Thesis Outline

This thesis consists of seven chapters which cover the numerical modelling of turbulent flows, droplet break-up and droplet atomisation (Chapter 2); a domain definition and characterisation for non-reacting spray modelling (Chapter 3); a comparison of break-up models between codes (Chapter 4); the application of a novel switching method to reacting sprays (Chapter 5), and an investigation on the impact of the vaporising match to combustion prediction (Chapter 6). Each chapter begins with a short introduction, with relevant literature discussion contained within the chapter.

Chapter 2 summarises the common methods for modelling turbulent flows within diesel spray modelling. The important sub-models (turbulence, atomisation and break-up) used within this thesis are shown and discussed. Chapter 3 applies these models to a computational domain that emulates a commonly used diesel combustion bomb, allowing for a grid sensitivity study to be undertaken that provides a domain that is used for the rest of the thesis.

Chapter 4 utilises the domain defined in Chapter 3 to compare the Reitz-Diwakar and KH-RT break-up models, initially by a comparison of baseline setups from two commercially available CFD codes, Star-CD and CONVERGE. Comparisons of both to experimental data from Sandia show differences between the models' transient prediction, believed to be caused by the difference in break-up models used by each CFD code. Further studies of the KH-RT model within Star-CD show issues with the model's implementation, which are investigated and discussed. A new method for implementing the KH-RT model is used, utilising an Ohnesorge number based switching position that improves transient response as well as matching both liquid and vapour lengths. The impact of altering the switching position on the vapour fields is also considered.

Chapter 5 applies the new implementation of the KH-RT model to a combusting "Spray A" case, comparing it against the baseline Reitz-Diwakar case. Combusting criteria including lift-off-lengths, ignition delays and scalar fields are compared,

showing a good match between the two models. The two sub-models of the KH-RT model are considered in isolation by utilising the newly implemented switching criterion, showing instabilities in the liquid prediction when the RT model is applied to the whole spray. Discrepancies in the liquid length prediction after the end of injection are also considered, with "empty" parcels that remain in the domain found to be the cause of this discrepancy.

Chapter 6 utilises the improved matching capability of the new implementation of the KH-RT model to test the combusting performance of the "Spray A" simulation at combinations of high, matched and low liquid and vapour lengths. Particular attention is paid to the impact of various model constants (both turbulence and break-up) on the combustion fields. The turbulence model constant $C_{1\varepsilon}$ is found to have little impact on the combustion fields, especially in comparison to the break-up model constants. Differences are found in the spray centreline temperatures based on the ratio of liquid length to combustion zone position, with the application of changes to spray break-up model constants causing a large change in combustion temperature and OH radical magnitudes.

Chapter 7 brings together and summarises the conclusions from the main body of work presented in the thesis. It also suggests further work that could be done to improve the quality of the work considered in these studies.

1.5 Publications Related to this Thesis

The content in Chapter 4 has been peer reviewed and published as follows:

- Louis Nicholson, XiaoHang Fang, Joseph Camm, Martin Davy and David Richardson. "Comparison of Transient Diesel Spray Break-Up between Two Computational Fluid Dynamics Codes". *In SAE Technical Paper 2018-01-0307.* SAE International, 2018

The work undertaken in Chapters 5 and 6 is in preparation for publication, and will be published in future.

2 Spray Modelling Methodology

Computing turbulent spray injection within the context of internal combustion engines presents a large number of challenges, given the flow within the cylinder is compressible, multi-phase, multi-scale, unsteady and three-dimensional. As a result, a number of assumptions need to be made to reduce the complexity of the simulation in order to reduce the computational run-time to acceptable levels. Firstly, the flow prediction is split into a series of sub-models, among which are the turbulence, atomisation and break-up sub-models. The models used within this thesis are presented within this chapter, detailing the governing equations for each model and the assumptions made within their formation. Work on comparing the break-up models will be detailed in Chapter 4, with the results from this comparison being tested further in Chapters 5 and 6.

2.1 Governing Equations

Within this body of work Reynolds Averaged Navier-Stokes (RANS) modelling is used to predict the spray formation and propagation. This theory is based around the Navier-Stokes equations (Equations 2.1 to 2.5), which are used to model three-dimensional fluid flow within a finite volume [77].

$$\frac{\partial p}{\partial t} + \mathrm{div}(\rho \mathbf{u}) = 0 \tag{2.1}$$

$$\frac{\partial (\rho u)}{\partial t} + \mathrm{div}(\rho u \mathbf{u}) = -\frac{\partial p}{\partial x} + \mathrm{div}(\mu \ \mathrm{grad}(u)) + S_{Mx} \tag{2.2}$$

$$\frac{\partial (\rho v)}{\partial t} + \mathrm{div}(\rho v \mathbf{u}) = -\frac{\partial p}{\partial y} + \mathrm{div}(\mu \ \mathrm{grad}(v)) + S_{My} \tag{2.3}$$

$$\frac{\partial(\rho w)}{\partial t} + \text{div}(\rho w \mathbf{u}) = -\frac{\partial p}{\partial z} + \text{div}(\mu \text{ grad}(w)) + S_{Mz} \tag{2.4}$$

$$\frac{\partial(\rho E_i)}{\partial t} + \text{div}(\rho E_i \mathbf{u}) = -p \; div(\mathbf{u}) + \text{div}(k \text{ grad}(T)) + \Phi + S_i \tag{2.5}$$

There are three major equation types within the Navier-Stokes equations; the continuity equation (Equation 2.1), the x, y and z momentum equations (Equations 2.2, 2.3 and 2.4 respectively) and the internal energy equation (Equation 2.5). Reynolds Averaging involves splitting the instantaneous flow variables (3-D velocity and pressure) seen in the Navier-Stokes equations into a mean value and a fluctuating value; taking the x-velocity (u) as an example yields the form shown in Equation 2.6.

$$u_i = U_i + u_i' \tag{2.6}$$

With U_i denoting the mean value and u_i' denoting the fluctuating value. This can be applied to the three-dimensional velocity in much the same way, as shown in Equation 2.7.

$$\mathbf{u} = \mathbf{U} + \mathbf{u'} \tag{2.7}$$

The relationships shown in Equations 2.6 and 2.7 can be substituted into the continuity and x-momentum equations (Equations 2.1 2.2) whilst also applying time averaging shown by Versteeg and Malalasekera [77] (examples are shown in Equation 2.8) to yield the time averaged continuity and x-momentum equations, shown in Equations 2.9 and 2.10.

$$\overline{\text{div}(u\mathbf{u})} = \text{div}(U\mathbf{U}) + \text{div}(\overline{u'\mathbf{u'}}); \;\; \overline{\frac{\partial u}{\partial t}} = \frac{\partial U}{\partial t}; \;\; \overline{\vartheta \text{ div}(\text{grad}(u))} = \vartheta \text{ div}(\text{grad}(U)) \tag{2.8}$$

$$\text{div}(\mathbf{U}) = 0 \tag{2.9}$$

$$\frac{\partial U}{\partial t} + \text{div}(U\mathbf{U}) + \text{div}(\overline{u'\mathbf{u'}}) = -\frac{1}{\rho}\frac{\partial P}{\partial x} + \vartheta \text{ div}(\text{grad}(U)) \tag{2.10}$$

This method can also be applied to the remaining momentum equations (Equations 2.3 and 2.4) to yield the fully time-averaged equations.

$$\frac{\partial V}{\partial t} + \text{div}(V\mathbf{U}) + \text{div}(\overline{v'\mathbf{u'}}) = -\frac{1}{\rho}\frac{\partial P}{\partial y} + \vartheta \text{ div}(\text{grad}(V)) \tag{2.11}$$

$$\frac{\partial W}{\partial t} + \text{div}(W\mathbf{U}) + \text{div}(\overline{w'\mathbf{u'}}) = -\frac{1}{\rho}\frac{\partial P}{\partial z} + \vartheta \text{ div}(\text{grad}(W)) \tag{2.12}$$

As can be seen, a new term has been added to the previous, non-averaged, set of equations. This is a term describing the convective momentum transfer due to turbulent eddies, and is a differential of a product of fluctuating velocities (div($\overline{u'\mathbf{u'}}$) from Equation 2.10). It is customary to have this term on the right hand side of the equation; applying this to the time averaged equations above yields the Reynolds Averaged Navier-Stokes equations (Equations 2.9 and 2.13 to 2.15).

$$\frac{\partial U}{\partial t} + \text{div}(U\mathbf{U}) = -\frac{1}{\rho}\frac{\partial P}{\partial x} + \vartheta \text{ div}(\text{grad}(U)) + \frac{1}{\rho}\left[\frac{\partial(-\rho\overline{u'^2})}{\partial x} + \frac{\partial(-\rho\overline{u'v'})}{\partial y} + \frac{\partial(-\rho\overline{u'w'})}{\partial z}\right] \tag{2.13}$$

$$\frac{\partial V}{\partial t} + \text{div}(V\mathbf{U}) = -\frac{1}{\rho}\frac{\partial P}{\partial y} + \vartheta \text{ div}(\text{grad}(V)) + \frac{1}{\rho}\left[\frac{\partial(-\rho\overline{u'v'})}{\partial x} + \frac{\partial(-\rho\overline{v'^2})}{\partial y} + \frac{\partial(-\rho\overline{v'w'})}{\partial z}\right] \tag{2.14}$$

$$\frac{\partial W}{\partial t} + \text{div}(W\mathbf{U}) = -\frac{1}{\rho}\frac{\partial P}{\partial z} + \vartheta \text{ div}(\text{grad}(W)) + \frac{1}{\rho}\left[\frac{\partial(-\rho\overline{u'w'})}{\partial x} + \frac{\partial(-\rho\overline{v'w'})}{\partial y} + \frac{\partial(-\rho\overline{w'^2})}{\partial z}\right] \tag{2.15}$$

In this form, the time averaged velocity fluctuation terms within the square brackets are analogous to stress terms, with a set of three normal stresses (Equation 2.16) and three shear stresses (Equation 2.17).

$$\tau_{xx} = -\rho\overline{u'^2};\ \tau_{yy} = -\rho\overline{v'^2};\ \tau_{zz} = -\rho\overline{w'^2} \tag{2.16}$$

$$\tau_{xy} = \tau_{yx} = -\rho\overline{u'v'};\ \tau_{xz} = \tau_{zx} = -\rho\overline{u'w'};\ \tau_{yz} = \tau_{zy} = -\rho\overline{v'w'}; \tag{2.17}$$

These stresses are collectively known as the Reynolds Stresses. Within standard two equation turbulence models these are modelled using the Boussinesq hypothesis; which relates the Reynolds Stresses to the mean deformation rate (S_{ij}) occurring on each element due to the eddy viscosity (μ_t). This is shown in Equation 2.18. The eddy viscosity (μ_t) is of extreme importance within two equation turbulence modelling, as it determines the flow of energy from larger eddies to smaller eddies and as such will impact the momentum transfer of the entire spray. Further detail on the way it is modelled is given in Section 2.2.

$$\tau_{ij} = -\rho\overline{u_i' u_j'} = 2\mu_t S_{ij} - \frac{2}{3}\rho k \delta_{ij} \tag{2.18}$$

The Reynolds Stresses are also dependent on the Kronecker delta (δ_{ij} from Equation 2.18), which has a value of 0 if i $\neq$ j and a value of 1 if i = j. The mean deformation rate is defined as in Equation 2.19.

$$S_{ij} = \frac{1}{2}\left(\frac{\partial U_i}{\partial x_j} + \frac{\partial U_j}{\partial x_i}\right) \tag{2.19}$$

2.2 Turbulence Modelling

Turbulent flow has no formal definition [78], however it exhibits a number of characteristics that allow turbulent flows to be studied and modelled. Turbulent flows are always chaotic (and thus dependent on initial conditions), unsteady, rotational and three-dimensional and act over a wide range of both length and time scales [79]. Despite turbulence's chaotic nature it is deterministic, and as such is governed by the Navier-Stokes equations (Equations 2.1 to 2.5). A classical way of representing the energy of a turbulent system is with an energy spectrum, relating the turbulent energy of the system ($E(\kappa)$) to the wave number (κ), which is inversely proportional to the length scale the turbulence is acting on. A classical energy spectrum is shown in Figure 2.1.

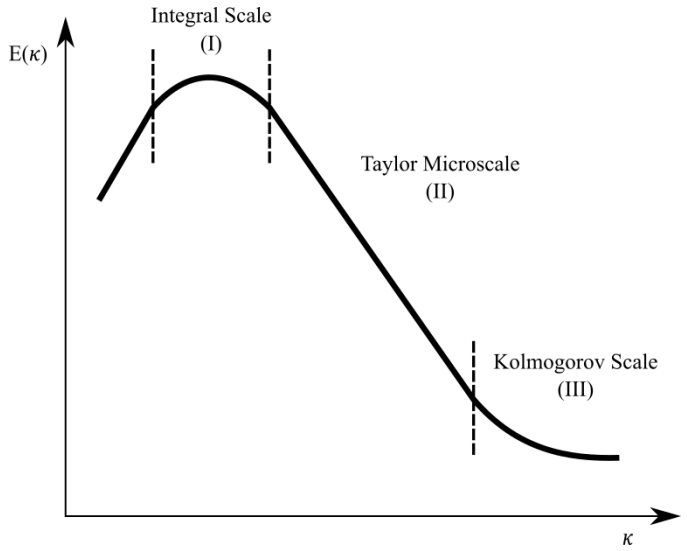

Figure 2.1: Turbulent energy spectrum, adapted from [80].

The total turbulent kinetic energy of the system (k) can be calculated from the area under the spectrum, as shown in Equation 2.20.

$$k = \int_0^\infty E(\kappa)\, d\kappa \tag{2.20}$$

This spectrum can also be represented as an energy cascade, showing the energy flowing from large eddies to small eddies, before being dissipated at the Kolmogorov scales. This is illustrated in Figure 2.2.

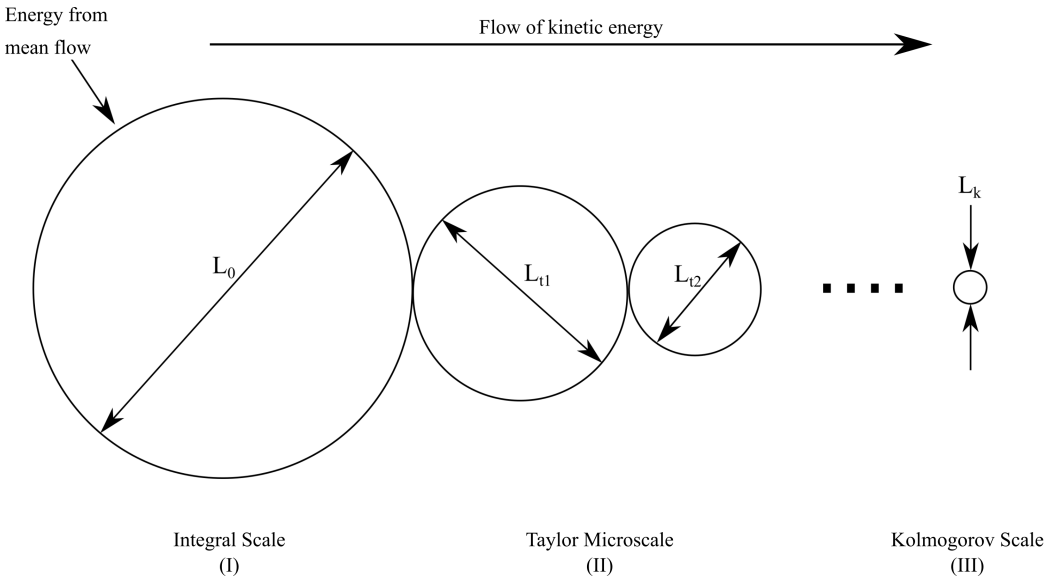

Figure 2.2: Turbulent energy cascade, adapted from [79].

Figure 2.1 shows that the majority of the turbulent energy of a system is contained within the largest eddies; this energy is provided by the mean flow of the system as shown in Figure 2.2. The cascade of energy from large to small eddies is caused by the eddy interactions, which transfers kinetic energy down the eddy scale. At the lowest eddy length scales the viscous stresses begin to dominate and diffuse the energy to the surroundings in the form of thermal energy. This energy transfer is constant per unit time for each eddy size, and is called the turbulent diffusion rate (ε); ε is proportional to the kinematic viscosity (ϑ) and the square of the fluctuating velocity between the eddies [77]. Within the Kolmogorov scales the dissipation dominates, and can account for approximately 90% of the total energy dissipated from the system [79].

Diesel sprays are highly turbulent in nature given their high injection pressures (1500 bar or more) and hence high injection velocities, commonly above 300 m/s within most of the liquid region of the spray [46]. Modelling the effect of the turbulent flow on the injected parcels and vapour fields for a diesel spray is crucial for predicting the spray formation, propagation and combustion. Within this body of work the standard k-ε model will be used; it is described in detail in the following section.

2.2.1 The k-ε Turbulence Model

The k-ε model considers the transport of the turbulent kinetic energy (k) and the turbulent dissipation rate (ε) throughout the domain being considered. This model and its variants are extremely commonly used due to their versatility of application and, within spray modelling, their ability to capture global spray characteristics (such as the liquid and vapour lengths, as well as lift-off-lengths) with very small tuning requirements [49, 81–84]. Within this study the standard k-ε model will be used due to its improved ability to predict spray formation. The transport equations for both k and ε are shown in Equations 2.21 and 2.22 [77].

$$\frac{\partial(\rho k)}{\partial t} + \mathrm{div}(\rho k \mathbf{U}) = \mathrm{div}\left[\frac{\mu_t}{\sigma_k}\mathrm{grad}(k)\right] + 2\mu_t S_{ij}.S_{ij} - \rho\varepsilon \tag{2.21}$$

$$\frac{\partial(\rho\varepsilon)}{\partial t} + \mathrm{div}(\rho\varepsilon\mathbf{U}) = \mathrm{div}\left[\frac{\mu_t}{\sigma_\varepsilon}\mathrm{grad}(\varepsilon)\right] + C_{1\varepsilon}\frac{\varepsilon}{k}2\mu_t S_{ij}.S_{ij} - C_{2\varepsilon}\rho\frac{\varepsilon^2}{k} \tag{2.22}$$

Both equations are of a very similar format with 5 major terms in each. The k transport equation (Equation 2.21) is broken down into its constituent parts below, with a brief explanation of the role of each term in the transport of k.

$\frac{\partial(\rho k)}{\partial t}$	+	$\mathrm{div}(\rho k\mathbf{U})$	=	$\mathrm{div}[\frac{\mu_t}{\sigma_k}\mathrm{grad}(k)]$	+	$2\mu_t S_{ij}.S_{ij}$	-	$\rho\varepsilon$
(I)		(II)		(III)		(IV)		(V)
Rate of Change of TKE		Convective Transport of TKE		Diffusive Transport of TKE		Rate of Production of TKE		Rate of Destruction of TKE

The eddy viscosity (μ_t) is calculated based off the density, turbulent kinetic energy and dissipation and is shown in Equation 2.23 [77].

$$\mu_t = \rho C_\mu \frac{k^2}{\varepsilon} \tag{2.23}$$

From Equations 2.21, 2.22 and 2.23 there are 5 model constants in total; the common values for these are shown in Table 2.1. These constants were analytically derived during the derivation of the model [80], however are tunable for different situations. σ_k and σ_ε are the turbulent Prandtl-Schmidt numbers for TKE and turbulent dissipation rate respectively [77, 85].

Table 2.1: k-ε model constants and their common values for diesel spray modelling

Constant	**Value**
C_μ	0.09
$C_1\varepsilon$	1.44
$C_2\varepsilon$	1.92
σ_k	1
σ_ε	1.3

The two prominently used tunable constants are $C_{1\varepsilon}$ and $C_{2\varepsilon}$, as seen in the ε transport equation (Equation 2.22). These control the levels of production and destruction of turbulent dissipation respectively, and as such are powerful tuning tools for matching experimental spray prediction [74].

2.3 Spray Atomisation Modelling

Atomisation modelling simulates the near-nozzle flow and initial break-up of the liquid just after injection, otherwise known as primary break-up. The differences between primary and secondary break-up are detailed in Figure 2.3, with the models acting on each break-up regime noted. The primary break-up pertains to modelling the initial surface wave growth on the droplets, with the secondary break-up modelling the effect of the aerodynamic forces on the droplets. Both break-up regimes act to reduce the diameter of the droplets, with droplet volume lost through either surface waves or aerodynamic forces causing smaller droplets to be shed from the initial, larger, droplet.

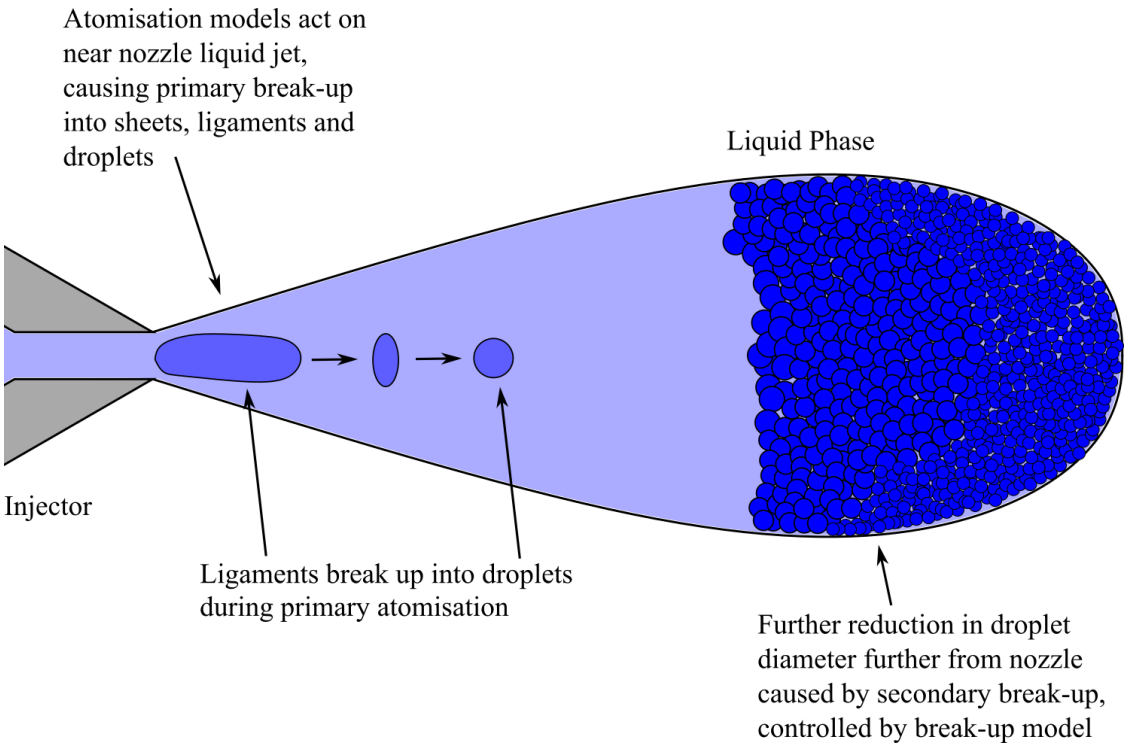

Figure 2.3: Simplified primary and secondary break-up regime schematic, showing where relevant models apply to the liquid phase of the spray

As the liquid is injected into the domain the liquid jet disintegrates into sheets, ligaments and droplets [28]. When the droplets have formed from the liquid jet disintegration secondary break-up forces act on the droplets, causing a further reduction in the droplet diameter due to the stresses on the surface of the droplet causing shedding of mass [28]. Approximations of both primary and secondary break-up mechanisms are shown within this Chapter, with the assumptions made about each mechanism shown.

Computational modelling cannot feasibly track every droplet injected into a system, and as a result droplets are collected into parcels containing droplets of similar size [47]. It is on these parcels that the atomisation and break-up models act, along with all the other models.

Primary break-up can either be handled by the break-up model alone (as is the case for the KH-RT model, explained in Section 2.4.2) or by a standalone atomisation model (as is used for the Reitz-Diwakar model). In this second case, the Huh-Gosman model is used to simulate the atomisation of the liquid into droplets in the near nozzle region. Both methods of handling the primary break-up have been heavily used [49, 81–84, 86] and are well matched to experimental data. The initial droplet diameter in both cases is set to the nozzle diameter, an injection method called "blob" injection [34].

2.3.1 Huh-Gosman Atomisation Model

The Huh-Gosman model is based on the assumption that the gas inertia and initial turbulent stresses within the nozzle are the dominant factors for spray atomisation [35]. As a result, the model simulates the turbulence within the nozzle that acts on the jet surface in the injection phase, then applies Taylor wave theory to simulate the initial surface wave growth caused by this turbulence [35]. The inputs for this model are the mean injection velocity (calculated from the mass flow rate), and the nozzle length and diameter, with the model outputting the spray cone angle and child droplet diameter.

The nozzle turbulence is modelled using a modified, reduced k-ε model, as shown in Equations 2.24 and 2.25 [35, 87].

$$k_A = \frac{\overline{U_{inj}}^2}{8\frac{L}{D_{inj}}}\left(\frac{1}{c_d^2} - K_c - 1\right) \tag{2.24}$$

$$\varepsilon_A = \frac{K_\varepsilon \overline{U_{inj}}^3}{2L}\left(\frac{1}{c_d^2} - K_c - 1\right) \tag{2.25}$$

With $\overline{U_{inj}}$ defined as the mean injection velocity, L the length of the injector nozzle, c_d the nozzle discharge coefficient, D_{inj} the injector nozzle diameter, K_c the "form loss" model constant and K_ε an empirically derived model constant. All model constants are shown in Table 2.2. Following on from the modified k-ε model, the turbulent length and time scales can also be calculated as in Equations 2.26 and 2.27.

$$L_t^0 = C_\mu^{0.75}\frac{k_A^{1.5}}{\varepsilon_A} \tag{2.26}$$

$$\tau_t^0 = C_\mu^{0.75}\frac{k_A}{\varepsilon_A} \tag{2.27}$$

With C_μ defined as in Section 2.2, Table 2.1. The decay of the scales shown in Equations 2.26 and 2.27 due to turbulence is dependent on time and two more model constants, as shown in Equations 2.28 and 2.29.

$$L_t(t) = L_t^0\left(1 + C_{a1}\frac{t}{\tau_t^0}\right)^{C_{a2}} \tag{2.28}$$

$$\tau_t(t) = \tau_t^0\left(1 + C_{a1}\frac{t}{\tau_t^0}\right) \tag{2.29}$$

Where C_{a1} and C_{a2} being model constants. Further scales include the atomisation length scale, the wave perturbation length scale and the atomisation time scale. The atomisation length scale is proportional to the turbulent length scale, with the wave perturbation length scale related to the atomisation length scale (shown in Equations 2.30 and 2.31). The atomisation time scale is taken to be a linear combination of the turbulent and wave time scales, and is shown in Equation 2.32.

$$L_A = C_1 L_t \tag{2.30}$$

$$L_w = \frac{L_A}{C_2} \tag{2.31}$$

$$\tau_A = C_3 \tau_t + C_4 \tau_w \tag{2.32}$$

Where the wave time scale (τ_w) is the inverse of the surface wave frequency (ω_A), which is calculated as in Equation 2.33 [88].

$$(\omega_A + 2\vartheta\kappa^2)^2 + \frac{\sigma_{st}\kappa^3}{\rho_d} - 4\vartheta^2\kappa^3\left(\kappa^2 + \frac{\omega_A}{\vartheta}\right)^{0.5} + (\omega_A + jU\kappa)^2\frac{\rho_g}{\rho_d} = 0 \tag{2.33}$$

With σ_{st} the surface tension coefficient and j the imaginary unit $\sqrt{-1}$. The common values for the model constants shown throughout this section are shown in Table 2.2.

Table 2.2: Huh-Gosman model constants and their values [35]

Model Constant	**Constant Value**
K_c	0.45
K_ε	0.5
C_{a1}	0.92
C_{a2}	0.4565
C_1	2
C_2	0.5
C_3	1
C_4	1.5

Now, a droplet size distribution is defined. The droplets are initialised with a diameter equal to the nozzle diameter, and shown as D_d. The break-up rate within this model is shown in Equation 2.34.

$$\frac{dD_d}{dt} = -\frac{2L_A}{0.1\tau_A} \tag{2.34}$$

This holds true until the spontaneous time scale ($C_3\tau_t$) exceeds the exponential time scale ($C_4\tau_w$). The diameter of the child droplets formed after the primary break-up is derived from a probability density function, from which the new droplet diameter is selected. The probability density function is defined in Equation 2.35.

$$f(D) = C\frac{\Phi(D)}{\tau_A(D)} \tag{2.35}$$

With C a normalisation constant and $\Phi(D)$ the dimensionless turbulent energy spectrum, defined in Equation 2.36.

$$\Phi(D) = \frac{(\kappa(D)/\kappa_e)^2}{(1+(\kappa(D)/\kappa_e)^2)^{11/6}} \tag{2.36}$$

With the peak wavenumber (κ_e) defined based on the turbulent length scale, as shown in Equation 2.37.

$$\kappa_e = \frac{1.5\pi}{L_t} \tag{2.37}$$

The full distribution function, *F(D)*, is the integral of the original pdf from Equation 2.35, and is defined in Equation 2.38.

$$F(D) = \int_{D_{min}}^{D} f(D)\ dD \tag{2.38}$$

The lower limit for the integral is the minimum droplet diameter, which is calculated from Kelvin-Helmholtz instability theory, described in Equation 2.39.

$$D_{min} = 2\pi\frac{\sigma_d(\rho_d+\rho_g)}{U^2\rho_d\rho_g} \tag{2.39}$$

When applied, the new droplet diameter is chosen from the probability distribution in Equation 2.38, shown in Figure 2.4, with the new droplet velocity equal to the previous droplet velocity given conservation of mass is applied.

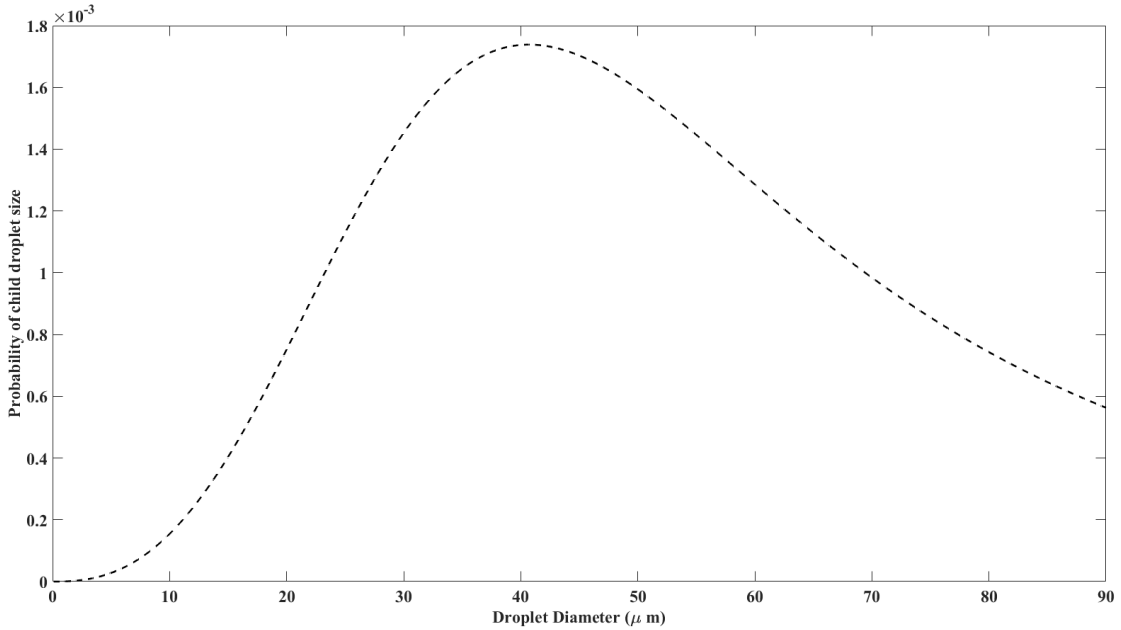

Figure 2.4: Droplet size probability distribution from the Huh-Gosman atomisation model, using values in Table 2.2 [35]

Finally, the spray semi-cone angle (β) is calculated. This is determined based off the injection velocity and atomisation length and time scales, and shown in Equation 2.40.

$$\tan(\beta) = \frac{L_A/\tau_A}{U} \tag{2.40}$$

This also sets the maximum radial velocity, which would occur if the droplet was injected directly along the axis of injection. However, this does not always occur physically, and as such the components for the droplet velocity in the x, y and z direction are calculated from β and the characteristic velocity (u_{ch}), the calculated injection velocity from the fuel mass flow rate. These components are defined in Equations 2.41 to 2.43.

$$u_{d,x} = u_{ch}\sin(\beta_d)\cos(\alpha_d) \tag{2.41}$$

$$u_{d,y} = u_{ch}\sin(\beta_d)\sin(\alpha_d) \tag{2.42}$$

$$u_{d,z} = u_{ch}\cos(\beta_d) \tag{2.43}$$

Where the angles β_d and α_d are randomised angles, based on the relationships shown in Equations 2.44 and 2.45.

$$\beta_d = X_{r,1}\beta \tag{2.44}$$

$$\alpha_d = 2\pi X_{r,2} \tag{2.45}$$

With $X_{r,1}$ and $X_{r,2}$ being random numbers in the range of [0,1]. A schematic of the spray cone angle is shown in Figure 2.5.

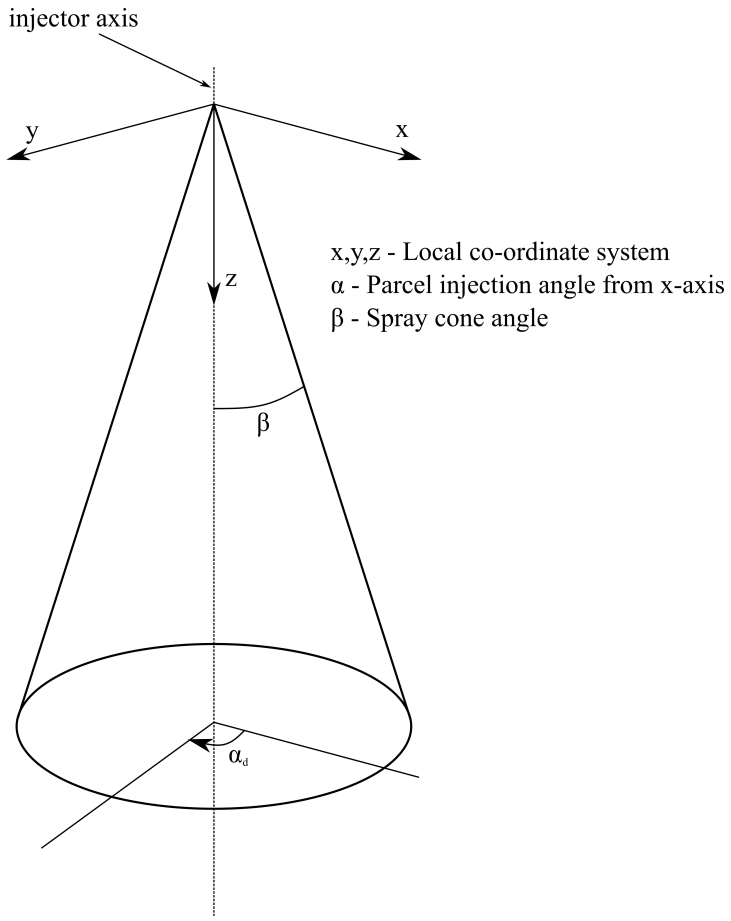

Figure 2.5: Schematic of injection system, with cone angle noted. Adapted from [87]

2.4 Spray Break-Up Modelling

A key model for simulating the spray formation and propagation is the spray break-up model, which governs how the injected Lagrangian parcels break-up during the injection period. The break-up model considers the secondary break-up of the spray, whereby the already atomised droplets reduce in size over time. Two models are considered in this thesis, the Reitz-Diwakar model [89] and the Kelvin-Helmholtz/Rayleigh-Taylor (KH-RT) model [45] in the viscous form [44].

Within both models, a droplet break-up rate ($\frac{dD_d}{dt}$) is required to compute the diameter of the droplets after break-up. This is shown in Equation 2.46 [87]. This break-up rate is based on the current droplet diameter (D_d), the stable droplet diameter ($D_{d,stable}$) and the droplet break-up time scale (τ). The stable droplet diameter and droplet break-up time scale are calculated within each model.

$$\frac{dD_d}{dt} = -\frac{D_d - D_{d,stable}}{\tau} \tag{2.46}$$

For both models shown, the liquid and ambient properties are required, along with the droplet size and velocity for inputs; the KH-RT model also requires the cone angle of the spray as an input. The droplet break-up time scale and stable diameter are the outputs of the models, which are used in Equation 2.46 to calculate the droplet break-up rate. The Reitz-Diwakar model is applied to droplets that have already undergone break-up from the atomisation model, whereas the KH-RT model is applied for the whole spray, with the Kelvin-Helmholtz model considering the primary break-up of the droplets and the Rayleigh-Taylor model considering the secondary break-up. Within Star-CD the application of either of the sub-models (bag/strip for Reitz-Diwakar or KH/RT) is decided based on the break-up time scale calculated, with the shortest predicted time scale chosen as the dominant break-up mode. The applicability of this will be discussed further in Chapter 4.

2.4.1 Reitz-Diwakar Model

Within the Reitz-Diwakar model two types of break-up are considered: a bag break-up and a strip break-up, with both being modelled to have been caused by aerodynamic forces acting on the droplet [89]. The difference between these break-up mechanisms are shown in Figure 2.6.

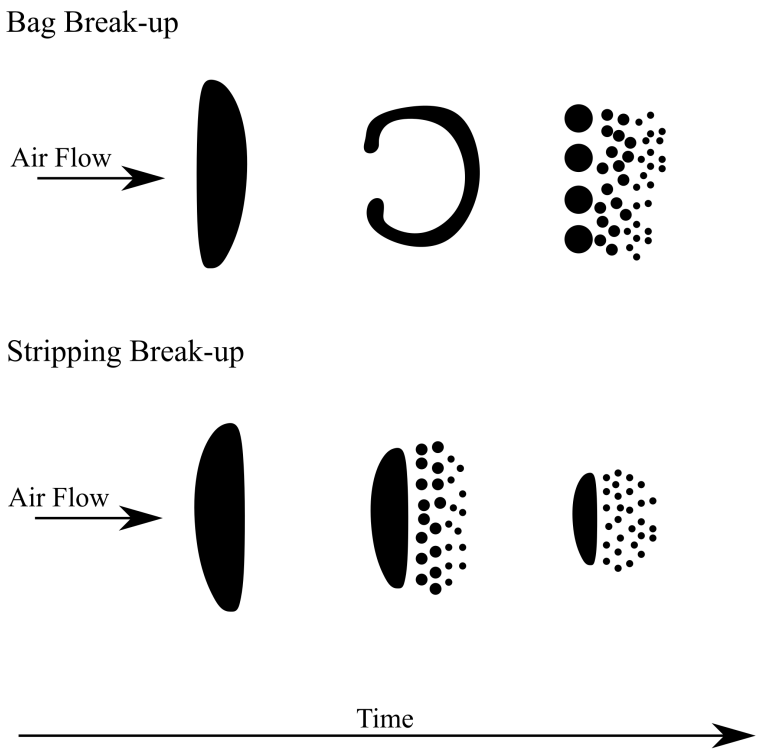

Figure 2.6: Bag and strip break-up mechanisms. Adapted from [90].

Bag Break-Up Modelling

For bag break-up to occur the droplet Weber (We_b) number (as shown in Equation 1.3) must exceed a critical value, defined as C_{b1}, which is tunable by the user. Given the Weber number compares the drag force and the droplet's surface tension it is an excellent dimensionless number to use to predict droplet formation and break-up. This yields the relationship shown in Equation 2.47.

$$We_b \equiv \frac{\rho_d U^2 D_d}{2\sigma_d} \geq C_{b1} \tag{2.47}$$

This allows the stable droplet diameter to be found at the point when the critical value is met and break-up just begins, as shown in Equation 2.48.

$$D_{d,stable} = \frac{2C_{b1}\sigma_d}{\rho_d U^2} \tag{2.48}$$

The corresponding break-up time scale is defined in Equation 2.49 [89].

$$\tau_b = \frac{C_{b2}\rho_d^{0.5} D_d^{1.5}}{4\sigma_d^{0.5}} \tag{2.49}$$

With C_{b2} defined as another model constant. All model constants and their common values for the Reitz-Diwakar break-up model are shown in Table 2.3.

Strip Break-Up Modelling

A different criterion to that seen in Equation 2.47 is used for stripping break-up to occur, this is shown in Equation 2.50.

$$\frac{We_d}{\sqrt{Re_d}} \geq C_{s1} \tag{2.50}$$

When this criterion is just met then stripping break-up begins to occur. As with before, at this point the stable droplet diameter can be calculated, and is shown in Equation 2.51.

$$D_{d,stable} = \frac{4\sigma_d C_{s1}^2}{\rho_d U^2 \mu_d} \tag{2.51}$$

Where C_{s1} being a model constant. The time scale is defined as in Equation 2.52 [89].

$$\tau_s = \frac{C_{s2}}{2}\left(\frac{\rho_d}{\rho_g}\right)^{0.5}\frac{D_d}{U} \tag{2.52}$$

Where C_{s2} is the final model constant for the Reitz-Diwakar break-up model. The baseline values whenever used in this thesis for all of these constants can be found in Table 2.3.

Table 2.3: Reitz-Diwakar model constants and their values and boundaries [87, 89]

Model Constant	Baseline Value	Value Boundaries
C_{b1}	6	3.6 - 8.4
C_{b2}	π	π
C_{s1}	0.5	0.5
C_{s2}	20	2 - 20

2.4.2 Kelvin-Helmholtz/Rayleigh-Taylor Model

For the KH-RT model the droplet radii are used within calculations, with the parent droplet radius (r_p) and child droplet radius (r_c) corresponding to the droplet diameter (D_d) and stable droplet diameter ($D_{d,stable}$) respectively. These can be easily converted to diameters for use within Equation 2.46 after the stable radius has been calculated. As with the Reitz-Diwakar model, within Star-CD the KH and RT models act simultaneously with the time scales determining which model acts at any one time. A visualisation of the KH and RT models effects on the droplet is shown in Figure 2.7, with the droplets noted with their child radii.

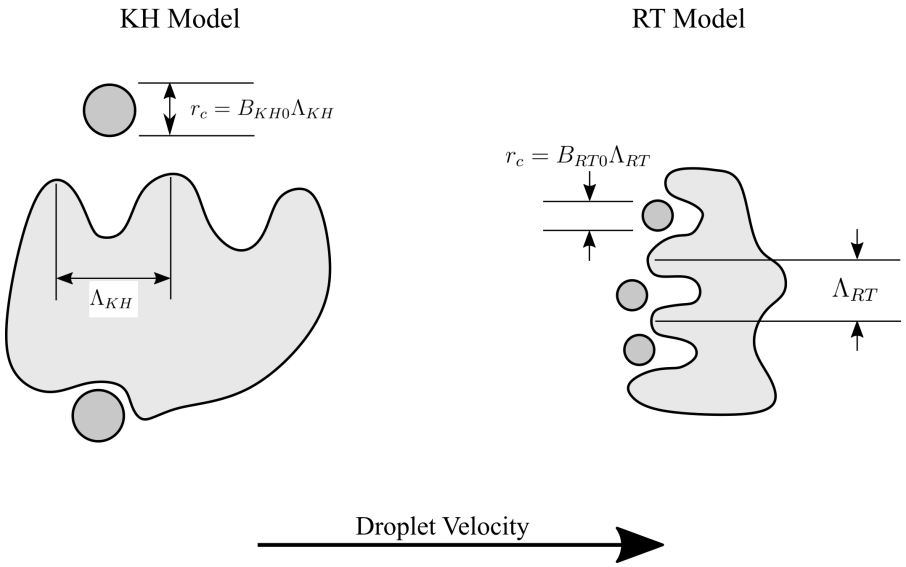

Figure 2.7: KH and RT break-up model visualisations. Adapted from [34, 44, 87]

KH Break-Up Model

The KH model predicts the wavelength and growth rate of surface waves as they develop on the droplet based on the flow conditions [34]. Knowledge of the flow conditions allow for the stable droplet diameter and break-up time scale to be calculated. The maximum computed surface growth rate is defined as the cause of break-up, and the wavelength corresponding to this growth rate is calculated as in Equation 2.53.

$$\Lambda_{KH} = 9.02 \frac{r_p\left(1 + 0.45Z_d^{0.5}\right)\left(1 + 0.4T^{0.7}\right)}{\left(1 + 0.87We_g^{1.67}\right)^{0.6}} \tag{2.53}$$

With Z_d being the droplet Ohnesorge number (Equation 2.54) and T being the Taylor number (Equation 2.55).

$$Z_d = \frac{\sqrt{We_d}}{Re_d} \tag{2.54}$$

$$T = Z_d\sqrt{We_g} \tag{2.55}$$

The corresponding maximum surface growth rate to Equation 2.53 is calculated as in Equation 2.56.

$$\Omega_{KH} = \left(\frac{\sigma_d}{\rho_d r_p^3}\right)^{0.5} \frac{0.34 + 0.38We_g^{1.5}}{(1 + Z_d)(1 + 1.4T^{0.6})} \tag{2.56}$$

When the growth rate and wavelength are calculated the child droplet radius and time scale can be calculated as in Equations 2.57 and 2.58.

$$r_c = B_{KH0}\Lambda_{KH} \tag{2.57}$$

$$\tau_{KH} = \frac{3.726B_{KH1}r_p}{\Lambda_{KH}\Omega_{KH}} \tag{2.58}$$

With B_{KH0} and B_{KH1} being two model constants, with their values being shown in Table 2.4.

RT Break-Up Model

The RT model simulates instabilities based on the aerodynamic forces acting on the droplet causing disturbances on the droplet surface. This is simulated using an acceleration which is then applied to the viscid model [44]. The acceleration is calculated as in Equation 2.59.

$$a_{RT} = \frac{3}{8} C_d \frac{\rho_g U^2}{\rho_d r_p} \tag{2.59}$$

With the value for the drag coefficient (C_d) based on the Reynolds number, shown in Equation 2.60.

$$C_d = \begin{cases} \frac{24}{Re_d}(1 + \frac{1}{6} Re_d^{0.6667}) & Re_d < 1000 \\ 0.424 & Re_d \geq 1000 \end{cases} \tag{2.60}$$

As in the KH model, the maximum surface growth rate is the critical break-up factor for the RT model. Within the viscid RT model the surface growth rate is defined as in Equation 2.61 [44].

$$\omega_{RT} = \kappa_{RT}^2 \left(\frac{\mu_d + \mu_g}{\rho_d + \rho_g} \right) + \sqrt{\kappa_{RT} \left(\frac{\rho_d - \rho_g}{\rho_d + \rho_g} \right) a_{RT} - \kappa_{RT}^3 \frac{\sigma_d}{\rho_d + \rho_g} + \kappa_{RT}^4 \left(\frac{\mu_d + \mu_g}{\rho_d + \rho_g} \right)^2} \tag{2.61}$$

With κ_{RT} being the wavenumber. The wavenumber that corresponds to the maximum growth rate is K_{RT}, and can be found using a numerical bisection method of Equation 2.61, leading to a maximum surface wave growth rate of Ω_{RT}. The methodology used for the numerical bisection method used is presented in Appendix A. The wavelength for the maximum surface growth rate is calculated as shown in Equation 2.62.

$$\Lambda_{RT} = \frac{2\pi}{K_{RT}} \tag{2.62}$$

From the calculated wavelength and growth rate the child droplet radius and break-up time scale can be calculated as shown in Equations 2.63 and 2.64.

$$r_c = B_{RT0}\Lambda_{RT} \tag{2.63}$$

$$\tau_{RT} = \frac{B_{RT1}}{\Omega_{RT}} \tag{2.64}$$

With B_{RT0} and B_{RT1} being the final model constants for the KH-RT model. The constants and their baseline values whenever used in this thesis are shown in Table 2.4.

Table 2.4: KH-RT model constants and their values and boundaries [34, 45, 87]

Model Constant	**Baseline Value**	**Value Boundaries**
B_{KH0}	0.6	0.6 - 0.61
B_{KH1}	7	5 - 40
B_{RT0}	0.1	0.05 - 0.1
B_{RT1}	1	1

3 Domain Characterisation

Before undertaking investigations into the break-up of diesel spray the spray domain needs to be suitably characterised. To this end, a grid sensitivity study was undertaken along with sub-model testing to ensure that the domain refinement is sufficient to capture the spray characteristics and that the models chosen to predict the spray are correct. The initial ambient turbulence and dissipation are also defined for the study to best match the experimental data, with the impact of changing these also characterised. Utilising these studies, a baseline domain can be generated for use in future research which is well characterised and converged to an acceptable level of accuracy to the baseline conditions.

3.1 Grid Sensitivity Study

3.1.1 Background

The first step in any domain characterisation is to undertake a grid sensitivity study to ensure that various spray parameters are well captured and grid independent. This grid sensitivity study is in the style presented by Senecal [46], which builds on the work by Lippert [53]. This study has also been used on combusting cases in both RANS and LES [54, 55]. The goal of a grid sensitivity study is to develop a domain where key spray parameters have converged with respect to the cell size, whilst also keeping run times to an acceptable level.

For this study the Engine Combustion Network (ECN) "Spray A" condition will be used. The "Spray A" test point is a high temperature and pressure case with well characterised experimental data available for validation [24, 27], with the conditions for this test point shown in Table 3.1. Within the Sandia set-up the

Table 3.1: ECN vaporising "Spray A" experimental conditions [24, 27]

Fuel Surrogate	n-dodecane
Ambient Temperature (K)	900
Ambient Gas Density (kg/m^3)	22.8
Ambient Gas Composition	89.71 % N_2, 6.52 % CO_2, 3.77 % H_2O
Injection Pressure (bar)	1500
Fuel Injection Temperature (K)	363
Nozzle Diameter (μm)	90
Injection Duration (ms)	1.5
Injection Mass (mg)	3.5

conditions are reached using a pre-burn chamber, whereby a small amount of fuel is ignited before the test, and the injection of note is started when the ambient conditions reach the desired temperature and pressure. As a result, the ambient gas composition contains combustion products in small quantities in comparison to the N_2 quantity. Further information on the exact Sandia set-up can be found in Pickett's initial paper on the ECN project [24].

The experimental data is taken from Sandia [24], with Mie Scattering used to obtain the liquid lengths and schlieren imaging used for the vapour lengths. Further details on the methodology used for obtaining the liquid lengths can be found in the work of Siebers [91]. For this study the liquid and vapour lengths are presented as ranges, based on the 95 % confidence interval obtained from the standard deviation and errors obtained by Sandia. The transient period of the spray is defined as the first 0.3 ms of injection, after which the spray is in its "steady state" and the mean liquid length can be taken.

A grid sensitivity study was undertaken to investigate the impact of the cell size on the spray formation and propagation. This study is in the style presented by Senecal [46], which builds on the work by Lippert [53]. This study has also been used on combusting cases in both RANS and LES [54, 55]. The goal of this study

is to develop a domain where key spray parameters have converged with respect to the cell size, whilst also keeping run times to an acceptable level.

3.1.2 Methodology

The CFD code Star-CD is used for this study, which uses a structured, pre-generated cubic mesh to compute the injection. The injection was computed as a transient problem, utilising the PISO solver to solve the RANS equations. A time step of 0.5 μs was chosen through tests as a good compromise between number of time steps and maintaining a low Courant number (<0.1). As a result targeted refinement has been employed around the liquid region to ensure convergence of key parameters within this region of the spray. This refinement is defined by an Embed Scale (ES), with the cell size (dx) being calculated based on a base cell size (dx_{base}) as shown in Equation 3.1.

$$dx = dx_{base} \times 2^{-\mathrm{ES}} \tag{3.1}$$

For this study a base cell size of 2 mm was chosen, and embed scales of 0 to 5 are utilised. The domain being modelled is a 108 mm cube, yielding the cell sizes and cell counts shown in Table 3.2. With each refinement of the grid the parcel number was increased by a factor of 4 to ensure that an over-prediction in liquid length is not seen due to an under-prediction in drag outside the liquid core [46]. This would be caused by parcels containing a much higher mass than that contained within a cell, and as such the momentum transfer between the parcel and the cell would bring the cell's velocity up to that of the parcel, which outside the liquid core would be undesirable. By increasing the parcel count the mass within each parcel is reduced, and as such this parcel-cell interaction's effects are reduced [46]. The parcel counts selected here are estimates based on previous knowledge, and will be discussed further in Section 3.1.4.

Table 3.2: Embed scales and corresponding cell sizes and cell counts

Embed Scale	0	1	2	3	4	5
dx	2mm	1mm	0.5mm	0.25mm	0.125mm	0.0625mm
Cell Count	157464	212344	380344	491672	778056	1063950
Parcel Count	50000	200000	800000	3200000	12800000	51200000

The refinement of the mesh is shown in Figure 3.1, with the refinement targeted around the injector location. The baseline set-up utilises the models shown in Table 3.3, which are the baseline models used in Star-CD. Almost all of the constants are at their standard values, except for the $C_1\varepsilon$ constant which is raised from 1.44 to 1.52; this constant controls the production of turbulent dissipation [77, 92] and is often varied to match liquid and vapour lengths within RANS modelling. The models can be found in more detail in literature [35, 77, 87, 89, 92]. In this case the value of 1.52 was chosen from previous knowledge, however it can be altered based on the results of this study.

Eight different spray parameters were chosen to determine grid convergence, these are as follows:

- Liquid Length
- Vapour Length
- Vapour Mass Fraction
- Density
- Eddy Viscosity
- Turbulent Length Scale
- Velocity
- Turbulent Kinetic Energy

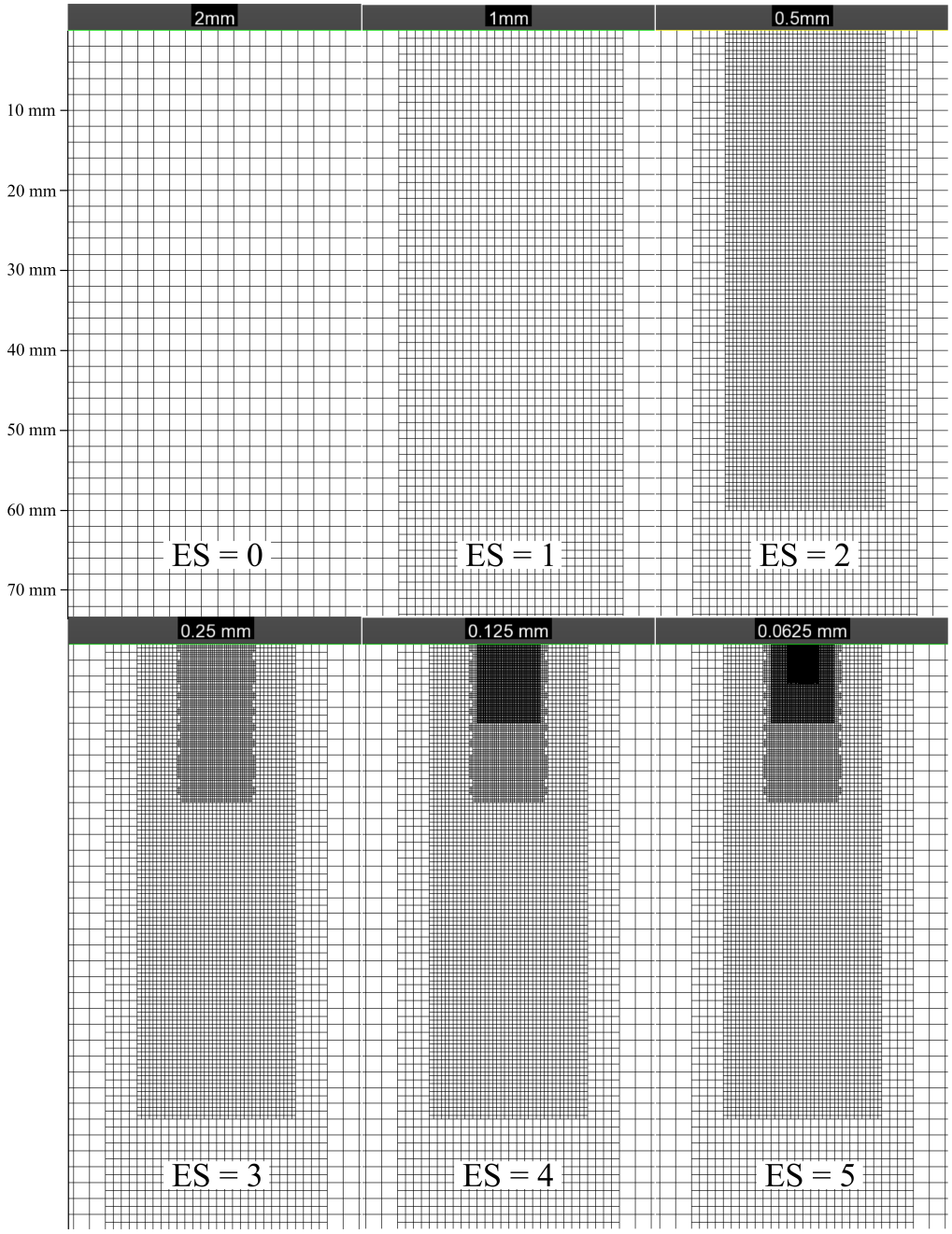

Figure 3.1: Spray domains used for grid sensitivity study, showing increasing targeted refinement. Embed scales are noted for comparison

All of these parameters are measured along the axis of injection at 1 ms ASOI, Figure 3.2 shows a screenshot from the post-processing suite ENSIGHT showing how this was taken. The liquid and vapour lengths are defined by the Engine Combustion Network (ECN), with the liquid length currently defined as the length encompassing 97 % of the liquid mass, and the vapour length defined as the furthest cells containing a mass fraction of fuel greater than 0.1 % [27].

Table 3.3: Sub-models used in grid sensitivity study

Model Class	**Model Used**
Atomisation	Huh-Gosman [35]
Break-Up	Reitz-Diwakar [42]
Drag	Dynamic [87]
Collision	None
Evaporation	Ranz-Marshall [87]
Turbulence	Standard k-ε [92]

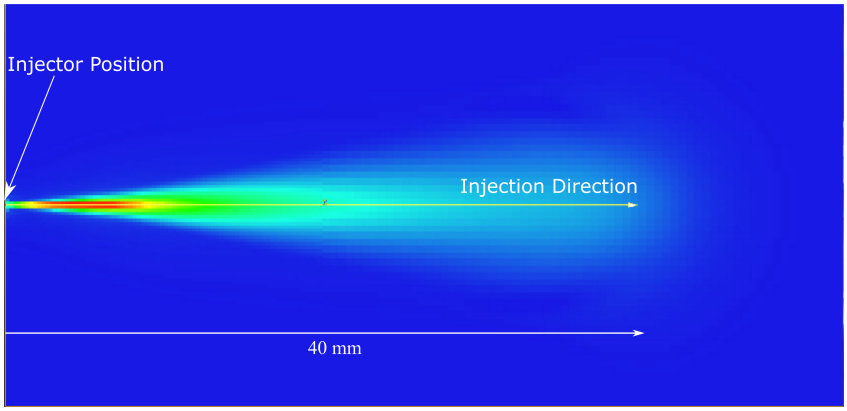

Figure 3.2: Measurement axis visualisation from ENSIGHT for extracting spray parameters

3.1.3 Results

The first comparators of note are the liquid and vapour lengths; these are generally grid convergent at larger cell sizes than other comparators and as such are a good initial test of convergence within a study. These can be seen in Figures 3.3 and 3.5, which show the liquid and vapour lengths respectively. The liquid length shows a

clear convergence towards the mean, with good results being shown in embed scales between 3 and 5. The transient period is noteworthy in this study, as in all cases above an embed scale of 1 there is a transient overshoot. This is believed to be a product of either the break-up or atomisation models and this will be discussed in more detail in Chapter 4 with a comparison between CFD codes. The steady state liquid length means for each case are compared to the experimental steady state liquid length mean in Table 3.4, showing that for embed scales of 4 and higher the simulated steady state liquid length lies within the experimental uncertainty, which is also shown in Figure 3.3. It should be noted that a small increase in the $C_{1\varepsilon}$ constant will remedy the slight under-prediction of liquid length seen in the embed scale 3 case. From the work of Senecal et al. [46], should the embed scale increase from 5 to 6 the liquid length mean will remain mostly unchanged, given the change in liquid length mean between each embed scale has been reducing as the embed scale increases. Another point of note in Figure 3.3 is the transient overshoot seen in all embed scales around 0.1 ms ASOI. This is of interest given the importance of correctly predicting short injections (as discussed in the introduction), and will be examined further in Chapter 4.

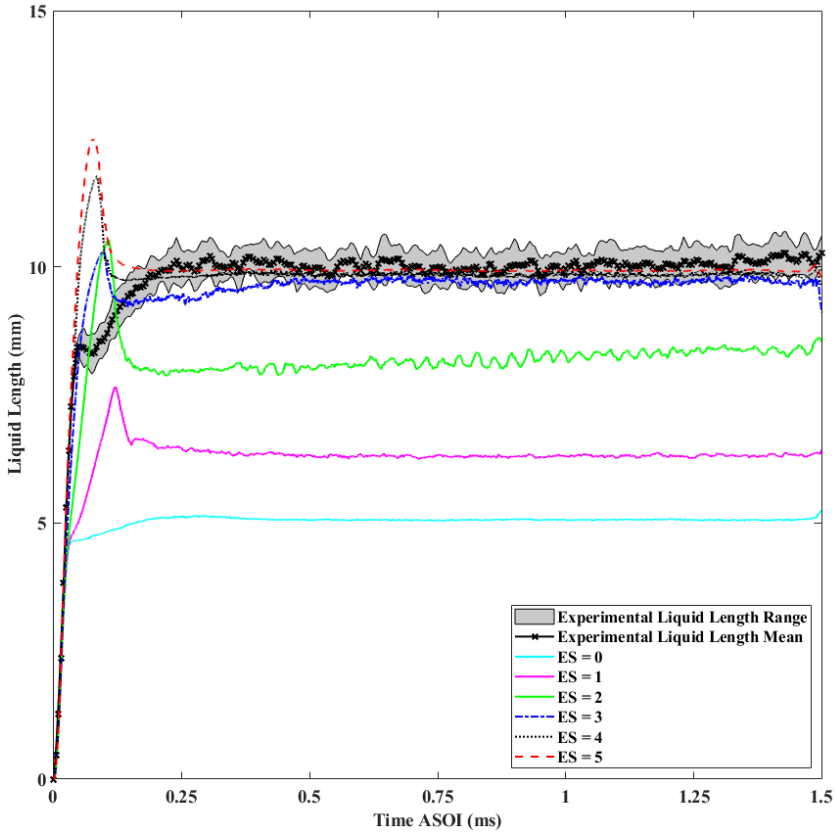

Figure 3.3: Liquid length against time ASOI for all embed scales

Table 3.4: Liquid length means and final vapour lengths for all embed scales

Embed Scale	Liquid Length Mean	Final Vapour Length
0	5.07 mm	47 mm
1	6.32 mm	57.5 mm
2	8.18 mm	53.75 mm
3	9.71 mm	53.25 mm
4	9.86 mm	53.25 mm
5	9.93 mm	53.25 mm
Experimental	10.08 ± 0.34 mm	56.85 ± 2.56 mm

The run time trade off against liquid length mean prediction can be seen in Figure 3.4, which clearly shows the increasing run time caused by the increased cell count and parcels injected. The run time is also shown to have a knee around an embed scale of 3, with the simulation run time exponentially increasing past this point.

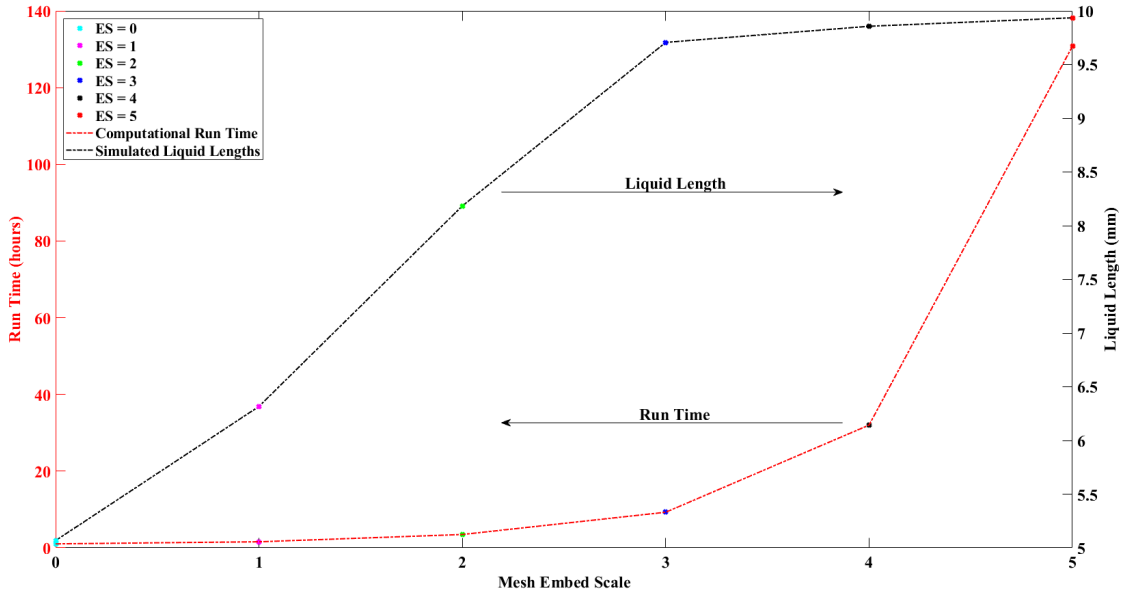

Figure 3.4: Liquid length convergence with run time variation against increasing embed scales

Figure 3.5 shows the convergence trend amongst the vapour lengths; with an increasing embed scale showing a reduction in final vapour length, however the final vapour length converges at an embed scale of 2. This mirrors the findings of Senecal et al. [46], who also found smaller cell sizes showing a lower vapour length than predicted by experiments. As with the liquid length the convergence is clear to see, with embed scales of 2 and above all predicting a very similar vapour length after 0.5 ms. Higher embed scales show an improved prediction of the initial vapour length, however they diverge once beyond the refined zone of the domain. Slight reductions in the initial gradients of the vapour lengths can be seen in the embed scale 3 and above cases around 0.2 ms ASOI, this is believed to be caused by the transient overshoot seen in Figure 3.3 causing a higher than expected initial vapour penetration.

The vapour mass fraction is plotted in Figure 3.6. The trend of convergence is seen in the maximum values, with small differences between embed scales 3-5 being seen before the maximum value. The peak at 5 mm from the injector seen at the highest embed scales suggests some very early vaporisation occurs at this

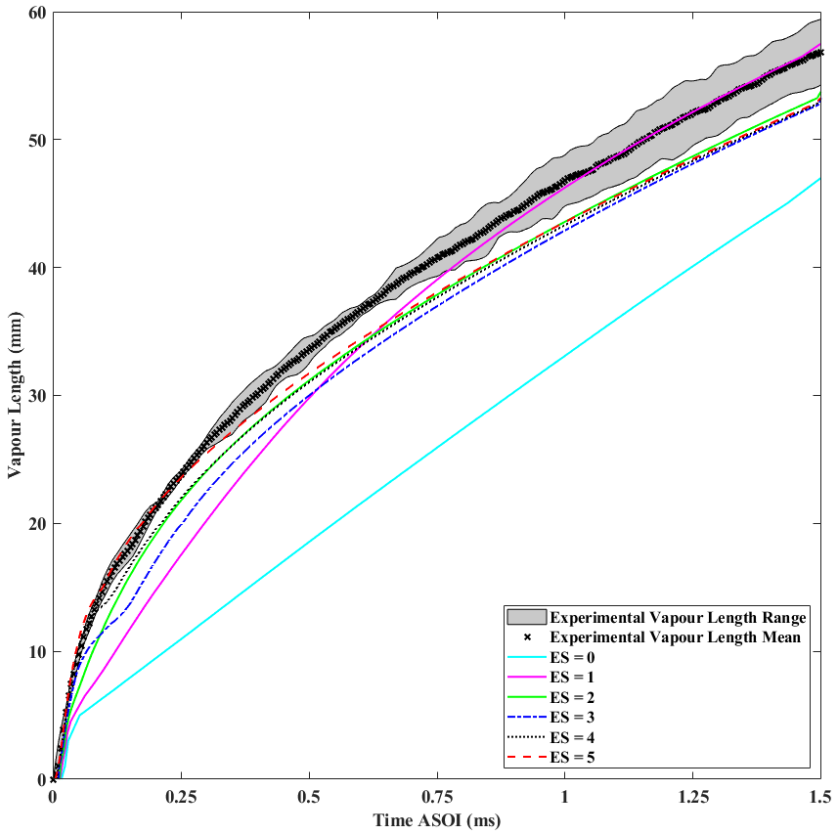

Figure 3.5: Vapour length against time ASOI for all embed scales

distance, however the position of the maximum vapour mass fraction is just beyond the liquid length of 10 mm, which is to be expected.

The density closely follows the vapour mass fraction trends, and can be seen in Figure 3.7. Very similar trends are seen with the local maxima for the two highest embed scales seen at ∼5 mm from the injector, and all three of the highest embed scales having very similar global maxima. In both of these two previous cases the embed scale of 2 has been capturing the trends of the higher embed scales, but failing to catch the finer details; with the two lowest embed scales failing to capture either the trend or the details with any precision.

The eddy viscosity is also underpredicted by lower embed scales, as seen in Figure 3.8. The convergence trend is weaker in this case compared to before; whilst the values at ∼40 mm from the injector tip are converged for embed scales greater than 2 the eddy viscosities before 20 mm from the injector tip show variation with

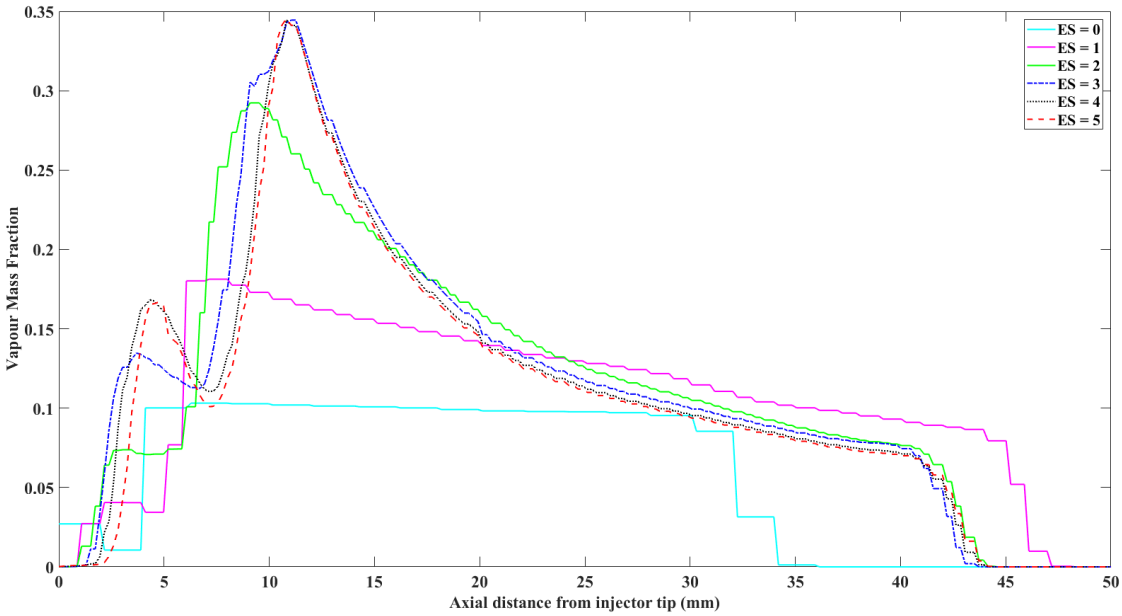

Figure 3.6: Vapour mass fraction against axial distance from injector tip for all embed scales @ 1 ms ASOI

each embed scale. There is still a trend towards convergence however, with the difference clearly decreasing with each successive refinement.

Correct prediction of the eddy viscosity is important, given its impact on the both the turbulent kinetic energy and turbulent dissipation rate of the system. Figure 3.8 shows that for an embed scale of 3 the eddy viscosity is lower than the higher embed scales up until approximately 20 mm from the injector tip. Despite this, the liquid length is not under-predicted to the same level as the eddy viscosity, and the other comparators used in this study suggest that this under-prediction is not as important as the saving in run-time utilising a lower embed scale provides.

The turbulent length scales (TLS) at varying embed scales will show if the spray is being properly resolved for the majority of the spray. The TLS is calculated as shown in Equation 3.2, with the TLS varying based on the Turbulent Kinetic Energy (k), the Turbulent Dissipation Rate (ε) and a model constant (C_μ).

$$TLS = C_\mu^{0.75} \frac{k^{1.5}}{\varepsilon} \tag{3.2}$$

If the TLS is larger than the cell size at that point in time, the spray is considered to be well defined. Near to the nozzle this will be extremely difficult due to the

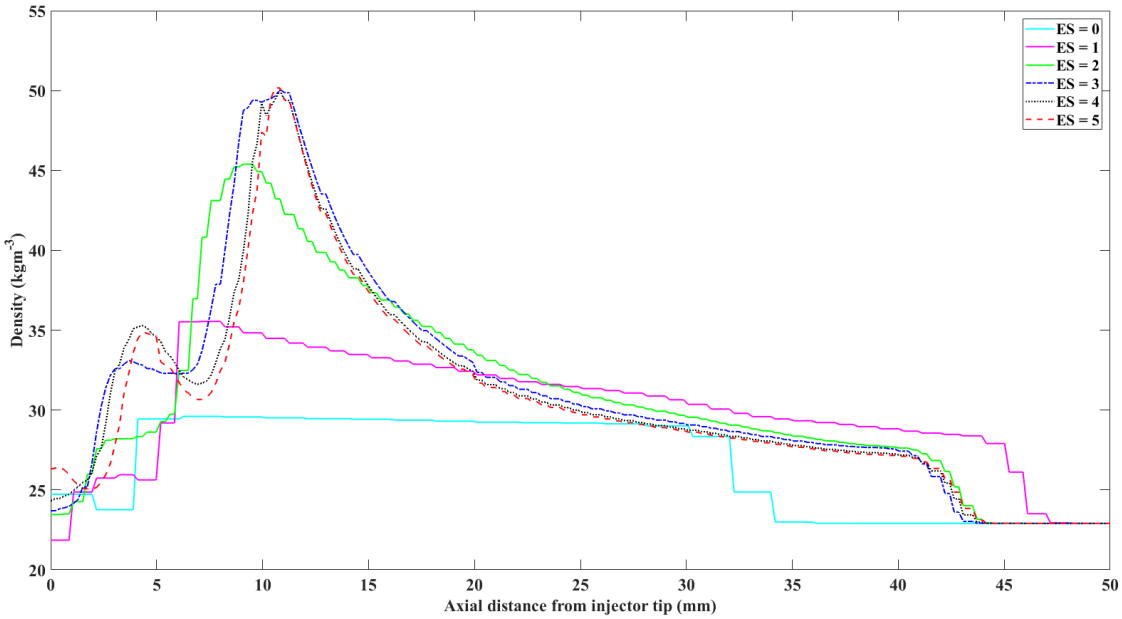

Figure 3.7: Density against axial distance from injector tip for all embed scales @ 1 ms ASOI

extremely high turbulence in the near nozzle region. The TLS plots for this study can be seen in Figure 3.9. The TLS is larger than the cell size for the embed scale of 5 for almost all of the spray, with each successive drop down in refinement yielding less of the spray TLS being larger than the cell size. Figure 3.9 also clearly shows why the two lowest embed scales poorly predict the spray, with neither being able to resolve the turbulence at any position in the spray.

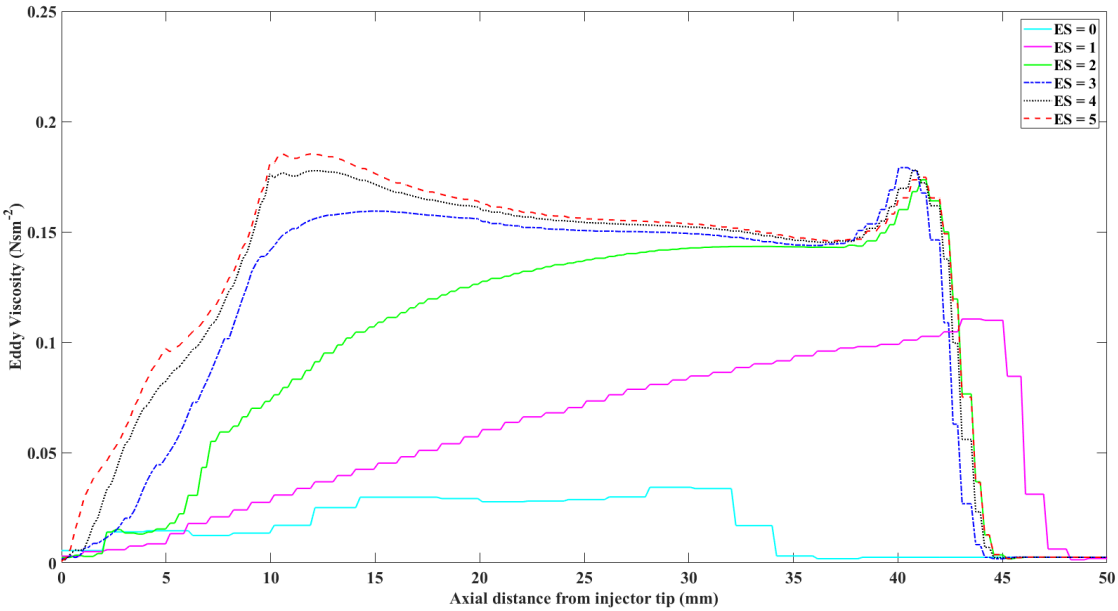

Figure 3.8: Eddy viscosity against axial distance from injector tip for all embed scales @ 1 ms ASOI

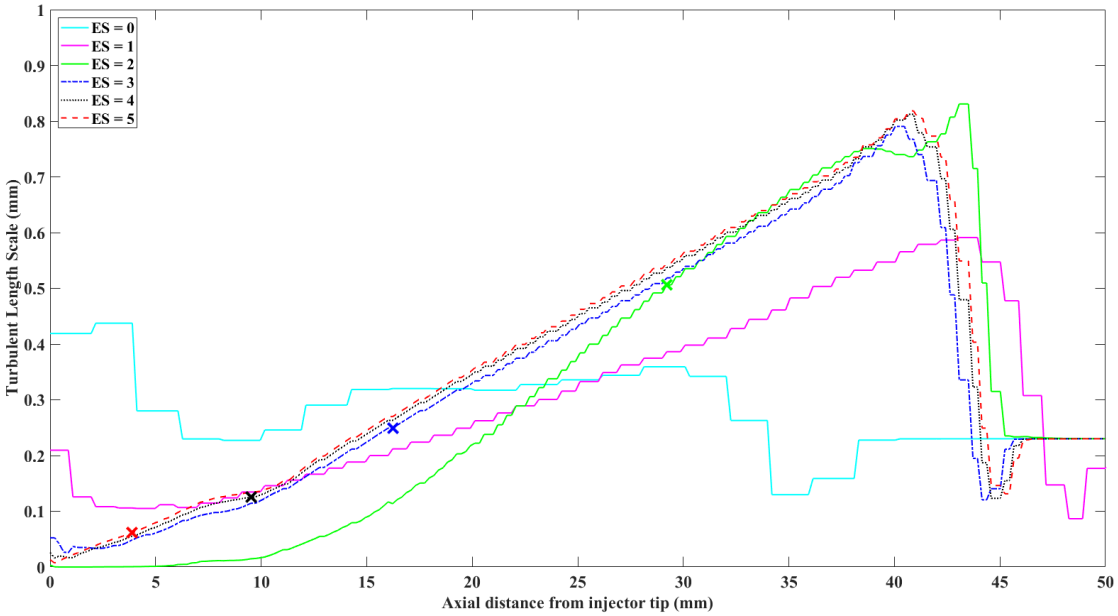

Figure 3.9: Turbulent length scale against axial distance from injector tip for all embed scales @ 1 ms ASOI. The coloured crosses signify the point at which the spray becomes "well resolved" for each embed scale

Finally, the velocity and turbulent kinetic energy (TKE) are considered. Senecal et al. [46] found that convergence for the velocity was not found below an embed scale of 6 (0.0325 mm), and that before this the velocity approximately increased linearly with each subsequent refinement of the grid. The velocity for this study can be found in Figure 3.10. It can be seen that convergence is not reached for the maximum velocity in any embed scale, with each refinement increasing the maximum velocity in an approximately linear fashion. As a result, given the relationship shown between velocity and TKE (shown in Equation 3.3), the maximum TKE should increase exponentially between refinements. This is shown in Figure 3.11, and is shown to qualitatively hold true.

$$k = 1.5\overline{u'^2} \tag{3.3}$$

The peak in the velocities seen the embed scales of 4 and 5 are believed to be due to more accurate resolving of the droplet drag near to the nozzle with the reduction in cell size. During the steady state period of the spray the near nozzle droplets are expected to have little to no drag acting on them, and as a result with each reduction in cell size the drag on the droplet reduces near nozzle. The

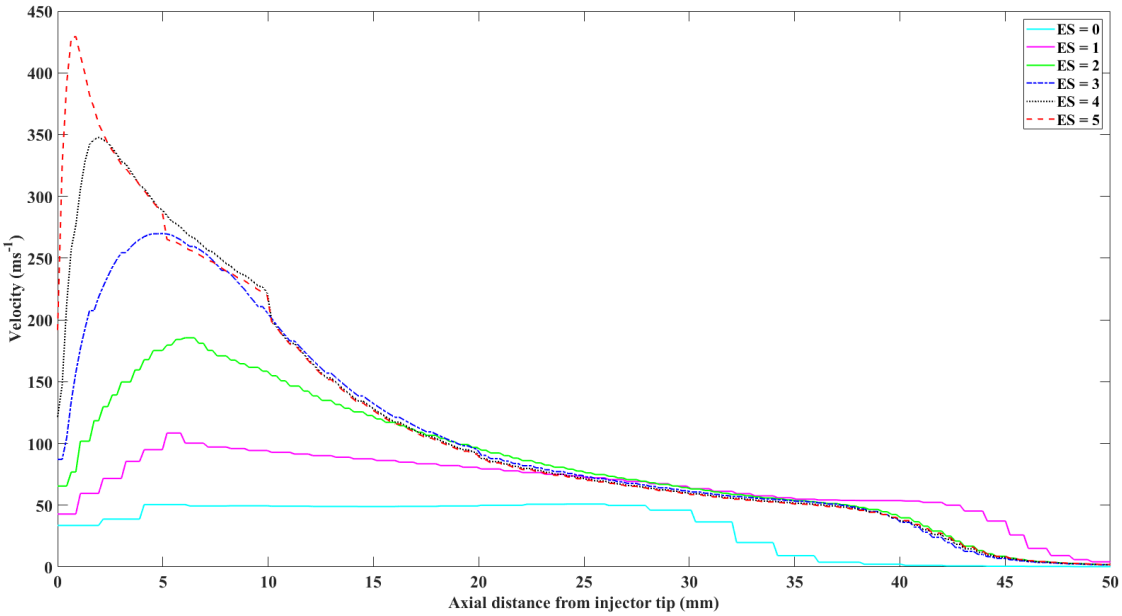

Figure 3.10: Velocity against axial distance from injector tip for all embed scales @ 1 ms ASOI

convergence of the embed scales 3 to 5 after 5 mm from the injector tip suggests it is adequately resolved after this point however.

A clearer demonstration of the convergence seen within this study can be seen in Figure 3.11, showing the maximum values of each parameter shown previously. It can be seen at embed scales of 3 and above in almost all parameters convergence has been reached, with only the velocity (Figure 3.11h) and TKE (Figure 3.11g) not showing convergence; however displaying the expected linear and exponential relationships with respect to embed scale. This lack of convergence has also been seen in other studies at these embed scales [46] and as such is not deemed to be representative of a poorly refined domain.

Considering the showings of Figures 3.4 and 3.11, convergence is reached above an embed scale of 3 for almost all criteria, with the run time increasing exponentially above an embed scale of 3. However, with a possible reduction in parcel count the embed scale of 4 could also be used, so long as this reduction does not adversely affect the results or spray patterns due to under-resolution of the liquid phase within the higher refined domain. As a result, a study on the impact of the parcel count on the results is needed to find an optimum value for the parcel count for both embed scales 3 and 4, and hence find the best trade off between refinement, parcel count, run time and accuracy for this domain.

3.1.4 Impact of Parcel Count on Spray Prediction

Parcel Study Methodology

From the results of the previous study there was a choice of domains to be used, with embed scales 3 and 4 both providing good data and convergent trends. The major differences between the domains were in the liquid length predictions, with 3 being outside of experimental range and 4 within; this can be improved with some simple tuning of the $C_{1\varepsilon}$ constant and as such is not deemed important. The other major difference was in the run time, with 3 taking approximately 9 hours to run and 4 taking approximately 32 hours. This is less easily tuned, however a large contributor to the extended run time is the parcel count injected. As Table

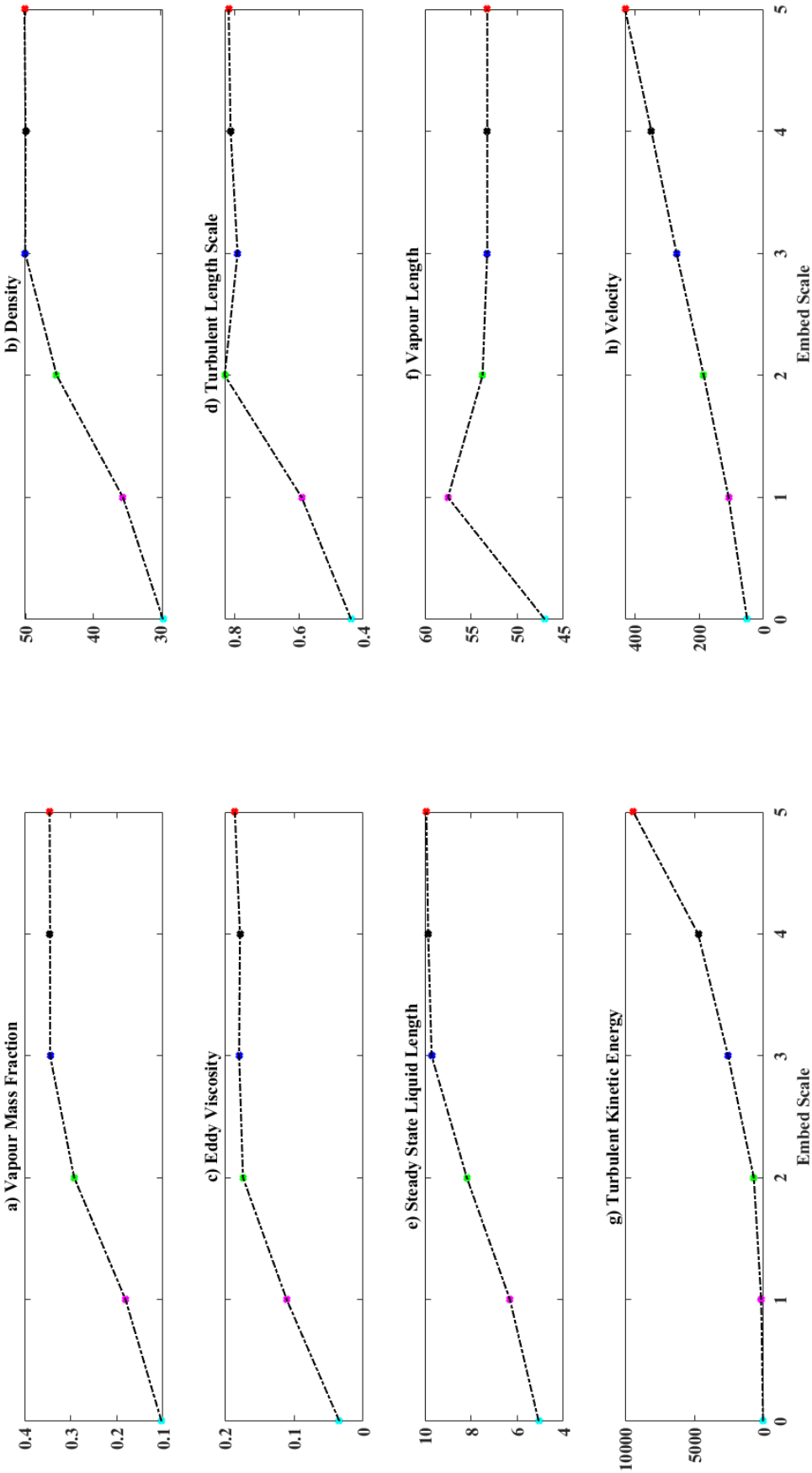

Figure 3.11: Maximum values for each parameter considered as a function of grid embed scale

3.2 shows, there is a factor of 4 difference between the two, with both injecting over 3 million parcels into the domain. This is considered too many parcels for either domain, and as a result a saving in run time can be found by reducing the injected parcel count. This study was conducted on both domains, and the liquid and vapour lengths are compared along with the run time to see how great a saving can be found by simply reducing the parcel number.

Results

Utilising the embed scale 3 and 4 domains from the previous grid sensitivity study (Section 3.1), the parcel numbers were reduced from the maximum numbers seen in that study (Table 3.2) in 4 stages, which are approximately equal in difference. The different parcel numbers tested for each simulation are shown in Table 3.5, with a parcel scaling number used for each increase in parcels injected into each domain.

Table 3.5: Parcel scaling for each domain tested

Parcel Scaling	1	2	3	4	5
ES 3 Parcel Number	714084	1428769	2138577	2853326	3421899
ES 4 Parcel Number	2666886	5331919	7998184	10664073	13652327

All other model constants are kept the same between runs, with the only variable being the parcel number. The liquid and vapour lengths, along with the run times, are compared to see if there is any impact on the global spray properties from reducing the parcel number. Initially, the liquid and vapour lengths are compared over the whole injection period; for the embed scale 3 domain this is shown in Figure 3.12 and for the embed scale 4 domain this is shown in Figure 3.13. Similar effects of the transient overshoot on the vapour length are seen in both cases at around 0.15 ms ASOI, mirroring that shown in the grid sensitivity study.

These Figures show that there is very little difference in either the liquid or vapour lengths when the parcel number is changed; which is further confirmed when considering the steady state liquid lengths for each embed scale. This is demonstrated in Figure 3.14.

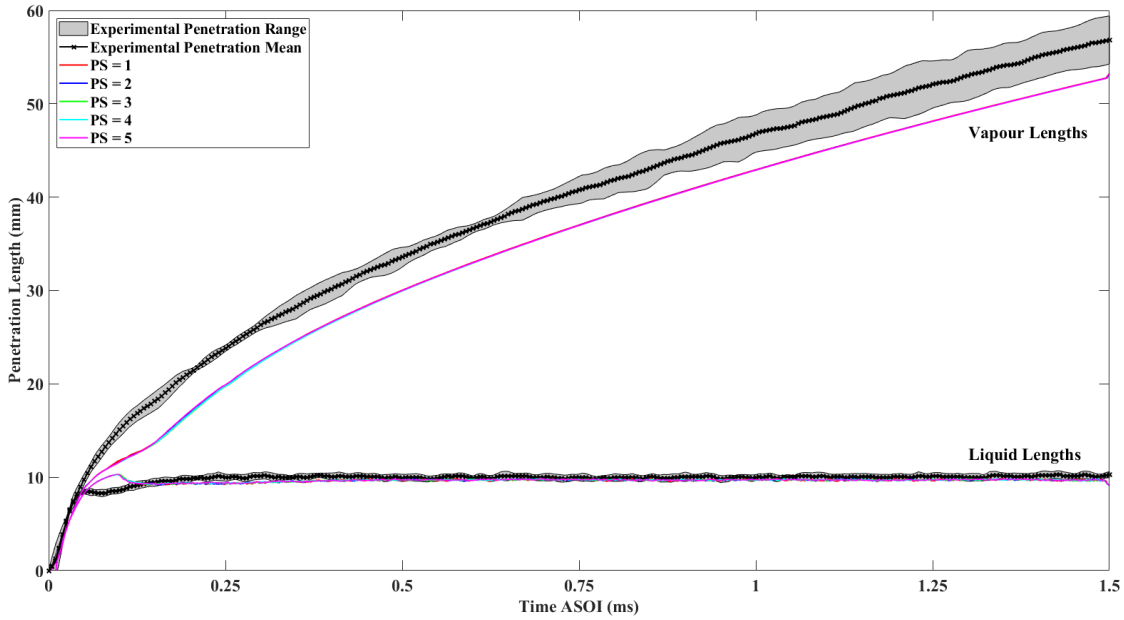

Figure 3.12: Liquid and vapour penetrations for varying parcel numbers with the embed scale 3 domain, plotted against time ASOI. Liquid and vapour lengths are shown on the plot for reference, these are consistent throughout the thesis

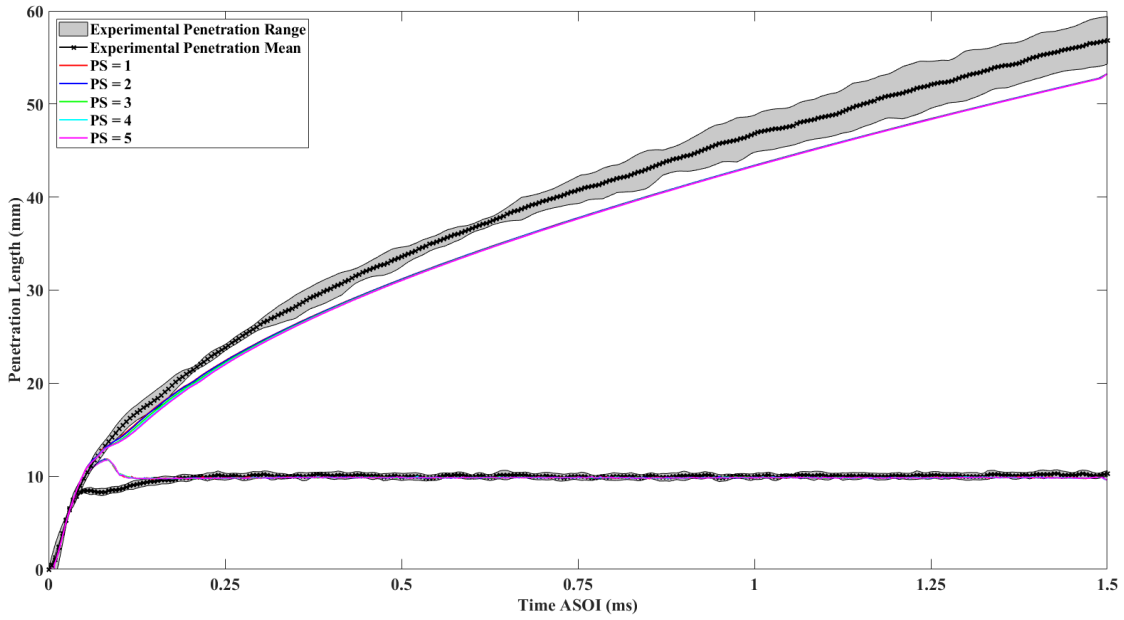

Figure 3.13: Liquid and vapour penetrations for varying parcel numbers with the embed scale 4 domain, plotted against time ASOI

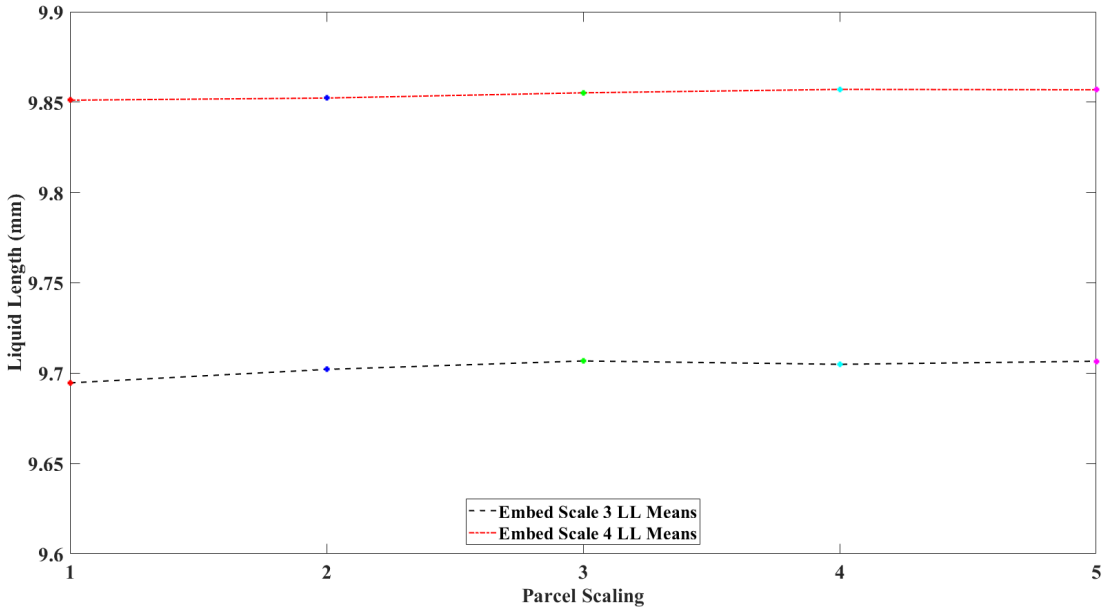

Figure 3.14: Steady state liquid length means for both embed scales considered for varying parcel numbers

From Figure 3.14 there is no obvious linear relationship between an increase in parcel number and the steady state liquid length mean, and as a result it can be determined that the liquid length (at these parcel numbers considered) is independent of the parcel number. This suggests that the initial estimate for the parcel count made in Table 3.2 was too high, and the parcel count could have been reduced without impacting the liquid length predictions. For the embed scale 3 domain the means lie around 9.7 mm, and for the embed scale 4 domain the means lie around 9.85 mm, which is what was seen in the previous grid sensitivity study.

The other major computational parameter considered within this study was the computational run time. Given each parcel has to be tracked throughout the domain at all timesteps until evaporation it suggests that increasing the number of parcels injected into the domain will increase the run time. This is confirmed in Figure 3.15, which show both the increase in parcels with the parcel scaling and the run time's variation with respect to the parcel number for both cases considered. Along with this, both figures show that the relationship between parcels injected and run time is highly linear, as expected, with R^2 values of 0.9999 and 0.9995 for the embed scales 3 and 4 respectively shown in Figure 3.15b and Figure 3.15d.

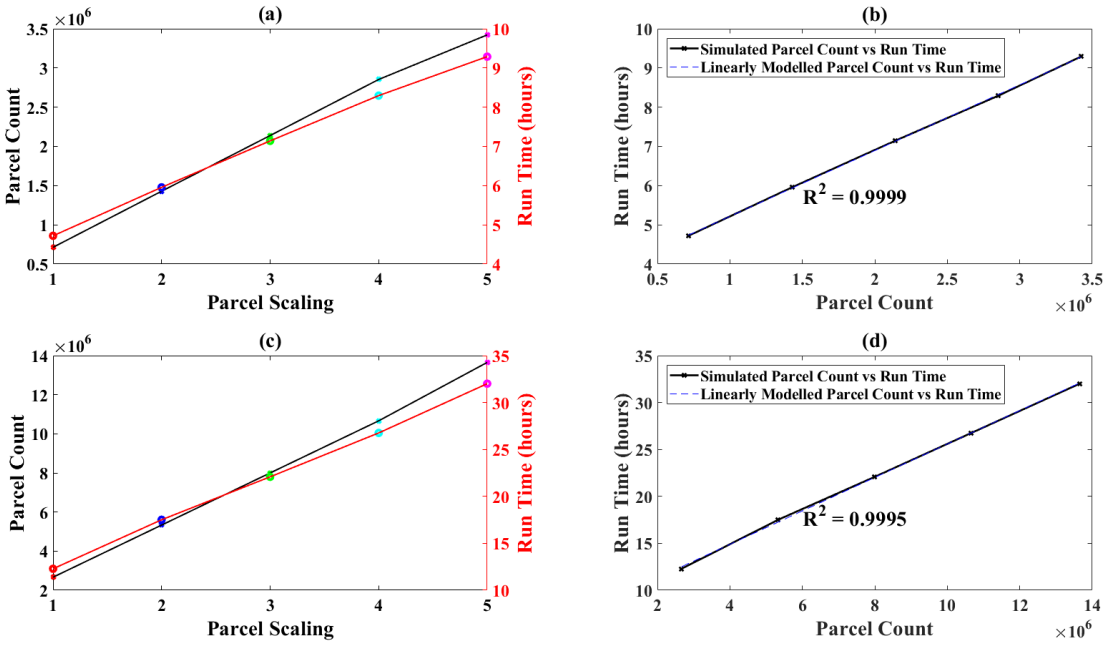

Figure 3.15: Run time as a function of parcel number for both domains, **(a)** and **(b)** for embed scale 3, **(c)** and **(d)** for embed scale 4

Going forward, the PS value of 1 will be used for the domain for all future simulations.

3.2 Impact of Ambient Turbulence Criteria on Spray Predictions

3.2.1 Background

The values for the initial ambient turbulence and dissipation rates can be modified within Star-CD, allowing for matching to different spray combustion chambers. Given the common values of ambient velocity shown in Pickett's paper [24] ranging from 0.1 to 2 m/s, the impact of the ambient turbulence and dissipation needs to be quantified for the domain presented to ensure correct predictions are obtained. It has also been shown that slight differences in the turbulence of the domain have impacts on the OH fields of a combusting spray [93], and as such correctly defining the turbulence in the domain is critical for all parts of the spray.

Values for the ambient TKE were derived from Pickett's paper [24]; with some additions above and below the values from the paper for further extrapolation,

shown in Figure 3.16. The dissipation values were taken from commonly used values within Star-CD for spray modelling. The values considered are shown in Table 3.6.

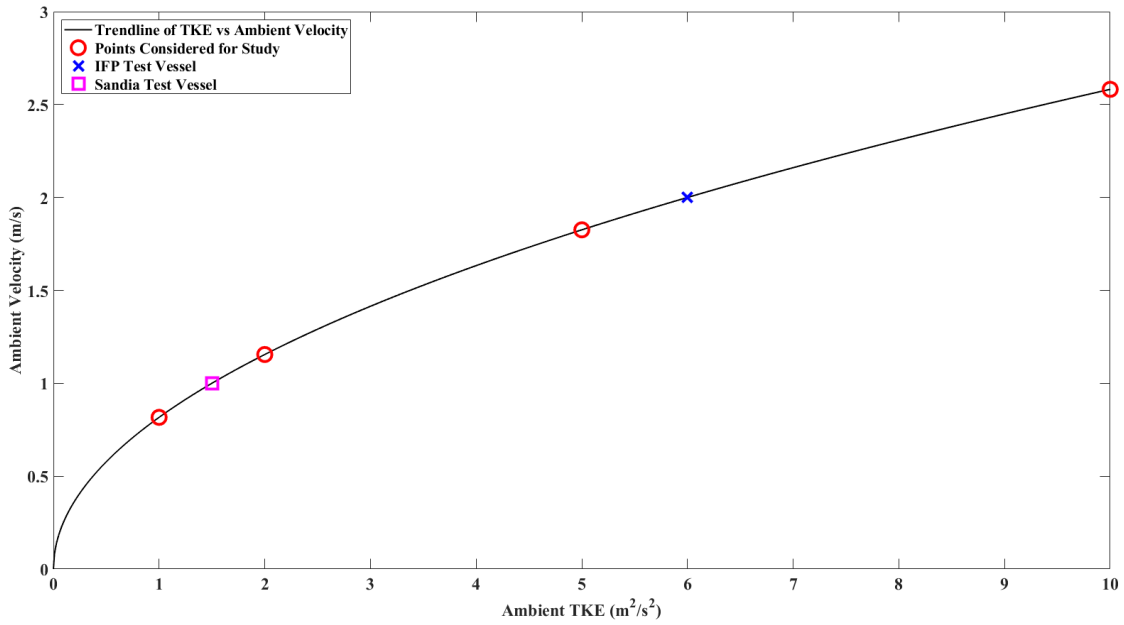

Figure 3.16: Ambient TKE as a function of velocity, with the Sandia and IFP spray chambers noted along with points taken for this study

Table 3.6: Ambient TKE and dissipation values used in study

k (m^2/s^2)	ε (m^2/s^3)
1	1000
2	2000
5	**3000**
10	5000

The baseline conditions for the study are bolded in Table 3.6; when the TKE value is varied the dissipation is set to 3000 m^2/s^3, similarly whilst the dissipation is varied the TKE is set to 2 m^2/s^2.

3.2.2 Ambient Turbulent Kinetic Energy Results

As was shown in the work of Ameen et al. [93], the ambient turbulence can have an impact on combusting sprays, however the spray structures only were shown,

with no comparison of the impact on the liquid and vapour lengths of the spray. As a result, the impact of this alteration in ambient TKE is needed to be quantified for this domain as well, to ensure accurate predictions of different spray chambers (especially important with validating data from the CDST in future). Considering the values of k from Table 3.6, the liquid and vapour lengths can be plotted for the different values, as shown in Figure 3.17. As can be seen, there is little change in the mean liquid lengths by varying the TKE, however the initial transient overshoot is reduced with an increase in ambient TKE. This is to be expected, as a higher ambient turbulence will cause a quicker aerodynamic break-up for the first parcels entering the domain, and hence will reduce the overshoot seen. The vapour lengths are consequently impacted by this reduced overshoot, with larger discrepancies between ambient TKE values seen in the first millisecond of injection than in the final half millisecond. The comparisons of liquid length means, final vapour lengths and transient overshoot is shown in Table 3.7.

Table 3.7: Liquid lengths, overshoots and vapour lengths for varying ambient TKE

k (m^2/s^2)	**Liquid Length (mm)**	**Transient Overshoot (mm)**	**Vapour Length (mm)**
1	9.91	3.74	52.25
2	9.89	2.17	51.75
5	9.83	1.00	51.25
10	9.79	-0.04	50.75

The reduction in vapour length is small compared to the increase in ambient TKE, suggesting that there is only a weak interaction between turbulent kinetic energy and the vapour penetration. This is in sharp contrast to the large reduction in the transient overshoot seen with increasing TKE, especially when the liquid length for each increase in TKE is only slightly reduced (by approximately 1 %). It is also notable that for the highest ambient TKE considered there is no overshoot of the steady state liquid length, with a peak being seen that is lower than the steady state liquid length. One interesting point is that with an increase in TKE the "dip" after the transient overshoot in liquid length is increased, suggesting that the liquid

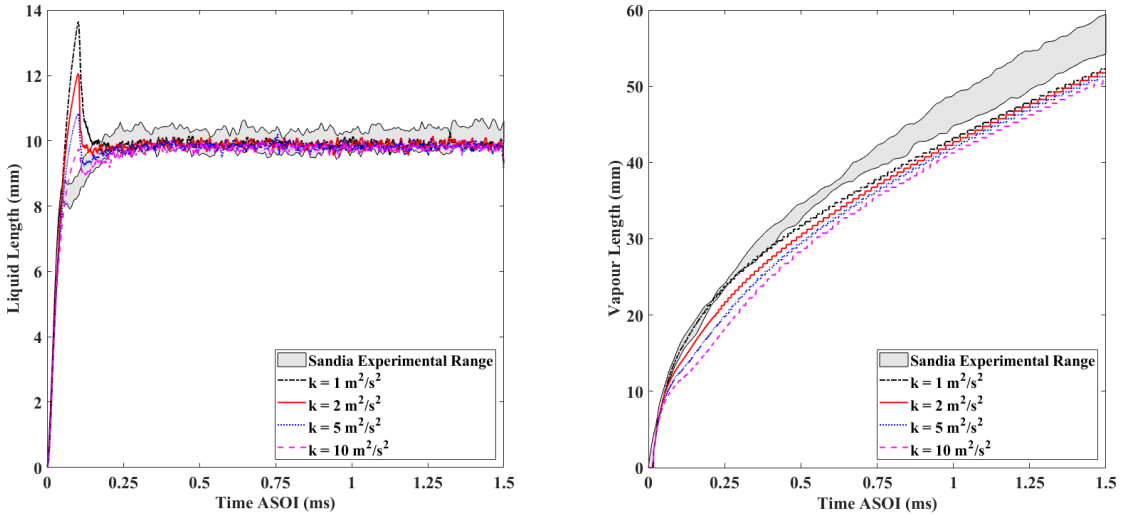

Figure 3.17: Liquid and vapour lengths for varying ambient TKE against time ASOI

tip is sheared away from the liquid core for a short period of time before the steady state liquid length is established. Both the reduced (or non-existent) overshoots and the "dips" after the liquid length peaks are shown in more detail in Figure 3.18, showing a zoom in of the transient region of the liquid length plot.

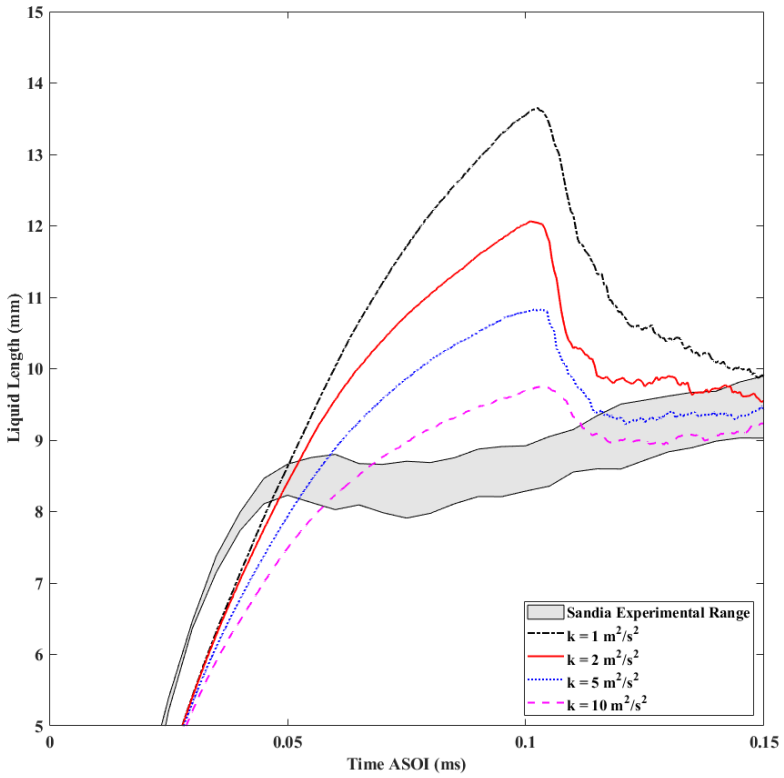

Figure 3.18: Zoom of the transient liquid length predictions with varying ambient TKE against time ASOI

From Figure 3.18 it is clear that the liquid length drop-off after the peak increases in gradient with an increase in ambient TKE, with each successive increase in ambient TKE leading to a quicker settling to the steady state liquid length mean. One possible reason for this is the shape of the liquid spray formed in each test, with a "fatter" spray with a lower overshoot dropping to steady state faster. Figure 3.19 shows the parcel positions for each test at 0.1 ms ASOI.

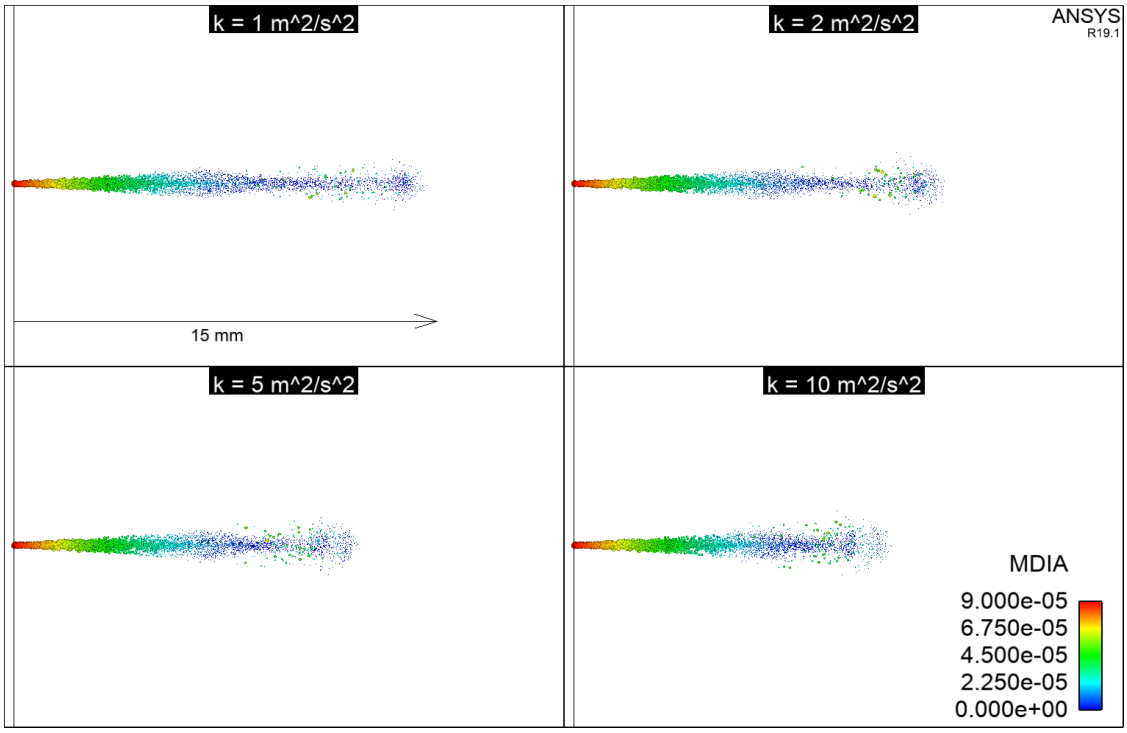

Figure 3.19: Parcel plots for varying ambient TKE at 0.1 ms ASOI. MDIA is droplet diameter in metres

The overshoot can be clearly seen reducing with each increase in ambient TKE, with the spray tip increasing in width in each successive increase. This behaviour can also be seen with the vapour fields, given the parcels at the liquid tip will be the first to evaporate the shape of the liquid tip should correspond to the vapour field at that timestep. As Figure 3.20a shows, the increase in ambient TKE causes a "fatter" initial vapour field to be formed, along with the vapour length being shorter at that timestep. This does not translate to a major difference in the later injection vapour field, shown in Figure 3.20b, with a marginal reduction

in vapour length seen at 1 ms ASOI, however the vapour field structure is very similar between ambient TKE values.

Considering the work of Ameen et al. [93], there is a difference of predictions of the vapour fields with increasing ambient TKE, with Ameen's work predicting a slight increase in vapour length, and Figures 3.17 and 3.20 showing that in this study the vapour length would reduce slightly as the ambient TKE is increased. However, it should be noted that there are important differences between this work and that of Ameen et al.; with this study being a non-combusting RANS case and Ameen et al. using a combusting LES case for their study [93]. As a result, there would be differences in the predictions of the eddy viscosity given its reliance on TKE and dissipation, both of which will change with the differences in temperatures seen between the combusting and non-combusting cases. As such, this comparison is purely qualitative.

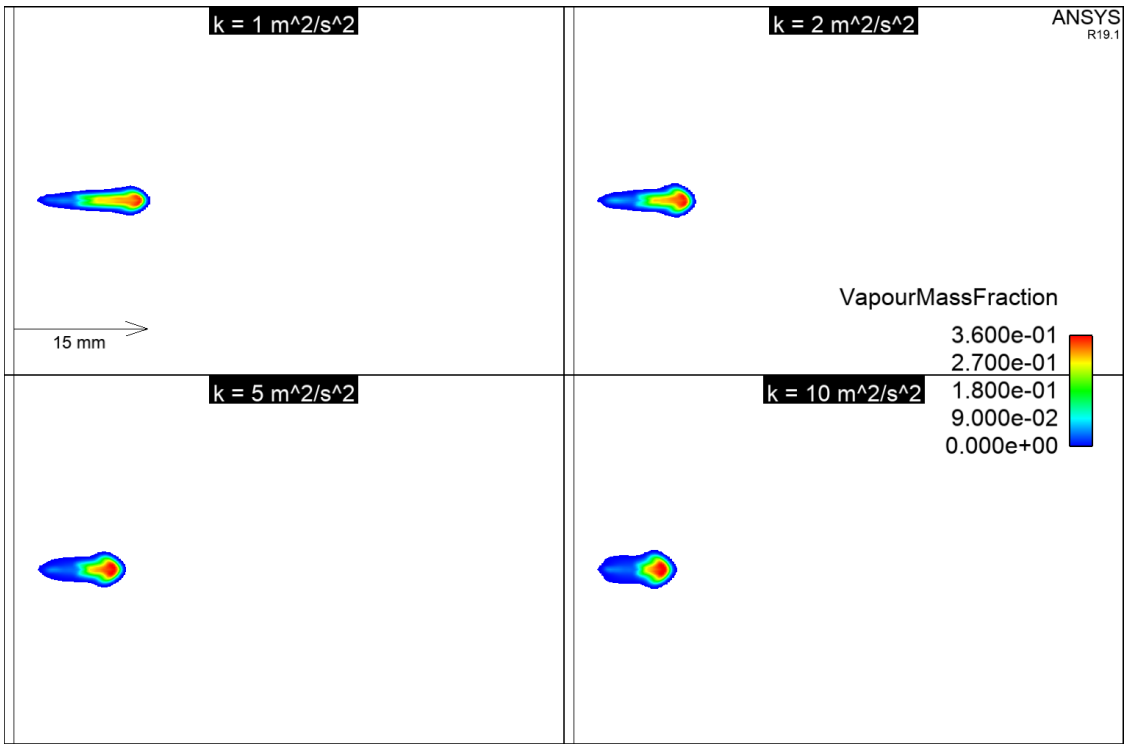

(a)

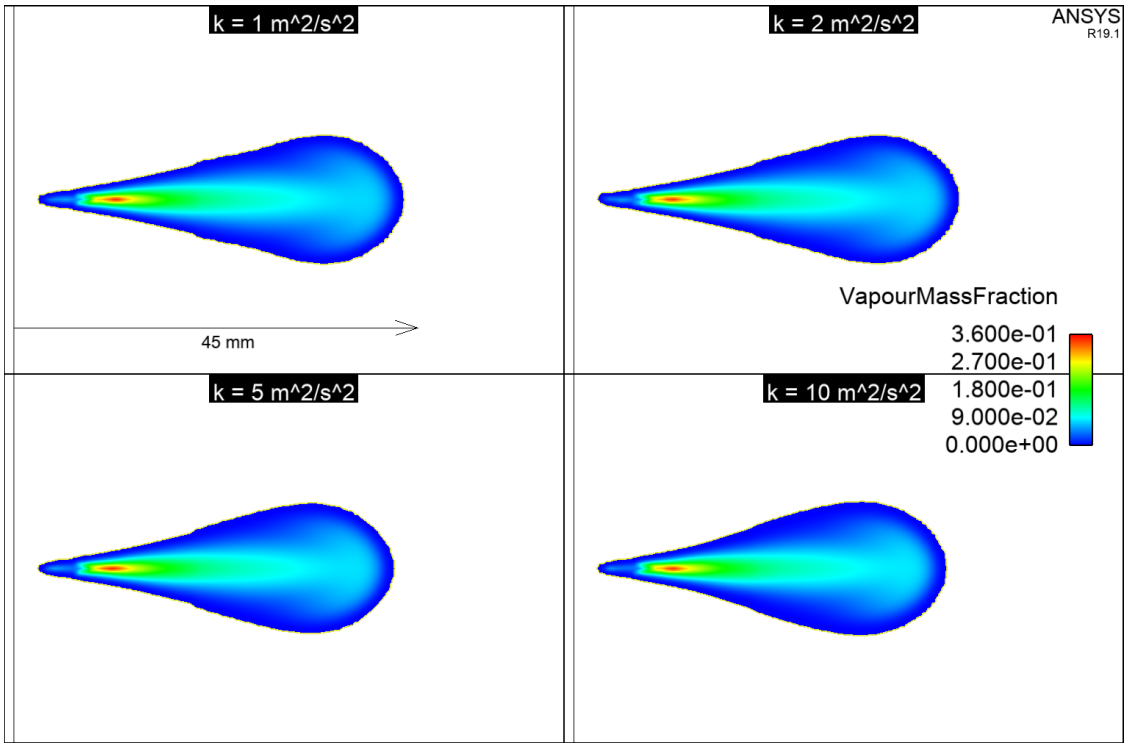

(b)

Figure 3.20: Vapour fields for varying ambient TKE at **(a)** 0.1 ms and **(b)** 1 ms ASOI.

3.2.3 Ambient Turbulent Dissipation Results

The ambient turbulent dissipation rate is crucial to set correctly, as too high a value set will lead to a quicker breakdown in the ambient turbulence compared to experimental data, and as such poor predictions of the spray characteristics. As such, the impact of changing this value needs to be determined to ensure good spray predictions. The values shown in Table 3.6 are considered, with the liquid and vapour lengths plotted for this varying ε in Figure 3.21.

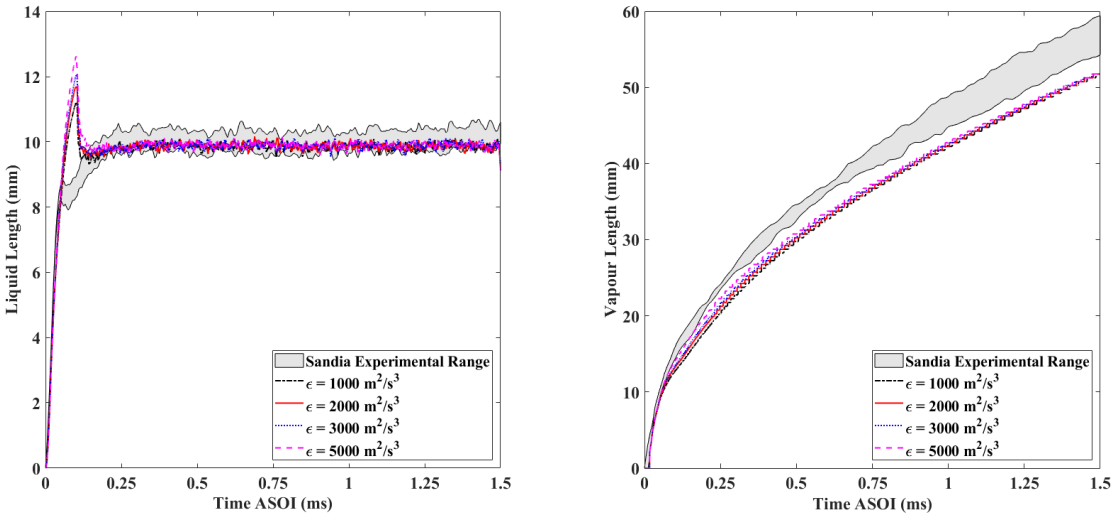

Figure 3.21: Liquid and vapour lengths for varying ambient turbulent dissipation against time ASOI

Figure 3.21 shows that there is a small variance in the liquid length means and final vapour lengths, however there is a small difference in the transient overshoot. It is clear from Table 3.8 that the increase in turbulent dissipation also leads to an increase in the transient overshoot with no major impact on either the liquid or vapour lengths. This is to be expected, as an increase in turbulent dissipation will ensure that the turbulence will have less of an effect on the initial droplets injected into the domain, leading to them travelling further through the domain before evaporating and becoming vapour. As was shown in the ambient TKE study, this increase in the transient overshoot directly impacts the vapour length at that time, with a slight increase in vapour length seen around 0.15 ms ASOI for the higher ambient turbulent dissipation values compared to the lower values.

Table 3.8: Liquid lengths, overshoots and vapour lengths for varying ambient turbulent dissipation

ε (m^2/s^3)	**Liquid Length (mm)**	**Transient Overshoot (mm)**	**Vapour Length (mm)**
1000	9.86	1.35	51.75
2000	9.89	1.82	51.75
3000	9.90	2.17	51.75
5000	9.90	2.73	52.25

To further illustrate the differences in the transient overshoots, the parcel plots for the sprays are shown in Figure 3.22. The increase in liquid length is clear, with the tip of the liquid spray slightly increasing in each successive increase of turbulent dissipation. As with the TKE tests in Figure 3.19, the main body of the spray is unaffected by the change in ambient turbulent dissipation, however the spray tip remains thin in this case, not become noticeably fatter in this case as the transient overshoot is reduced. The impact of the change in turbulent dissipation rate on the vapour fields is shown in Figure 3.23, showing that there is very little change in the vapour fields between turbulent dissipation values. Figure 3.23a shows a very slight "fattening" of the vapour field with a reduction in turbulent dissipation, however the magnitude of this is far reduced from that seen in the TKE tests, shown in Figure 3.20. The vapour fields at later injection times are extremely similar, with negligible differences in vapour lengths and field widths. As a result, it can be concluded that the turbulent dissipation only impacts the transient overshoot and the very early evaporation period of the spray, with the liquid and vapour lengths and vapour fields only being effected by very small amounts.

To ensure consistent modelling practices throughout this thesis, the baseline values for k and ε (2 m^2/s^2 and 3000 m^2/s^3 respectively) are used due to their matching of experimental conditions and suggested values for spray modelling from Star-CD. Applying everything shown in this chapter, a final domain can be shown to predict the "Spray A" case for future work. This domain will be used in the following chapters to test the KH-RT spray break-up model against both known

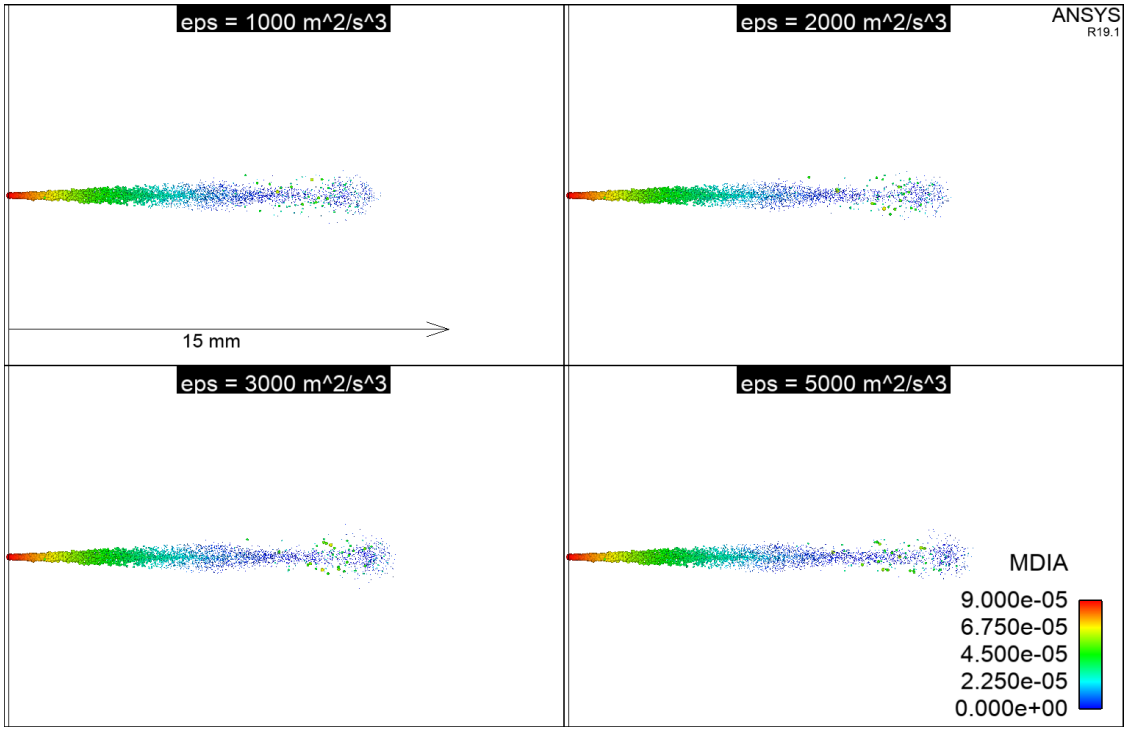

Figure 3.22: Parcel plots for varying ambient turbulent dissipation at 0.1 ms ASOI. MDIA is droplet diameter in metres

experimental data and another commercially available CFD code (in Chapter 4), and from this will be used to test the new break-up length KH-RT model that is implemented in Star-CD at different conditions (in Chapter 5).

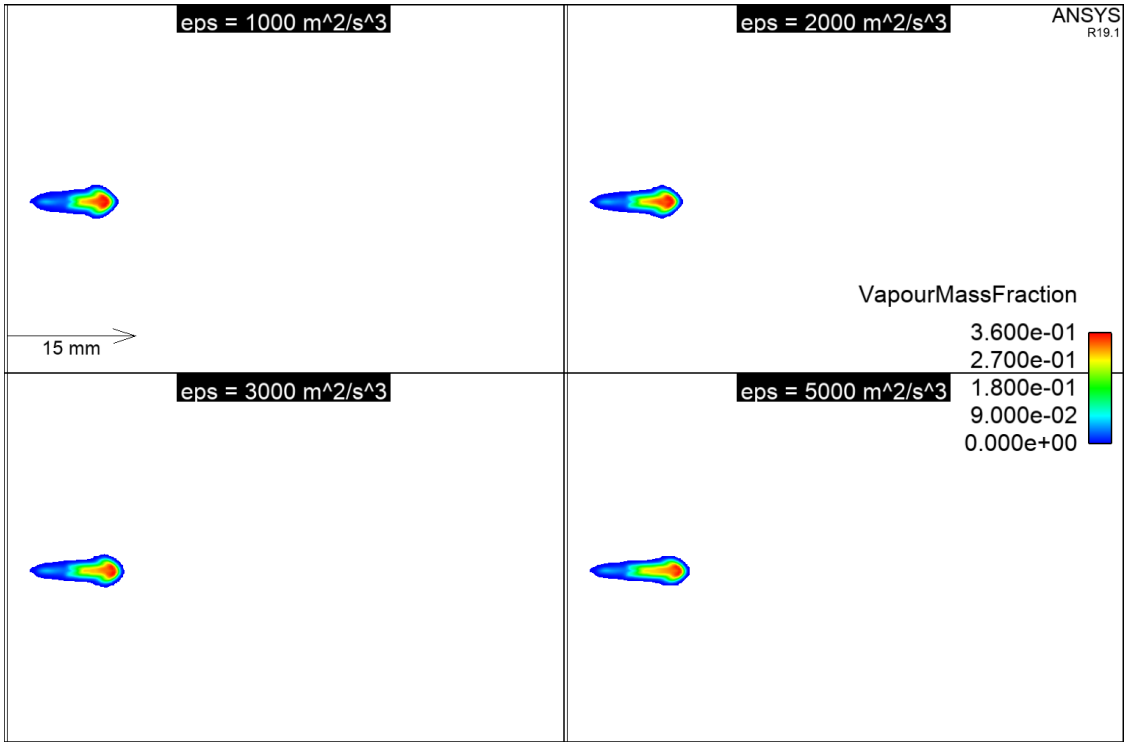

(a)

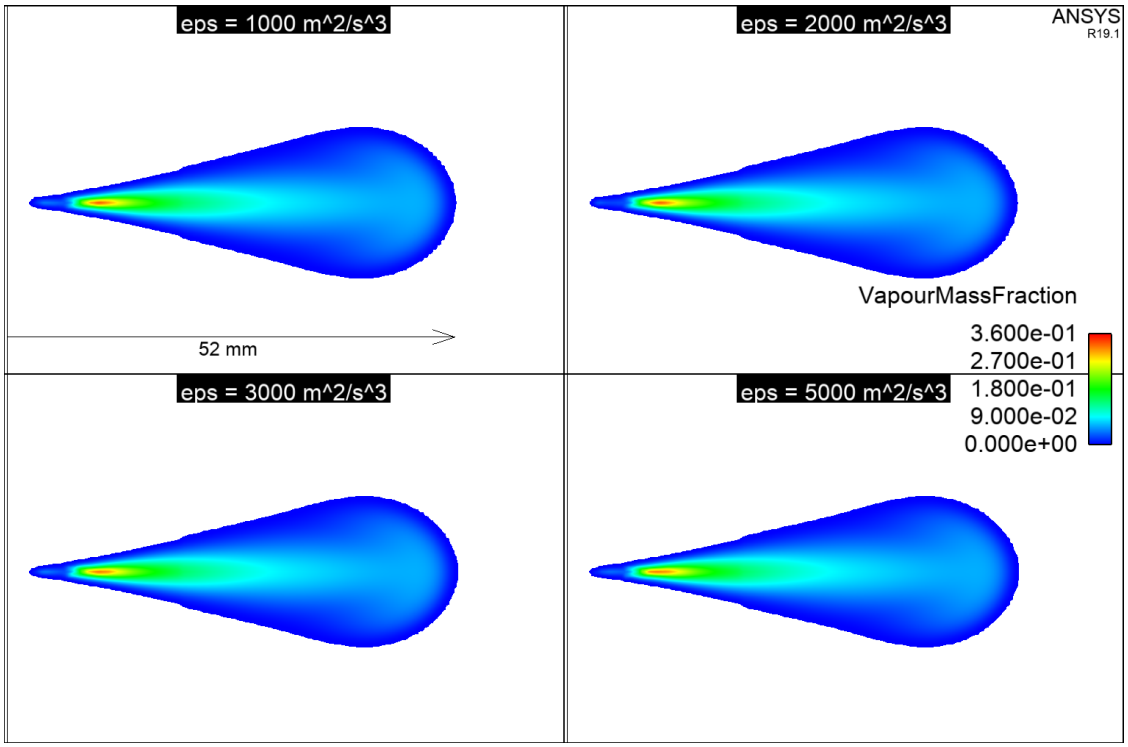

(b)

Figure 3.23: Vapour fields for varying ambient turbulent dissipation at **(a)** 0.1 ms and **(b)** 1 ms ASOI.

3.3 Conclusions

Within this chapter the computational domain has been created and characterised at the "Spray A" vaporising condition, employing the best practices of Star-CD and the recommended turbulence, break-up and atomisation models (k-ε, Reitz-Diwakar and Huh-Gosman respectively). The domain was characterised using a grid sensitivity study, with different levels of embedding employed near to the nozzle to determine the optimum cell size for simulations. The following observations have been made utilising this domain:

- A cell size of 0.25 mm was found to be the best trade-off between accuracy, run time and convergence of most key spray criteria. Any un-converged spray criteria were found to converge either at 0.125 mm or just after, and are not deemed critical enough to warrant a smaller minimum cell size.

- The impact of the parcel count in the simulation was also considered, showing a strong linear relationship between parcel count and run time with negligible impact on the liquid or vapour lengths. This suggests the initial parcel counts selected for the grid sensitivity study were too high, and are reduced for the domain going forward. 700,000 parcels are found to be the optimum parcel count for the simulation.

- Finally, the initial ambient turbulence criteria were also investigated, with the ambient turbulent kinetic energy having a strong impact on both the transient overshoot of the liquid length and the initial vapour field formation. The turbulent dissipation rate had a weaker impact on the transient overshoot than the ambient TKE with little impact on the liquid length. Considering these results suitable values for both were chosen to use going forward, with a ambient TKE value of 2 m^2/s^2 and an ambient turbulent dissipation rate of 3000 m^2/s^3 used in future.

4 Novel Switching Method for the KH-RT Model

This chapter presents a novel method for determining the switch between the KH and RT models. Initially, this was derived through comparison between two commercially available CFD codes, Star-CD and CONVERGE, for the vaporising "Spray A" case from Sandia [24]. Elements of this Chapter have been published in [94], with additions for this thesis. The initial comparison of the nominally identical KH-RT break-up models within Star-CD and CONVERGE show major differences in both the liquid length and Sauter Mean Diameter (SMD) predictions between the codes. This was found to be caused by the differing implementations of the KH-RT model, with Star-CD applying the two models (KH and RT) in competition based on the break-up timescale predicted, compared with CONVERGE's implementation of applying the KH model to parent droplets and the RT model to the child droplets. By applying a break-up length model within Star-CD, the KH and RT models can be applied sequentially, yielding qualitatively similar results between the new break-up length model within Star-CD and the child droplet model of CONVERGE. The impact of the application of this model on the vapour fields is also investigated, with an early switching position observed to cause more oscillatory and unstable behaviour within the inside of the vapour field. This model is then applied to a combusting spray in Chapter 5, with comparisons of the lift-off length, ignition delay and vapour fields made between the new model and experimental data.

Declaration

The content in this chapter is as a result of a collaborative effort between the author and Dr. XiaoHang Fang. The author is responsible for all Star-CD simulations and the development of the novel switching method definition. Dr. XiaoHang Fang is responsible for the CONVERGE simulations. Figures 4.1 and 4.3 are shared between the author and Dr. XiaoHang Fang. However, the analysis of the results is the author's own independent work. The work in this chapter has been published in [94].

4.1 Background

4.1.1 Spray Definitions

It is important to define various parameters used within this study, with the major parameters being used for comparison being the liquid length, the vapour length and the transient region for the vaporising spray, with the ignition delay and lift-off length used for the combusting spray. The liquid and vapour lengths are as defined in Section 3.1.2. From the grid sensitivity study undertaken by the author the transient region of the spray is defined as the time between the start of injection and 0.3 ms ASOI, as this is the time at which almost all previous studies have shown the liquid length to reach its steady state. As with the liquid and vapour lengths, the ignition delay and lift-off-lengths are defined by the ECN. Both are based on the OH mass fraction, with the ignition delay defined as the first point in time this mass fraction reaches 2 % of its simulation long maximum, and the lift-off-length defined as the axial distance from the injector at which this mass fraction of 2 % is reached [27].

4.1.2 Motivation for Improved Transient Modelling

From the grid sensitivity study shown in Section 3.1 a transient overshoot of the liquid length was seen, with this being explicitly shown in Figure 4.1a. This transient overshoot was not repeated in a similar grid sensitivity study undertaken within CONVERGE, shown in Figure 4.1b. There are clear differences between the two codes' predictions of the transient region, with Star-CD clearly over-predicting the initial liquid length before dropping to the steady state length, and CONVERGE

having a slower initial prediction, but reaching steady state around 0.1 ms ASOI and then holding at this length for the remainder of injection. As was discussed in Section 1.2, the application of digital rate shaping has enabled injections of less than 0.2 ms, and as such ensuring correct modelling of this transient period is essential for correct engine simulations.

The reason for the overshoot seen within Star-CD can be observed by looking at the movement of the parcels through the initial transient region, shown in Figure 4.2. The circled parcels within Star-CD are approximately half nozzle diameter and move past the spray tip; given the definition of the liquid length as a liquid mass threshold the overshoot of these parcels past the spray tip will cause the overshoot of the liquid length seen in Figure 4.1a. Once the circled parcels have penetrated beyond the spray tip, they reduce in diameter quickly until they evaporate. This yields the rapid drop in liquid length seen in Figure 4.1a at around 0.1 ms ASOI, and after this point the spray is stable with no further droplets penetrating beyond the spray tip.

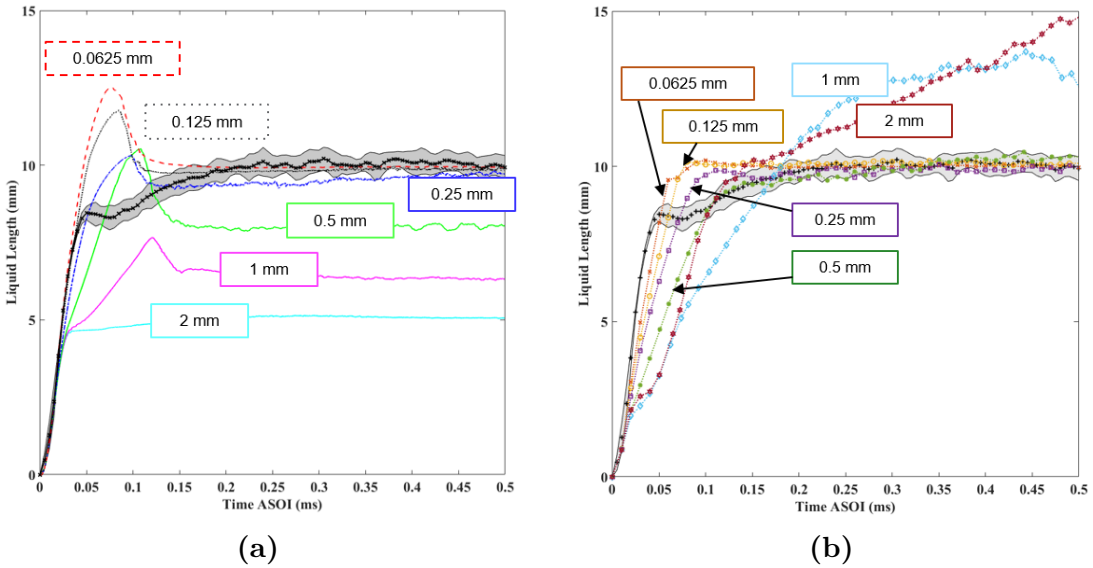

Figure 4.1: Comparison of grid convergence study liquid length results against time ASOI, with cell sizes noted. Experimental data presented as a range by the grey filled area. **(a)** Star-CD grid convergence results, **(b)** CONVERGE grid convergence results from Fang [94].

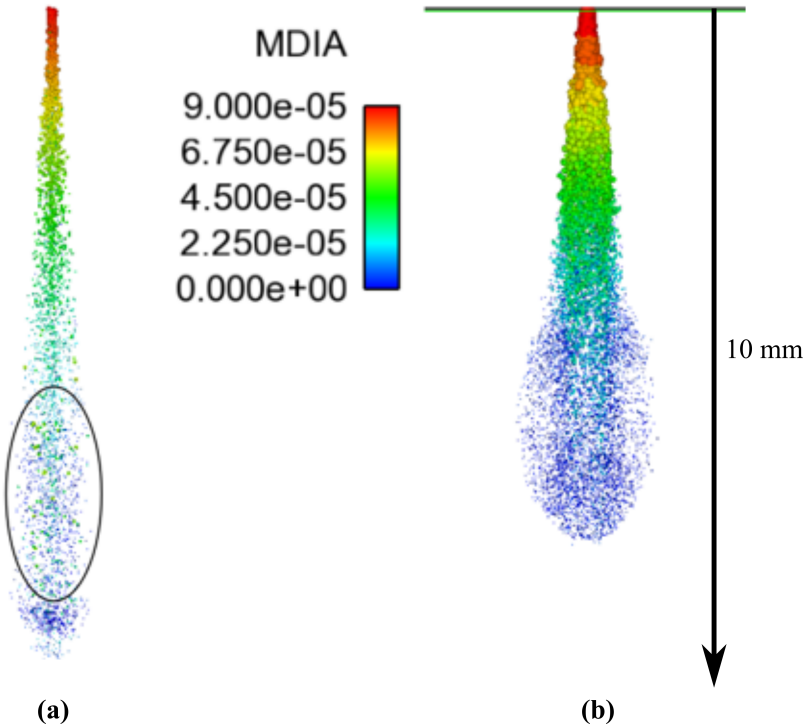

Figure 4.2: Parcel plots for **(a)** Star-CD and **(b)** CONVERGE baseline (from Fang [94]) simulations at 0.06 ms ASOI. The parcels causing Star-CD's transient overshoot are circled. MDIA is the droplet diameter in metres.

4.1.3 Comparison of Baseline Setups

Despite the use of different CFD codes for the comparison, attempts were made to ensure as much similarity as possible existed in their operation. Both codes model the spray with a Lagrangian-Eulerian approach, with the droplets modelled as parcels, as defined by Dukowicz [47]; the gas flow field is modelled by the standard k-ε model [77, 92]. The grid sensitivity study shown in Section 4.1.2 selected a minimum cell size of 0.25 mm for Star-CD, while a grid convergence study undertaken by Fang found a similar minimum cell size for CONVERGE [94]. The grids generated for both codes cover the liquid region of the spray with their minimum cell size, as shown in Figure 4.4.

Table 4.1 shows the major differences between the baseline setups of the two codes, with the break-up, atomisation and evaporation models differing code to code. The "effective" injection model is the same as the blob model in all but name, with the parcels injected at nozzle diameter with a calculated injection velocity

based on the mass flow rate. Whilst the break-up and atomisation models can be altered within Star-CD, the evaporation model is not possible to change and as such cannot be made equivalent to the CONVERGE case.

Table 4.1: Comparison of baseline sub-models and grid set-up between codes. Numerical values for the models can be found in Table 4.2

Model Setup	**Star-CD**	**CONVERGE**
Spray Sub-Models		
Turbulence	Standard k-ε, with modified constants [92]	Standard k-ε, with modified constants [92]
Injection	Effective [34, 87]	Blob [34]
Break-up	Reitz-Diwakar [89]	KH-RT [45]
Atomisation	Huh-Gosman [35]	KH-RT [45]
Collision	None	None
Evaporation	Ranz-Marshall [95]	Frossling [96]
Turbulent Dispersion	Stochastic [87]	Stochastic [96]
Heat Transfer	Ranz-Marshall [97]	Ranz-Marhsall [96]
Grid Setup		
Grid Type	Structured	Structured with AMR [96]
Dimensionality	3D	3D
Maximum Cell Count	491672	291463

The other major difference between the codes is in the grid generation. Within Star-CD the grid is pre-defined, with a domain selected and then split into cells. Refinement can be applied, however this is done before the simulation and is restricted to splitting the pre-existing cells into eight smaller cells, halving the cell size. Within CONVERGE the domain is specified before simulation, however a grid is not pre-generated. A base cell size is set, and some fixed embedding is applied around the injector; however after this mesh refinement is applied based on the velocity gradients between cells, allowing for highly spray based refinement to be employed. This is called Adaptive Mesh Refinement (AMR), and can be applied based on velocity or temperature gradients, depending on the case being considered;

more information on AMR can be found in the CONVERGE methodology [96]. Figure 4.4 shows the clear difference between the purely embedded refinement of Star-CD (Figure 4.4a) and the velocity gradient based AMR used in CONVERGE (Figure 4.4b). Despite these differences the liquid region of the spray is still fully contained by the 0.25 mm cell size, with only the vapour region being covered by different cell sizes (0.5 mm for Star-CD compared to 0.25 mm for CONVERGE). Given the vapour penetrations shown in Figure 4.3a this is expected to have negligible impact on the vapour prediction. This is further proved by considering the CONVERGE grid convergence vapour length results, seen in Figure 4.3b, suggesting the difference in cell size for the vapour region has little impact on the prediction from each code. The trends between codes are very similar, with the largest cell size under-predicting the vapour length, followed by an oscillation around the converged vapour length as the cell size is reduced. This is more prevalent in the Star-CD case (Figure 4.3a), however this has also been seen in literature [46].

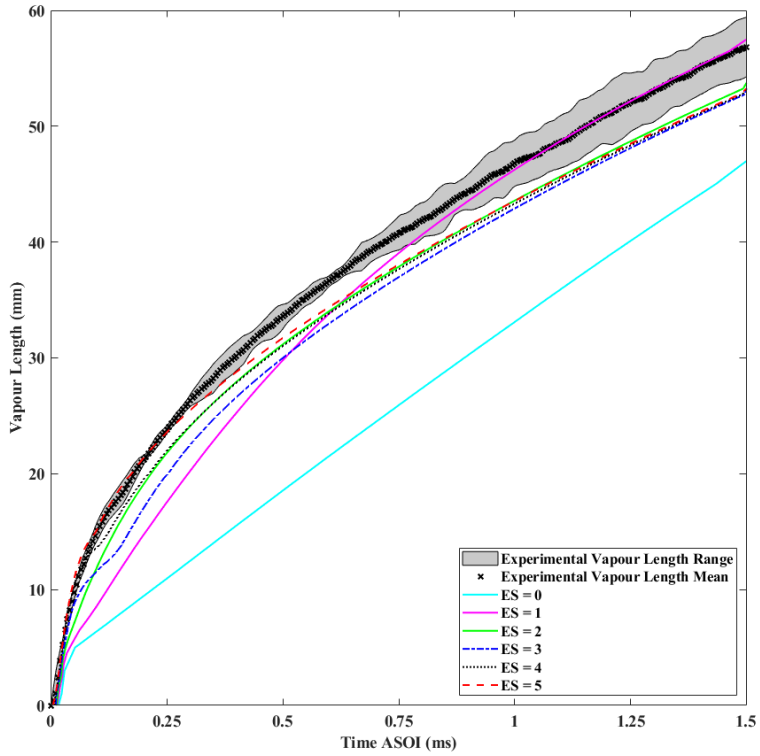

(a)

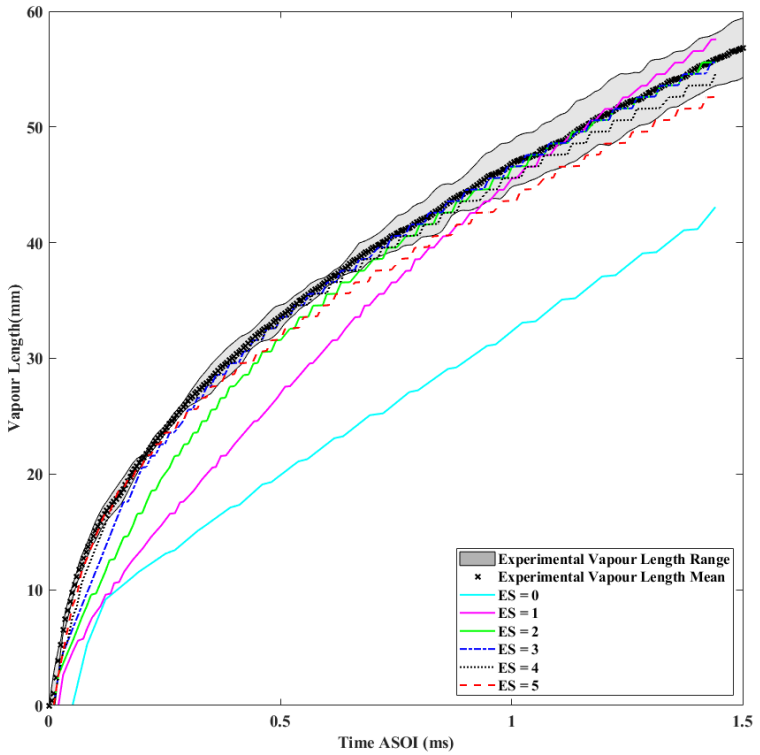

(b)

Figure 4.3: Comparison of grid convergence study vapour length results against time ASOI. **(a)** Star-CD grid sensitivity results, **(b)** CONVERGE grid convergence results from Fang [94].

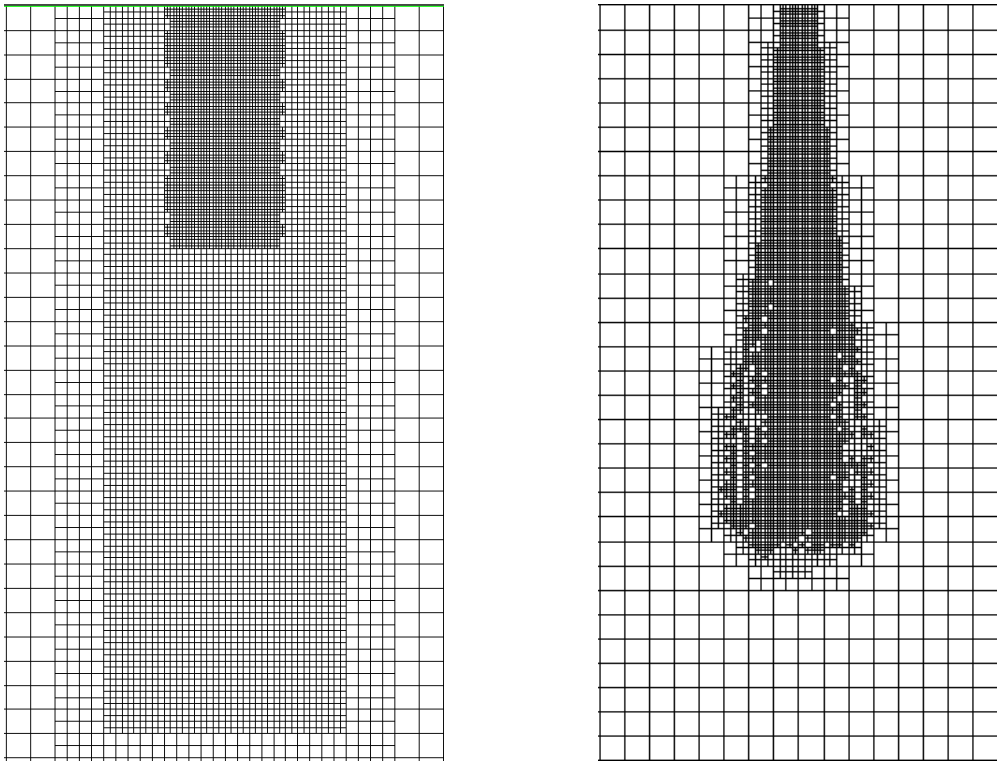

(a) **(b)**

Figure 4.4: Comparison of Star-CD and CONVERGE meshes at 1 ms ASOI, **(a)**: Star-CD mesh, **(b)**: CONVERGE (from Fang [94]) mesh

This initial comparison between the codes took place with the codes using their "baseline" setups. Both baseline setups are tuned to match the steady state liquid length, achieved by tuning the turbulence model constants and spray break-up model constants. A comparison of these can be found in Table 4.2. The differences seen in the transient liquid lengths shown in Figure 4.1 were initially thought to be caused by the differences in the spray break-up models. As a result, the Star-CD set-up was matched to the CONVERGE setup, using the KH-RT model and applying the constants shown in Table 4.2. By applying these models on as similar a grid as possible, it is hoped that a direct comparison between the codes can be achieved.

Table 4.2: Comparison of baseline constant values for Star-CD and CONVERGE

Constant	Star-CD	CONVERGE
k-ε Turbulence Model		
$\mathbf{C}_{\mu}$ (Eq 2.23)	0.09	0.09
$\mathbf{C}_{1\varepsilon}$ (Eq 2.22)	1.53	1.58
$\mathbf{C}_{2\varepsilon}$ (Eq 2.22)	1.92	1.96
$\boldsymbol{\sigma}_{k}$ (Eq 2.21)	1	1
$\boldsymbol{\sigma}_{\varepsilon}$ (Eq 2.22)	1.3	1.3
Break-up Model Constants (Reitz-Diwakar / KH-RT)		
$\mathbf{C}_{b1}$ (Eq 2.47) / $\mathbf{B}_{KH0}$ (Eq 2.57)	6	0.6
$\mathbf{C}_{b2}$ (Eq 2.49) / $\mathbf{B}_{KH1}$ (Eq 2.58)	π	7
$\mathbf{C}_{s1}$ (Eq 2.50) / $\mathbf{B}_{RT0}$ (Eq 2.63)	0.5	0.1
$\mathbf{C}_{s2}$ (Eq 2.52) / $\mathbf{B}_{RT1}$ (Eq 2.64)	20	1

4.2 Direct KH-RT Comparison

4.2.1 KH-RT Model Results

Given the nominal equivalence of the two setups, it is expected that the predictions of liquid and vapour length will be more similar now than was seen previously. The full injection results for both codes can be seen in Figure 4.5, which shows the differences between the two codes in more detail.

The vapour length prediction is improved by utilising the KH-RT model, however there is a clear under-prediction in steady state liquid length when the model is switched. This under-prediction is shown in Table 4.3, and is outside of the experimental range; whilst also having a worse prediction of the transient liquid length. The transient liquid length predictions are shown in Figure 4.6, and illustrate the difference in predictions more clearly. One similarity between the simulations is the slower ramp in initial liquid length when compared to the Reitz-Diwakar model; with the KH-RT model exhibiting similar behaviour in Star-CD when compared to CONVERGE.

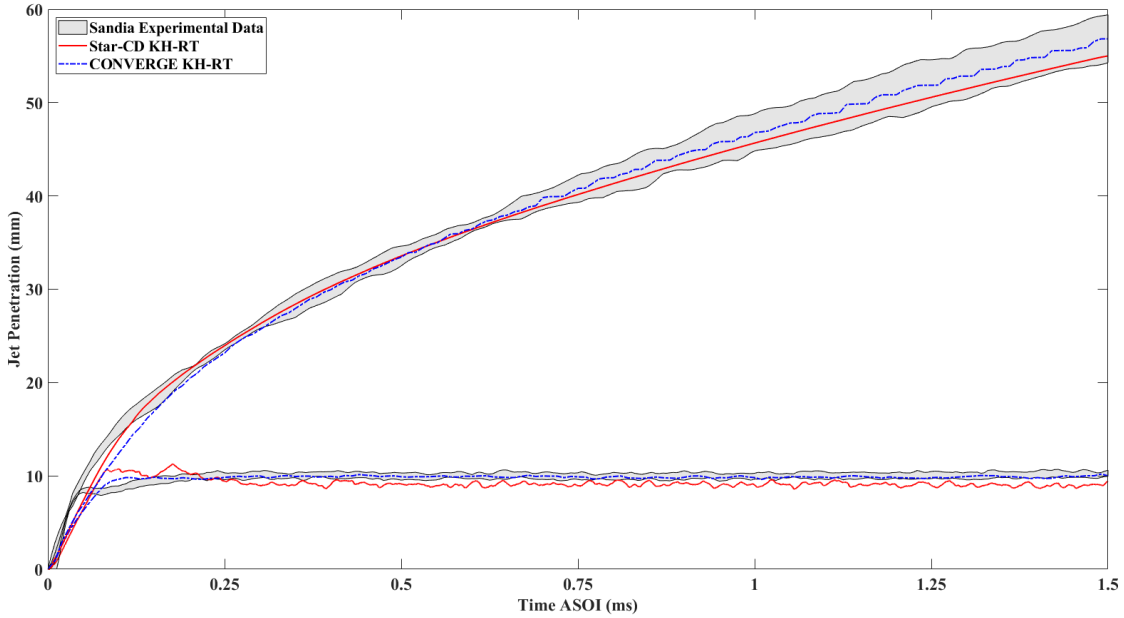

Figure 4.5: Direct comparison of Star-CD and CONVERGE KH-RT liquid and vapour lengths against time ASOI

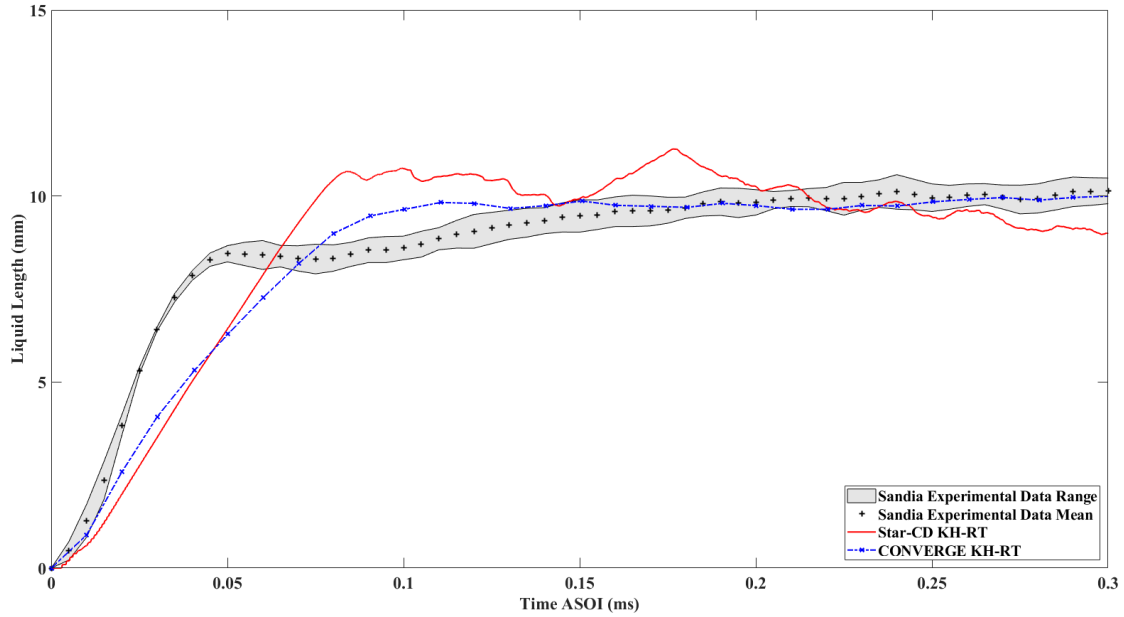

Figure 4.6: Direct comparison of each code's transient liquid length prediction against time ASOI

The differences in predictions between the nominally identical models suggests that there is an underlying issue with the Star-CD KH-RT model. This is further confirmed when the model is tested more thoroughly, as is shown in the next section.

Table 4.3: Simulated and experimental liquid length means for baseline cases

CFD Code	Maximum Transient Liquid Length	Steady State Liquid Length
Star-CD R-D	11.11 mm	10.13 mm
Star-CD KH-RT	11.26 mm	9.09 mm
CONVERGE	9.99 mm	9.98 mm
Experimental	9.46 ± 0.43 mm	10.08 ± 0.34 mm

4.2.2 KH-RT Implementation Differences

Within both codes the governing equations are unchanged, with both using the formulations of Reitz and Joseph (with Xin's alterations) [34, 44, 98]. The major difference between the codes is the way the models are applied. Within CONVERGE, the KH model is applied to parent droplets, with the droplets formed by the break-up of these droplets then being acted on by the RT model. Within Star-CD, both models will compete at all positions and droplet diameters to determine which causes break-up, with the model predicting the shortest break-up time being classed as the "critical" model and hence causing the break-up of the droplet. Within the current Star-CD simulation with the base KH-RT model applied, this causes issues with the SMD values, as can be seen in Figure 4.7; with a cliff edge in SMD being seen when the KH-RT model is used in comparison to the R-D model in Star-CD and the KH-RT model in CONVERGE. A cliff edge in SMD predictions is not seen within experiments when considering the axial droplet SMD [99–101], however very sharp drops in droplet SMD are seen near to the nozzle and henne would be predicted early in the injection cycle as well [100, 101]. These drops in SMD are similar to the drop seen in the CONVERGE SMD prediction, with a larger negative gradient than in the Star-CD Reitz-Diwakar model.

This can also be visualised by the parcel plots comparing the two KH-RT models, shown in Figure 4.8. Star-CD shows a rapid break-up of the nozzle diameter droplets to a large amount of very small droplets, very quickly after injection. This rapid break-up correlates well with just the RT model causing break-up, as a stripping

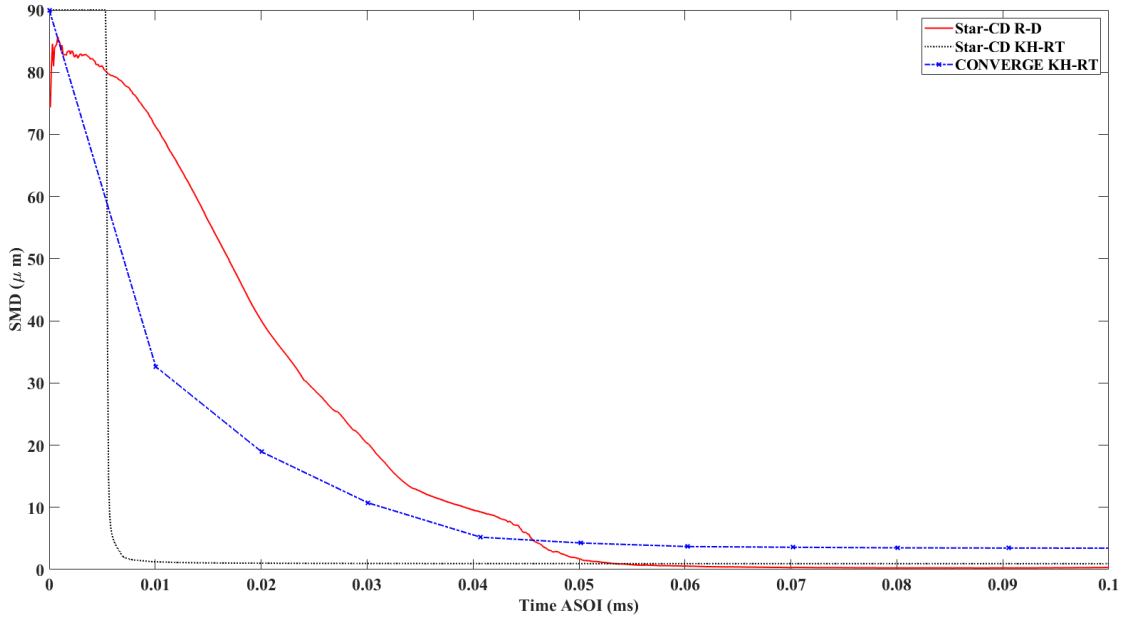

Figure 4.7: SMD values for the baseline cases for both codes, and the KH-RT case for Star-CD, against time ASOI

break-up model will cause many very small droplets to be formed after break-up. This suggests that within Star-CD the RT model is dominating break-up, even within the liquid core. This theory can be tested by reducing the B_{KH1} constant, seen in Equation 2.58. Reducing this from the initial value of 7 to 6 will cause the KH model to predict a timescale approximately 15 % lower than previously, and hence should have an impact on the global spray parameters and the SMD values.

Figures 4.9, 4.10 and 4.11 show the impact of altering the B_{KH1} constant on the simulation results. There is clearly minimal impact outside of the transient region on the spray penetration lengths, and even within the transient period the spray is minimally different between B_{KH1} values. This is especially apparent in the SMD plots, where for all values of B_{KH1} tested the SMD's are identical. Hence, it can be concluded that the alteration of the B_{KH1} constant provides little impact on the spray penetration lengths, and hence the RT model is dominating even at small values of B_{KH1}, consistent with the findings of Wang using an outward opening injector [102]. This is not physically consistent with what one might expect, as this suggests a drag based break-up model is causing break-up in the liquid core, in which the droplets have a very low drag force acting on them. As a result, a

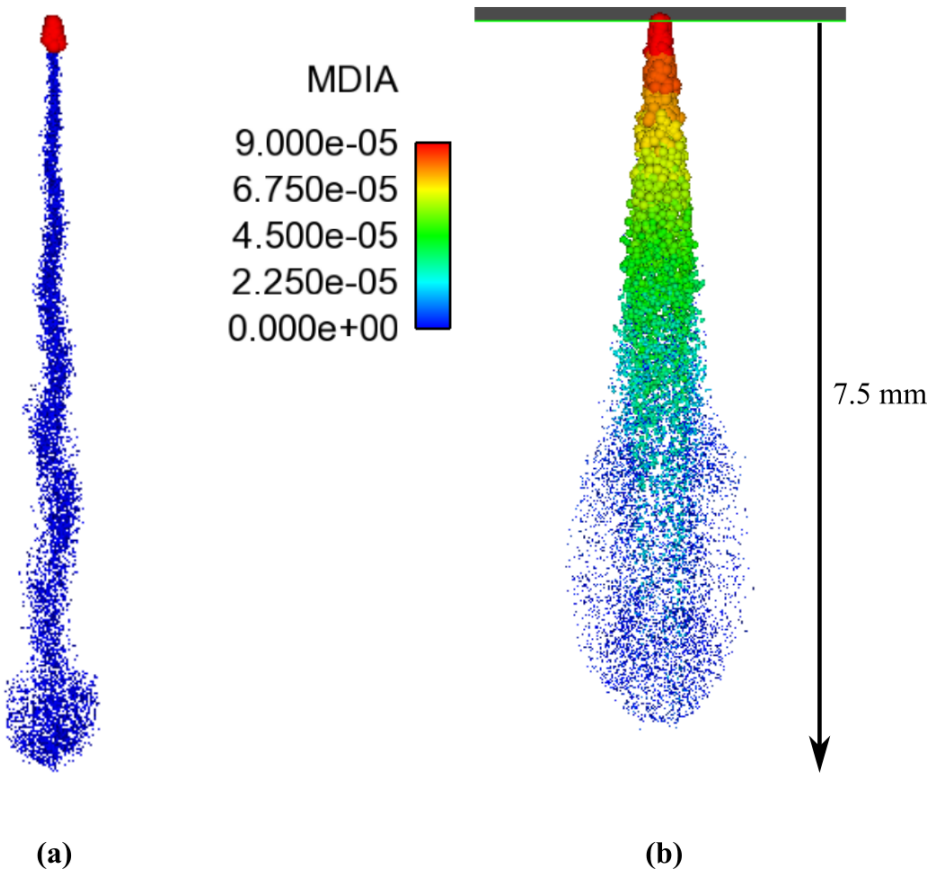

Figure 4.8: Parcel plots of **(a)** Star-CD and **(b)** CONVERGE KH-RT direct comparison simulations, 0.06 ms ASOI. MDIA is the droplet diameter in metres.

new implementation of the KH-RT model is needed to ensure the KH and RT models act "correctly" through the use of a tunable constant; the CONVERGE methodology is not possible to recreate within Star-CD due to the lack of a child droplet flag, and as a result a break-up length switch is used.

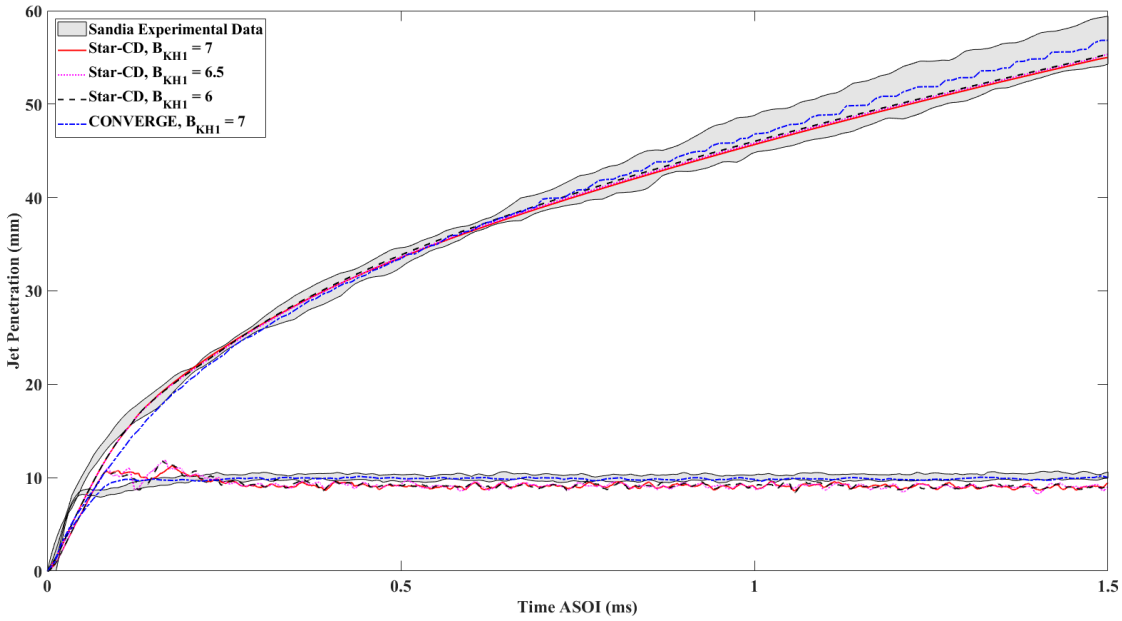

Figure 4.9: Penetration lengths for varying B_{KH1} values against time ASOI

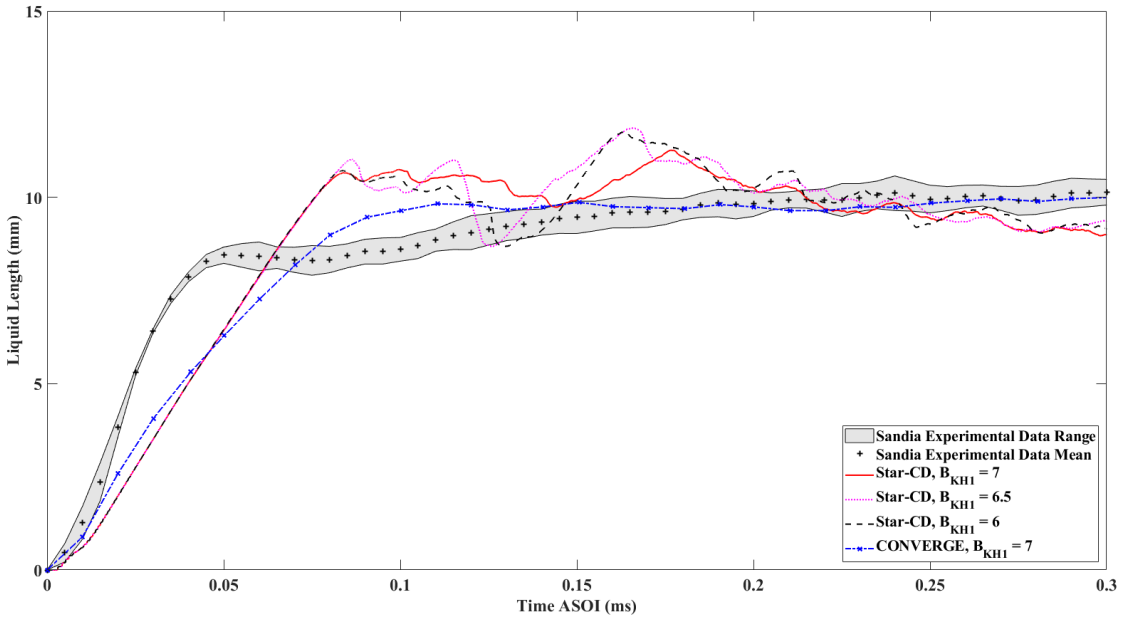

Figure 4.10: Comparison of transient liquid length predictions for varying B_{KH1} values against time ASOI

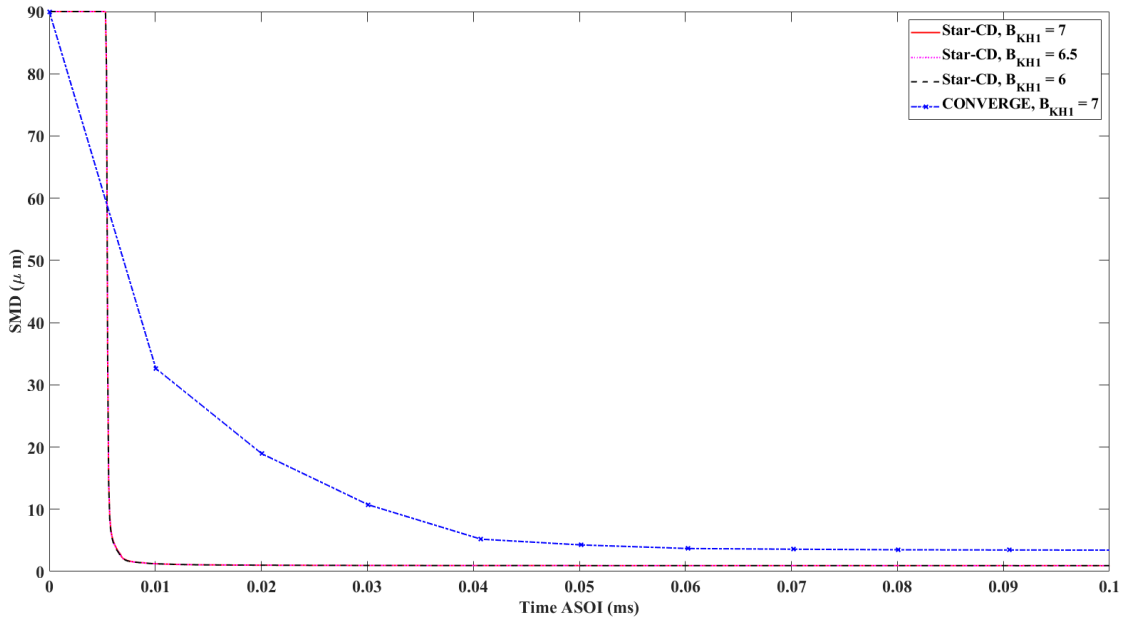

Figure 4.11: SMD values for varying B_{KH1} values against time ASOI

4.3 KH-RT "Switch" Model Implementation

Break-up length methods for switching between the KH and RT models are not new, with a notable example being the Levich theory [103] (Equation 4.1); which is commonly used within CONVERGE [96] and other literature (in both vaporising and combusting cases) [49,57,74,104,105]. However, given the emphasis on primary atomisation seen within this study a simple ratio of densities was deemed inadequate to accurately define a switch between atomisation and break-up regimes. Given the Ohnesorge number's use in predicting the tendency for a droplet to break-up (as described in Equation 1.4), it is used for the new criteria.

$$L_b = C_{bl}\sqrt{\frac{\rho_l}{\rho_g}}d_0 \tag{4.1}$$

To implement the new switching method a User Defined Function (UDF) was written and input into Star-CD, continuing to use the KH-RT model's governing equations [34,44,98] and converting the radii used within these equations to diameters to be compatible with the Star-CD conventions [87]. A switch criterion was added to the model to determine the position at which the two sub-models are active, this takes the form of a break-up length criterion similar to that of Levich [103]

(Equation 4.1), however based on the initial Ohnesorge number (Z_0) instead. In this case, the KH model solely acts before the criterion is met, and after this the KH and RT models compete to cause breakup, in the standard way for Star-CD. The break-up length is calculated from the nozzle tip, and is denoted by SW_1. The definition of the criterion is shown in Equation 4.2.

$$SW_1 = 10 S_N D_{noz} Z_0 \tag{4.2}$$

Within the definition of SW_1 there is a scaling number (S_N) to alter the position at which the switch occurs, the nozzle diameter (D_{noz}) and initial Ohnesorge number (Z_0, Equation 2.54, 0.01635 in "Spray A") are also used. Given this comparison is at one data point a single non-dimensional group is used, this dimensional analysis can be expanded to fit more points. The Ohnesorge number is chosen due to its definition, based on the droplet viscosity and surface tension. In general, atomisation effects on a droplet are dependent on these parameters along with the aerodynamic forces; as a result the Ohnesorge number captures the atomisation regime within its definition (as described in Chapter 1 and shown in Figure 1.4) and hence can be used to define a switch between atomisation and break-up regimes.

Tests were undertaken to ascertain the impact of the switching criterion, along with finding the optimum value of S_N for the "Spray A" condition. The values tested are shown in Table 4.4, with their corresponding values of SW_1. For these tests all the turbulence and break-up model constants are kept as in Table 4.2 for the KH-RT model to ensure consistency in testing.

Table 4.4: S_N values and their corresponding SW_1 values tested for optimisation of switch model

S_N value	SW_1 value (mm)
68.0	1
203.9	3
543.8	8
815.6	12

It should be noted that the largest value for S_N is outside the liquid region completely, and as such will apply only the KH model for the whole liquid spray. The full injection results for the largest three S_N values are shown in Figure 4.12, with the transient liquid length comparisons shown in Figure 4.13. The S_N value of 68.0 was not plotted to avoid clutter, however its data is still presented in Table 4.5 along with the others to compare maximum transient liquid lengths and the steady state liquid lengths seen for each S_N value.

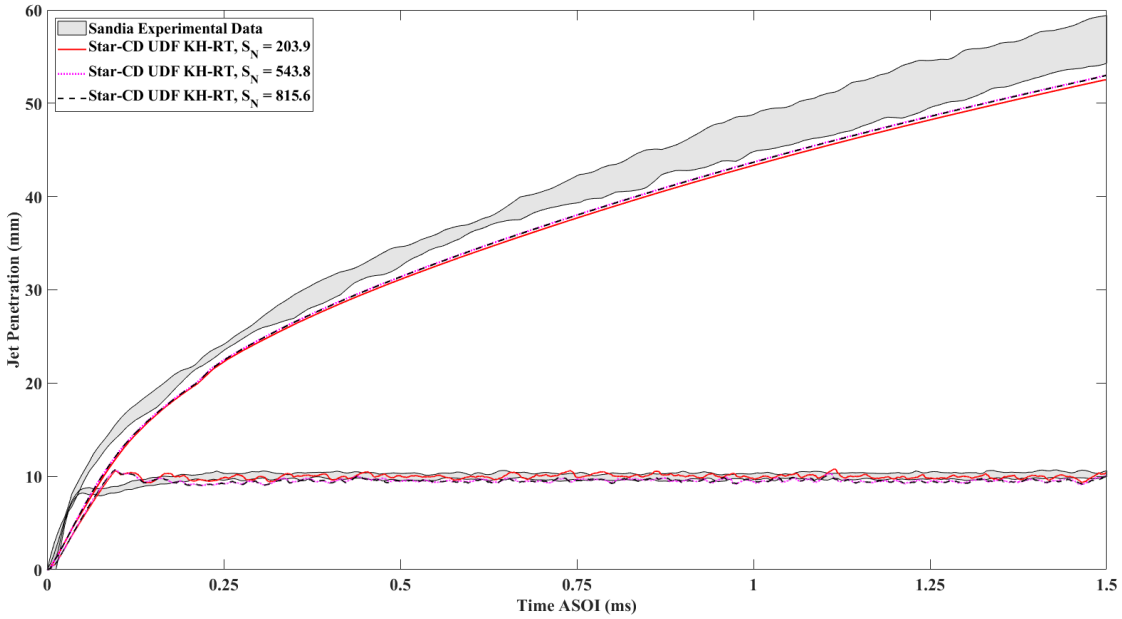

Figure 4.12: Penetration lengths for varying S_N values against time ASOI, with inset showing liquid lengths between 0.8 and 1 ms ASOI

As Figure 4.12, Figure 4.13 and Table 4.5 show, reducing the S_N number tends to reduce the transient overshoot until a value of 203.9, after which the overshoot again increases. The steady state liquid length tends to increase with a reduction in S_N. The value of 203.9 was chosen as giving the best overall performance, as shown in Table 4.5. This reduction in S_N corresponds to the criterion seen in Equation 4.2 being met earlier in the spray and closer to the nozzle. Therefore, the liquid core seen within these simulations is quite small and aerodynamic effects could occur fairly early in the spray.

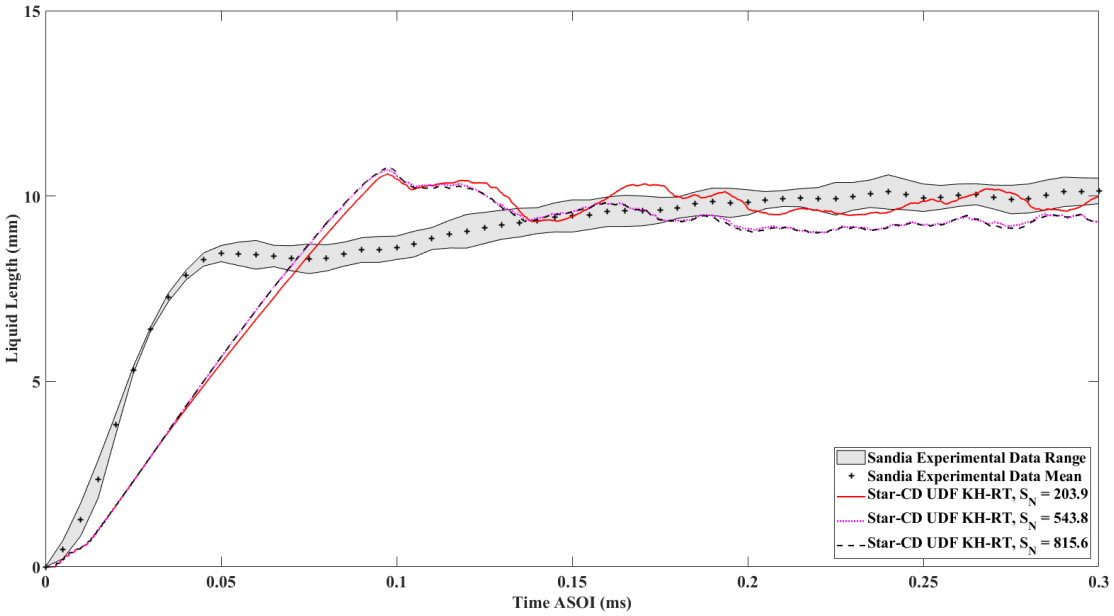

Figure 4.13: Transient liquid length predictions for varying S_N values against time ASOI

Table 4.5: Comparison of S_N value impact on maximum and steady state liquid length predictions

S_N value	**Maximum Transient Liquid Length**	**Steady State Liquid Length**
68.0	10.73 mm	10.11 mm
203.9	10.60 mm	10.01 mm
543.8	10.72 mm	9.55 mm
815.6	10.78 mm	9.53 mm
Experimental	9.46 ± 0.43 mm	10.08 ± 0.34 mm

Figure 4.12 also shows that varying values of S_N has minimal impact on the vapour length prediction. This suggests that the liquid and vapour lengths have been uncoupled, allowing for altering the liquid length without impacting the vapour length through the use of the KH-RT "Switch" model.

4.4 UDF Model Results

4.4.1 KH-RT "Switch" Model Results

Using the Star-CD KH-RT "Switch" model introduced in the previous section, a more direct KH-RT model comparison between models is now presented. The baseline cases for both codes will be compared to the "Switch" model with an S_N value of 203.9. The full injection results can be seen in Figure 4.14. Figure 4.14 shows that the vapour penetration for both Star-CD baseline and "Switch" simulations are matched well with each other; however both under-predict the experimental vapour penetration. In addition, all simulations predict the steady state liquid length very well, as can be seen in Table 4.6. The transient comparison can be seen in Figure 4.15.

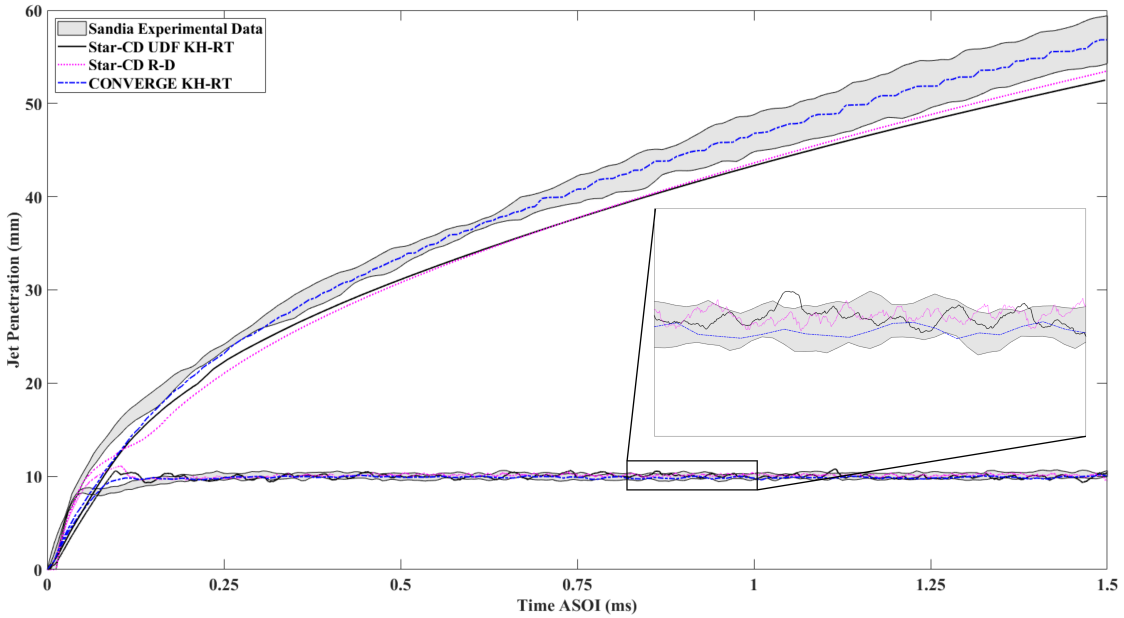

Figure 4.14: Comparison of penetration lengths from baseline and "Switch" models against time ASOI, with inset showing liquid lengths between 0.8 and 1 ms ASOI

Figure 4.15 shows the improvement in transient overshoot prediction between the baseline and "Switch" models within Star-CD; however the initial rate of increase of the liquid length is not predicted as well by the UDF. This could be due to the KH-RT model having a greater grid dependency than the Reitz-Diwakar model used in the baseline case. It has been seen in the CONVERGE grid convergence study (Figure 4.1b) and other works [46, 54] that a finer grid increases the initial

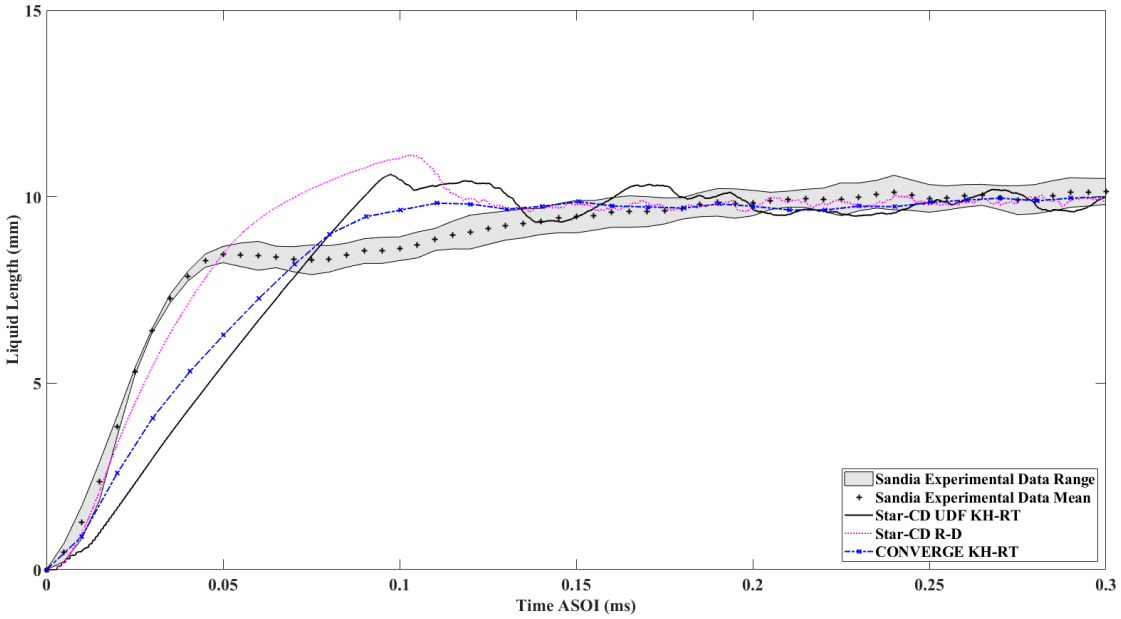

Figure 4.15: Transient liquid length predictions for baseline and "Switch" models against time ASOI

Table 4.6: Comparison of baseline and UDF "Switch" model impacts on maximum and steady state liquid length predictions

Code Setup	**Maximum Transient Liquid Length**	**Steady State Liquid Length**
Star-CD RD	11.11 mm	10.13 mm
"Switch" model	10.60 mm	10.01 mm
CONVERGE KH-RT	9.99 mm	9.98 mm
Experimental	9.46 ± 0.43 mm	10.08 ± 0.34 mm

gradient of the liquid length and as such brings the prediction more closely in line with the experimental data. Also, a finer grid will better predict the liquid core region, as when the cell size approaches the nozzle diameter the void fraction will increase, reducing drag on the liquid phase, as expected within the liquid core.

The issues seen in the previous KH-RT model within Star-CD were believed to be due to the RT model suddenly causing break-up of nozzle diameter droplet to very small droplets, as seen in Figure 4.7; by implementing the switch model into Star-CD the cliff-edge in SMD has been removed, with the KH model acting to break droplets up quickly, however not in a single timestep. This can be seen

in Figure 4.16, with the drop in SMD for the switch model being faster than the baseline cases for either code, however over a longer time than the previous KH-RT model. This behaviour has been seen in other works [100–102, 106], which also show a rapid drop in SMD from nozzle diameter to a steady value, at lower ambient temperatures and pressures, whilst also using the KH-RT model. This would represent a very short liquid core region before a dense region of small droplets form the majority of the spray. This is best shown in Figure 4.17, with the insets showing the differences between the original KH-RT model and the KH-RT "Switch" model implemented within Star-CD.

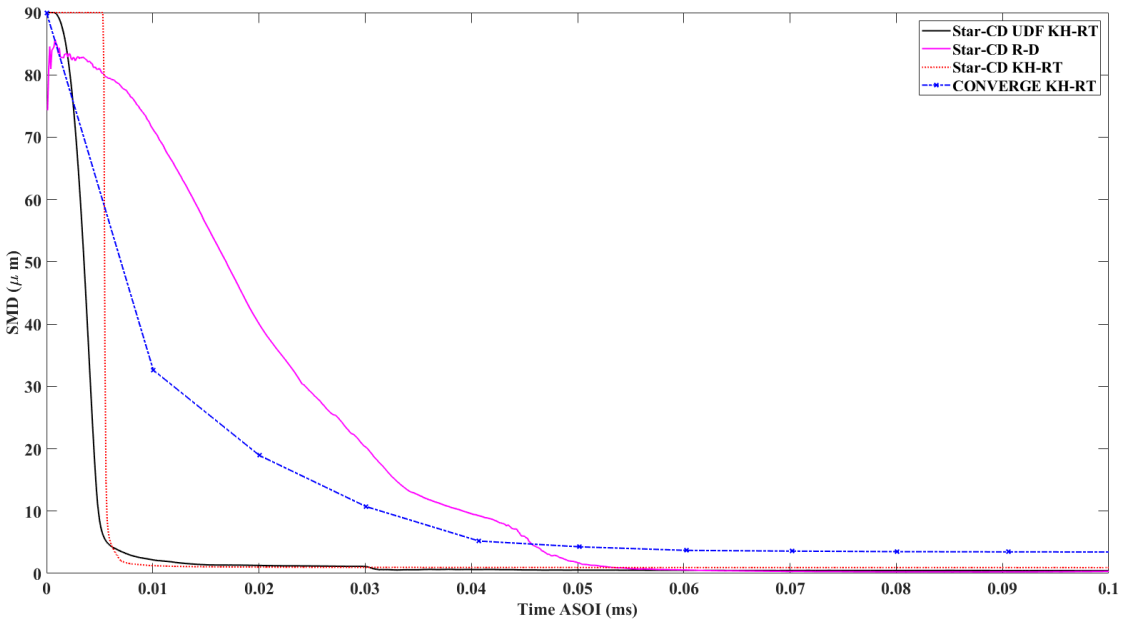

Figure 4.16: SMD for baseline, KH-RT and "Switch" models against time ASOI

Figure 4.17 shows the improvement in modelling within Star-CD, with the insets showing the new ramp down in droplet diameter from Figure 4.17b in comparison to the cliff edge change in droplet diameter in Figure 4.17a. Both Star-CD simulations predict a thinner spray with smaller droplets closer to the nozzle than the CONVERGE simulation shown in Figure 4.17c. Comparisons to experimental data are shown in Figure 4.18, with the Star-CD KH-RT "Switch" model (Figure 4.18b) and CONVERGE (Figure 4.18a) simulations compared to Sandia Mie Scattering results (Figure 4.18c) and Sandia DBI results (Figure 4.18d);

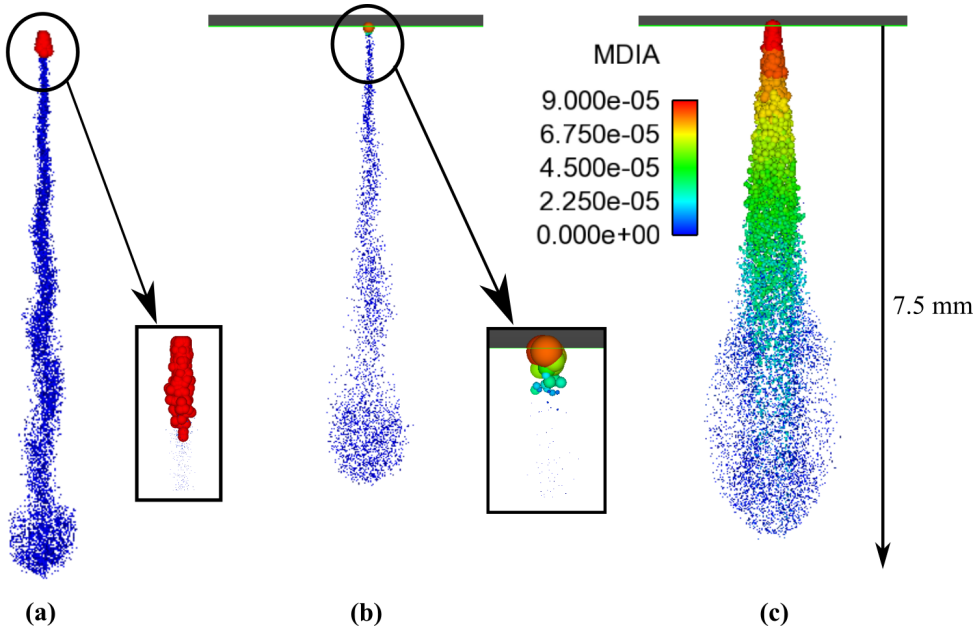

Figure 4.17: Parcel plots of **(a)** original Star-CD KH-RT model, **(b)** Star-CD KH-RT "Switch" model and **(c)** CONVERGE KH-RT (from Fang [94]) simulations, all at 0.06 ms ASOI. MDIA is droplet diameter in metres.

the differences between the Mie Scattering and DBI results are explained by the chosen threshold for the maximum light intensity for the Mie Scattering; the 3 % threshold used in Figure 4.18c predicts a longer liquid length than the DBI results [107]. The largest difference between the Mie Scattering and DBI experiments is the interaction with the light source; Mie Scattering works through scattering of the light as it passes through the liquid, whereas DBI is based on the extinction of the light as it passes through the spray [107, 108]. The Sandia experimental images suggest a thinner spray is seen experimentally, however the spray seen is not as thin as that seen in the Star-CD KH-RT "Switch" model. It should also be noted the under-prediction in initial liquid length ramp can also be seen within Figure 4.18, confirming the liquid length results seen from Figure 4.15. Finally, the wider region of recirculation of smaller droplets at the liquid tip is observed to a lesser extent with the Star-CD models than in the CONVERGE simulation, which may more accurately represent the experimental data.

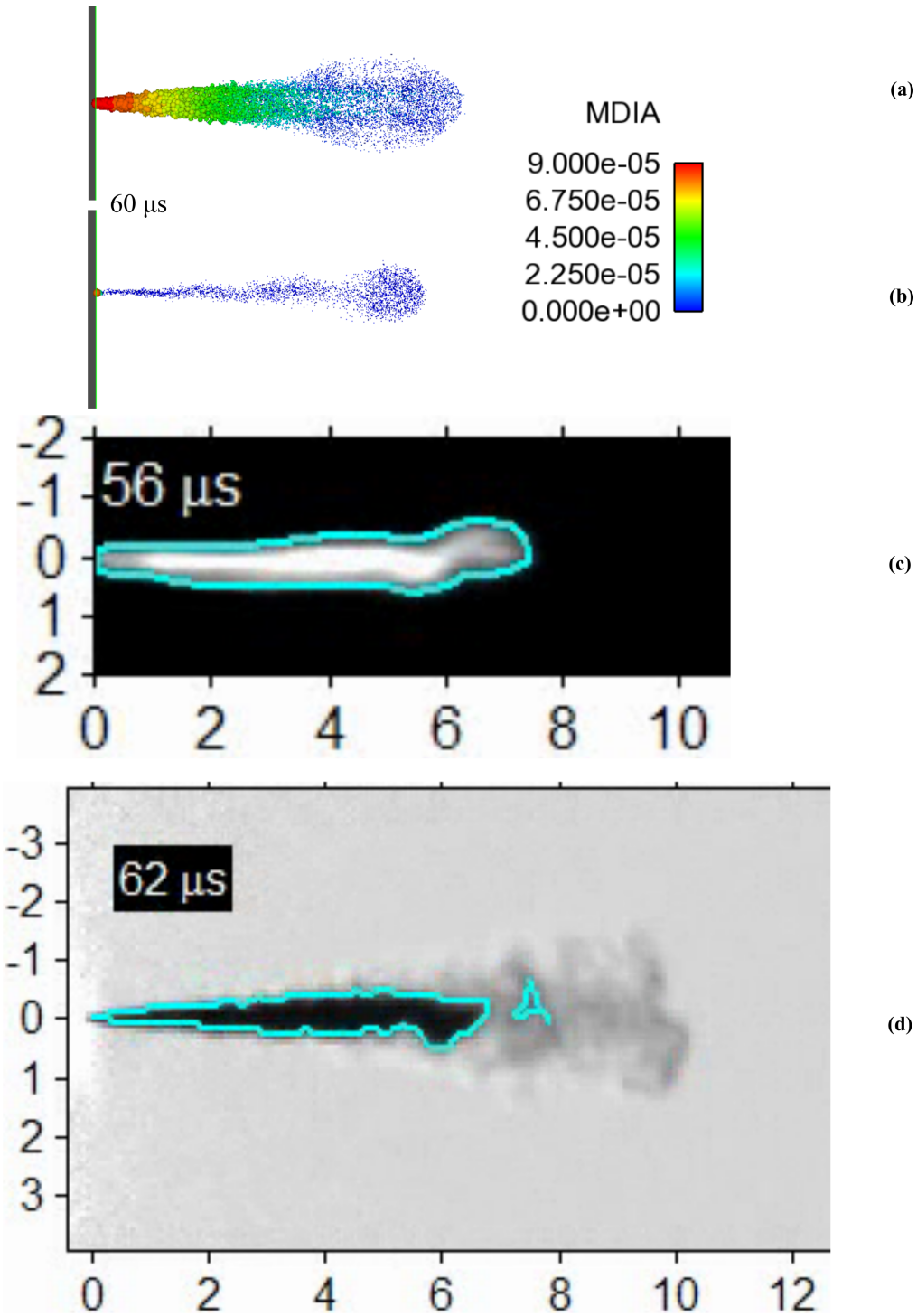

Figure 4.18: Comparison of the transient liquid regions for **(a)** CONVERGE simulation (from Fang [94]), **(b)** Star-CD KH-RT "Switch" simulation, **(c)** Sandia mie scattering, **(d)** Sandia DBI, all at approximately 0.06ms ASOI. **(c)** and **(d)** are available at [27]. Blue lines in **(c)** and **(d)** are the liquid boundaries, found by removing the background through frame comparison [24]. MDIA is droplet diameter in meters, scaling in **(c)** and **(d)** are in millimeters.

4.4.2 Improved Matching Using "Switch" Model

With this new KH-RT model implemented within Star-CD, a greater level of matching for both liquid and vapour lengths is available in comparison to before. Within this case, applying the constant changes shown in Table 4.7 the liquid and vapour lengths can be better matched with the switch model than previously, and is an improvement over the baseline case as well. These values were obtained using a small parametric study of the four constants, adjusting the $C_{1\varepsilon}$ constant to match the vapour length and then using the break-up model constants to reduce the liquid length. $C_{1\varepsilon}$ was altered in increments of 0.005, S_N was altered to sweep the switching position between 3 and 10 mm from the injector tip, B_{KH1} was swept between 5 and 7 in increments of 0.25 and B_{RT0} was swept between 0.05 and 0.1 in increments of 0.01. The full injection period is shown in Figure 4.19, which clearly shows the improvement in the vapour predictions from the original to the matched UDF switch model.

Table 4.7: Tuning parameters changed to improve liquid and vapour matches using the KH-RT "Switch" model

Sub-Model	**Constant**	**Original (Fig 4.14)**	**Tuned (Fig 4.19)**
Turbulence	$C_{1\varepsilon}$	1.58	1.61
KH-RT "Switch"	S_N (Eq 4.2)	203.9	543.8
KH	B_{KH1} (Eq 2.58)	7	6
RT	B_{RT0} (Eq 2.63)	0.1	0.07

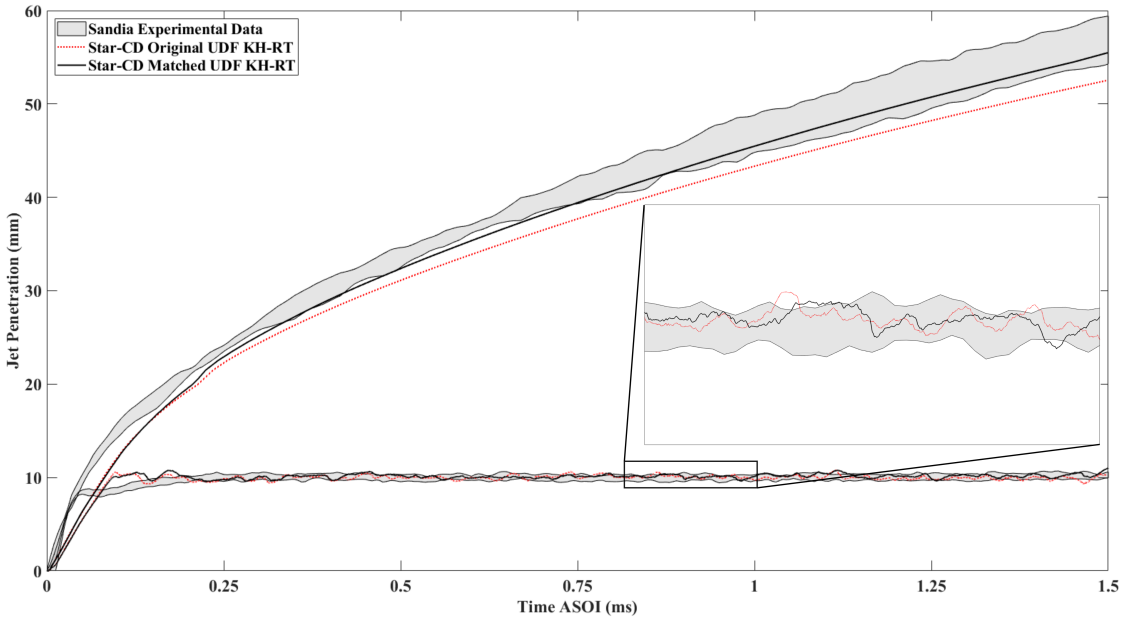

Figure 4.19: Comparison of matched and original UDF "Switch" model liquid and vapour penetrations against time ASOI, with inset showing liquid lengths between 0.8 and 1 ms ASOI

Considering Figure 4.19, there is a clear improvement in vapour length match seen using the constant changes shown in Table 4.7 when compared to the original UDF vapour lengths seen before. This is achieved with little impact on the overall liquid length, as seen in Table 4.8 when comparing the previous constants to the matched constants.

Table 4.8: Simulated and experimental transient and steady state liquid lengths for old and new UDF constants

Model Setup	**Maximum Transient Liquid Length**	**Steady State Liquid Length**
Original UDF	10.60 mm	10.01 mm
Tuned UDF	10.75 mm	10.15 mm
Experimental	9.46 mm	10.08 ± 0.34 mm

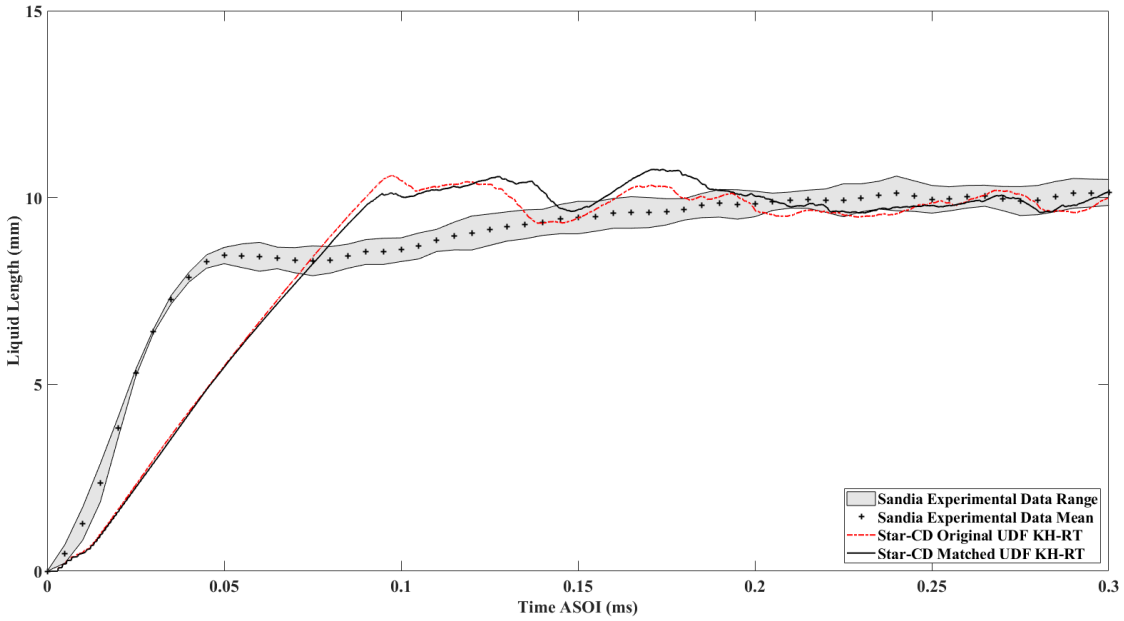

Figure 4.20: Comparison of matched and original UDF "Switch" model transient liquid length predictions against time ASOI

The difference in the transient region is shown in Figure 4.20, with the initial peak reduced in the new tune however the second peak (at approximately 0.175 ms ASOI) being larger than before. When compared to CONVERGE this is still an over-prediction, however this is still an improvement over the baseline Reitz-Diwakar case, with an improved vapour length match as well. The impact of utilising this improved matching capability will be considered in Chapter 6, where the KH-RT "Switch" model will be used to alter the liquid and vapour lengths independently at the vaporising case before then applying these cases to a combusting spray.

4.4.3 Impact of Switching Position on Vapour Fields

Whilst the previous sections focused on the liquid and vapour lengths, the impact of the implementation of the "Switch" model on the characteristics of the vapour fields were not considered. The composition of the vapour field is extremely important for combustion prediction, and as a result if the implementation of the "Switch" model has any impact on this it will change the characteristics of a combusting spray. To begin with, the vaporising case considered in the derivation of the KH-RT "Switch" Model will be used to ascertain the impact of the S_N constant on the vapour fields. Both a cross-sectional slice of the spray, showing the vapour mass fraction distribution along the centreline plane of the spray, and the spray vapour boundary will be shown, the vapour boundaries are based on either the computational definition of the vapour field as the area encompassing a vapour mass fraction of greater than 0.1 %, or the experimental boundary found through frame comparison. An example of this is seen in Figure 4.21. As can be seen from Figure 4.21, the vapour boundary fails to capture some of the oscillatory behaviour seen within the cross-sectional slice, shown most prominently at ∼10 mm from the injector in Figure 4.21a at approximately 25 mm from the injector tip. Along with this, due to the assumptions in its formation [77], RANS modelling fails to capture the eddies on the outside of the experimental vapour field, shown in Figure 4.21b. This is further confirmed by looking at the baseline break-up model implementations within Star-CD, shown in Figure 4.21c. All of the baseline cases predict a uniform spray, with the KH-RT models (baseline and "Switch") predicting very similar spray structures and the RD model predicting a slightly wider spray. Apart from the eddies being incorrectly captured, all the baseline models qualitatively predict the spray well, which is further confirmed when considering the cone angles later in the injection phase.

Along with the baseline cases, three different values for S_N are also considered, of 68.0, 203.9 and 543.8. From Table 4.4, these correspond to switching positions (SW_1) of 1, 3 and 8 mm respectively. Table 4.9 shows the cone angles calculated from the vapour fields for the baseline cases and varying S_N numbers. Given the definition of

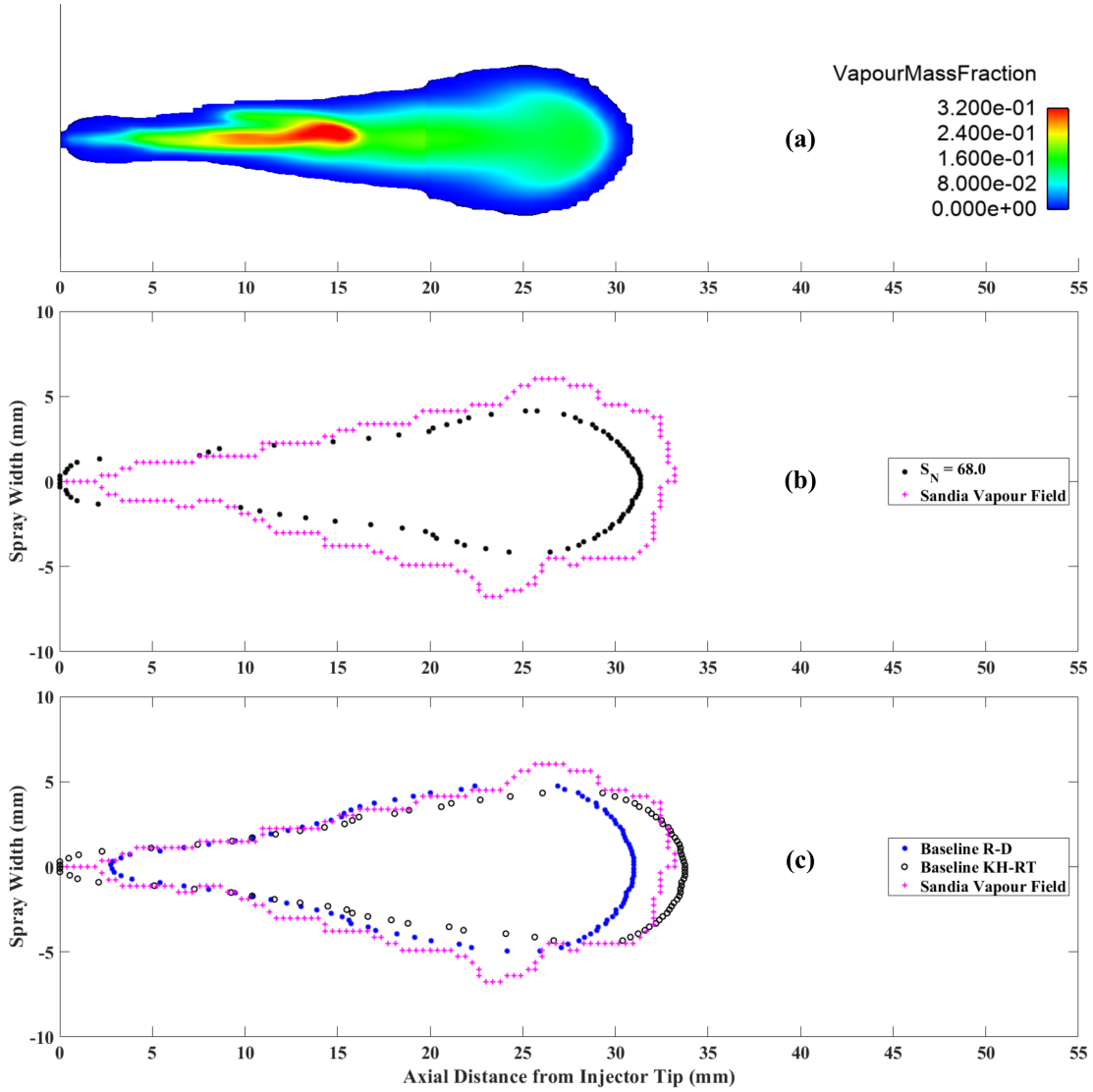

Figure 4.21: Plots at 0.5 ms ASOI of the **(a)** vapour mass fraction distribution for the $S_N = 68.0$ case and **(b)** spray vapour boundary fields for the case $S_N = 68.0$. **(c)** shows the baseline Reitz-Diwakar and KH-RT results for Star-CD, shown with the experimental vapour field

cone angle is taken from the work of Naber and Siebers [109], where the cone angle is the angle encompassed by the spray up to half the penetration, the oscillation seen in Figure 4.21 is mostly removed from the cone angle calculations. As a result the cone angles align fairly closely with the computational data, with the baseline Star-CD RD model proving the best fit. This is clear from Figure 4.21c, as the fields are closely aligned at ∼16 mm from the injector tip, at approximately half their vapour lengths. All of the KH-RT models predict cone angles within 1° of each other,

Table 4.9: Computational and experimental cone angles calculated from the vapour fields at varying times ASOI. Cone angles are in degrees, calculated as in Naber and Siebers [109]

Break-Up Model	**0.5 ms**	**0.75 ms**	**1 ms**	**1.25 ms**	**Mean**
Baseline RD	23.4	22.3	22.5	22.5	22.7
Baseline KH-RT	18.4	19.4	20.0	20.2	19.5
"Switch", SW_1 = 1 mm	18.2	19.4	19.2	19.3	19.0
"Switch", SW_1 = 3 mm	19.1	19.0	19.4	19.8	19.4
"Switch", SW_1 = 8 mm	18.7	19.3	19.6	20.0	19.4
Experimental	23.4	22.1	24.3	23.2	23.3

which is unsurprising given the cone angle for all these models is specified as 20°.

The oscillatory behaviour seen in the low S_N case in Figure 4.21a is not repeated in other switching positions, shown in the 0.5 ms ASOI vapour fields in Figure 4.22. The oscillation at the tip of the high fuel vapour mass fraction seen in the low S_N case is smoothed in higher S_N cases, with this carrying through to later in the injection phase. This is shown in the 1.25 ms ASOI vapour fields in Figure 4.22; with the tip of the vapour field (vapour mass fraction of approximately 8e-2) in the low S_N case clearly non-symmetrical, especially when compared to the vapour tips of the other S_N values. Its noteworthy that the boundaries of all three vapour fields are extremely similar, with the only changes seen due to the oscillation in the low S_N case, along with a slightly thinner near-nozzle vapour field in higher S_N values.

4.5 Conclusions

Within this chapter, a single-hole non-reacting diesel spray has been simulated in two separate commercial CFD codes using a Lagrangian-Eulerian approach. The spray simulated was based on the ECN "Spray A" operating condition, making use of the available experimental data from the ECN database. Comparisons between the two CFD codes, Star-CD and CONVERGE, were made as follows:

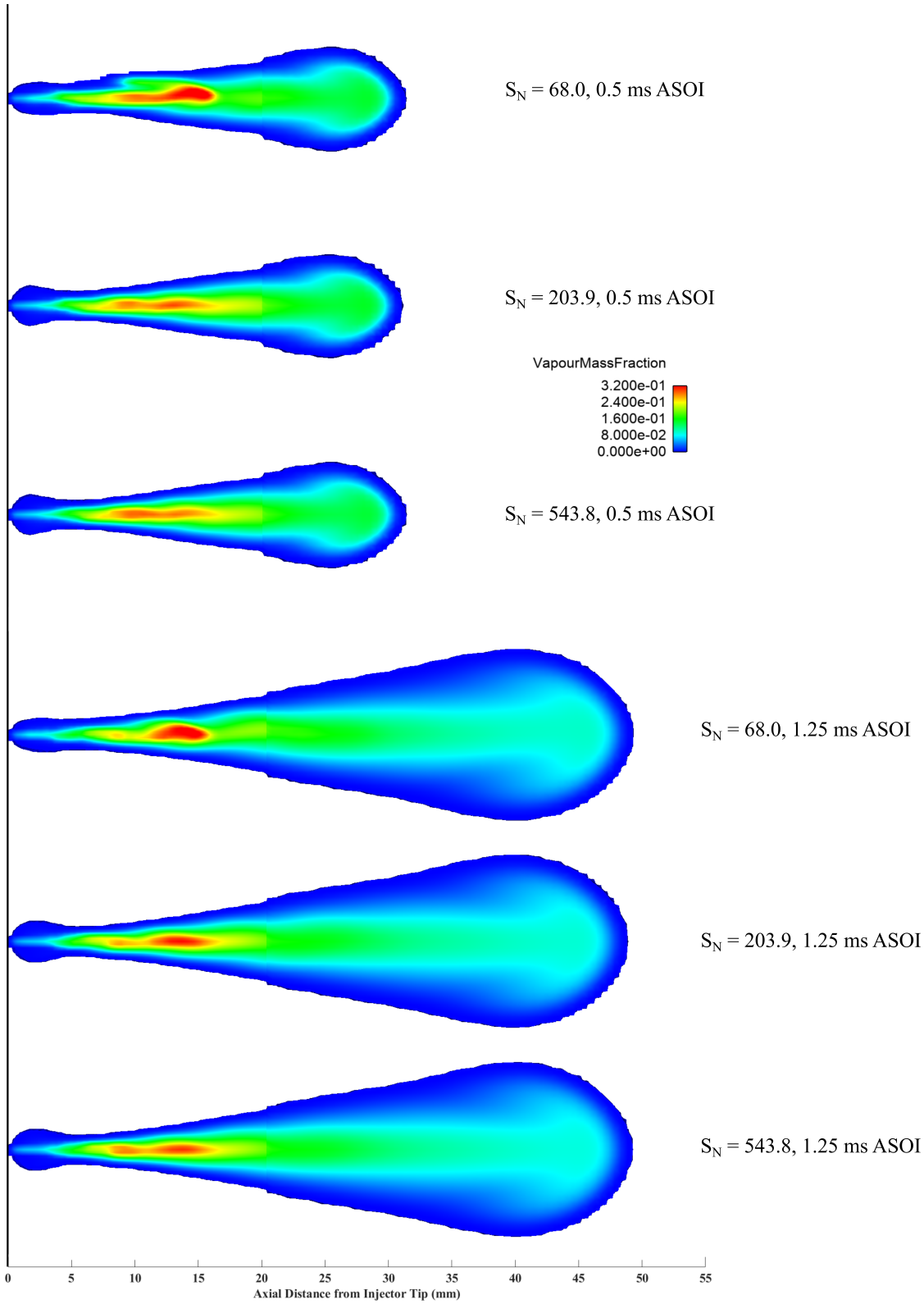

Figure 4.22: Vapour mass fraction distributions for S_N values of 68.0, 203.9 and 543.8 at 0.5 ms ASOI (top) and 1.25 ms ASOI (bottom)

- Baseline comparisons have been made between the two codes at initial set-ups optimized for steady state liquid lengths. Discrepancies in transient predictions have been observed between the codes, with the break-up model considered to be one of the principle causes of these differences.

- A direct comparison between codes has shown a difference in implementation between seemingly identical break-up models (known as the KH-RT model), leading to a difference in overall liquid length prediction between codes. Star-CD allowed the KH and RT models to be applied at any time and position, and to any droplet parcel, with the two models competing, whereas CONVERGE employed only the KH model to parcels initially and then the RT model to all child droplets after they had undergone break-up once.

- A new implementation of the KH-RT model has been introduced for use within Star-CD, allowing for the two models to act at different regions of the spray. This implementation shows a similar match to steady state liquid length with a reduction in the transient overshoot, moving closer to the liquid lengths seen in CONVERGE. The new implementation allows Star-CD to utilize the KH-RT model to match more closely the experimentally observed liquid length, and also match the vapour length without compromising the liquid length prediction as seen in the baseline KH-RT model.

- The impact of the new KH-RT "Switch" model on the spray vapour fields has been characterised, with earlier switching positions showing oscillatory behaviour throughout injection near to the nozzle exit, however at no impact to the cone angle of the spray.

Further work will be required to develop the criterion to control usage of the KH and RT models, utilizing experimental data at both higher and lower pressures and temperatures, a range of injection pressures and with different fuels, to extend the predictive capability of this model. Results for simulations applying the model to a combusting spray can be found in the following chapter.

5 Application of a Novel KH-RT Switching Length Definition to a Combusting Spray

Within this chapter the KH-RT "Switch" model derived in Chapter 4 will be tested in a combusting case against the baseline Reitz-Diwakar case shown previously. Both model setups predict very similar ignition delays, lift-off-lengths and combustion fields, suggesting the KH-RT "Switch" model is on par with the Reitz-Diwakar model for combustion prediction. Different criteria for judging the ignition delays and lift-off-lengths are compared, with all methods predicting very similar results. The KH and RT sub-models are also compared, with the RT model showing similar instabilities in the liquid and vapour predictions as were seen in Chapter 4.

5.1 Combusting Test Point

5.1.1 Combusting Case

For this case, the experimental data used for comparison is the work presented by Lillo et al. [110], utilising the 15 % O_2 case. The ambient gas composition is shown in Table 5.1, with the ambient conditions being the same as before (shown in Table 3.1). The mean combustion criteria are shown in Table 5.2, with the full injection lift-off-length shown in Figure 5.1. It is important to note that the time frame considered differs, with a simulation time of 2 ms used compared to the 1.5 ms of the previous sections.

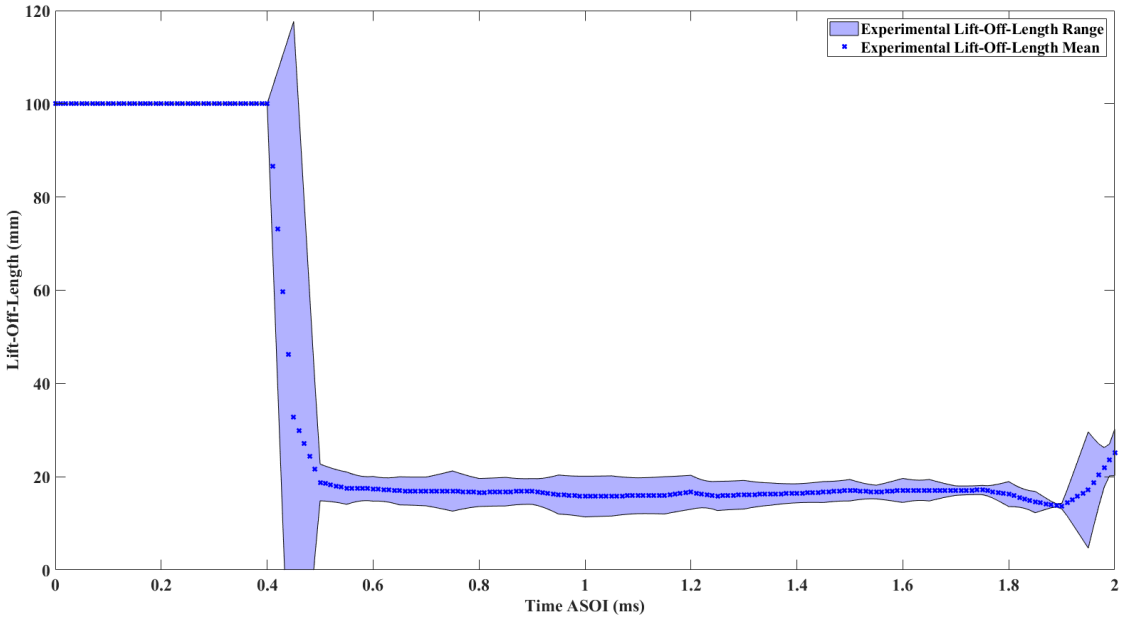

Figure 5.1: Sandia experimental data for combusting "Spray A" case showing lift-off-length range and mean [110]

Table 5.1: ECN combusting "Spray A" gas composition [27, 110]

Gas	**Mass Fraction (%)**
N_2	75.15
O_2	15
CO_2	6.22
H_2O	3.62

Table 5.2: Mean experimental lift-off-length and ignition delay for the combusting "Spray A" case [110]

Lift-Off-Length (mm)	**Ignition Delay (ms)**
16.60 ± 3.98	0.43

The lift-off-length mean is calculated after the end of its transient period to the end of injection, however the end of the lift-off-length transient period is different to that of the liquid length period as defined in Chapter 4. The reasoning for this can be seen by looking at Figure 5.1, as between 0.4 ms and 0.5 ms ASOI the lift-off-length has an extremely large error compared to the mean, whilst at around 0.5 ms ASOI

the lift-off-length levels off. This is unsurprising given the ignition delay for this case is 0.43 ms ASOI, and there will be a time delay between the ignition delay and the formation of a steady state lift-off-length. As a result, the lift-off-length mean is calculated between 0.5 ms and 1.5 ms ASOI. As before, all the experimental results presented in Figure 5.1 are presented as the ranges encompassing the 95 % confidence interval, with the means including this experimental error.

The lift-off-length for the "Spray A" condition is generally influenced by the auto-ignition chemistry [111], with the flame speed and injection velocity determining the position of the lift-off-length. As such, the auto-ignition species such as CH_2O along with OH are important in lift-off-length predictions [111]. The ignition delay can also be shown to correlate with the lift-off-length [111, 112]. Along with this the position of the lift-off-length also correlates to the soot production of the combusting flame, given the position of the lift-off-length correlates to the stoichiometric flame front, after which the fuel burns in a oxygen-deprived environment [113], thus "burning off" the soot formed through incomplete combustion.

5.1.2 Combustion Modelling in Star-CD

For the simulations of a combusting spray within Star-CD, the domain will be set up as was seen in Chapter 4, with the k-ε turbulence model being used along with a set-up of either the Huh-Gosman/Reitz-Diwakar atomisation/break-up models or the KH-RT model being applied to both. The only difference between the combusting domain and the non-combusting domain is the application of detailed chemistry to model the combustion of n-dodecane. The numerical model for this is detailed below, with a time-split method applied alongside a dynamic multi-zone method to help reduce the computational expense of modelling combustion. The combustion is modelled using a "well mixed" method, where each transport equation is solved at the same resolution as the cell size. The mean chemical source terms are calculated based on the mean cell temperature, pressure and species mass fractions, as such ignoring the turbulent fluctuations within the system. This method has been

compared to more complex combustion systems, such as conditional moment closure, showing good matches to ignition delays and over-predictions of lift-off-lengths [114].

Within Star-CD combustion can be handled by the application of a time-split method for solving detailed chemistry [115] with the transport equations for all species solved within Star-CD, utilising provided transport and thermal data for each species from CHEMKIN. The transport equations for species mass fractions (y_i) are calculated as in Equation 5.1, with $F_{i,j}$ being the diffusion flux component which is influenced by the mass fraction (y_i), the temperature (T) and the eddy viscosity (μ_t). The production rate of the species i (S_i) is considered a sum of the mole concentrations of the species i from all the reactions within the mechanism, and is simplified using the time-split method.

$$\frac{\delta}{\delta t}(\rho y_i) + \frac{\delta}{\delta x_j}(\rho u_j y_i - F_{i,j}) = S_i \tag{5.1}$$

The time-split method splits Equation 5.1, allowing for two simultaneous equations to be solved to reduce the "stiffness" of the single equation caused by the large differences in reaction time scales. The time-split method is shown in Equations 5.2 and 5.3, with $\mathbf{y}$ and $\mathbf{S}$ as the sets of species mass fractions and production rates for all species considered. Splitting Equation 5.1 in this way transfers the "stiffness" to Equation 5.3, however this can be reduced again by utlising a Dynamic Multi-Zone (DMZ) method [116].

$$\frac{\delta}{\delta t}(\rho y_i) + \frac{\delta}{\delta x_j}(\rho u_j y_i - F_{i,j}) = 0 \tag{5.2}$$

$$\frac{d}{dt}(\rho \mathbf{y}) = \mathbf{S} \tag{5.3}$$

The DMZ method is a standard method within Star-CD, and it consists of a three step system, firstly constructing the group of cells with similar thermo-chemical states, then solving the chemistry equations within each group before finally mapping the group solution to each cell within the group. Four characteristic quantities are used by Star-CD to construct the groups, these are the temperature (representing

combustion progress), mixture fraction (representing mixing progress), enthalpy (representing energy level) and mass fraction of species such as CH_2O and H_2O_2 to capture the auto-ignition process [114, 115, 117] with no requirement for specific models such as the Shell auto-ignition model [118].

Group mean quantities are calculated by averaging the corresponding quantity for all cells in each group, with the mixture fraction mean taken as an example and shown in Equation 5.4, with the subscript g pertaining to the group being considered.

$$y_{ig} = \frac{\mathbf{\Sigma} y_i \rho_i \nu_i}{\mathbf{\Sigma} \rho_i \nu_i} \tag{5.4}$$

With the groups of cells constructed, the calculated mean mass fractions within the group can be calculated using the time-split method above, with Equation 5.3 being solved in the form of Equation 5.5 by replacing the production rate ($\mathbf{S}$) with the reaction rate of species i in group g (ω_{ig}) evaluated on the group mean quantities.

$$\rho \frac{\delta y_{ig}}{\delta t} = \omega_{ig} \tag{5.5}$$

Lastly, after solving Equation 5.5 for each group the mean reaction rate of all species in a group ($\overline{\omega_{ig}}$) can be calculated, as is shown in Equation 5.6 at time-steps n and $n+1$. Utilising this mean reaction rate, the mass fraction of each species can be mapped to each cell within a certain group as shown in Equation 5.7.

$$\overline{\omega_{ig}} = \frac{y_{ig}^{n+1} - y_{ig}^{n}}{\delta t} \tag{5.6}$$

$$y_i^{n+1} = y_i^n + \delta t \; . \; \overline{\omega_{ig}} \tag{5.7}$$

Given the construction of the groups for the DMZ method the important quantities to compare between combusting set-ups when considering the combustion and mixing progress are the temperature and mixture fraction, as such these will be used for ascertaining the differences between break-up models in this chapter, and the vaporising match in Chapter 6.

5.1.3 Combusting Domain Set-up

To model the combustion of n-dodecane within this thesis the skeletal mechanism of Yao et al. [119] will be used, which is a 54 species, 269 reaction mechanism, allowing for the combustion of n-dodecane to be viewed a series of reversible reactions. The equation for the ideal (complete) combustion of n-dodecane is shown in Equation 5.8.

$$C_{12}H_{26} + 18.5O_2 \rightarrow 12CO_2 + 13H_2O \tag{5.8}$$

Yao's mechanism was chosen due to its lower reaction count and hence quicker computational time than other available n-dodecane mechanisms like that of Wang et al. [120]. Given the combustion mechanism is used as a means of comparison and not as an in-depth combustion analysis a more complete mechanism isn't required. However, this mechanism has been used in DNS [121], LES [122] and RANS [123,124] simulations with good results being seen in all studies. This mechanism has been shown to overpredict the lift-off-length when compared to the "Spray A" condition using RANS models [125, 126], however given this mechanism is being used to solely compare the break-up models this is not a concern for this study.

To determine the lift-off-lengths and ignition delays for the Reitz-Diwakar and KH-RT "Switch" model two different methods will be used: a temperature based criterion and an OH mass fraction criterion. Both criteria have been used in previous studies to predict lift-off-lengths well [105, 120, 127], however the temperature criterion has not been used for predicting the ignition delays; for this study the maximum temperature gradient seen will determine the ignition delay [105]. The temperature criterion determines the ignition delay as the first timestep at which the temperature exceeds 400 K above the ambient temperature, and the lift-off-length is defined as the closest point to the injector at which the temperature exceeds 400 K above the ambient temperature, for "Spray A" this criterion is the point at which the temperature exceeds 1300 K. The OH mass fraction criterion is as defined in Section 4.1.1, with an additional OH threshold of 14 % of the simulation long OH mass fraction maximum also considered (as in [105, 127]) for both the

lift-off-lengths and ignition delay. The OH mass fraction is especially useful for predicting combustion locations due to the reaction shown in Equation 5.9 being the dominant mechanism for heat release in hydrocarbon combustion [120]. As such, the OH field is a good indicator for high temperature regions of the spray, and especially good for comparison to experimental imaging.

$$CO + OH \leftrightarrow CO_2 + H \tag{5.9}$$

For the combusting studies both the baseline Reitz-Diwakar model and the KH-RT "Switch" model will be tested and compared to determine if the break-up model has an impact on the combustion predictions. The KH-RT "Switch" model set-up is shown in Table 5.3, with the Reitz-Diwakar model set-up as before in Table 4.2.

Table 5.3: KH-RT "Switch" model constants for combustion simulations

Constant	**Value used in Simulation**
***k*-ε Turbulence Model**	
$\mathbf{C}_{\mu}$	0.09
$\mathbf{C}_{1\varepsilon}$	1.58
$\mathbf{C}_{2\varepsilon}$	1.96
$\boldsymbol{\sigma}_k$	1
$\boldsymbol{\sigma}_{\varepsilon}$	1.3
KH-RT "Switch" Break-up Model	
$\mathbf{B}_{KH0}$	0.6
$\mathbf{B}_{KH1}$	7
$\mathbf{B}_{RT0}$	0.1
$\mathbf{B}_{RT1}$	1
$\mathbf{S}_N$	203.9

The constants chosen are identical to the non-combusting case shown in Section 4.4.1, and are shown in Table 5.3. These are used due to the match provided to the baseline Reitz-Diwakar model, as shown in Figure 4.15, allowing for a detailed

comparison between the two break-up models given their similar liquid and vapour lengths. The fully matched KH-RT "Switch" model constants (as shown in Table 4.7) are not used due to the increase in vapour length when compared to the baseline Reitz-Diwakar model making combustion fields hard to compare back-to-back. However, the fully matched KH-RT "Switch" model will be compared to the constants shown in Table 5.3 in Chapter 6, along with other vaporising case matches.

5.2 Baseline Combusting Case Results

5.2.1 Ignition Delays

As Table 5.2 shows, the ignition delay for the experimental combusting "Spray A" case is 0.43 ms ASOI. For both the Reitz-Diwakar and KH-RT "Switch" models the OH mass fraction and temperature fields were extracted from the simulations, and the maximum values found for each model. After this, the criteria were applied and the time period between 0.3 and 0.45 ms ASOI are plotted for each model, shown in Figure 5.2.

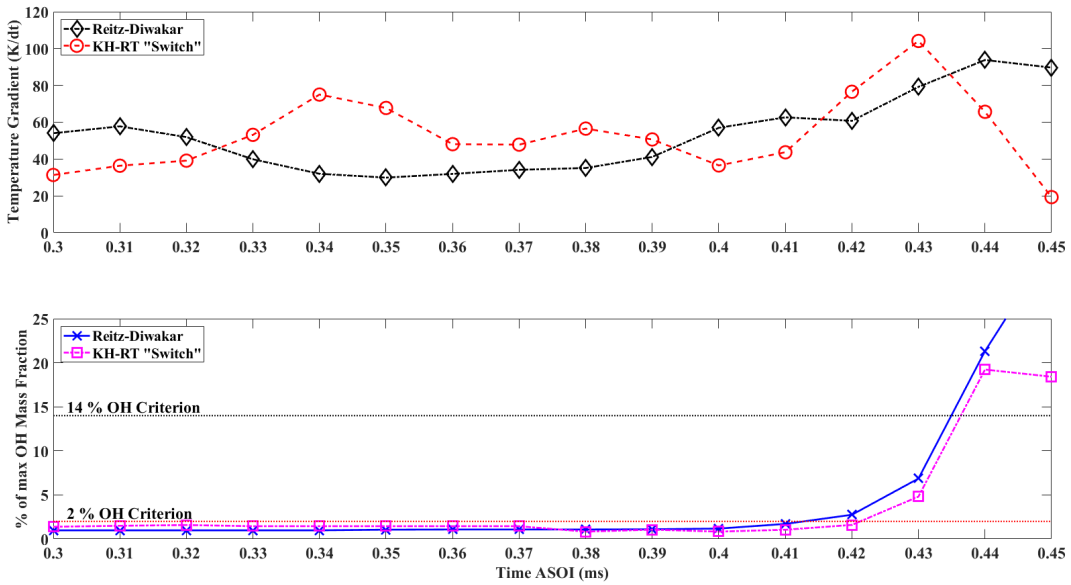

Figure 5.2: Maximum temperature gradient (top) and OH mass fractions (bottom) for both Reitz-Diwakar and KH-RT "Switch" models between 0.3 and 0.45 ms ASOI, with ignition delay criteria shown

Figure 5.2 shows that there is a slight difference in prediction of the 2 % OH_{max} criterion ignition delay between the models, with the Reitz-Diwakar model predicting

an ignition delay of 0.42 ms ASOI and the KH-RT "Switch" model predicting an ignition delay of 0.43 ms ASOI. Both models predict the same ignition delay for the 14 % OH_{max} criterion, of 0.44 ms ASOI. The temperature gradient criterion also predicts the ignition delay excellently, with the predictions very close to both the OH criteria and experimental ignition delays. Table 5.4 shows the predicted ignition delays between all models and criteria.

Table 5.4: Predicted ignition delays for both Reitz-Diwakar and KH-RT "Switch" models at both OH mass fraction and temperature criteria

Model and Criterion	**Ignition Delay (ms ASOI)**
Reitz-Diwakar 2 % OH_{max}	0.42
Reitz-Diwakar 14 % OH_{max}	0.44
Reitz-Diwakar T_{amb} + 400 K	0.44
KH-RT "Switch" 2 % OH_{max}	0.43
KH-RT "Switch" 14 % OH_{max}	0.44
KH-RT "Switch" T_{amb} + 400 K	0.43
Experimental	0.43

Figure 5.3 shows the comparison of the Reitz-Diwakar and KH-RT "Switch" models at the time of their measured temperature gradient ignition delays (0.44 and 0.43 ms ASOI respectively), with the pre-ignition species H_2O_2 and CH_2O, the mixture fractions and the temperatures shown. What is notable is the similarity in the peaks in the pre-ignition species, with the KH-RT "Switch" model's lower predicted vaporising SMD clearly showing an earlier and closer to nozzle ignition occurring in both pre-ignition species plots. The thinner spray of the KH-RT "Switch" model is also clearly visible, which is further shown when considering mixture fraction slices between the two models, as shown in Figure 5.4. Within this study, the mixture fraction is defined as the mass fraction of fuel within each cell, a definition commonly used within CFD along with Star-CD [93, 115, 128]. Within Section 5.2.3 the impact of this difference in mixture fraction will be considered, along with the temperature, OH and C_2H_2 predictions of each model.

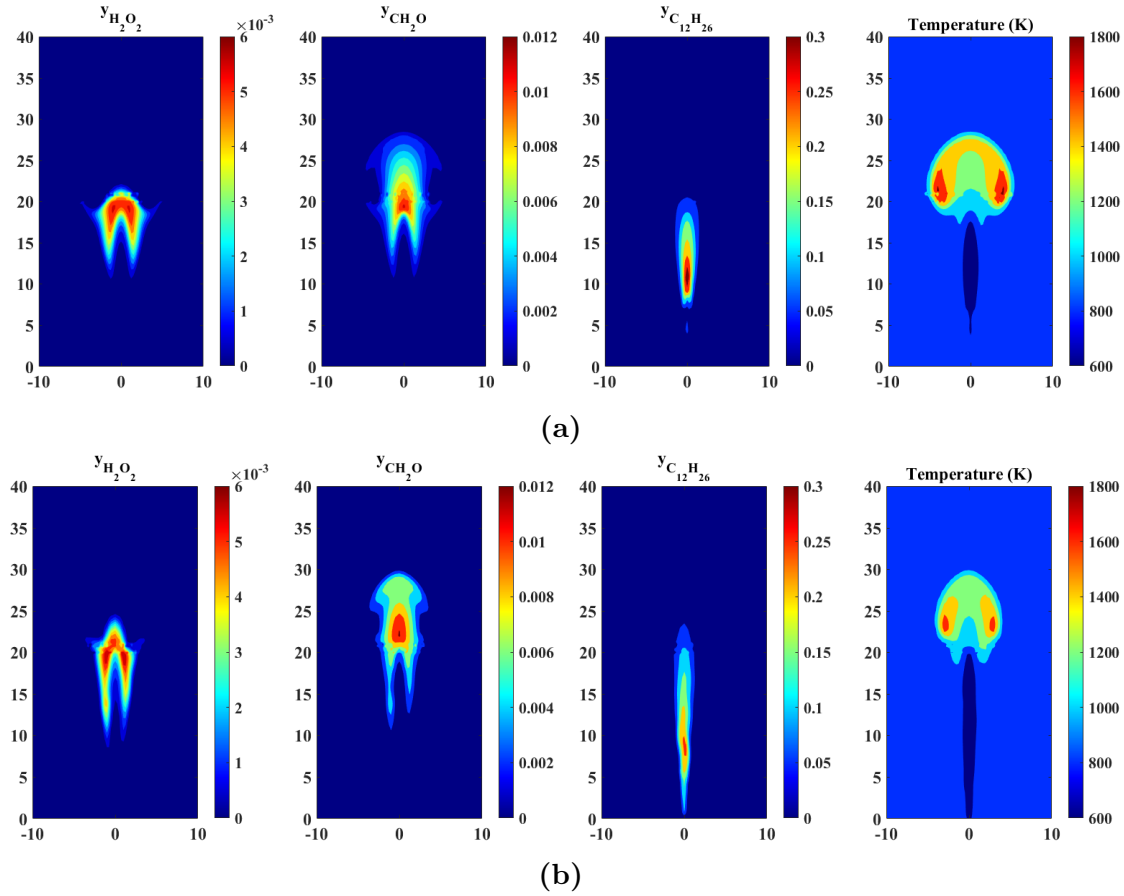

Figure 5.3: H_2O_2, CH_2O, $C_{12}H_{26}$ and temperature fields at the measured ignition delay for the **(a)** Reitz-Diwakar (at 0.44 ms ASOI) and **(b)** KH-RT "Switch" (at 0.43 ms ASOI) models

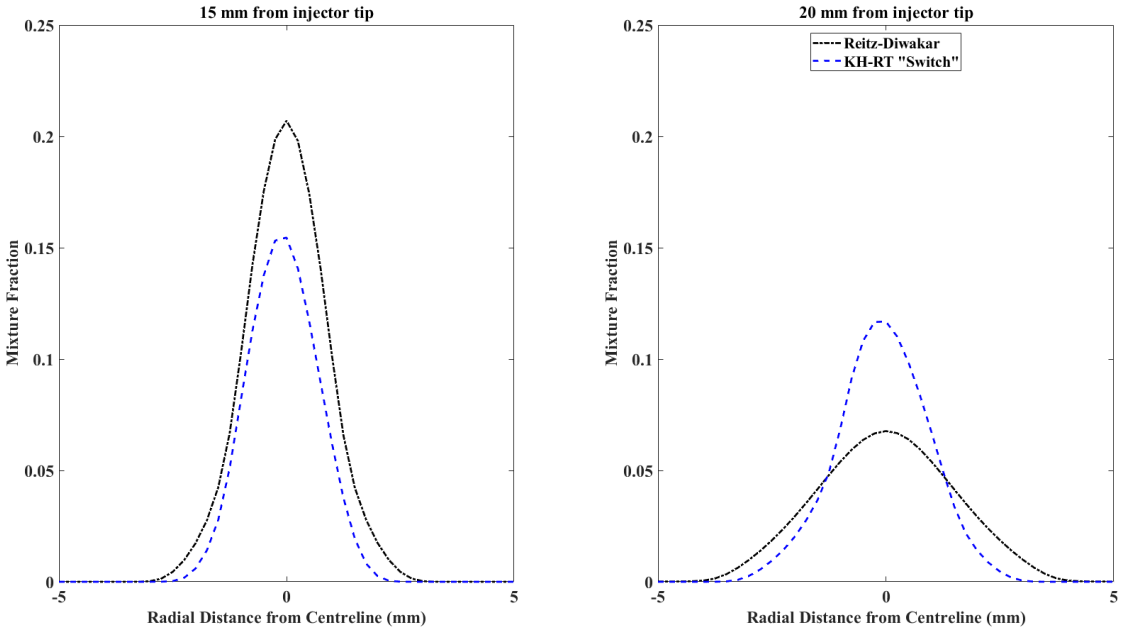

Figure 5.4: Mixture fractions for the Reitz-Diwakar and KH-RT "Switch" models at 1 ms ASOI at distances 15 and 20 mm from the injector tip

5.2.2 Lift-Off-Lengths

As with the ignition delays, the lift-off-lengths are calculated using the 2 % and 14 % OH_{max} criteria and the T_{amb} + 400 K criteria. Figure 5.5 shows the comparison of the lift-off-lengths after the start of combustion between the simulations and experimental data. As can be seen, initially the lift-off-lengths are predicted well, however as combustion continues the lift-off-lengths diverge from the experimental results before returning within the experimental error at the end of the simulated time. Comparing between the break-up models, the Reitz-Diwakar model predicts a slightly lower lift-off-length initially, however the models converge around the end of injection to predict very similar lift-off-lengths. Finally, the OH and temperature criteria appear to make very little difference to the predicted lift-off-lengths, with only a minor divergence seen in the Reitz-Diwakar model at 1.25 ms to 1.75 ms, however generally all criteria predict very similar lift-off-lengths. The over-prediction of lift-off-lengths seen in Figure 5.5 has been seen for both the well mixed model [114, 128, 129] and the Yao mechanism [125, 130], and as such is not considered an issue for this work.

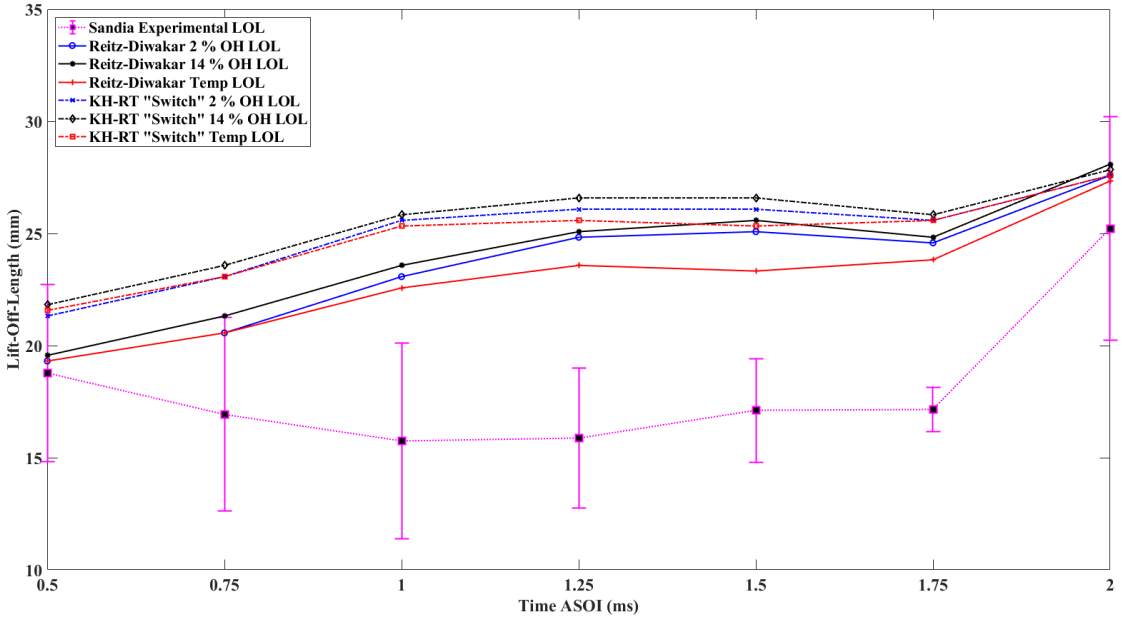

Figure 5.5: Simulated and experimental lift-off-lengths for the combusting "Spray A" case after start of combustion

5.2.3 Combustion Fields

Comparing the OH and temperature fields allows an insight into the relative difference in the combusting regions between the models; given the results in Section 4.4.3 show a difference in vapour field width it is expected that there should be differences in the combusting zones. Comparing results of both models against experimental images from Sandia shows good agreement in capturing the combustion zones, as shown in Figure 5.6. For this case the combustion zone is defined as the area of the spray that is above 950 K, as these areas will be bounded by the combusting spray and thus provide the best comparison to experimental data. A sweep of temperatures from 950 K to 1150 K was undertaken, with little difference seen in the areas above this temperature, and as such the threshold was set to 950 K to capture all the areas of increased temperature. Mirroring what was shown in Figure 5.5, the nearer nozzle combustion is not captured well in the simulations, however the main combustion field between 25 and 40 mm from the injector tip is broadly well captured, with a slight under-prediction in the field tip position, mirroring what was seen in the vaporising case's under-prediction of vapour length (shown in Figure 4.15).

Figure 5.7 shows the OH and temperature fields for both the Reitz-Diwakar and KH-RT "Switch" models at 1 ms and 1.5 ms ASOI. As can be seen, the Reitz-Diwakar case has a noticeably wider spray plume at both times shown, with the shorter lift-off-length shown in Figure 5.5 visible at 1 ms ASOI. The KH-RT "Switch" model also penetrates further with both the OH and temperature fields at 1 ms ASOI, however this difference in penetration is reduced as the injection continues. Another interesting observation is that the 2 % OH_{max} boundary matches very well with the high temperature regions of the spray confirming the initial reasoning behind selecting this criterion as a predictor of combustion zones. This comparison is shown in Figure 5.8, showing the 2 % OH_{max} boundary closely following the red temperature boundary of 2000 K within the spray plume, especially in the KH-RT "Switch" model.

It is also notable how the temperature within the centre of the spray is different between models, with the KH-RT "Switch" model showing a hotter core of the spray

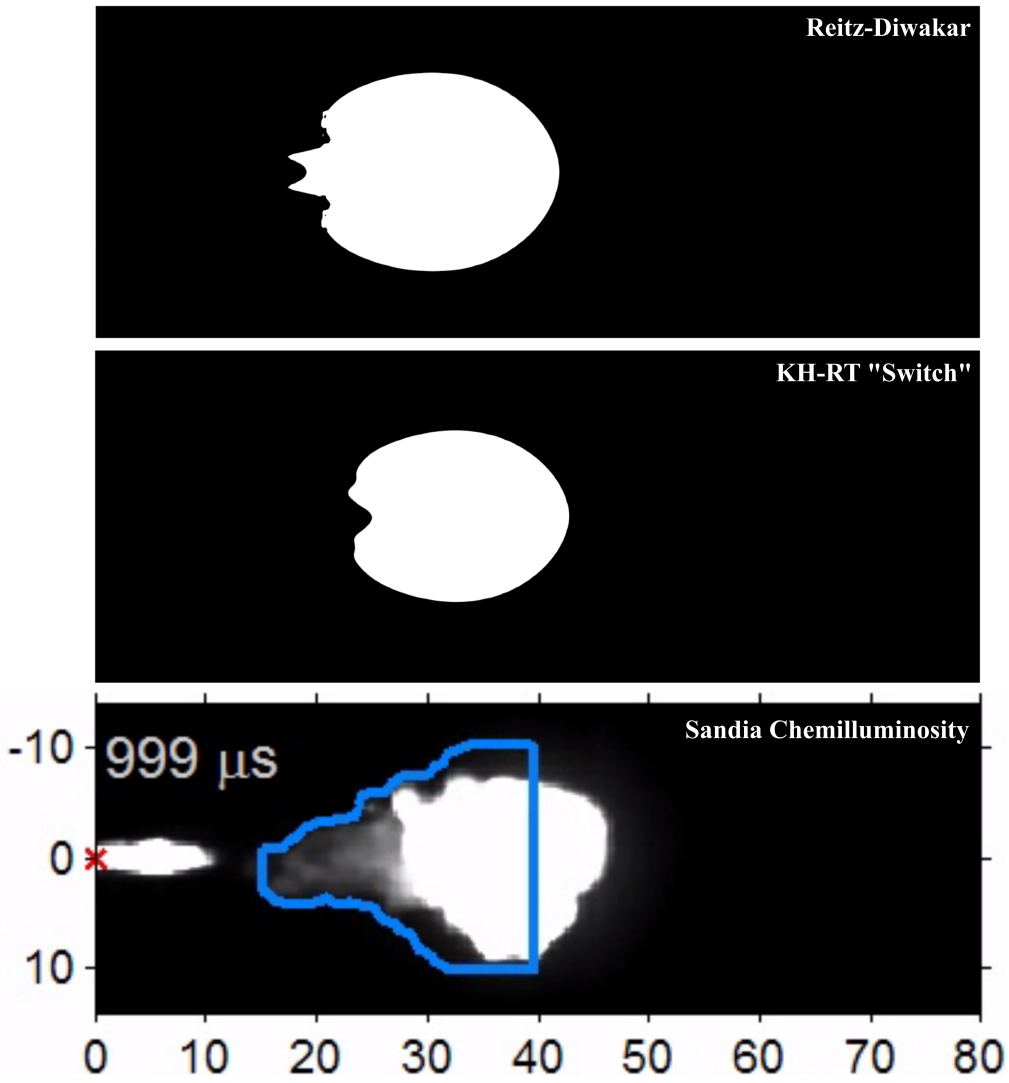

Figure 5.6: Comparison of simulated Reitz-Diwakar and KH-RT "Switch" combustion field predictions against Sandia experimental combustion field from [110, 131], all at 1 ms ASOI. White areas for the Reitz-Diwakar and KH-RT "Switch" models are above the 950 K threshold, the blue line for the Sandia image is the computed OH threshold

then the Reitz-Diwakar model. This suggests greater internal mixing of the fuel within the core of the spray, allowing for combustion to occur in more areas for the KH-RT "Switch" model. Along with this, the area encompassed by temperatures above ambient is lower in the KH-RT "Switch" model, suggesting a faster and locally hotter reaction than in the Reitz-Diwakar model. Considering Figure 5.9, it can be seen that this holds true throughout the simulated time after 0.75 ms ASOI, with the KH-RT "Switch" model having a maximum burning temperature approximately 45 K higher than that of the Reitz-Diwakar model. The spike in

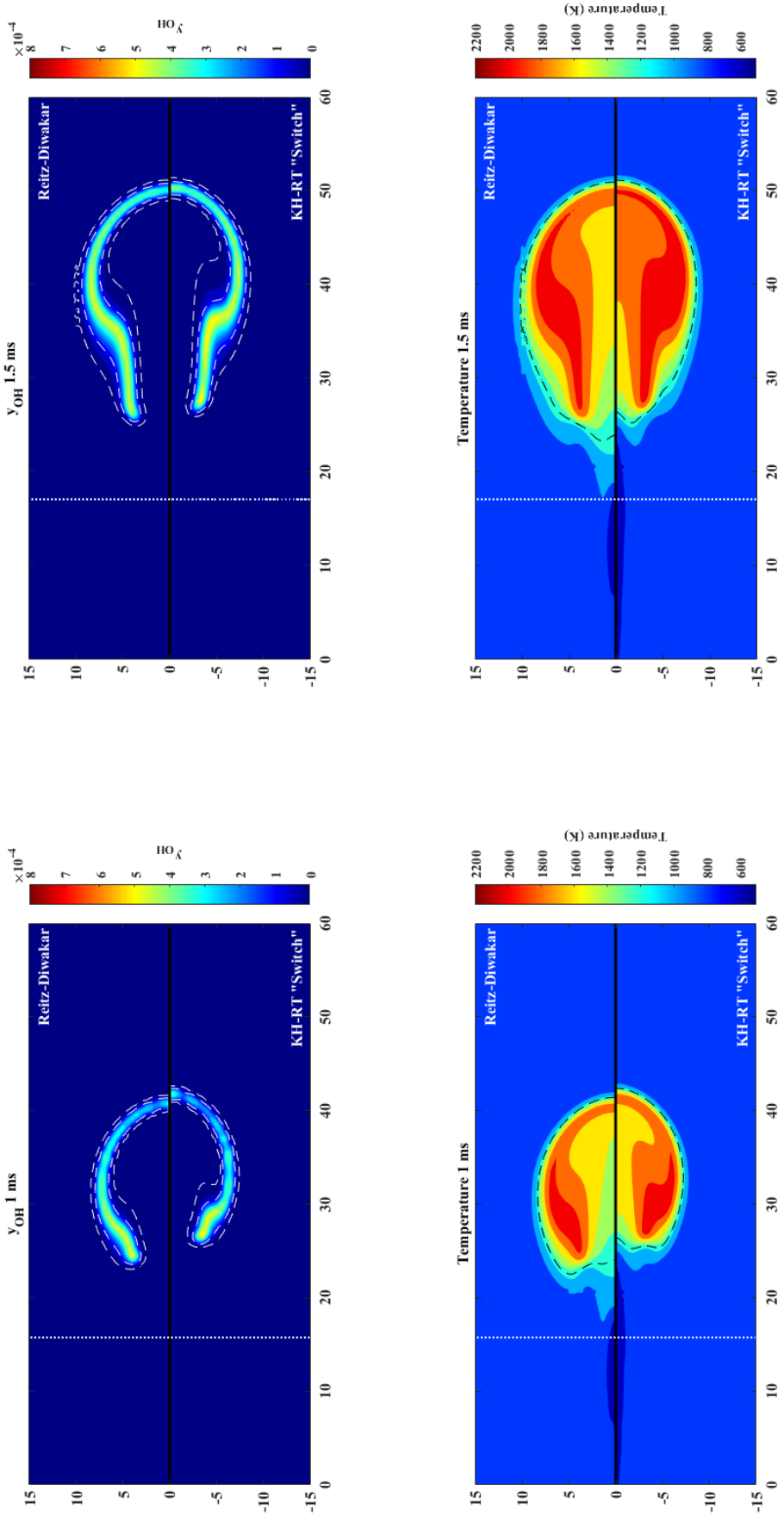

Figure 5.7: OH and temperature field plots for the Reitz-Diwakar and KH-RT "Switch" models at 1 ms and 1.5 ms ASOI. The 2 % and 14 % OH_{max} criteria are shown as dashed white lines with the temperature criterion shown as a dashed black line. The experimental lift-off-lengths are shown as a white dotted line

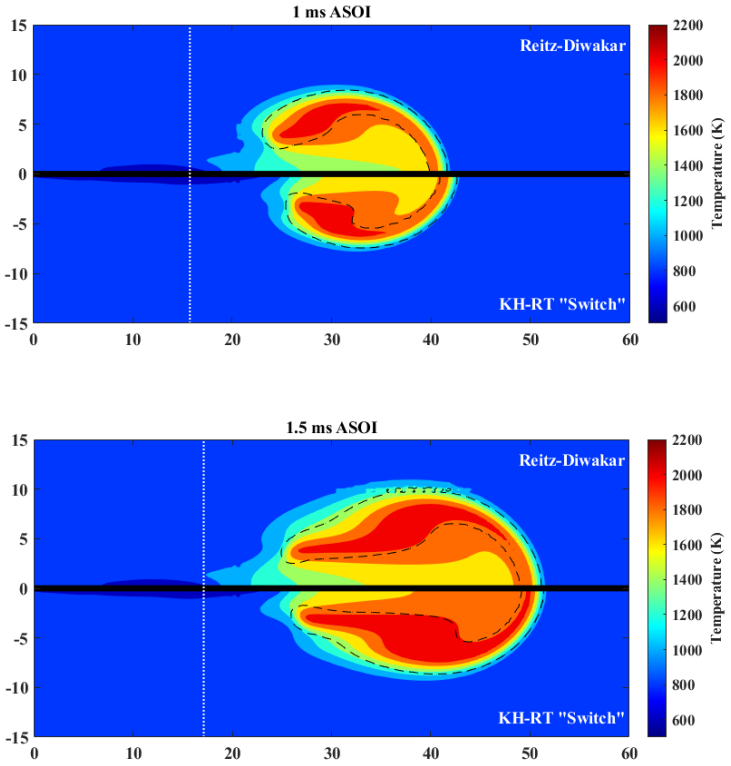

Figure 5.8: Temperature fields for the Reitz-Diwakar and KH-RT "Switch" models at 1 ms and 1.5 ms ASOI, with the 2 % OH_{max} boundary shown as a black dashed line. The experimental lift-off-lengths are shown as a white dotted line

heat release that Figure 5.8 suggests is also seen in Figure 5.9 between 0.5 and 0.75 ms ASOI, where the KH-RT "Switch" model's maximum burning temperature increases by approximately 130 K in comparison to the Reitz-Diwakar's increase of approximately 70 K. However, when considering Figure 5.10 it can be seen that the Reitz-Diwakar model has a higher mean temperature through the centreline plane of the spray when compared to the KH-RT "Switch" model at all timesteps. This is most likely due to the larger cone angles seen in the Reitz-Diwakar model (as seen in Table 4.9) ensuring that the combusting zone is larger for this model in comparison to the KH-RT "Switch" model. The larger combustion zone will ensure that more of the spray centreline plane is above the ambient temperature and hence this will lead to a larger mean temperature on that plane when compared to the KH-RT "Switch" model, by approximately 15 K at 0.5 ms ASOI to 35 K at 2 ms ASOI.

Comparing the mixture fractions between the two models will allow for a comparison of how the combustion model is impacted by the change in break-up

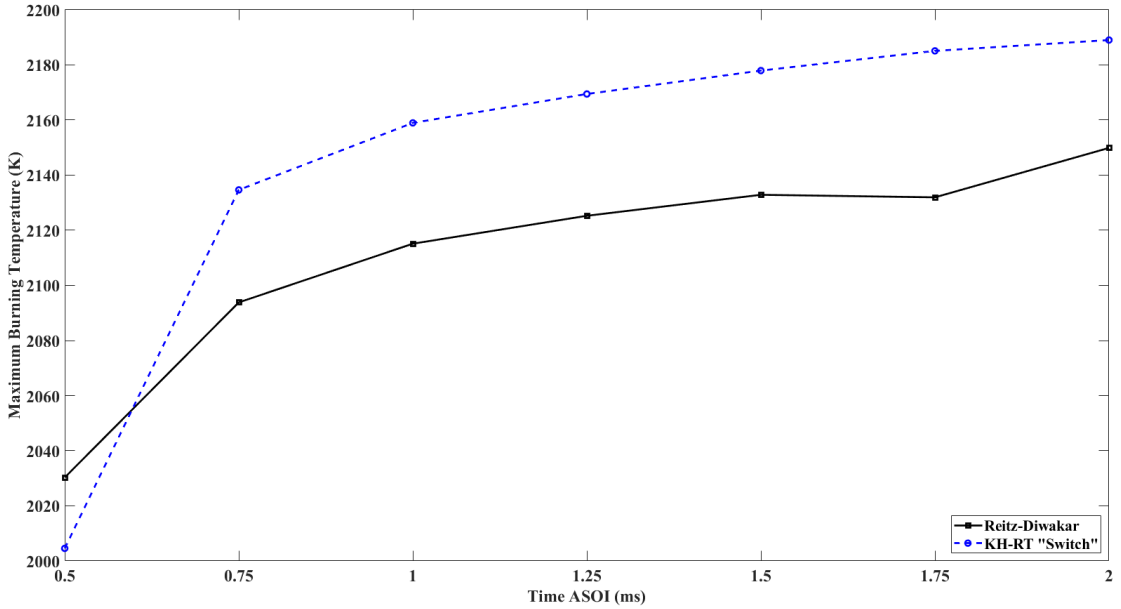

Figure 5.9: Maximum centreline plane burning temperatures for the Reitz-Diwakar and KH-RT "Switch" models for the combusting "Spray A" case against time ASOI

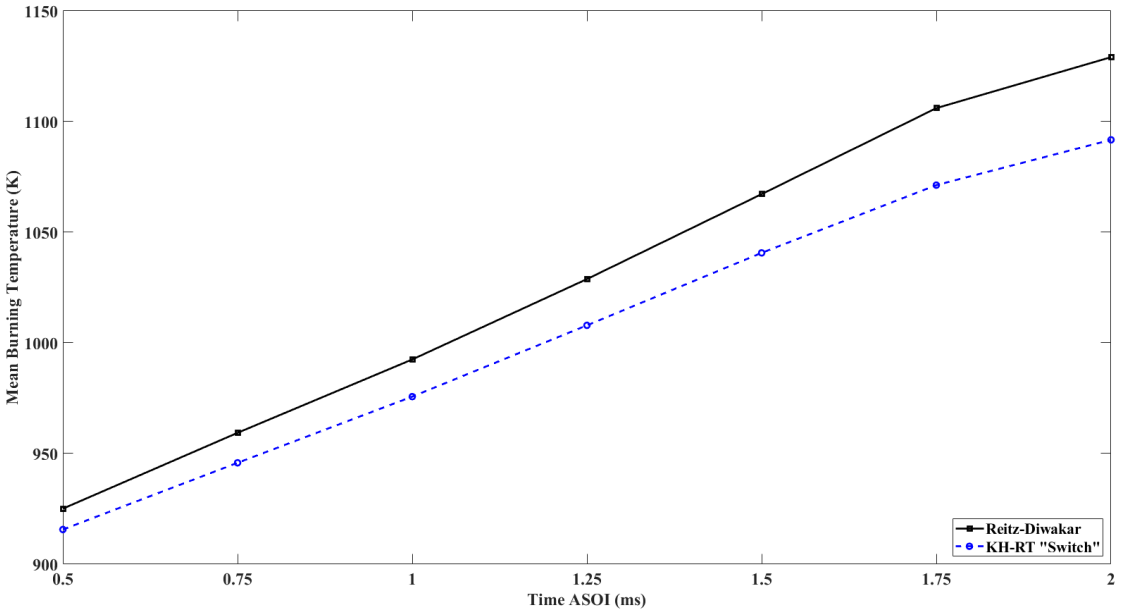

Figure 5.10: Mean centreline plane temperatures for the Reitz-Diwakar and KH-RT "Switch" models for the combusting "Spray A" case against time ASOI

model, given as shown in Section 5.1.2 the mixture fraction in highly impactful on the mixing progress of combustion. The mixture fractions for both models at 1 ms ASOI, at distances of 15 mm and 20 mm from the injector tip are shown in Figure 5.4, which shows that closer to the nozzle the Reitz-Diwakar model predicts

a higher mixture fraction, however nearer to the combustion field this trend reverses. This is not unsurprising given the difference in droplet SMD prediction shown in Figure 4.16, and the difference in mixture fraction at 20 mm from the injector tip is believed to cause the differences in the temperature fields between the models.

5.2.4 KH and RT Model Influences

Within Section 4.4.3 it was found that setting the switching position close to the injector caused some numerical instabilities within the simulation. Within this section this will be tested on the combusting case, utilising the switch criteria to make only the KH or RT sub-model act on the spray. Given the closeness of the predictions of the lift-off-lengths shown between the different critera before (as shown in Figure 5.5), the 2 % OH_{max} criteria will be used for the lift-off-lengths here for simplicity.

The lift-off-lengths for the KH and RT sub-models are shown in Figure 5.11, showing a clear difference in the lift-off-length prediction between the two sub-models. The RT sub-model predicts a much lower lift-off-length than the KH sub-model throughout the injection period, and broadly matches the experimental data. Meanwhile, the KH sub-model matches the original KH-RT "Switch" model's

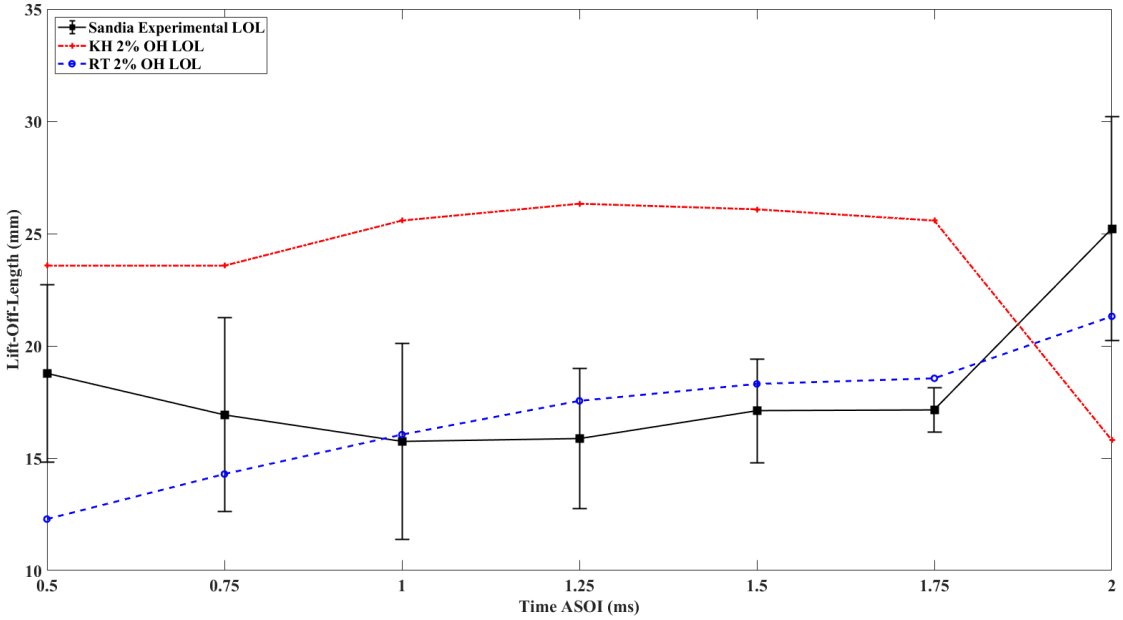

Figure 5.11: Lift-off-lengths for the KH and RT sub-models, compared with the ECN "Spray A" experimental lift-off-length, plotted against time ASOI

lift-off-length (from Figure 5.5) closely throughout the injection period, showing good agreement with the other simulated combusting cases. The RT OH field is highly asymmetrical however, with the lift-off-length being determined by the lower half of the OH field which protrudes further from the spray tip and closer to the injector. This behaviour is shown in Figure 5.12. In comparison, the KH OH field is highly symmetrical, with the lift-off-lengths between the two halves of the OH field being very close. The reason for this difference between the sub-models is believed to be instabilities in the liquid region of the RT sub-model's injection, with much more extreme oscillatory behaviour seen than was shown in Section 4.4.3.

These instabilities are shown in Figure 5.13, clearly showing large oscillations near the spray tip early on in the injection phase. Given the large amount of parcels below the spray centreline in comparison to above it the differences in the OH fields shown in Figure 5.12 can be explained by these parcels combusting closer to the spray tip than the ones above the spray centreline. Similar instabilities were seen when S_N was set to very low values in Section 4.4.3, with numerical errors generating the oscillatory behaviour. This holds true when the RT sub-model is the only one to act on the spray, however having an aerodynamic based break-up regime acting on the entirety of the spray is not realistic to a real life situation. The instabilities seen within the RT model case also have a large impact on the mixture fraction predictions, as is shown in Figure 5.14. This figure shows the increasingly off-centre position of the maximum mixture fraction as the distance to the nozzle tip is increased from 15 mm to 20 mm at 1 ms ASOI, along with the corresponding reduction in mixture fraction as expected. This change in position of the maximum mixture fraction matches both the parcel plots shown in Figure 5.13 and OH fields shown in Figure 5.12, with the RT model predicting an extremely offset lift-off-length skewed towards the right hand side of the injector.

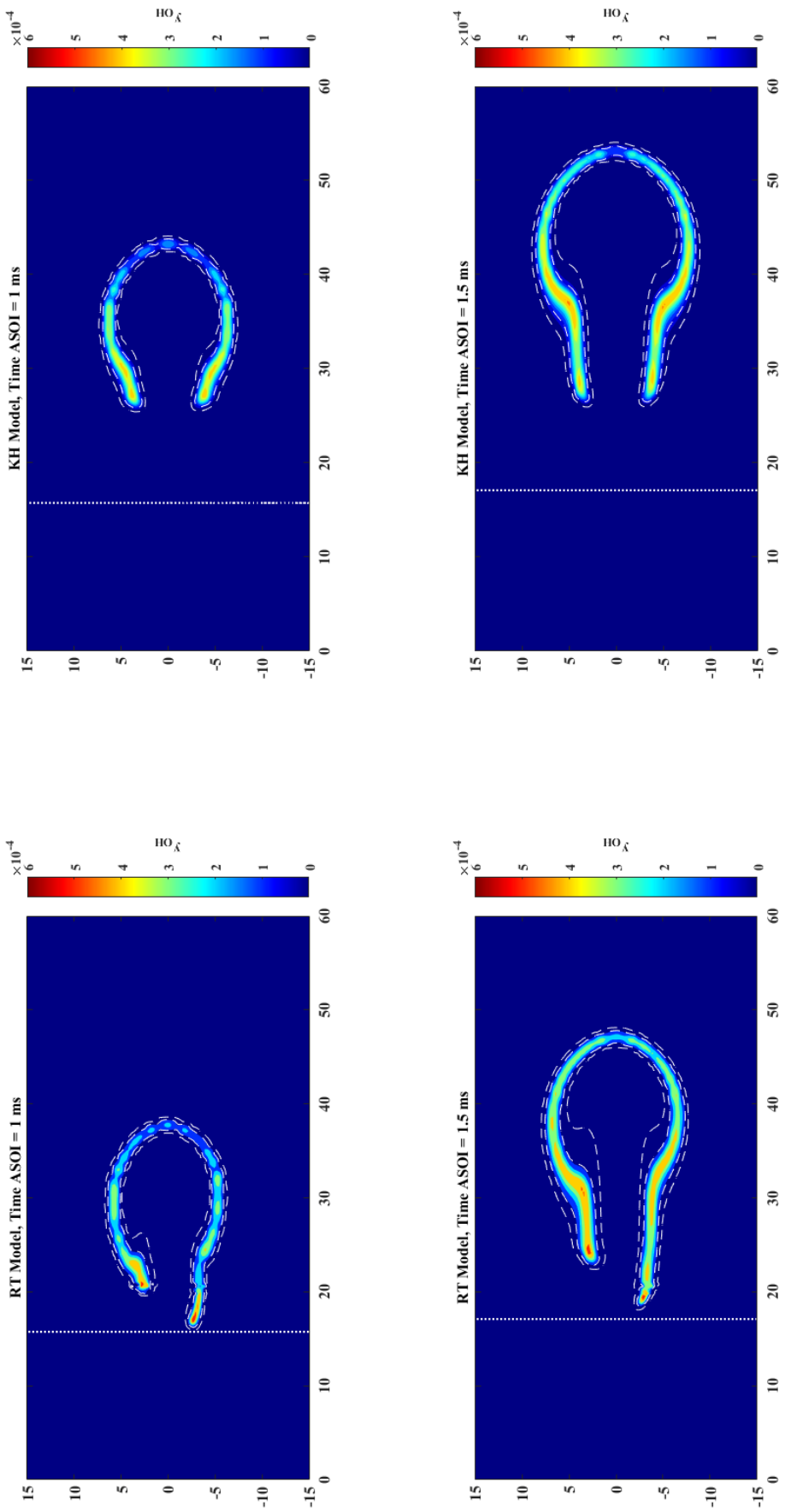

Figure 5.12: OH field plots for the KH and RT sub-model tests at 1 ms and 1.5 ms ASOI. The 2 % and 14 % OH_{max} fields are shown as white dashed lines, and the experimental lift-off-length is shown by a dotted white line

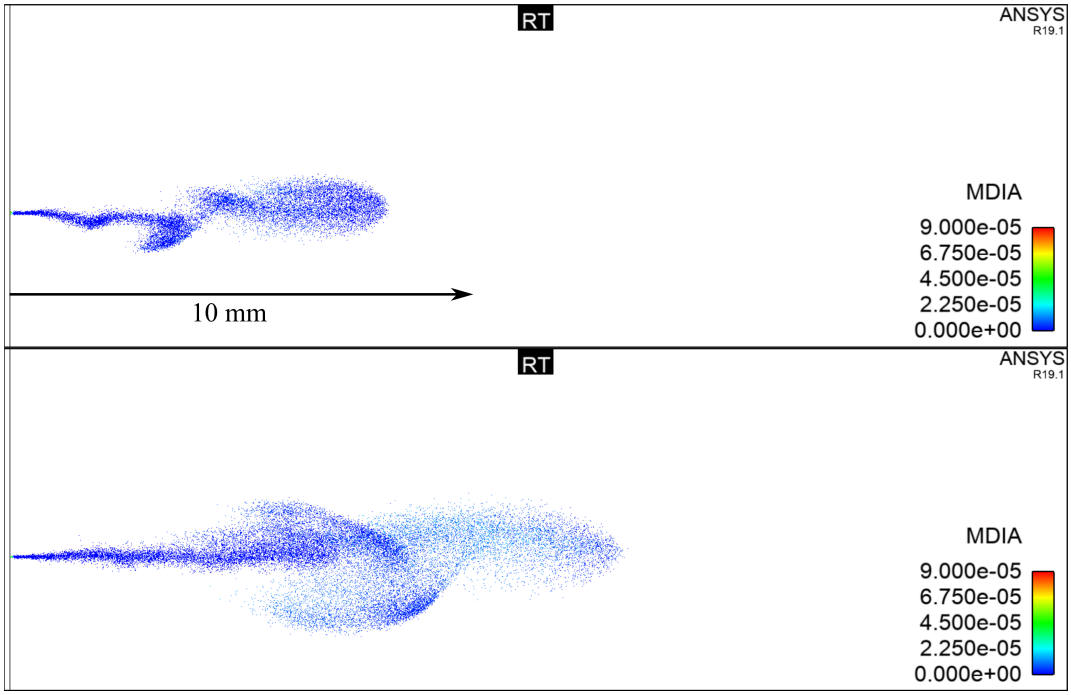

Figure 5.13: Parcel plots for the RT sub-model simulation of the combusting "Spray A" case, at 0.1 ms ASOI (top) and 0.2 ms ASOI (bottom). MDIA is the droplet diameter in metres

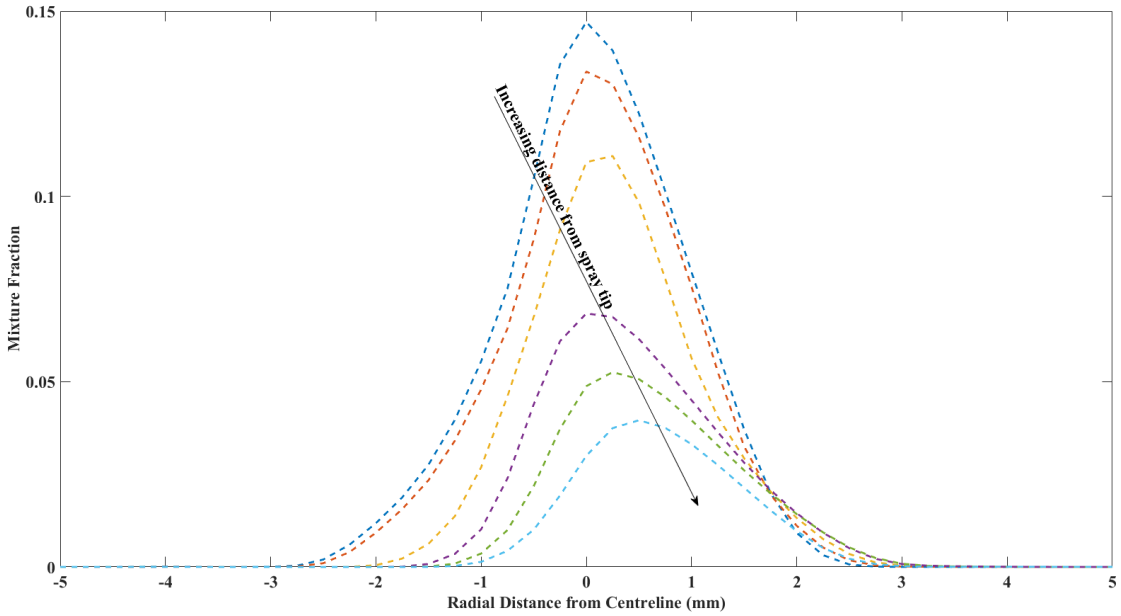

Figure 5.14: Mixture fractions for the RT sub-model at distances of 15 to 20 mm, in increments of 1 mm, all taken at 1 ms ASOI

5.3 Conclusions

This chapter has taken the KH-RT "Switch" model derived in the previous chapter and applied it to a combusting "Spray A" condition, with a good match found between the KH-RT "Switch" model and the baseline Reitz-Diwakar case when both models utilised the same reduced n-dodecane mechanism. The following differences and phenomena were also found and discussed:

- Both models were found to over-predict the lift-off-length of the spray when compared to experimental results, with the Reitz-Diwakar model showing an over-prediction of the lift-off-length by approximately 7 mm and the KH-RT "Switch" model over-predicting the lift-off-length by approximately 10 mm. This was deemed to not be an issue given this result has been seen previously when the combination of the well mixed combustion model and Yao mechanism was used. The ignition delay was predicted excellently on the other hand, with both break-up models matching experimental data to within 0.01 ms.

- Differences in the mixture fractions were seen between the two models, with the results complementing the SMD results from the KH-RT "Switch" model derivation; these differences are also believed to cause the small differences seen in the temperature predictions.

- The influence of each sub-model of the KH-RT break-up model was also considered, utilising the implemented switch to ensure that only one model acted for the spray. The results showed that the RT sub-model caused a highly unstable liquid prediction, leading to a much lower lift-off-length than that of the KH sub-model. These instabilities mirrored those seen previously when the switch position was set too close to the injector, further suggesting a boundary on the switching constant is required.

6 Impact of Vaporising Match on Combusting Spray Metrics

Within this chapter the greater matching potential of the KH-RT "Switch" model is used to test the impact of varying the liquid and vapour lengths on the combusting results. Variances are seen within the internal spray temperatures, as well as the OH and C_2H_2 distributions, when the liquid length is varied with a matched vapour length. Note is drawn to the impact of the B_{RT0} constant on the internal spray temperatures and OH fields. Vapour length sweeps are also undertaken to ascertain the effect of both the turbulence and break-up model constants on the combustion fields. The vapour length sweeps show minimal changes on combustion criteria from the $C_{1\varepsilon}$ constant, with only the position of the combustion field impacted. The relationship between the combustion zone position and the internal spray temperature is also considered, showing that the spray break-up model constants have a large effect on the internal spray temperature.

6.1 Methodology

Within this section, the impact of applying the improved matching using the KH-RT "Switch" model shown in Section 4.4.2 on the combusting criteria will be tested. The emphasis on closely matching vaporising cases often takes up a large amount of computational time when creating domains and models. As such, quantifying the impact of differences in the vaporising liquid and vapour lengths on the combusting criteria allows future domains to be created faster as acceptable ranges for each can be found. Some effort has been put into determining the impact of various model constants on the combusting criteria, however these

studies have not considered the combustion fields or emission results [132, 133]. Within this study the C_2H_2 precursor will also be considered along with the criteria studied in the previous section. C_2H_2 is an excellent guide for soot production [134] given the structure of PM is commonly found to be graphite-like, and result from the polymerisation of C_2H_2 to form aromatics; graphite precursors are polycyclic aromatic hydrocarbon (PAH) compounds. Particulates can be found to grow through the hydrogen-abstraction-carbon-addition (HACA) mechanism, which involves the addition of C_2H_2 to each other to form PAH [1]. This formation of PAH is challenging to compute [135], as such no soot model is used within this study to reduce computational cost. Given this "double usage" of C_2H_2 within soot formation, different predictions of C_2H_2 between cases is important to identify and allows for estimations of the different soot predictions of each case.

To test the impact of matching the liquid and vapour lengths on the combusting spray metrics, a test matrix was created to test different combinations of liquid lengths and vapour lengths. This test matrix is shown in Table 6.1. The vapour lengths were matched predominantly using the $C_{1\varepsilon}$ constant, with sweeps done between 1.54 and 1.65 to achieve the vapour length matches, using the LL match/VL low case as a baseline. The liquid lengths were then matched with alterations to the break-up model constants (S_N, B_{KH1}, B_{RT0}) and the $C_{1\varepsilon}$ constant, again through sweeps between the boundaries for each constant (as shown in Chapter 2). Some cases were not possible to attain with the model, this is due to the model running up to the edges of the tuning parameter boundaries within the KH-RT sub-model, and as such the LL low/VL high, LL match/VL high and LL high/VL low cases are not considered for this study. It should be noted that, as in Chapter 5, at an S_N value of 203.9 no instabilities were seen, and as such the comparisons made in this Chapter are valid given this is the minimum value of S_N used.

Table 6.1: Test matrix for combusting spray metric tests, with adjustments to model parameters from the stock model (Table 5.3) shown to achieve required case. VL and LL are vapour length and liquid length respectively

VL \ **LL**	**Low**	**Match**	**High**
High	N/A	N/A	$C_{1\varepsilon}$: 1.65 S_N: 203.9 B_{KH1}: 7 B_{RT0}: 0.1
Match	$C_{1\varepsilon}$: 1.58 S_N: 543.8 B_{KH1}: 5 B_{RT0}: 0.1	$C_{1\varepsilon}$: 1.61 S_N: 543.8 B_{KH1}: 6 B_{RT0}: 0.07	$C_{1\varepsilon}$: 1.62 S_N: 203.9 B_{KH1}: 7 B_{RT0}: 0.1
Low	$C_{1\varepsilon}$: 1.54 S_N: 203.9 B_{KH1}: 7 B_{RT0}: 0.1	$C_{1\varepsilon}$: 1.58 S_N: 203.9 B_{KH1}: 7 B_{RT0}: 0.1	N/A

Differences between cases will be quantified by using a modified version of the Weighted Magnitude Index (WMI) proposed by Willman et al. [136], however utilising the mean value of the arrays instead of the median due to the high volume of zero and near zero values in the C_2H_2 and OH field arrays. As a result, the altered WMI definition is as shown in Equation 6.1, with Q_A and Q_B being the baseline case and case being compared to the baseline case arrays respectively, considered over co-ordinates x and y.

$$WMI(x_i, y_i) = \frac{Q_A(x_i, y_i) - Q_B(x_i, y_i)}{\text{mean}(Q_A)} \tag{6.1}$$

This WMI will be normalised between -1 and 1 to create the Normalised WMI (NWMI), as shown in Equation 6.2, for field plots. This will allow for identification of areas of large difference between each case, showing which case is having the largest impact on the WMI. This is visualised in Figure 6.1, showing how the definition of the normalised WMI allows for ascertaining which case has the largest impact on the WMI field.

$$NWMI(x_i, y_i) = \frac{WMI(x_i, y_i)}{\max(|WMI_{x_i,y_i}|)} \tag{6.2}$$

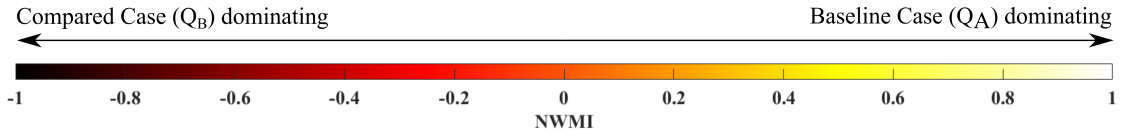

Figure 6.1: Normalised WMI definition showing impact of each case on NWMI value

To begin with, a liquid length sweep will be undertaken at a matched vapour length to ascertain the impact of altering the break-up model constants on the combustion fields. With this knowledge, vapour length sweeps at each liquid length case will be undertaken to see how the difference in both turbulence model constants and break-up model constants impact the combustion fields.

6.2 Results

6.2.1 Liquid Length Sweep

For the liquid length sweep, given the changes to the model constants shown in Table 6.1 the liquid and vapour lengths are as shown in Table 6.2. As can be seen, the vapour lengths are all within the experimental range at both 1 ms and 1.5 ms ASOI, and within 1.5 mm of each other at the end of injection. Table 6.2 also shows some of the limitations of the matching, as achieving a lower liquid length than the 9.46 mm seen whilst still matching the vapour length is impossible within the model constant boundaries defined, showing why the LL low/VL high case is impossible to obtain.

Table 6.2: Liquid and vapour lengths for the matched vapour length vaporising cases

	Low LL	**Matched LL**	**High LL**	**Experimental**
LL Mean	9.46 mm	10.15 mm	13.34 mm	10.08 ± 0.34 mm
VL @ 1 ms	45.8 mm	45.5 mm	46.3 mm	46.8 ± 2.0 mm
VL @ 1.5 ms	55.3 mm	55.5 mm	56.8 mm	56.9 ± 2.6 mm

Comparing the low and matched liquid length cases, it can be seen that the internal temperatures are higher in the low liquid length case in comparison to the matched case, with the NWMI plot in Figure 6.2 showing a larger area of negative NWMI, with a small area of positive NWMI at the spray tip, where the

matched liquid length case extends further into the domain. This is reflected in the mean temperatures for each case combustion zone, with the low liquid length case having a mean temperature of 1488 K at 1.5 ms ASOI, compared to the matched liquid length case's mean temperature of 1391 K at 1.5 ms ASOI. This follows on to the C_2H_2 predictions, shown in Figure 6.3, with the higher temperatures seen in the low liquid length case resulting in less C_2H_2 production, especially at 1.5 ms ASOI. The high C_2H_2 concentrations seen in the matched liquid length case coincide with the temperature areas of around 1600 K, near areas of the combustion zone where some internal recirculation occurs. Finally, the OH fields shown in Figure 6.4 show that the matched liquid length case has much lower maximum OH concentrations, especially clear at 1.5 ms ASOI. The lift-off-lengths are very similar however, suggesting that the difference in liquid length has minimal impact on the predicted lift-off-length; however this is to be expected given the small difference in liquid length between the two cases.

When comparing the matched and high liquid length cases, the internal temperature for the high liquid length case is much higher than that of the matched case, with almost all of the internal spray being above 2000 K at 1.5 ms ASOI; for the high liquid length combustion zone the mean temperature is 1535 K compared to the

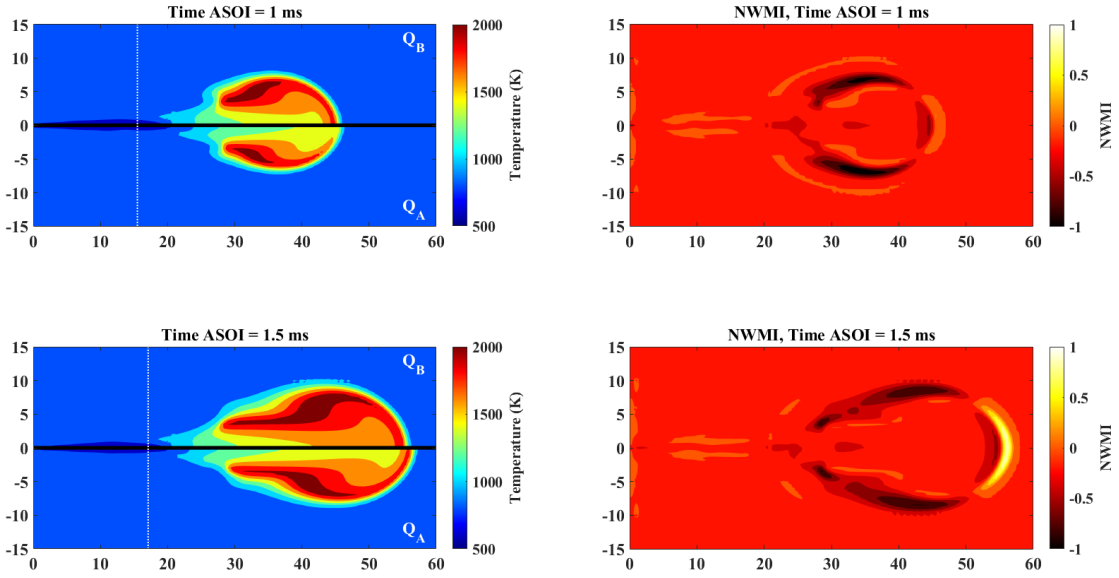

Figure 6.2: Temperature fields for the low (Q_B) and matched (Q_A) liquid length cases at a matched vapour length, 1 and 1.5 ms ASOI, with the NWMI comparison shown

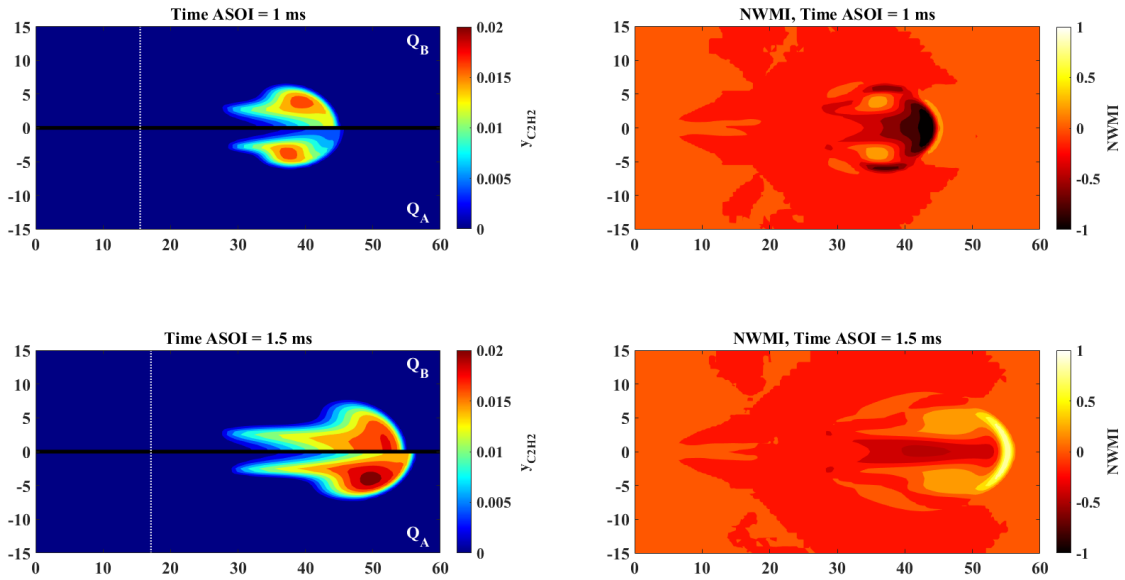

Figure 6.3: C_2H_2 fields for the low (Q_B) and matched (Q_A) liquid length cases at a matched vapour length, 1 and 1.5 ms ASOI, with the NWMI comparison shown

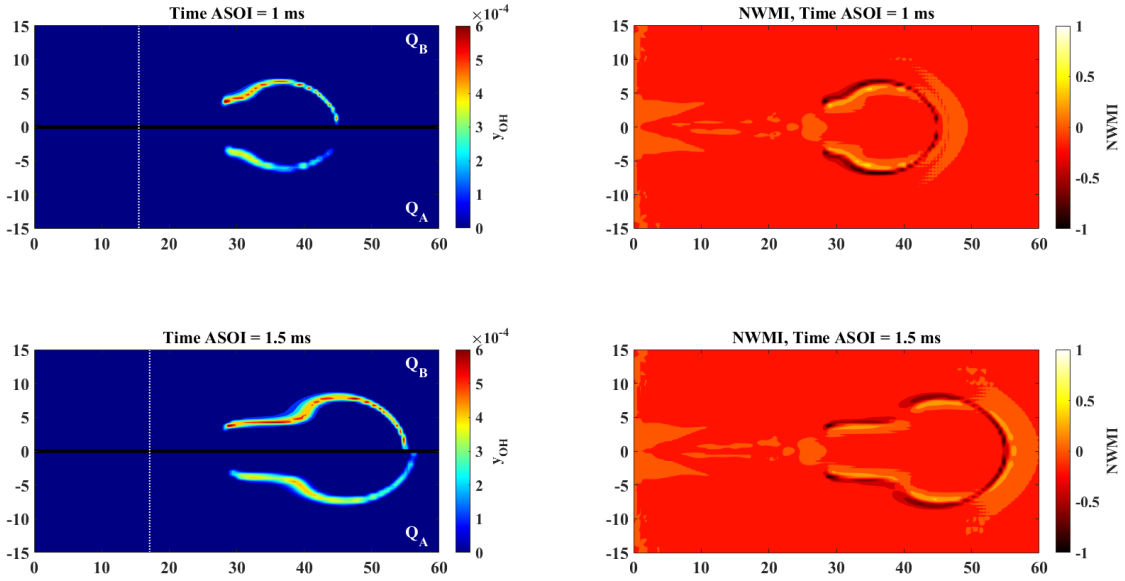

Figure 6.4: OH fields for the low (Q_B) and matched (Q_A) liquid length cases at a matched vapour length, 1 and 1.5 ms ASOI, with the NWMI comparison shown

matched liquid length's 1391 K. This difference is shown in Figure 6.5, showing that even at 1 ms ASOI the mean internal temperature is much higher in the high liquid length case than the matched. The NWMI plot also shows clear areas where the sprays are mismatched, with very high values seen at the spray tip due to the matched liquid length case penetrating further into the domain than the high liquid

length case. This is noteworthy due to the predicted vaporising vapour lengths as seen in Table 6.2, in which the high liquid length case has a higher vapour length at both 1 and 1.5 ms ASOI. This mismatch is also seen in the OH fields, shown in Figure 6.6, especially at 1.5 ms ASOI. The NWMI plot shows this mismatch extremely clearly, with the matched liquid length case again penetrating further into the domain, however the high liquid length case has a both a thinner initial OH field, where the lift-off-length is measured, as well as a higher OH concentration within the OH field. The lift-off-lengths are also clearly different at 1.5 ms ASOI, with the higher liquid length leading to a higher lift-off-length; the full comparison of lift-off-lengths is shown in Figure 6.7. The comparison of lift-off-lengths shows the similarities between the low and matched liquid length cases, however after the end of injection these lift-off-lengths diverge.

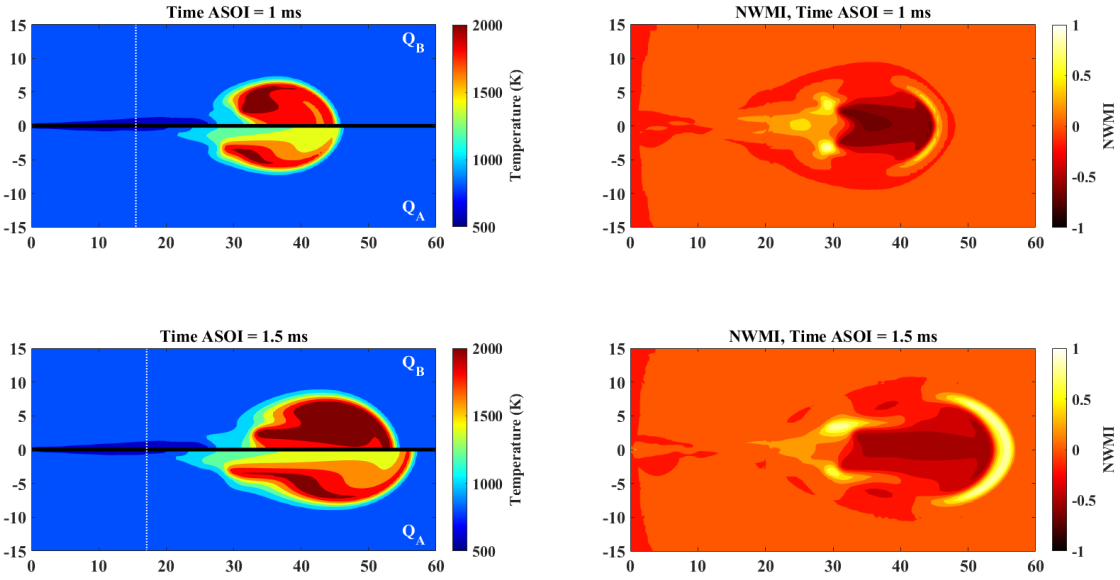

Figure 6.5: Temperature fields for the high (Q_B) and matched (Q_A) liquid length cases at a matched vapour length, 1 and 1.5 ms ASOI, with the NWMI comparison shown

Figure 6.7 also shows the difference in lift-off-lengths seen in the high liquid length case, with the lift-off-length between 1 and 1.75 ms ASOI being between 2 and 4 mm higher in the high liquid length case. This difference in lift-off-length is much lower than the difference in the liquid lengths however, suggesting a weaker correlation between liquid lengths and lift-off-lengths than might be assumed. The

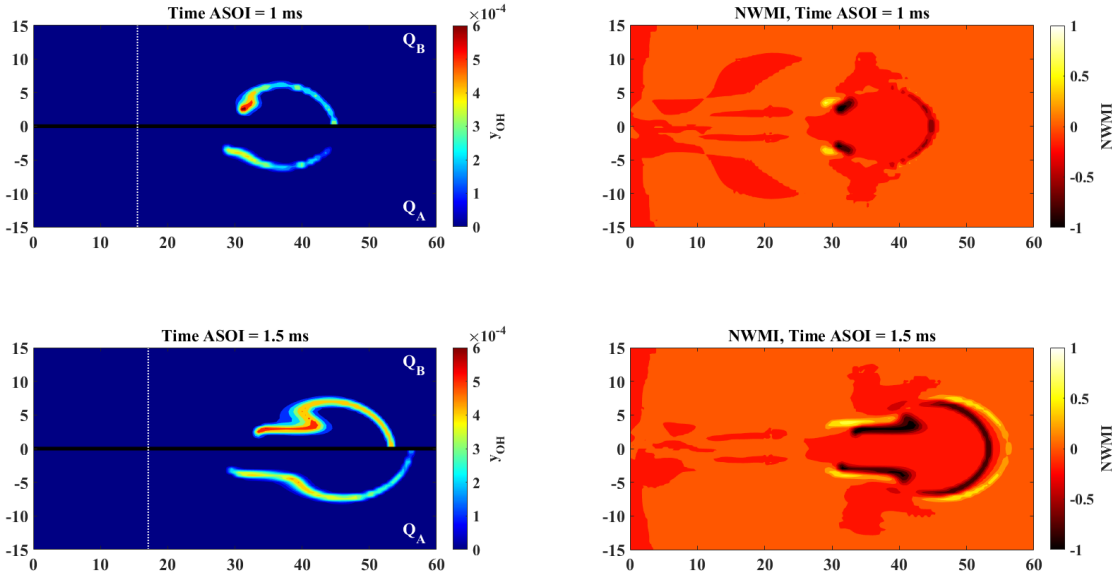

Figure 6.6: OH fields for the high (Q_B) and matched (Q_A) liquid length cases at a matched vapour length, 1 and 1.5 ms ASOI, with the NWMI comparison shown

C_2H_2 plots shown in Figure 6.8 illustrate the impact of the higher temperatures at 1.5 ms ASOI, with the concentration of the soot precursor being extremely low in the high liquid length case when compared to the matched liquid length case. The C_2H_2 fields at 1 ms ASOI are also notably different, with the two peaks seen in the matched liquid length case not seen in the high liquid length case. This is as expected, as a higher temperature leads to lower soot production [6, 7], and given the large difference in internal spray temperature seen in this comparison the lower C_2H_2 levels follow the expected trend.

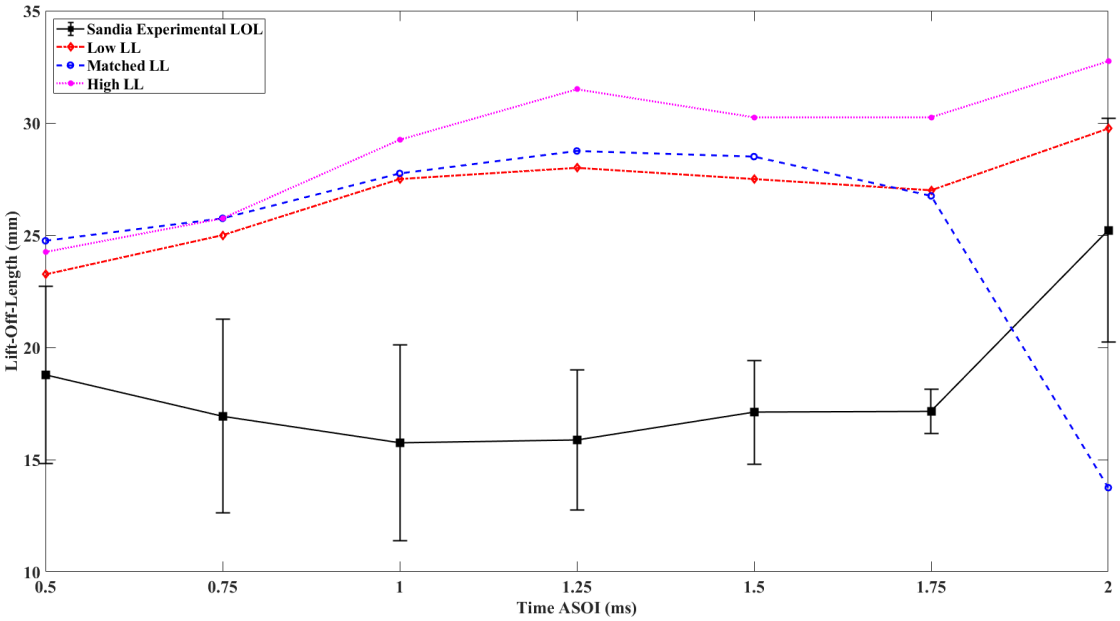

Figure 6.7: Lift-off-lengths for the liquid length sweep with Sandia experimental data against time ASOI

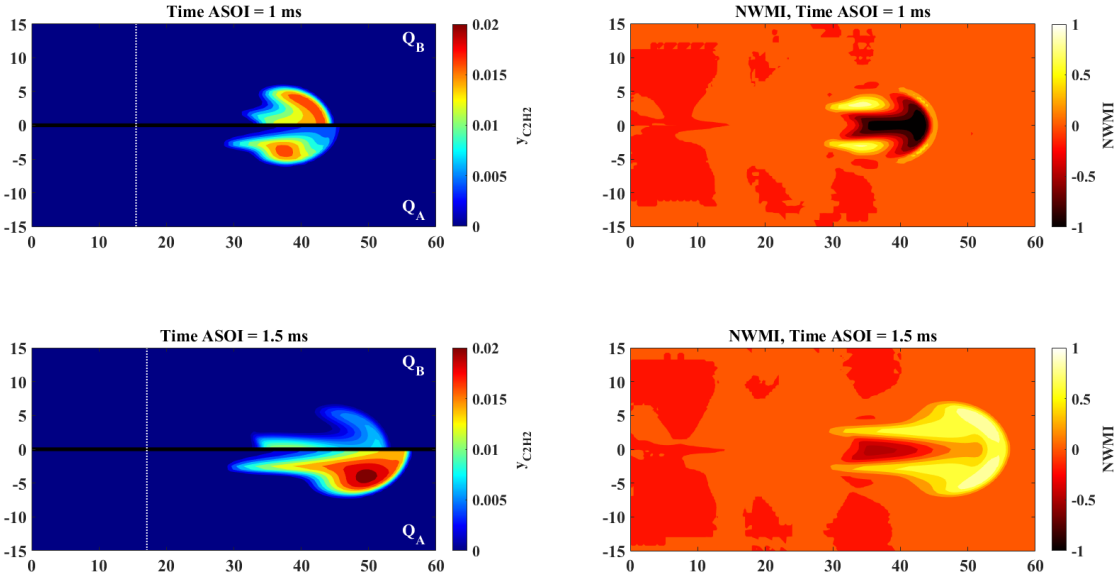

Figure 6.8: C_2H_2 fields for the high (Q_B) and matched (Q_A) liquid length cases at a matched vapour length, at 1 and 1.5 ms ASOI, with the NWMI comparison shown

Throughout all the comparisons made previously both the temperature and OH fields for the matched liquid length case show lower values both in peaks and averages than in the other cases. This is believed to be due to the change in the B_{RT0} constant, which alters the child parcel droplet size caused by the RT break-up from Equation 2.63. By reducing this constant the final parcels to evaporate will

be smaller, which ensures that they will evaporate earlier and hence increase the mixture fraction nearer to the spray tip, as is shown in Figure 6.10. This ensures the initial burn of the fuel is richer than the high liquid length case, leading to a higher initial burn temperature [137]. Later combustion clearly causes a higher temperature in the high liquid length case, which is believed to be due to the lower initial mixture fraction; this will be considered further in Section 6.2.3. This higher temperature can clearly be seen within Figure 6.5, with the temperature at approximately 40 mm from the nozzle tip being lower in the matched liquid length case than the high liquid length case. The temperature gradient along the spray centreline is more shallow however, suggesting the high liquid length case combusts further into the domain but at a higher temperature, which can also clearly be seen. The spray centreline temperatures at 1.5 ms ASOI are shown in Figure 6.9, which clearly shows the lower temperature within the matched liquid length case when compared to the other cases, as well as the much higher gradient in temperature seen in the high liquid length case.

Considering the mixture fractions, Figure 6.10 shows a clear difference in mixture

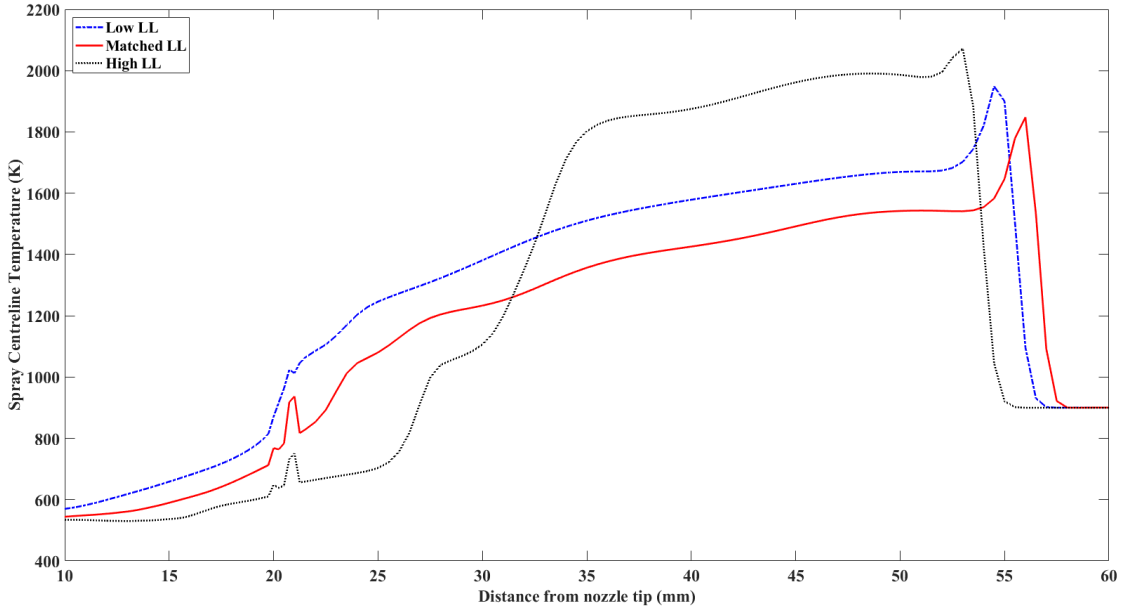

Figure 6.9: Spray centreline temperatures for the low, matched and high liquid length cases at a matched vapour length, at 1.5 ms ASOI, plotted against the distance from the nozzle tip

fraction predictions between the three cases, with the matched and low liquid length cases predicting a higher mixture fraction at both positions considered compared to the high liquid length case. This is believed to be caused by the alteration of the break-up model constants in defining the cases, with special note drawn to the influence of the B_{RT0} constant alteration on the mixture fractions; which appears to cause a much higher mixture fraction prediction at both positions considered. These differences in mixture fraction are believed to cause the large differences in temperatures seen in Figures 6.2 and 6.5, given the higher mixture fractions near to the combustion zone will mean a richer fuel/air mixture and as such initially a higher temperature.

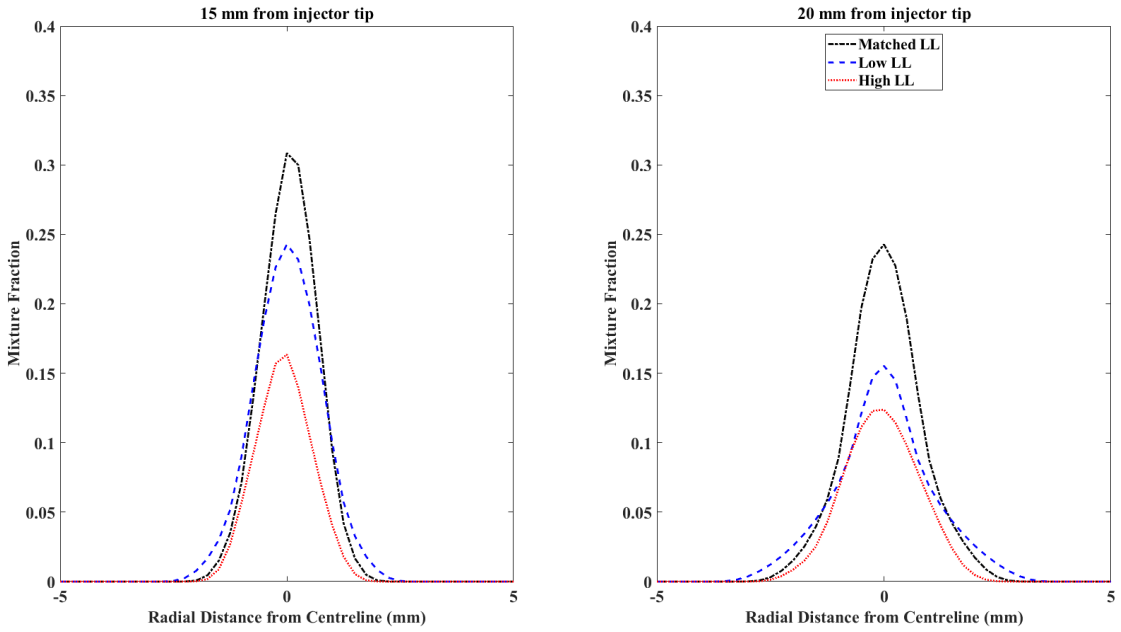

Figure 6.10: Mixture fractions for the low, matched and high liquid length cases at a matched vapour length, at 1 ms ASOI at 15 and 20 mm from the injector tip

6.2.2 Vapour Length Sweeps

Two separate vapour length sweeps will be undertaken to ascertain the impact of the vapour length match on combustion. These will take place at the high and low liquid length conditions, with each condition having a different set of constants changed in order to influence the vapour length match, as shown in Table 6.1. The constant changes made for the matched liquid and vapour length case are already considered in the previous section, and as a result considering the vapour length sweep for a matched liquid length is not necessary. As a result, the impact of other break-up constants on the combusting spray can be isolated from the low liquid length case, along with the effect of the $C_{1\varepsilon}$ constant which is considered in the high liquid length case.

To begin with, the two high liquid length cases from Table 6.1 will be compared to ascertain the impact of altering the $C_{1\varepsilon}$ constant on the combustion fields. Table 6.3 shows the liquid and vapour lengths for the vaporising case for each of the high liquid length cases, showing the differences in the vapour lengths. The liquid length mean for the high vapour length case is approximately 2 mm higher than the matched vapour length case, however the vapour lengths at both 1 and 1.5 ms ASOI are outside the experimental range for the high vapour length case. Given the increase in $C_{1\varepsilon}$ between the matched and high vapour length cases is 0.03, this suggests that each increase in $C_{1\varepsilon}$ of 0.01 increases the liquid length mean by approximately 0.7 mm and the vapour length by approximately 1.2 mm at the end of injection.

Table 6.3: Liquid length means and vapour lengths at 1 and 1.5 ms ASOI for the high liquid length vaporising cases

	Matched VL	**High VL**	**Experimental**
LL Mean	13.34 mm	15.48 mm	10.08 ± 0.34 mm
VL @ 1 ms	46.3 mm	49.3 mm	46.8 ± 2.0 mm
VL @ 1.5 ms	56.8 mm	60.5 mm	56.9 ± 2.6 mm

Considering the temperature fields, Figure 6.11 shows the temperature fields at 1 and 1.5 ms ASOI for both high liquid length cases. The high internal temperatures

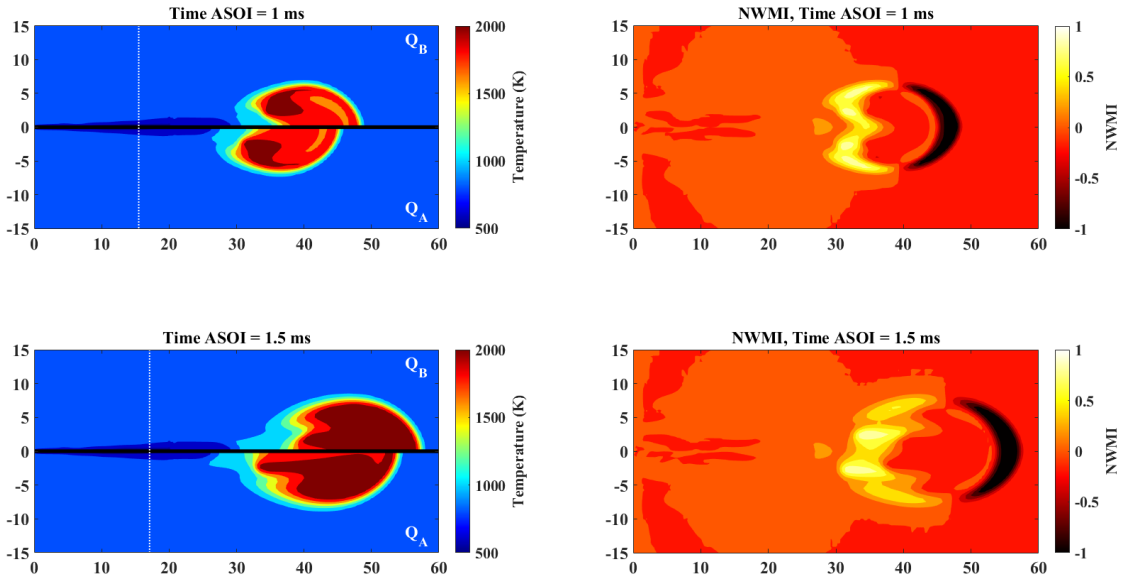

Figure 6.11: Temperature fields for the high (Q_B) and matched (Q_A) vapour length cases at a high liquid length, at 1 and 1.5 ms ASOI, with the NWMI comparison shown

seen in Figure 6.5 are replicated within this sweep, with both cases showing temperatures above 2000 K in the majority of the spray at 1.5 ms ASOI. This suggests that the liquid length influences the internal spray temperature, especially when compared to the location of the combustion zone. This will be explored further in Section 6.2.3, when it will be considered for all cases considered in this study. The mean combustion zone temperatures for these cases are very similar, with the high vapour length case having a mean temperature of 1549 K and the matched vapour length having a mean of 1535 K. Figure 6.11 also shows the differences in the size of the combustion fields, with the NWMI plots showing that the expected positions of the combustion zones hold true; with the high vapour length case extending further into the domain and the matched vapour length case dominating closer to the nozzle. This behaviour holds true when considering the OH field plots, as shown in Figure 6.12, which again shows the high vapour length case's OH field penetrating further into the domain. There are differences in the magnitudes of the OH radicals and the position of the nearest part of the fields to the nozzle at 1.5 ms ASOI, however the fields are mostly quite closely matched apart from the offset.

The C_2H_2 fields show a similar field to that seen in the high liquid length case shown in Figure 6.8, with the higher internal temperatures leading to a smaller, lower

magnitude, C_2H_2 field. The results from the high liquid length cases considered here are shown in Figure 6.13, showing how both cases have small, similarly sized C_2H_2 fields, with the matched vapour length case having a slightly higher magnitude at the trailing edge of the field at both 1 and 1.5 ms ASOI.

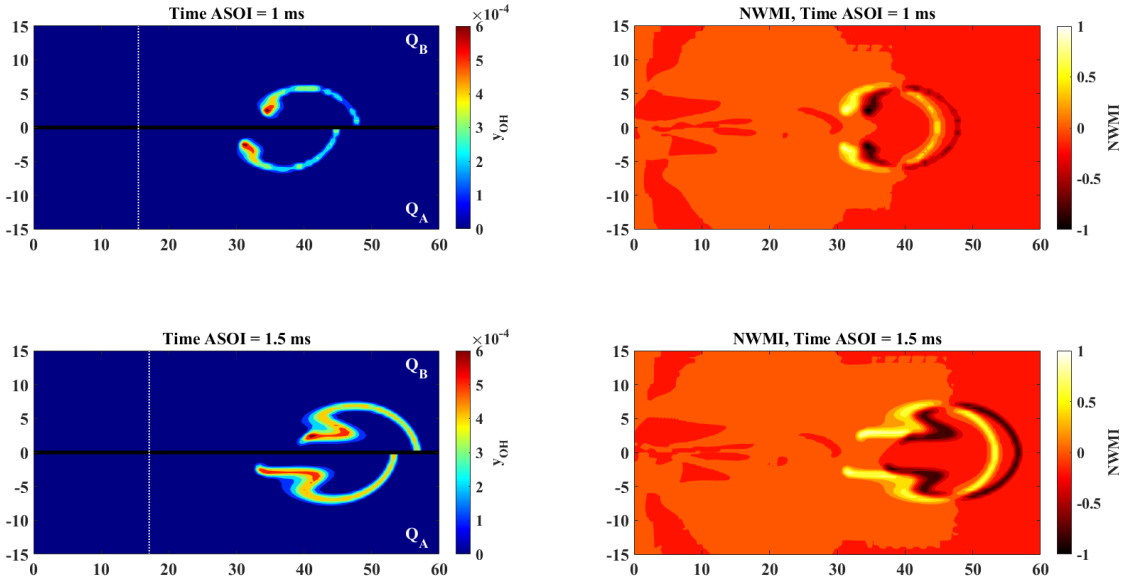

Figure 6.12: OH fields for the high (Q_B) and matched (Q_A) vapour length cases at a high liquid length, at 1 and 1.5 ms ASOI, with the NWMI comparison shown

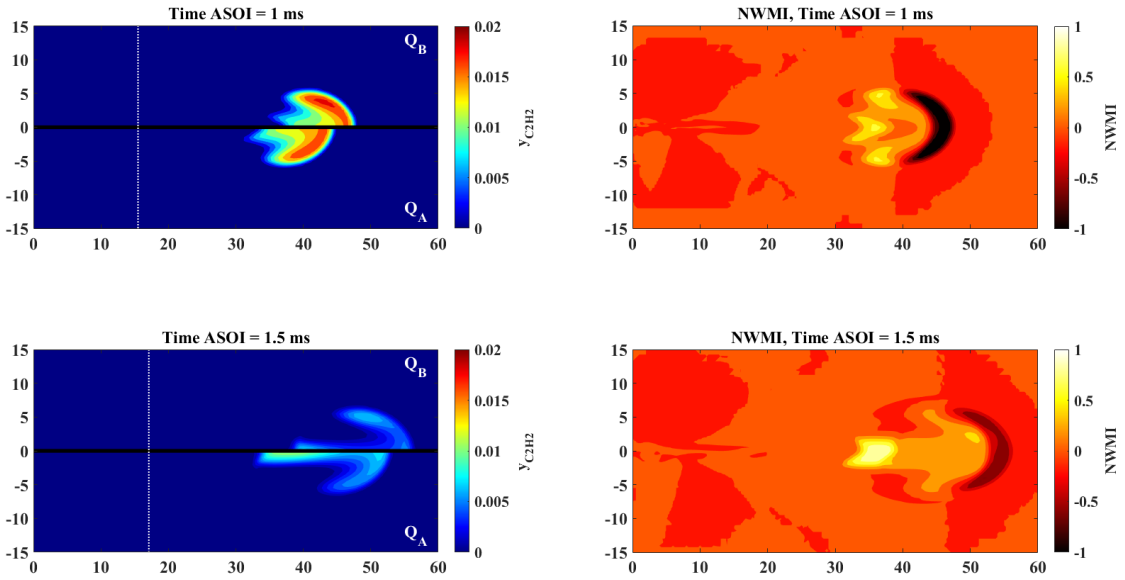

Figure 6.13: C_2H_2 fields for the high (Q_B) and matched (Q_A) vapour length cases at a high liquid length, at 1 and 1.5 ms ASOI, with the NWMI comparison shown

The spray centreline temperatures are shown in Figure 6.14, showing a small difference between the two cases with the high vapour length case yielding a slightly higher centreline temperature. The offset between the temperatures is expected given the change in vapour length, however the gradients of the temperature rises after 25 mm from the nozzle tip are very similar, suggesting the difference in liquid length seen is offset by the increase in vapour length.

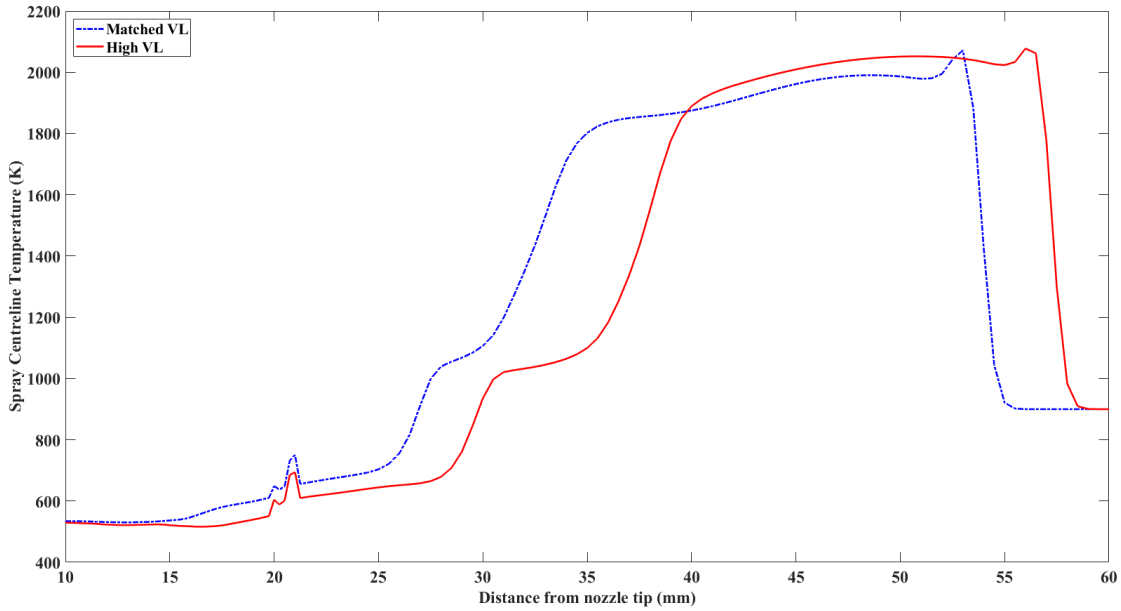

Figure 6.14: Spray centreline temperatures for the matched and high vapour length cases at a high liquid length, at 1.5 ms ASOI, plotted against the distance from the nozzle tip

Given the similarities in temperatures, OH and C_2H_2 seen in this sweep, it can be determined that the $C_{1\varepsilon}$ constant has very little influence on the combustion criteria, especially in comparison to the break-up model constants changed in the liquid length sweep. The major influence of the $C_{1\varepsilon}$ constant's change is on the position of the combustion field, which is to be expected given its influence on the liquid and vapour lengths. This trend continues when considering the mixture fractions, as shown in Figure 6.15, which clearly shows very minimal differences between the two cases. Given these points are taken before any combustion occurs within either case the similarities seen within this sweep show further that the $C_{1\varepsilon}$ constant has a minimal impact on the combustion performance of the KH-RT

"Switch" model. This further correlates with the "well mixed" model used to simulate combustion within Star-CD, wherein the turbulent fluctuations in the system are ignored when processing the chemistry of combustion.

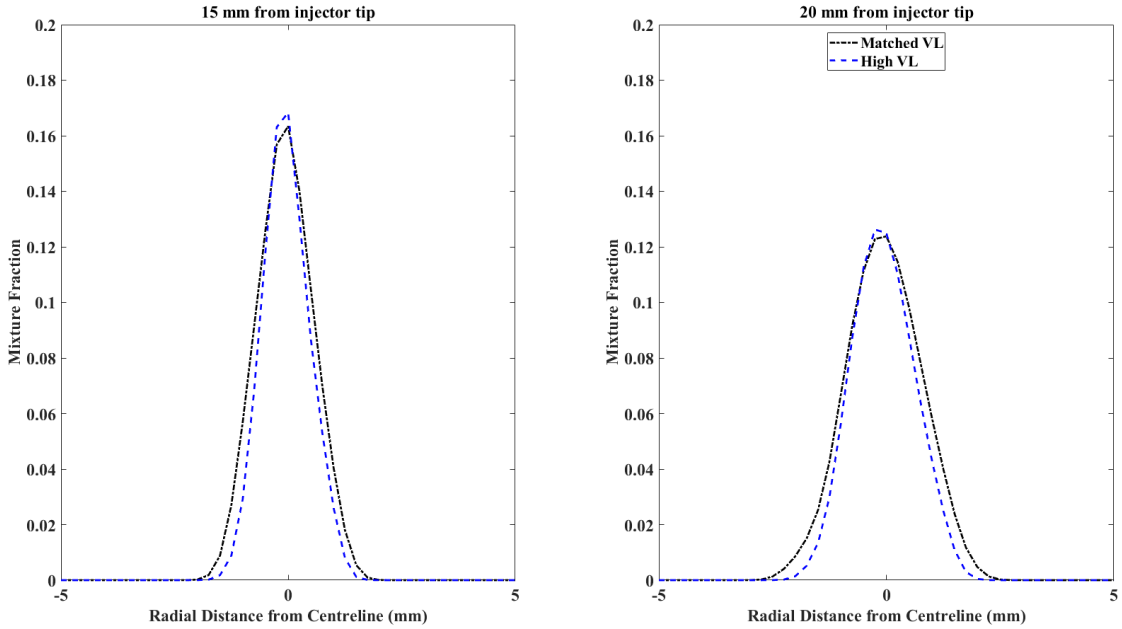

Figure 6.15: Mixture fractions for the matched and high vapour length cases at a high liquid length, at 1 ms ASOI at 15 and 20 mm from the injector tip

Moving to the comparison of the low liquid length cases, the impact of changing the S_N and B_{KH1} constants on combustion can be ascertained, with the changes made shown in Table 6.1. Given the findings of the previous sweep, the decrease of $C_{1\varepsilon}$ can be discounted as a change to the combustion fields, and the break-up model constant changes can be considered isolated within this sweep. From the previous study, the increase in $C_{1\varepsilon}$ should increase the liquid length by approximately 2.8 mm and the vapour length by approximately 4.8 mm, with the decreased drop in liquid length caused by the reduction in the S_N constant and the increase in B_{KH1} constant. The liquid and vapour lengths for both cases are shown in Table 6.4, showing very similar liquid length means and a large difference in vapour lengths at both 1 and 1.5 ms ASOI.

The temperature fields shown in Figure 6.16 show small differences in the positions of the fields, with the matched vapour length case both penetrating further into the domain and closer to the nozzle. The magnitudes of the temperature

Table 6.4: Liquid length means and vapour lengths at 1 and 1.5 ms ASOI for the low liquid length vaporising cases

	Low VL	Matched VL	Experimental
LL Mean	8.86 mm	9.46 mm	10.08 ± 0.34 mm
VL @ 1 ms	39.8 mm	45.8 mm	46.8 ± 2.0 mm
VL @ 1.5 ms	48.8 mm	55.3 mm	56.9 ± 2.6 mm

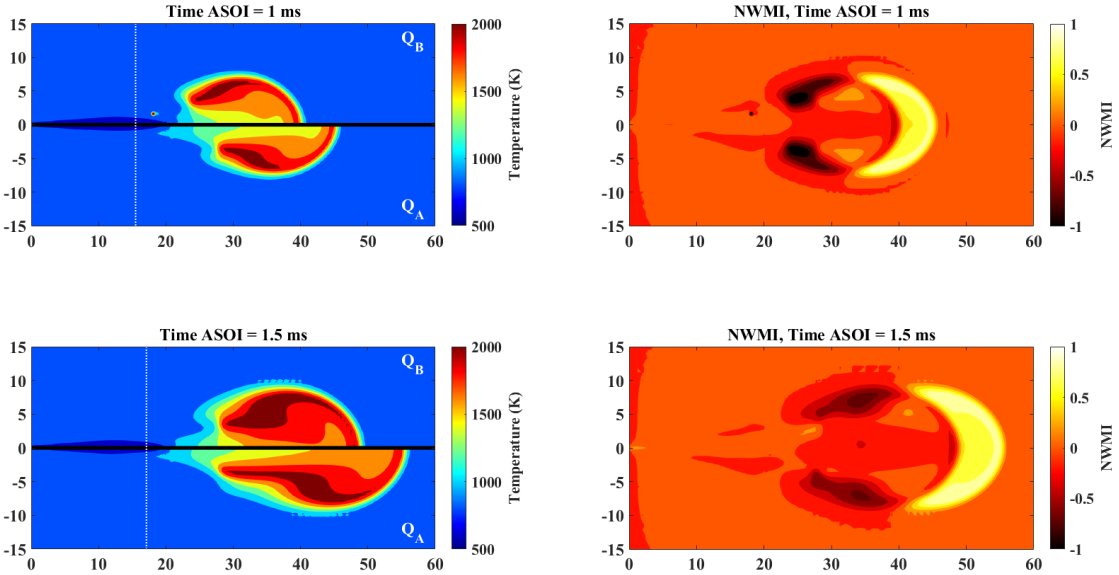

Figure 6.16: Temperature fields for the low (Q_B) and matched (Q_A) vapour length cases at a low liquid length, at 1 and 1.5 ms ASOI, with the NWMI comparison shown

fields are similar, with the mean combustion zone temperature for the matched vapour length case being 1448 K compared to the low vapour length case's mean of 1437 K. The NWMI plot shows the clear increase in penetration for the matched vapour length temperature field, along with the increased temperatures seen in the low vapour length seen at the nozzle end of the temperature field. The OH fields, shown in Figure 6.17 also shows the difference in penetrations, with the magnitudes of the maximum OH concentrations being very similar at 1.5 ms ASOI. The low vapour length OH field is more compressed, mirroring what is seen in the low vapour length temperature fields.

The C_2H_2 fields, shown in Figure 6.18, are similar in structure to each other, with the double peak structure seen in Figure 6.3 replicated. The low vapour

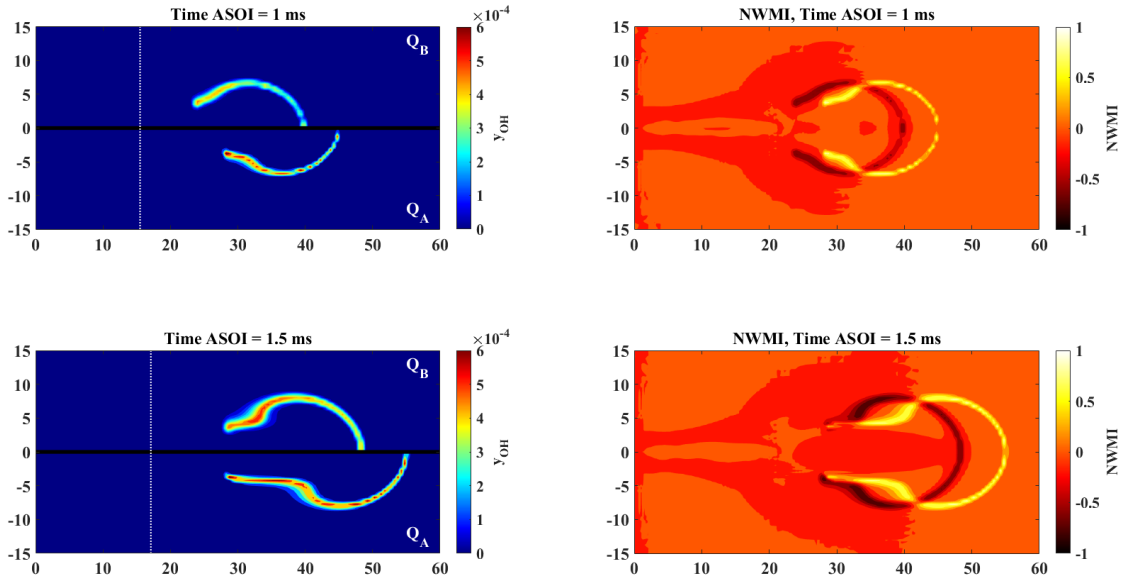

Figure 6.17: OH fields for the low (Q_B) and matched (Q_A) vapour length cases at a low liquid length, at 1 and 1.5 ms ASOI, with the NWMI comparison shown

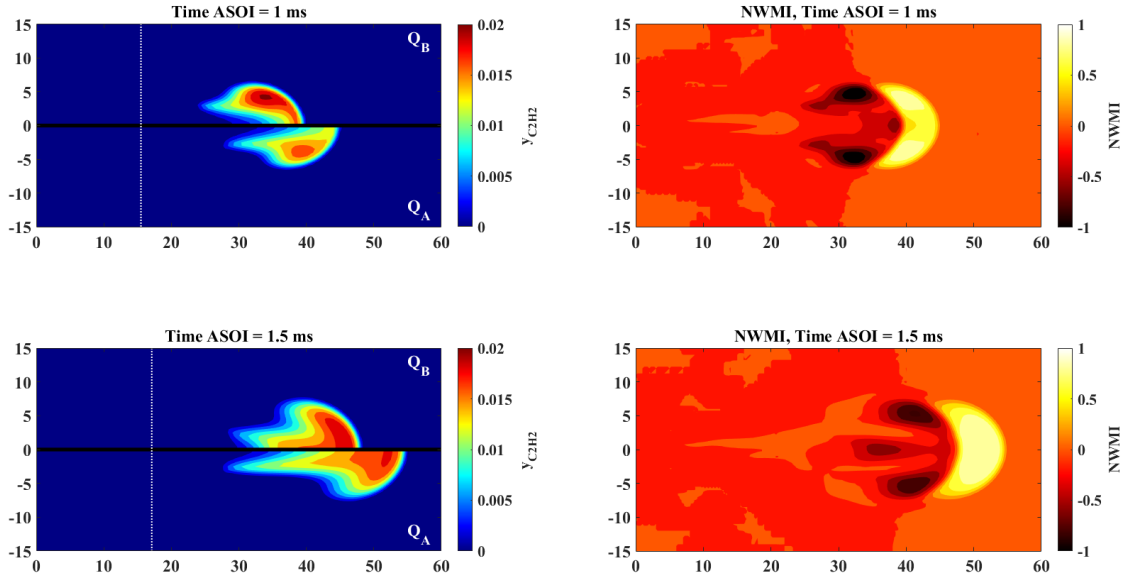

Figure 6.18: C_2H_2 fields for the low (Q_B) and matched (Q_A) vapour length cases at a low liquid length, at 1 and 1.5 ms ASOI, with the NWMI comparison shown

length case has a higher maximum C_2H_2 concentration at both 1 and 1.5 ms ASOI, however at 1.5 ms the field is more concentrated and the matched vapour length case extends closer to the injector. The higher C_2H_2 concentrations are shown in the NWMI plots, which also show the increased penetration of the matched vapour length case, consistent with the other fields shown for this comparison.

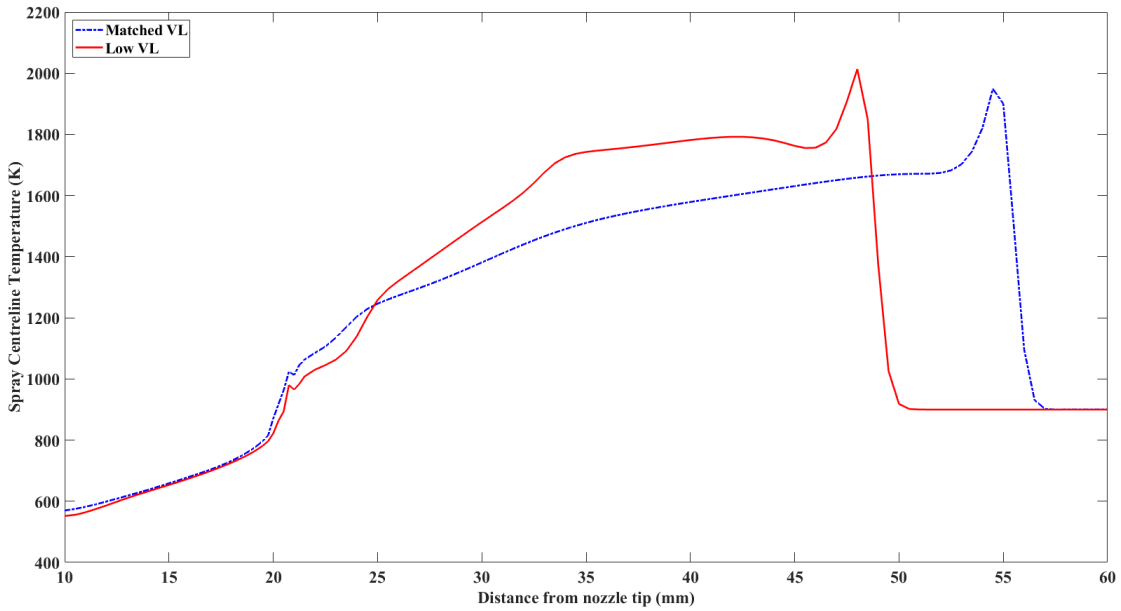

Figure 6.19: Spray centreline temperatures for the low and matched vapour length cases at a low liquid length, at 1.5 ms ASOI, plotted against the distance from the nozzle tip

The centreline temperatures are shown in Figure 6.19, clearly showing the reduction in temperature seen in the matched vapour length case at every point past 25 mm from the nozzle tip. The low vapour length case has a more rapid rise to its "steady" internal temperature and shows far less penetration into the domain, as expected and shown in Figure 6.16. The lift-off-lengths for all the vapour length sweeps shown in this section are plotted in Figure 6.20, showing that the vapour length is the dominant factor in determining the lift-off-length, with the liquid length having a small impact as shown by comparing the LL low/VL match case to the LL high/VL match case.

Considering the mixture fractions, Figure 6.21 shows the matched liquid length case predicting a higher mixture fraction than the low liquid length case. When comparing these trends to the temperatures a very similar trend to that seen in the liquid length sweeps of Figure 6.10 is seen, where a lower predicted mixture fraction leads to a higher predicted internal temperature. As with the liquid length sweeps, the major difference between the cases considered here is the alteration of the break-up model constants, which appear to reduce the internal temperature.

This observation will be considered in more detail in the next section.

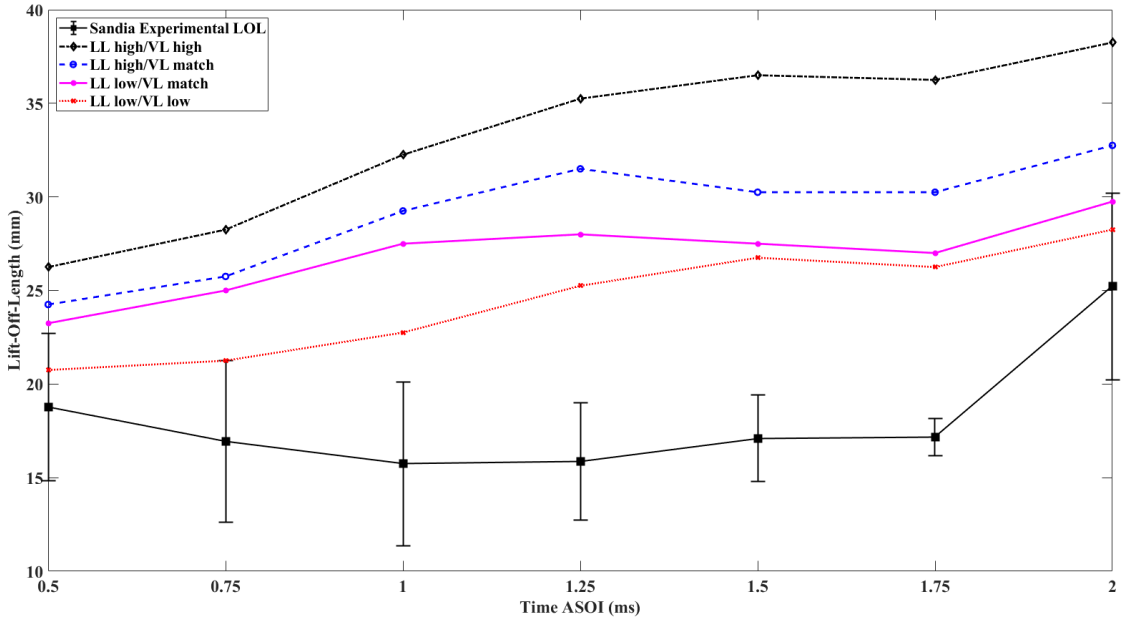

Figure 6.20: Lift-off-lengths for the vapour length sweeps with Sandia experimental data plotted against time ASOI

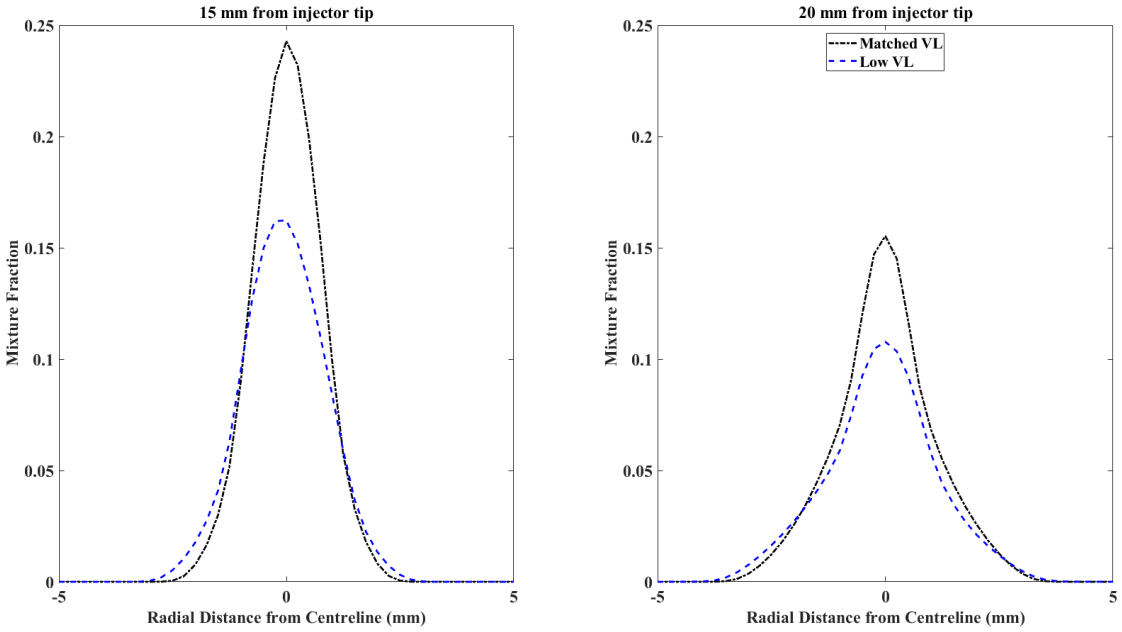

Figure 6.21: Mixture fractions for the low and matched vapour length cases at a low liquid length, at 1 ms ASOI at 15 and 20 mm from the injector tip

6.2.3 Influence of Mean Liquid Length and Combustion Field Position on Internal Spray Temperatures

The temperature comparisons shown in the previous section (Figures 6.2, 6.5, 6.11 and 6.16) suggest that the liquid length has an influence on the internal spray temperature. This effect is especially strong in cases where the combustion fields are similarly placed in the domain but the liquid lengths differ, with a longer liquid length leading to an increase in the temperature, best shown in Figure 6.5. To determine if there is an impact of this, the variable x_{comb} is defined as the point of maximum temperature gradient which takes the spray centreline temperature over 950 K without the temperature dropping below that threshold after. The definition of x_{comb} for the high liquid length/matched vapour length case is shown in Figure 6.22, showing how the value of 27.25 mm is found. This is replicated for all other cases, and these values are shown in Table 6.5. By dividing the mean liquid length by x_{comb}, a consistent comparison between cases of the fraction of the combusting edge to the liquid length can be obtained.

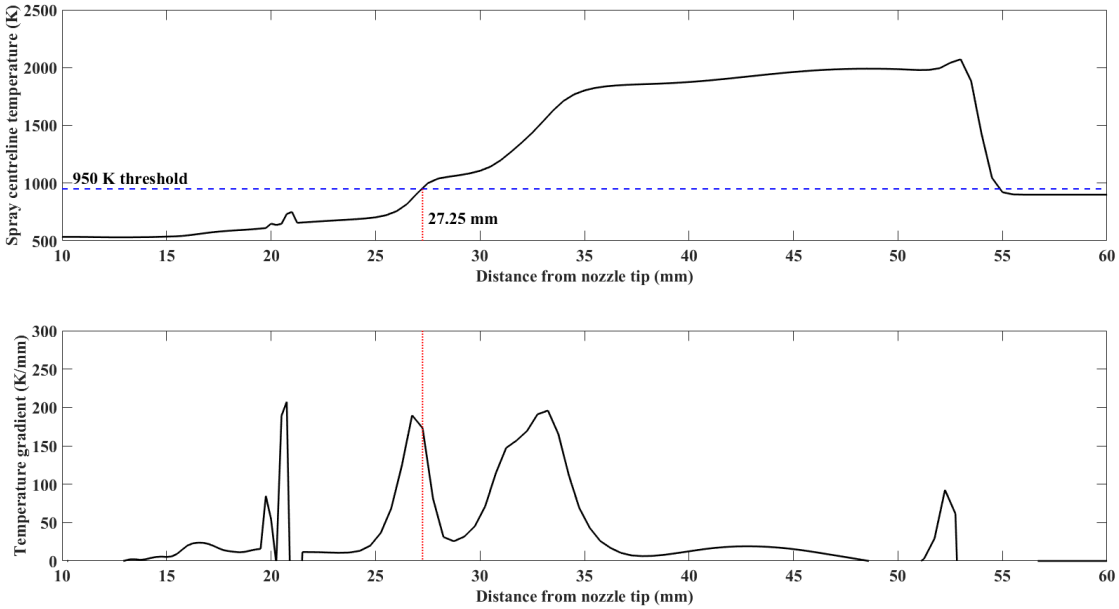

Figure 6.22: Spray centreline temperature and gradients for the high liquid length/matched vapour length case at 1.5 ms ASOI, with the 950 K temperature threshold shown, showing how x_{comb} is defined for this case

Table 6.5: Liquid length means and x_{comb} values for each combusting case in this study at 1.5 ms ASOI

Case	**LL mean (mm)**	**x_{comb} (mm)**	**LL/x_{comb}**
LL High/VL High	15.48	29.75	0.52
LL High/VL Match	13.34	27.25	0.49
LL Match/VL Match	10.15	22.75	0.45
LL Match/VL Low	10.01	24.5	0.41
LL Low/VL Match	9.46	20.5	0.46
LL Low/VL Low	8.86	20.5	0.43

Using the maximum spray centreline temperatures, a regression model can be fitted to the data to determine if the ratio of the liquid length to the x_{comb} variable influences the spray centreline temperature. The results of this are shown in Figure 6.23. It can be seen that there are two clear outliers, which are highlighted by the circle. When these data points are taken out the regression model fits much more closely to the other data points, with an R^2 value of 0.606 for the case without outliers in comparison to an R^2 value of 0.091 when the outliers are included. The regression model fit for the reduced data point set suggests that there is a moderately strong correlation between the ratio of liquid length mean to x_{comb} to the spray centreline temperature, however given the small data set size this is an area for further investigation. What is notable is that the outliers are the LL low/VL match and LL match/VL match cases, both of which alter the break-up model constants; all the other cases just alter the turbulence model constant $C_{1\varepsilon}$ without changing the break-up model constants. This suggests that the break-up model constants also have a large impact on the combusting spray temperatures as well as the vaporising liquid length and vapour length matches.

The impact of the break-up model constants can be further investigated by considering the mixture fraction's impact on the mean internal temperature. As Figures 6.10 and 6.21 show, altering the break-up model constants increases the mixture fraction predictions when compared to baseline cases. For all cases the

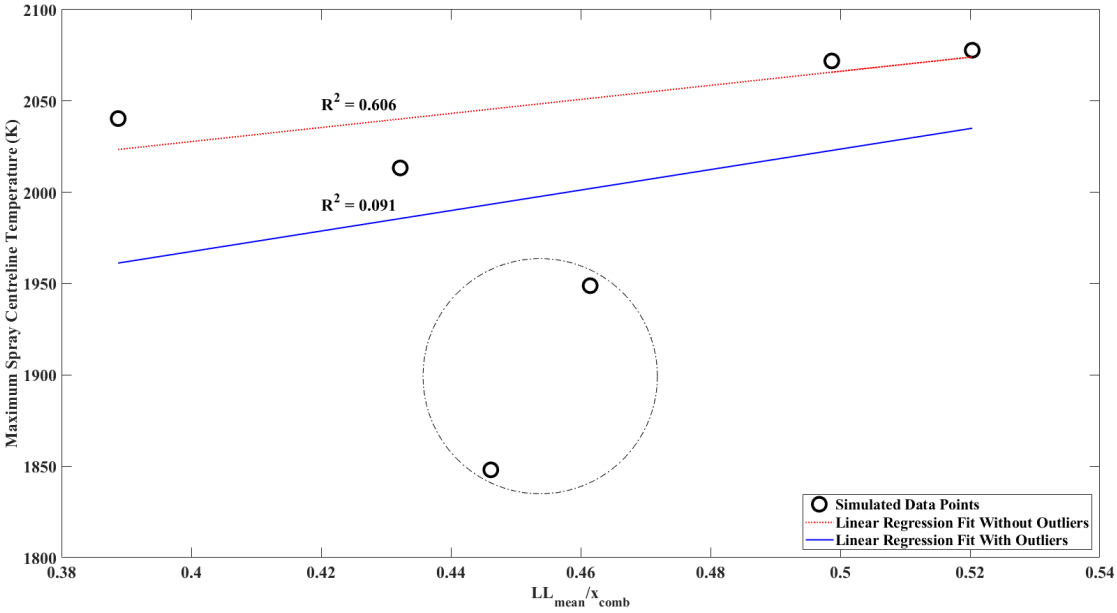

Figure 6.23: LL means/x_{comb} plotted against maximum spray centreline temperature, with regression models shown. Outliers are highlighted by the circle, and R^2 values for each model are shown with their fitted lines

mixture fraction was taken at a distance of 125 % the liquid length mean, as shown in Table 6.6, to ensure that the comparisons between each case is as fair as possible. Table 6.6 shows that the two cases which alter the break-up length constants show a much higher maximum mixture fraction at 125 % of the mean liquid length when compared to all the other cases.

Table 6.6: Liquid length means, mixture fraction position and maximum mixture fractions for each combusting case in this study at 1 ms ASOI

Case	**LL mean (mm)**	**Mixture Fraction position (mm)**	**Maximum Mixture Fraction**
LL High/VL High	15.48	19.35	0.127
LL High/VL Match	13.34	16.68	0.138
LL Match/VL Match	10.15	12.69	0.311
LL Match/VL Low	10.01	12.51	0.202
LL Low/VL Match	9.46	11.83	0.319
LL Low/VL Low	8.86	11.08	0.227

Comparing these mixture fractions to the mean temperature of the combustion zone yields Figure 6.24, which shows a highly linear correlation between the mixture fraction at 125 % of the mean liquid length to the mean internal temperature. Figure 6.24 clearly shows that a higher predicted mixture fraction yields a lower internal temperature, and as such the break-up model constant changes can clearly be linked to a reduction in internal temperature, as is also shown in Figure 6.23.

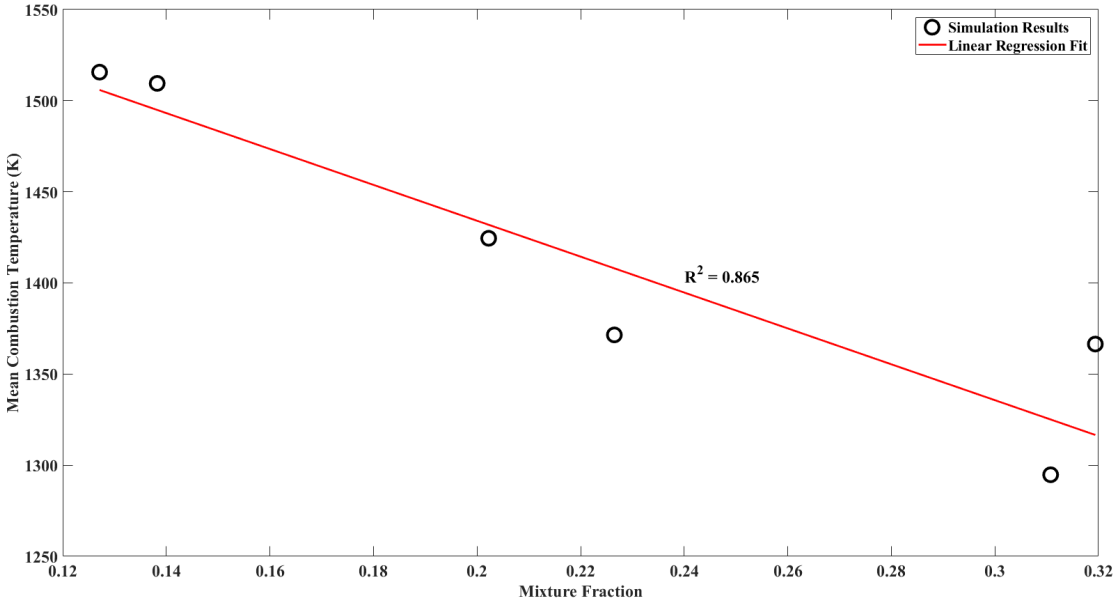

Figure 6.24: Maximum mixture fraction at 125 % of the mean liquid length against the mean internal spray temperature, with the linear regression fit shown

6.3 Conclusions

Following on from the characterisation of the KH-RT "Switch" model for a combusting spray, the vaporising liquid and vapour lengths were influenced using the improved matching capabilities seen in the previous chapter. This allowed for six variations of high, matched and low liquid and vapour lengths to be simulated at vaporising conditions, with the model set-ups used for the vaporising conditions transferred to the combusting condition. The following observations were made:

- A liquid length sweep was undertaken at a matched vapour length, showing differences in internal spray temperatures and C_2H_2 fields, with the high and

matched liquid length cases showing large differences in magnitudes. This was believed to be due to the influence of changing the B_{RT0} constant, which appeared to "cool" the flame in the matched case. The lift-off-lengths for all cases were found to fall in line with the liquid length predictions, however with a smaller difference in lift-off-lengths than was seen in liquid lengths.

- Two vapour length sweeps were also undertaken, at high liquid length and low liquid length. The high liquid length sweep showed that the $C_{1\varepsilon}$ constant has very little impact on the temperature, OH or C_2H_2 fields, with the only major changes being the position of the combustion field itself and the lift-off-lengths, both of which are as expected. The low liquid length case showed some minor discrepencies in the temperature and OH fields, however this was mostly due to the changing in position of the combustion field caused by the reduction in $C_{1\varepsilon}$. It was also found that altering the B_{RT0} constant, along with the other break-up model constants, had a large impact on the predicted mixture fractions; whereas altering the turbulence model constant $C_{1\varepsilon}$ had little difference on the mixture fraction.

- Finally, the influence of the position of the combustion field to the internal spray temperature was considered, with a fairly good match for the ratio of liquid length mean to combustion zone position to the spray centreline temperature found when two outliers were removed. These outliers were cases in which the spray break-up model constants had been altered, suggesting that these constants have a large impact on the spray centerline temperature seen. Given the small dataset considered however, this is an area for further investigation at both the "Spray A" condition and other temperatures and pressures.

7 Conclusions and Future Work

7.1 Conclusions

This study's objective was to investigate diesel spray modelling and combustion, with interest placed on the impacts of the various sub-models used within CFD on the spray formation. The dataset known as "Spray A" was chosen to provide the best comparison for this study, with its engine relevant temperatures and pressures of interest, as well as its applicability at both vaporising and combusting test points. Initially, the computational domain was created and characterised at the "Spray A" vaporising condition, employing the best practices of Star-CD and the recommended turbulence, break-up and atomisation models (k-ε, Reitz-Diwakar and Huh-Gosman respectively). The domain was characterised using a grid sensitivity study, with different levels of embedding employed near to the nozzle to determine the optimum cell size for simulations. The following observations have been made utilising this domain:

- A cell size of 0.25 mm was found to be the best trade-off between accuracy, run time and convergence of most key spray criteria. Any un-converged spray criteria were found to converge either at 0.125 mm or just after, and are not deemed critical enough to warrant a smaller minimum cell size.

- The impact of the parcel count in the simulation was also considered, showing a strong linear relationship between parcel count and run time with negligible impact on the liquid or vapour lengths. This suggests the initial parcel counts selected for the grid sensitivity study were too high, and are reduced for the

domain going forward. 700,000 parcels are found to be the optimum parcel count for the simulation.

- Finally, the initial ambient turbulence criteria were also investigated, with the ambient turbulent kinetic energy having a strong impact on both the transient overshoot of the liquid length and the initial vapour field formation. The turbulent dissipation rate had a weaker impact on the transient overshoot than the ambient TKE with little impact on the liquid length. Considering these results suitable values for both were chosen to use going forward, with a ambient TKE value of 2 m^2/s^2 and an ambient turbulent dissipation rate of 3000 m^2/s^3 used in future.

Utilising this domain a single-hole non-reacting diesel spray was simulated in both Star-CD and CONVERGE, using a Lagrangian-Eulerian approach. The Star simulations were performed by the author, and compared against a similar CONVERGE simulation from within the group. The spray simulated was based on the ECN "Spray A" operating condition, making use of the available experimental data from the ECN database. Comparisons between the two CFD codes, Star-CD and CONVERGE, were made as follows:

- Baseline comparisons were made between the two codes at initial set-ups optimized for steady state liquid lengths. Discrepancies in transient predictions were observed between the codes, with the break-up model considered to be one of the principle causes of these differences.

- A direct comparison between codes showed a difference in implementation between seemingly identical break-up models (known as the KH-RT model), leading to a difference in overall liquid length prediction between codes. Star-CD allowed the KH and RT models to be applied at any time and position, and to any droplet parcel, with the two models competing, whereas CONVERGE employed only the KH model to parcels initially and then the RT model to all child droplets after they had undergone break-up once.

- A new implementation of the KH-RT model was introduced for use within Star-CD, allowing for the two models to act at different regions of the spray. This implementation showed a similar match to steady state liquid length with a reduction in the transient overshoot, moving closer to the liquid lengths seen in CONVERGE. The new implementation allowed Star-CD to utilize the KH-RT model to match more closely the experimentally observed liquid length, and also match the vapour length without compromising the liquid length prediction as seen in the baseline KH-RT model.
- The impact of the new KH-RT "Switch" model on the spray vapour fields was characterised, with earlier switching positions showing oscillatory behaviour throughout injection near to the nozzle exit, however at no impact to the cone angle of the spray.

The newly derived KH-RT "Switch" model was then tested at the combusting "Spray A" condition, with a good match found between the KH-RT "Switch" model and the baseline Reitz-Diwakar case when both models utilised the same reduced n-dodecane mechanism. The following differences and phenomena were also found and discussed:

- Both models were found to over-predict the lift-off-length of the spray when compared to experimental results, with the Reitz-Diwakar model showing an over-prediction of the lift-off-length by approximately 7 mm and the KH-RT "Switch" model over-predicting the lift-off-length by approximately 10 mm. This was deemed to not be an issue given this result has been seen previously when the combination of the well mixed combustion model and Yao mechanism was used. The ignition delay was predicted excellently on the other hand, with both break-up models matching experimental data to within 0.01 ms.
- Differences in the mixture fractions were seen between the two models, with the results complementing the SMD results from the KH-RT "Switch" model derivation; these differences are also believed to cause the small differences seen in the temperature predictions.

- The influence of each sub-model of the KH-RT break-up model was also considered, utilising the implemented switch to ensure that only one model acted for the spray. The results showed that the RT sub-model caused a highly unstable liquid prediction, leading to a much lower lift-off-length than that of the KH sub-model. These instabilities mirrored those seen previously when the switch position was set too close to the injector, further suggesting a boundary on the switching constant is required.

Following on from the characterisation of the KH-RT "Switch" model for a combusting spray, the vaporising liquid and vapour lengths were influenced using the improved matching capabilities seen in the previous chapter. This allowed for six variations of high, matched and low liquid and vapour lengths to be simulated at vaporising conditions, with the model setups used for the vaporising conditions transferred to the combusting condition. The following observations were made:

- A liquid length sweep was undertaken at a matched vapour length, showing differences in spray combustion temperatures and C_2H_2 fields, with the high and matched liquid length cases showing large differences in magnitudes. This was believed to be due to the influence of changing the B_{RT0} constant, which appeared to "cool" the flame in the matched case. The lift-off-lengths for all cases were found to fall in line with the liquid length predictions, however with a smaller difference in lift-off-lengths than was seen in liquid lengths.

- Two vapour length sweeps were also undertaken, at high liquid length and low liquid length. The high liquid length sweep showed that the $C_{1\varepsilon}$ constant has very little impact on the temperature, OH or C_2H_2 fields, with the only major changes being the position of the combustion field itself and the lift-off-lengths, both of which are as expected. The low liquid length case showed some minor discrepencies in the temperature and OH fields, however this was mostly due to the changing in position of the combustion field caused by the reduction in $C_{1\varepsilon}$. It was also found that altering the B_{RT0} constant,

along with the other break-up model constants, had a large impact on the predicted mixture fractions; whereas altering the turbulence model constant $C_{1\varepsilon}$ had little difference on the mixture fraction.

- Finally, the influence of the position of the combustion field to the combustion temperature was considered, with a fairly good match for the ratio of liquid length mean to combustion zone position to the spray centreline temperature found when two outliers were removed. These outliers were cases in which the spray break-up model constants had been altered, suggesting that these constants have a large impact on the spray centerline temperature seen. Given the small dataset considered however, this is an area for further investigation at both the "Spray A" condition and other temperatures and pressures.

7.2 Future Work

Future work on this study should focus on increasing the dataset of the variations in liquid and vapour length impact on combustion prediction, along with testing the new KH-RT "Switch" model at further conditions. The present study suggests this model is able to capture combustion phenomena at a similar level to the baseline models considered, while also predicting the vaporising condition within experimental range. Future work on this study should include the following:

- Exploring the boundaries for the switching position value through testing at variations of ambient conditions. Given the sensitivity of the switching position at near-nozzle values work is required to determine the point at which this occurs at different conditions, with correlations able to be drawn between the ambient conditions and the switching position.

- Expansion of the KH-RT "Switch" model through additional non-dimensional analysis. Testing at different ambient vaporising conditions will allow for the non-dimensional analysis to be expanded, allowing for a more robust model for the switching position to be derived. Along with the increased robustness of

the switching position model, correlations can be found for how the turbulence and break-up model constants change at different ambient conditions.

- Improved combustion modelling. Within this study the combustion model was used as a comparator between cases, and the experimental conditions were not matched due to this. Utilising a more complex combustion model and increasing the domain accuracy for a combusting case should allow for combustion to be modelled more accurately to the experimental results. An expanded non-dimensional analysis can also be applied, ensuring the expansion of the model works at both vaporising and combusting cases.

- Matching with new experimental apparatus in Oxford. The Oxford Cold Driven Shock Tube (CDST) is a new piece of experimental apparatus designed around generating supercritical conditions for diesel injection investigation [138]. As such, characterising the KH-RT "Switch" model against in-house, known, conditions will help to improve the accuracy of the model.

Appendices

A Numerical Bisection Method

The entirety of the RT model code used within the user defined function for the KH-RT "Switch" model is presented below, with the bisection method loop shown in a separate box. The entirety of this UDF is coded in Fortran 77, in keeping with Star-CD's conventions. Initially, the drag coefficient (XCD) is calculated based on the gaseous Reynolds Number, which is then used to calculate the droplet acceleration (ACRT) with respect to the gas. Along with this, the density difference (DEND) is calculated and used to determine a critical value for the wavenumber (κ_{RT}), from which the high and low estimates for the wavenumber can be found. The incrementer (DK) for the bisection method is found from the high estimate for the wavenumber, and the terms from the growth rate equation are calculated for simplicity within the bisection method. The convergence metric (EPS) is also defined here.

```
C       Calculate Drop Drag Coeff

        if (REYG.GT.1000.0) then

        XCD = 0.424

        else

        XCD = (12/REYG)*(1.0+(1.0/6.0)*(REYG**(2.0/3.0)))

        endif

C       Calculate Drop Acceleration and density difference

        ACRT = ((3.0/8.0)*XCD*DEN*VRM2)/(DENDR*DRR)
        DEND = ABS(DENDR-DEN)+1.0E-10
```

```
C       Calculate crit, low and high values for k used
C       in iteration

        XKCRIT = SQRT(DEND*ACRT/SFTC)
        XKLOW = (1.0E-10)*XKCRIT

        if ((0.95*XKCRIT).GT.1.0E-99) then

        XKHIGH = 0.95*XKCRIT

        else

        XKHIGH = 1.0E-99

        endif

C       Define iteration constraints for upcoming
C       bisection method

        DK1 = 1.0E-7*XKHIGH

        if (DK1.GT.1.0) then

        DK = 1.0

        else

        DK = DK1

        endif

        EPS = 1.0E-4

C       Calculate the terms needed for growth rate
C       iteration (Joseph, 1999)

        TERM1 = (DRVIS + VISM)/(DENDR + DEN)
        TERM2 = ACRT*DEND/(DENDR + DEN)
        TERM3 = SFTC/(DENDR + DEN)
        TERM4 = (DRVIS + VISM)/(DENDR + DEN)
        TERM42 = TERM4*TERM4
        XCONV = (XKHIGH - XKLOW)
```

Below is the bisection loop, utilising a convergence criteria (XCONV) based on the high and low estimates for the value of κ_{RT}. The average of these estimates is used within the loop to calculate the surface growth rate. An incremented κ_{RT} is used to determine which of the high or low estimates is closer to the maximum surface growth rate, and as such the boundaries of the high and low estimates are changed for the next iteration. Finally, the convergence criteria is calculated before the loop returns to the original convergence check.

```
C       Do the iteration to find k for maximum growth rate

20      if (XCONV.GE.EPS) then

        XKK = 0.5*(XKLOW + XKHIGH)
        XKDK = XKK + DK

C       Equation below from viscid RT model,
C       see (Joseph, 1999) Eq.25

        OMK = -(XKK*XKK*TERM1) + SQRT((XKK*TERM2) -
        + ((XKK**3)*TERM3) + ((XKK**4)*TERM42))
        OMDK = -(XKDK*XKDK*TERM1) + SQRT((XKDK*TERM2) -
        + ((XKDK**3)*TERM3) + ((XKDK**4)*TERM42))

        DOMEGA = OMDK - OMK

        if (DOMEGA.GT.0.0) then

        XKLOW = XKK

        else

        XKHIGH = XKK

        endif

        XCONV = (XKHIGH - XKLOW)/XKK

        go to 20

        endif
```

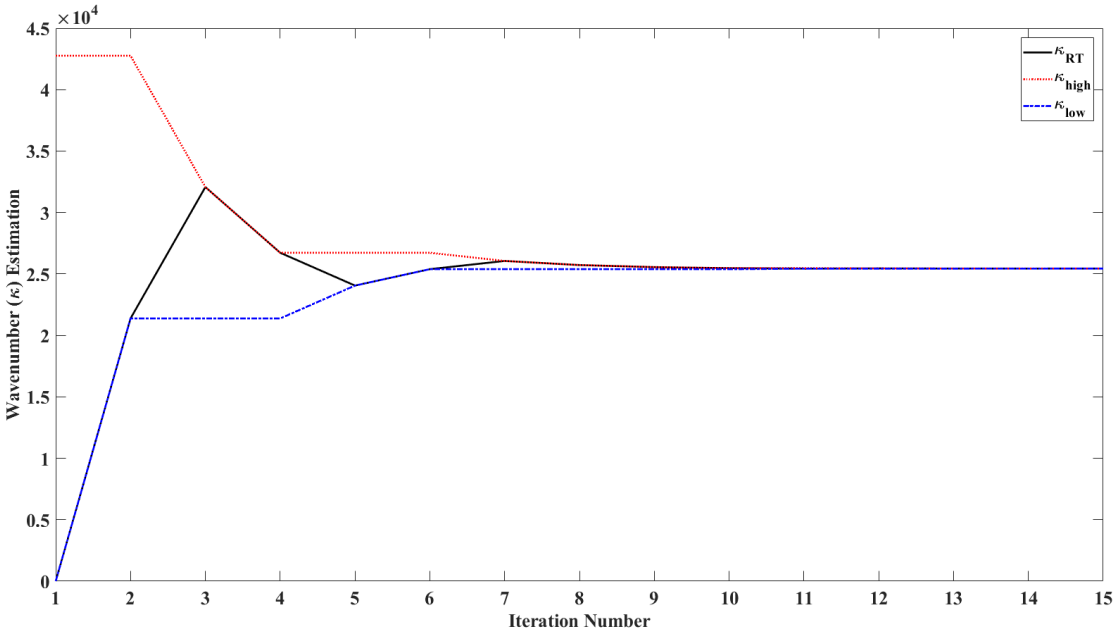

Figure A.1: Wavenumber estimation against iteration number for the RT bisection loop

The values of the high and low estimates for κ_{RT}, along with the value of κ_{RT} used in each iteration are shown in Figure A.1, with the values for the last 5 iterations shown in Table A.1. As can be seen, the wavenumber estimates converge towards a value of 25440, with iteration 15 showing the values having met the convergence limit as defined.

Table A.1: Values of the high and low estimates for the final five iterations of the bisection loop, along with the value of κ_{RT} taken forward and the convergence criteria value

Iteration Number	$\boldsymbol{\kappa_{low}}$	$\boldsymbol{\kappa_{high}}$	$\boldsymbol{\kappa_{RT}}$	**XCONV**
11	25431	25473	25431	8.20×10^{-4}
12	25431	25452	25452	4.10×10^{-4}
13	25431	25441	25441	2.05×10^{-4}
14	25436	25441	25436	1.03×10^{-4}
15	25439	25441	25439	0.51×10^{-5}

B Combusting Anomalies

During the investigation of the combusting spray in Chapter 5, some anomalies within the liquid length were noted. These anomalies are described in this appendix, with some discussion on the cause of the anomaly. However, this work is a subject of further work beyond this thesis. It should be noted that it is not the author's belief that these anomalies impact the combustion prediction in any meaningful way, given the temperature and OH fields are still symmetrical despite the predictions shown within, and as such the comparisons made in Chapter 6 are still valid.

Liquid Lengths

To begin with, the liquid lengths of the baseline simulations are plotted, as shown in Figure B.1. As can be seen, in their baseline cases neither model predicts the liquid length consistently within the experimental range, with the Reitz-Diwakar model predicting a mean liquid length of 9.78 mm and the "Switch" model predicting a mean liquid length of 7.57 mm over the same time period as the experimental liquid length mean. The "Switch" model liquid length is also notable for the dip in liquid length seen at approximately 0.3 ms ASOI, from a liquid length within the experimental range to its mean of 7.57 mm. The reason for this drop in liquid length is believed to be due to some artefacting seen in the parcels around the 0.3 ms region that causes a small subsection of parcels near the spray tip to disappear completely from the simulation. This artefacting is shown in Figure B.2.

Figure B.1 also shows that the trends seen in Chapter 4 regarding the baseline Reitz-Diwakar and KH-RT models hold true at a combusting test point, with the KH-RT model predicting a lower liquid length than the Reitz-Diwakar case. The liquid lengths predicted are slightly lower than the vaporising case, however

this is believed to be due to the change in gas composition, causing the average density for the combusting test point to be calculated at 23.4 kg/m^3 compared to 22.9 kg/m^3 for the vaporising case.

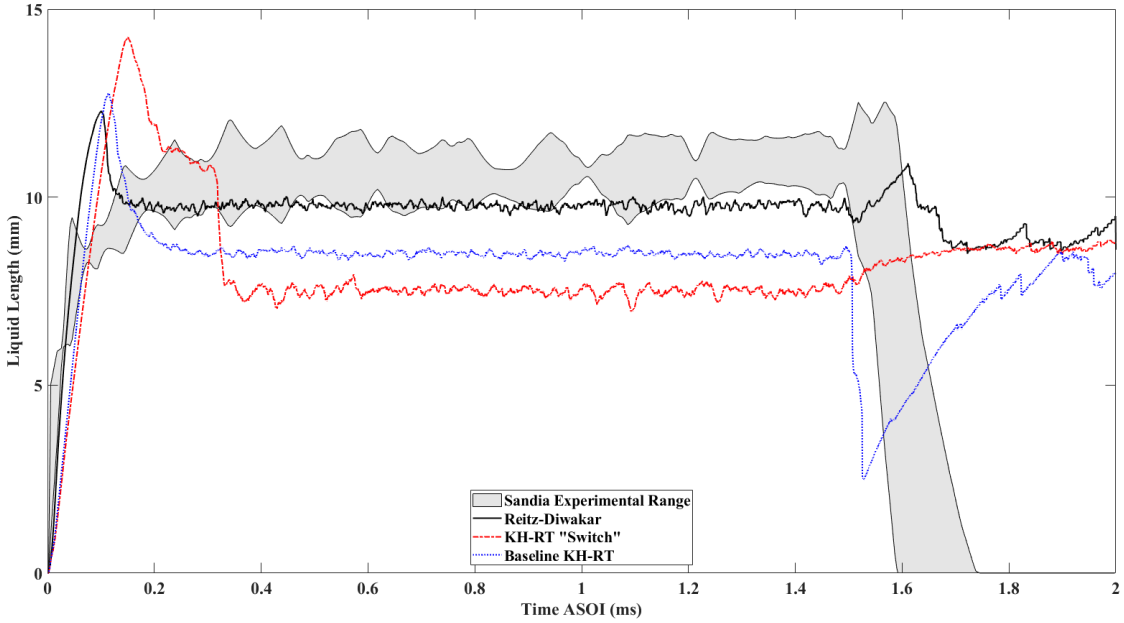

Figure B.1: Simulated and experimental liquid lengths for the combusting "Spray A" case

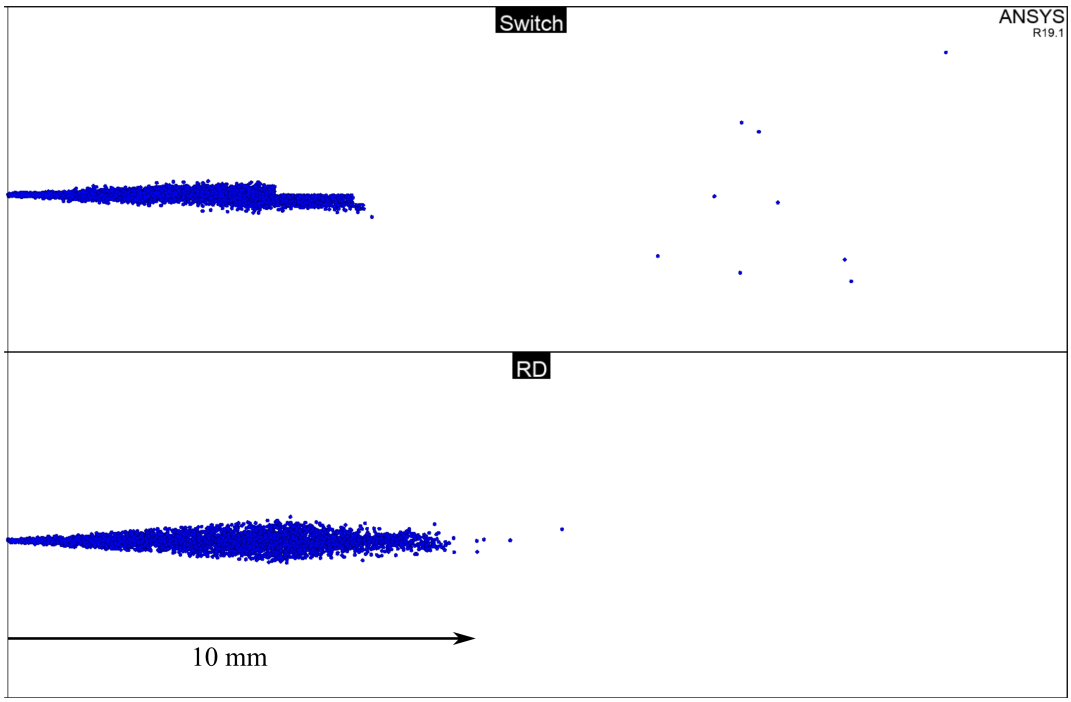

Figure B.2: Parcel plots for both KH-RT "Switch" and Reitz-Diwakar models at 0.5 ms ASOI, showing artefacting in the liquid for the "Switch" model

The other point of note from Figure B.1 is the after end of injection (EOI) liquid lengths from the simulations do not return to 0 mm as suggested by the experimental data; instead some liquid appears to remain in the domain after EOI. Considering the parcels in the domain after EOI it can be seen that a few parcels still remain, however when queried on the number of droplets contained within the parcels it is shown that ever parcel still in the domain has no droplets within them, as shown in Figure B.3. Given the methodology of extracting the liquid length from the Star-CD simulations depends on the mass of liquid in the domain, having parcels within the system with no droplets contained within them but a small mass will cause this calculation to yield a liquid length even though the parcels are "empty".

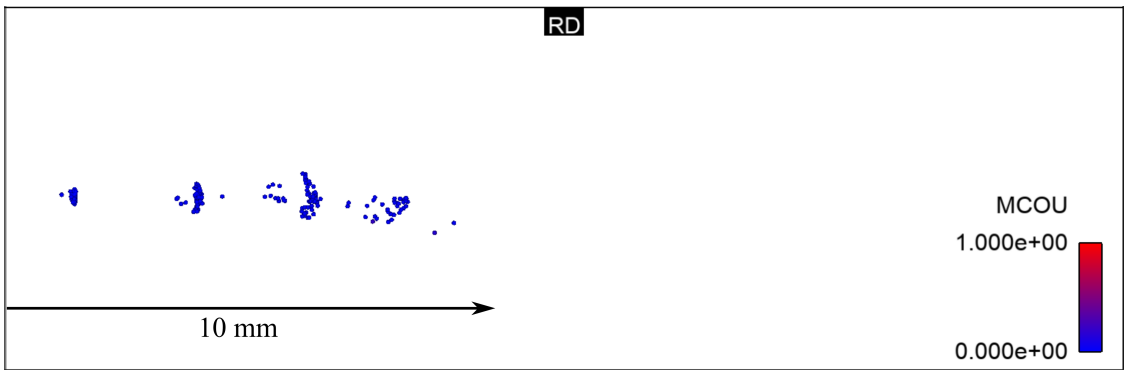

(a)

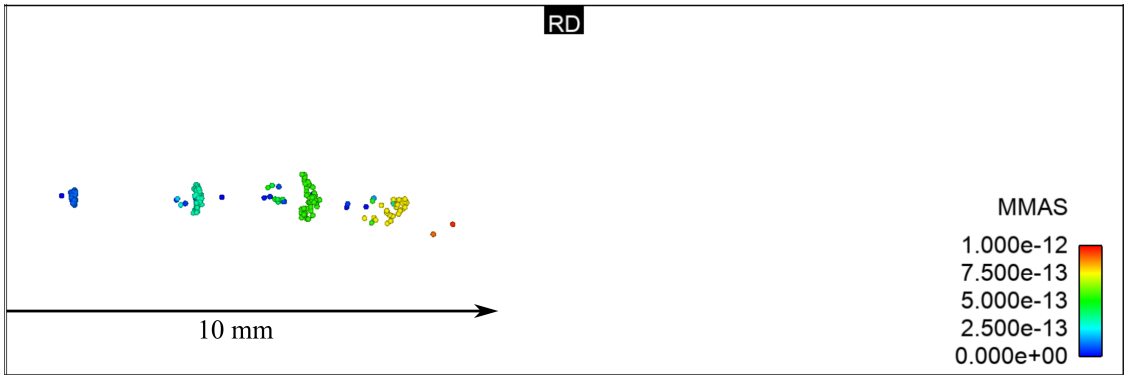

(b)

Figure B.3: Parcels remaining in the simulation domain after EOI at 1.9 ms ASOI, for the Reitz-Diwakar model, **(a)** shows the parcel counts and **(b)** shows the parcel masses. MCOU is the number of droplets within each parcel, MMAS is the mass of the parcel in kg

Droplet Artefacting

As Figure B.2 shows, there is some droplet artefacting occurring when the KH-RT "Switch" model is used in conjunction with the detailed chemistry as defined in Section 5.1.2. To test whether this is a random occurrence or not, 10 identical runs of the same case as in the previous section were run until 0.4 ms ASOI, as this encompasses the time at which artefacting was seen in Figure B.1. For this situation the time the artefacting is defined to have started is the timestep at which the liquid length drops 50 % of the difference between the pre-artefacting liquid length and the post-artefacting liquid length, as shown in Figure B.4 for run 2 of the test. This liquid length is approximately 9.2 mm in this case, and the time at which the liquid length drops below this is 0.3215 ms ASOI. This criterion is applied to the other cases, and the results for all the cases are shown in Table B.1. This clearly shows that the artefacting is not a random occurrence, however the time of the artefacting is not the same throughout the 10 tests, with it varying from 0.3115 ms to 0.3215 ms ASOI. This suggests the initial assumption that there

Table B.1: Artefact test for each of the 10 identical runs, with time ASOI artefacting begins for each run if artefacting occurs

Run	**Artefacting Occurs**	**Time ASOI of Artefact (ms)**
1	Yes	0.3125
2	Yes	0.3215
3	Yes	0.3125
4	Yes	0.321
5	Yes	0.3115
6	Yes	0.312
7	Yes	0.3215
8	Yes	0.3115
9	Yes	0.3215
10	Yes	0.313

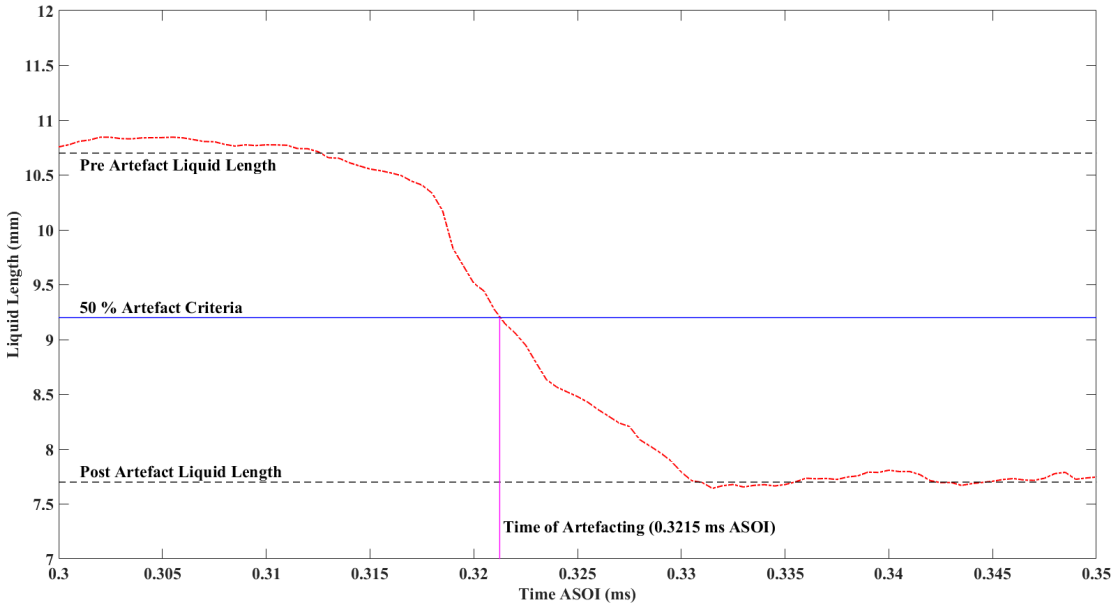

Figure B.4: Liquid length for test run 2 between 0.3 and 0.35 ms ASOI, showing artefacting criterion depending on the pre and post artefact liquid lengths

is some interaction occurring between the break-up model and the combustion chemistry is causing the artefacting is likely to be correct.

To test the assumption that there is an interaction between the break-up model and the combustion chemistry further, the KH and RT models will be individually tested within this combusting case. This can be achieved by turning one of the KH or RT models off within the UDF, ensuring that only one of them acts for the entirety of the simulation for all droplets. The liquid lengths for this test are shown in Figure B.5. The liquid length shows that artefacting occurs in the RT test at approximately 0.27 ms ASOI, earlier than was previously seen in the KH-RT "Switch" model tests. After the artefacting the liquid length is very similar to those seen in the previous tests, staying around a mean of approximately 7.5 mm before rising after the end of injection. In contrast, the KH model predicts a steady liquid length of approximately 10.1 mm throughout the injection.

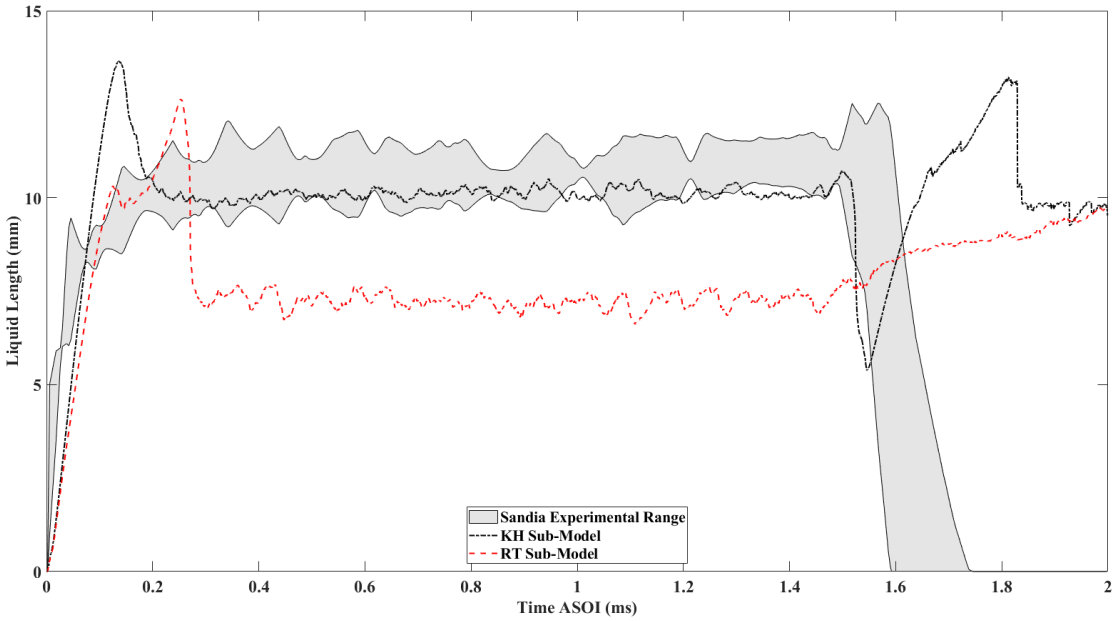

Figure B.5: Liquid lengths for the KH and RT sub-models compared with the Sandia experimental range against time ASOI

It is clear that there is an interaction between the RT sub-model and the CFD code causing this artefacting, however the full cause of this is not yet known. It is proposed that future work on this should be undertaken to ascertain what interaction is causing these parcels to be lost, and how it can be fixed.

References

[1] Stone R. Introduction to Internal Combustion Engines. 4th ed. Basingstoke: Palgrave Macmillan; 2012.

[2] Heywood JB. Internal Combustion Engine Fundamentals. 1st ed. New York: McGraw-Hill; 1988.

[3] Wei S, Wang F, Leng X, Liu X, Ji K. Numerical analysis on the effect of swirl ratios on swirl chamber combustion system of di diesel engines. Energy Conversion and Management. 2013;75:184–190. Available from: http://dx.doi.org/10.1016/j.enconman.2013.05.044.

[4] Fujimoto M, Iwai K, Kataoka M, Tabata M. Effect of combustion chamber shape on tumble flow, squish-generated flow and burn rate. JSAE Review. 2002;23(3):291–296.

[5] Hill PG, Zhang D. The effects of swirl and tumble on combustion in spark-ignition engines. Progress in Energy and Combustion Science. 1994;20(5):373–429.

[6] Leach F, Ismail R, Davy M, Weall A, Cooper B. The effect of a stepped lip piston design on performance and emissions from a high-speed diesel engine. Applied Energy. 2018;215(April):679–689. Available from: https://doi.org/10.1016/j.apenergy.2018.02.076.

[7] Leach F, Ismail R, Davy M. Engine-out emissions from a modern high speed diesel engine – The importance of Nozzle Tip Protrusion. Applied

Energy. 2018;226(June):340–352. Available from: https://doi.org/10.1016/j.apenergy.2018.05.117.

[8] Lee S, Reitz RD. Spray targeting to minimize soot and CO formation in Premixed Charge Compression Ignition (PCCI) combustion with a HSDI diesel engine. SAE Technical Paper. 2006;(2006-01-0918).

[9] Hanson R, Splitter D, Reitz R. Operating a heavy-duty direct-injection compression-ignition engine with gasoline for low emissions. SAE Technical Paper. 2009;(2009-01-1442).

[10] Kalghatgi GT, Risberg P, Ångström HE. Partially pre-mixed auto-ignition of gasoline to attain low smoke and low NOx at high load in a compression ignition engine and comparison with a diesel fuel. SAE Technical Paper. 2007;(2007-01-0006).

[11] Vehicle Tax Rates. Ministry of Transport; 2020. Available from: https://www.gov.uk/browse/driving/vehicle-tax-mot-insurance.

[12] Leipold FW, Hardenberg HO. Noise, Emissions and Performance of the Diesel Engine - A Comparison Between DI and IDI Combustion Systems. SAE Technical Papers. 1975;(950796).

[13] Panis LINT, Rabl A, Nocker LDE, Torfs R. Diesel or Petrol? An Environmental Comparison Hampered By Uncertainty. Proceedings of 11th International Symp Transport and Air Pollution. 2002;1.

[14] Gomaa M, Alimin AJ, Kamaruddin KA. Trade-off between NOx, soot and EGR rates for an IDI diesel engine fuelled with JB5. World Academy of Science, Engineering and Technology. 2010;4(2):1987–1993.

[15] Griffiths JF, Barnard JA. Flame and Combustion. 3rd ed. Oxford: The Alden Press; 1995.

[16] Zhu H, Bohac SV, Nakashima K, Hagen LM, Huang Z, Assanis DN. Effect of fuel oxygen on the trade-offs between soot, NOx and combustion efficiency in premixed low-temperature diesel engine combustion. Fuel. 2013;112:459–465. Available from: http://dx.doi.org/10.1016/j.fuel.2013.05.023.

[17] Hasegawa R, Yanaghira H. HCCI combustion in DI diesel engine. SAE Transactions. 2003;Jan:1070–7.

[18] Kimura S, Aoki O, Ogawa H, Muranaka S, Enomoto Y. New combustion concept for ultra-clean and high-efficiency small di diesel engines. SAE Technical Paper. 1999;(1999-01-3681).

[19] Alriksson M, Denbratt I. Low temperature combustion in a heavy duty diesel engine using high levels of EGR. SAE Technical Papers. 2006;(2006-01-0075).

[20] Sun Y, Reitz RD. Modeling diesel engine NOx and soot reduction with optimized two-stage combustion. SAE Technical Paper. 2006;(2006-01-0027).

[21] Soloiu V, Duggan M, Ochieng H, Harp S, Weaver J, Jenkins C, et al. Premixed charge of n-butanol coupled with direct injection of biodiesel for an advantageous soot-NOx trade-off. SAE Technical Paper. 2013;(2013-01-0916).

[22] Department for Enviornment Food and Rural Affairs, Department for Transport. UK Plan for tackling roadside nitrogen dioxide concentrations - Technical report; 2017. July. Available from: https://www.gov.uk/government/publications/air-quality-plan-for-nitrogen-dioxide-no2-in-uk-2017.

[23] Siebers DL, Higgins B. Flame Lift-Off on Direct-Injection Diesel Sprays Under Quiescent Conditions. SAE Technical Paper. 2001;(2001-01-0530). Available from: http://papers.sae.org/2001-01-0530/.

[24] Pickett LM, Genzale CL, Bruneaux G, Malbec Lm, Hermant L, Christiansen C, et al. Comparison of Diesel Spray Combustion in Different

High-Temperature, High-Pressure Facilities. SAE International Journal of Engines. 2010;3(2):156–181.

[25] Payri R, Salvador FJ, Gimeno J, Peraza JE. Experimental study of the injection conditions influence over n-dodecane and diesel sprays with two ECN single-hole nozzles. Part II: Reactive atmosphere. Energy Conversion and Management. 2016;126:1157–1167. Available from: `http://dx.doi.org/10.1016/j.enconman.2016.07.079`.

[26] Barlow RS. Turbulent Nonpremixed Flame Workshop;. Available from: `www.tnfworkshop.org`.

[27] Pickett LM. ECN Website; 2017. Available from: `http://www.ecn.sandia.gov`.

[28] Lefebvre A, Mcdonell V. Atomization and Sprays. 2nd ed. Boca Raton: Taylor and Francis; 2017.

[29] Reitz RD. Atomization and Other Breakup Regimes of a Liquid Jet. Princeton University; 1978.

[30] Haenlein A. Disintegration of a liquid jet. National Advisory Committee for Aeronautics; 1932.

[31] Giffen E, Muraszew A. The Atomization of Liquid Fuels. New York: John Wiley and Sons; 1953.

[32] Leach F, Ismail R, Davy M, Weall A, Cooper B. Comparing the Effect of Fuel/Air Interactions in a Modern High-Speed Light-Duty Diesel Engine. SAE Technical Paper. 2017;(2017-24-0075).

[33] Reitz RD, Bracco FV. Mechanism of atomization of a liquid jet. Physics of Fluids. 1982;25(10):1730–1742.

[34] Reitz RD. Modeling Atomization Processes in High-Pressure Vaporizing Sprays. Atomization and Sprays. 1987;3:309–337.

[35] Huh YK, Gosman AD. A Phenomenological Model of Diesel Spray Atomization. Proc of The International Conf on Multiphase Flows '91-Tsukuba. 1991;Available from: `http://ci.nii.ac.jp/naid/10018477579/en/`.

[36] Pilch M, Erdman CA. Use of breakup time data and velocity history data to predict the maximum size of stable fragments for acceleration-induced breakup of a liquid drop. International Journal of Multiphase Flow. 1987;13(6):741–757.

[37] Faeth GM, Hsiang LP, Wu PK. Structure and breakup properties of sprays. International Journal of Multiphase Flow. 1995;21:99–127.

[38] O'Rourke PJ, Amsden AA. The tab method for numerical calculation of spray droplet breakup. SAE Technical Paper. 1987;(872089).

[39] Tanner FX. Liquid jet atomization and droplet breakup modeling of non-evaporating diesel fuel sprays. SAE Technical Paper. 1997;(970050).

[40] Ibrahim EA, Yang HQ, Przekwas AJ. Modeling of spray droplets deformation and breakup. Journal of Propulsion and Power. 1993;9(4):651–4.

[41] Chryssakis C, Assanis DN. A unified fuel spray breakup model for internal combustion engine applications. Atomization and Sprays. 2008;18(5):375–426.

[42] Reitz RD, Diwakar R. Structure of High-Pressure Fuel Sprays. SAE Technical Paper. 1987;870598.

[43] Su TF, Patterson MA, Reitz RD, Farrell PV. Experimental and numerical studies of high pressure multiple injection sprays. SAE Technical Paper. 1996;(960861).

[44] Joseph DD, Belanger J, Beavers GS. Breakup of a liquid drop suddenly exposed to a high-speed airstream. International Journal of Multiphase Flow. 1999;25(2):1263–1303.

[45] Beale JC, Reitz RD. Modeling spray atomization with the Kelvin-Helmholtz/Rayleigh-Taylor hybrid model. Atomization and Sprays. 1999;9(6).

[46] Senecal PK, Pomraning E, Richards KJ, Som S. Grid-Convergent Spray Models for Internal Combustion Engine Computational Fluid Dynamics Simulations. Journal of Energy Resources Technology. 2013;136(1):12204. Available from: `http://energyresources.asmedigitalcollection.asme.org/article.aspx?doi=10.1115/1.4024861`.

[47] Dukowicz JK. A particle-fluid numerical model for liquid sprays. Journal of Computational Physics. 1980;35(2):229–253.

[48] Nordin PAN. Complex chemistry modeling of diesel spray combustion. Chalmers University of Technology; 2001.

[49] Senecal PK, Pomraning E, Richards KJ, Briggs TE, Choi CY, Mcdavid RM, et al. Multi-Dimensional Modeling of Direct-Injection Diesel Spray Liquid Length and Flame Lift-off Length using CFD and Parallel Detailed Chemistry. SAE Paper. 2003;2003-01-10(724).

[50] Lucchini AT, Errico GD, Ettorre D, Ferrari G, Sae S, Journal I, et al. Numerical Investigation of Non-Reacting and Reacting Diesel Sprays in Constant-Volume Vessels Linked references are available on JSTOR for this article : You may need to log in to JSTOR to access the linked references . Numerical Investigation of Non-Reac. SAE International Journal of Fuels and Lubricants. 2009;2(1):966–975.

[51] Som S, Senecal PK, Pomraning E. Comparison of RANS and LES turbulence models against constant volume diesel experiments. 24th Annual Conference on Liquid Atomization and Spray Systems, ILASS Americas. 2012;Di(May):1–11.

[52] Blomberg CK, Zeugin L, Pandurangi SS, Bolla M, Boulouchos K, Wright YM. Modeling Split Injections of ECN “Spray A” Using a Conditional Moment

Closure Combustion Model with RANS and LES. SAE International Journal of Engines. 2016;9(4):2107–2119.

[53] Lippert AM, Chang S, Are S, Schmidt DP. Mesh Independence and Adaptive Mesh Refinement For Advanced Engine Spray Simulations. SAE Technical Paper. 2005;(2005-01-0207).

[54] Xue Q, Som S, Senecal PK, Pomraning E. A Study of Grid Resolution and SGS Models for LES under Non-reacting Spray Condi- tions. ILASS Americas. 2013;25(May).

[55] Senecal PK, Pomraning E, Xue Q, Som S, Banerjee S, Hu B, et al. Large Eddy Simulation of Vaporizing Sprays Considering Multi-Injection Averaging and Grid-Convergent Mesh Resolution. Journal of Engineering for Gas Turbines and Power. 2014;136(11):111504. Available from: `http://gasturbinespower.asmedigitalcollection.asme.org/article.aspx?doi=10.1115/1.4027449`.

[56] Falgout Z, Rahm M, Wang Z, Linne M. Evidence for supercritical mixing layers in the ECN Spray A. Proceedings of the Combustion Institute. 2015;35(2):1579–1586. Available from: `http://dx.doi.org/10.1016/j.proci.2014.06.109`.

[57] Desantes JM, García-Oliver JM, Pastor JM, Pandal a. A comparison of diesel sprays CFD modeling approaches: DDM versus σ-γ Eulerian atomization model. Atomization and Sprays. 2016;26(7):713–737. Available from: `https://www.scopus.com/inward/record.uri?eid=2-s2.0-84952932168&partnerID=40&md5=c36b3db98ee47952f2519940128237b0`.

[58] Mulemane A, Subramaniyam S, Lu PH, Han JS, Lai MC, Poola R. Comparing cavitation in diesel injectors based on different modeling approaches. SAE Technical Paper. 2004;(2004-01-0027).

[59] Kärrholm FP, Tao F, Nordin N. Three-dimensional simulation of diesel spray ignition and flame lift-off using openfoam and KIVA-3V CFD codes. SAE Technical Papers. 2008;(2008-01-0961).

[60] Vijayraghavan Iyengar S, Tsang CW, Rutland C. Validating non-reacting spray cases with KIVA-3V and openfoam. SAE Technical Papers. 2013;(2013-01-1595).

[61] Som S, D'Errico G, Longman D, Lucchini T. Comparison and standardization of numerical approaches for the prediction of non-reacting and reacting diesel sprays. SAE Technical Papers. 2012;.

[62] Dahms RN. Understanding the breakdown of classic two-phase theory and spray atomization at engine-relevant conditions. Physics of Fluids. 2016;28(4).

[63] Dahms RN, Manin J, Pickett LM, Oefelein JC. Understanding high-pressure gas-liquid interface phenomena in Diesel engines. Proceedings of the Combustion Institute. 2013;34(1).

[64] Bellan J. Supercritical (and subcritical) fluid behavior and modeling: drops, streams, shear and mixing layers, jets and sprays. Progress in Energy and Combustion Science. 2000;26(4):329–366.

[65] Prausnitz J, Lichtenthaler R, de Azvedo E. Molecular thermodynamics for fluid-phase equilibrium. New Jersey: Prentice-Hall; 1986.

[66] Badami M, Mallamo F, Millo F, Rossi EE. Influence of Multiple Injection Strategies on Emissions, Combustion Noise and BSFC of a DI Common Rail Diesel Engine. SAE Technical Paper. 2002;(2002-01-0503). Available from: `http://papers.sae.org/2002-01-0503/`.

[67] Su J, Xu M, Yin P, Gao Y, Hung D. Particle Number Emissions Reduction Using Multiple Injection Strategies in a Boosted Spark-Ignition Direct-Injection (SIDI) Gasoline Engine. SAE International Journal of Engines. 2015;8(1). Available from: `http://papers.sae.org/2014-01-2845/`.

[68] Park W, Ra Y, Kurtz E, Willems W, Reitz RD. Use of Multiple Injection Strategies to Reduce Emission and Noise in Low Temperature Diesel Combustion. SAE Technical Paper. 2015;(2015-01-0831).

[69] Biswas S, Bakshi M, Shankar G, Mukhopadhyay A. Experimental Investigation on the Effect of Two Different Multiple Injection Strategies on Emmisions, Combustion Noise and Performances of an Automotive CRDI Engine. SAE Technical Paper. 2016;(2016-01-0871).

[70] Ferrari A, Mittica A. Response of different injector typologies to dwell time variations and a hydraulic analysis of closely-coupled and continuous rate shaping injection schedules. Applied Energy. 2016;169:899–911. Available from: http://dx.doi.org/10.1016/j.apenergy.2016.01.120.

[71] Jörg C, Schnorbus T, Jarvis S, Neaves B, Bandila K, Neumann D. Feedforward Control Approach for Digital Combustion Rate Shaping Realizing Predefined Combustion Processes. SAE International Journal of Engines. 2015;8(3). Available from: http://papers.sae.org/2015-01-0876/.

[72] Sapio F, Piano A, Millo F, Pesce FC. Digital Shaping and Optimization of Fuel Injection Pattern for a Common Rail Automotive Diesel Engine through Numerical Simulation. SAE Technical Paper. 2017;(2017-24-0025).

[73] Leach F, Davy M, Henry M, Tombs M, Zhou F. A new method for measuring fuel flow in an individual injection in real time. SAE Technical Paper. 2018;(2018-01-0285):1–9.

[74] Nsikane DM, Mustafa K, Ward A, Morgan R, Mason D, Heikal M. Statistical Approach on Visualizing Multi-Variable Interactions in a Hybrid Breakup Model under ECN Spray Conditions. SAE International Journal of Engines. 2017;10(5):104–2017. Available from: http://papers.sae.org/2017-24-0104/.

[75] Mohan B, Mubarak Ali MJ, Ahmed A, Hernandez Perez F, Sim J, Roberts W, et al. Numerical Simulations of High Reactivity Gasoline Fuel Sprays under Vaporizing and Reactive Conditions. SAE Technical Paper. 2018;(2018-01-0292):1–8.

[76] Lacaze G, Misdariis A, Ruiz A, Oefelein JC. Analysis of high-pressure Diesel fuel injection processes using LES with real-fluid thermodynamics and transport. Proceedings of the Combustion Institute. 2015;35(2):1603–1611. Available from: http://dx.doi.org/10.1016/j.proci.2014.06.072.

[77] Versteeg HK, Malalasekera W. An Introduction to Computational Fluid Dynamics. 2nd ed. Pearson Education Limited; 2007.

[78] Pope SB. Turbulent Flows. Journal of Turbulence. 2000;1:771.

[79] Davidson L. Fluid mechanics, turbulent flow and turbulence modeling. Lecture Notes in Physics. 2015;Available from: tfd.chalmers.se/$\sim$lada/postscript_files/solids-and-fluids_turbulent-flow_turbulence-modelling.pdf.

[80] Davidson L. An introduction to turbulence models. Lecture Notes in Physics. 2011;Available from: tfd.chalmers.se/$\sim$lada/postscript_files/kompendium_turb.pdf.

[81] Benajes J, Novella R, Pastor JM, Hernández-López A, Hasegawa M, Tsuji N, et al. Optimization of the combustion system of a medium duty direct injection diesel engine by combining CFD modeling with experimental validation. Energy Conversion and Management. 2016;110:212–229. Available from: http://dx.doi.org/10.1016/j.enconman.2015.12.010.

[82] Margot X, Payri R, Gil A, Chavez M, Pinzello A. Combined CFD-Phenomenological Approach to the Analysis of Diesel Sprays under Non-Evaporative Conditions. SAE Technical Paper. 2008;(2008-01-0962). Available from: http://dx.doi.org/10.4271/2008-01-0962.

[83] Maes N, Dam N, Somers B, Lucchini T, D'Errico G, Hardy G. Experimental and Numerical Analyses of Liquid and Spray Penetration under Heavy-Duty Diesel Engine Conditions. SAE International Journal of Fuels and Lubricants. 2016;9(1):861–2016. Available from: http://papers.sae.org/2016-01-0861/.

[84] Sazhina EM, Sazhin SS, Heikal MR, Babushok VI, Johns RJR. A detailed modelling of the spray ignition process in diesel engines. Combustion Science and Technology. 2000;160(1-6):317–344.

[85] Kralj C. Numerical Simulation Of Diesel Spray Processes. Imperial College; 1995.

[86] Showry KB. Modeling combustion and emissions of HSDI diesel engines using injectors with different included spray angles. International Journal of Aerospace and Mechanical Engineering. 2016;3(1):25–31. Available from: http://papers.sae.org/2006-01-1150/.

[87] CD-adapco. Star-CD®version 4.24 Methodology; 2015.

[88] TAYLOR GI. Generation of ripples by wind blowing over a viscous fluid. Reprinted in The Scientific Papers of Sir Geoffrey Ingram Taylor, Vol. 3. Cambridge Univ. Press, London; 1963.

[89] Reitz RD, Diwakar R. Effect of Drop Breakup on Fuel Sprays. SAE Technical Paper. 1986;860469.

[90] Sikroria T, Kushari A, Syed S, Lovett JA. Experimental Investigation of Liquid Jet Breakup in a Cross Flow of a Swirling Air Stream. Journal of Engineering for Gas Turbines and Power. 2014;136(6):61501. Available from: http://gasturbinespower.asmedigitalcollection.asme.org/article.aspx?doi=10.1115/1.4026244.

[91] Siebers DL. Liquid-Phase Fuel Penetration in Diesel Sprays. SAE Technical Paper. 1998;(980809). Available from: http://papers.sae.org/980809/.

[92] Launder BE, Spalding DB. The Numerical Computation Of Turbulent Flows. In: Numerical Prediction of Flow, Heat Transfer, Turbulence and Combustion. Elsevier; 1983. p. 96–116. Available from: http://linkinghub.elsevier.com/retrieve/pii/B9780080309378500167.

[93] Ameen MM, Pei Y, Som S. Computing Statistical Averages from Large Eddy Simulation of Spray Flames. SAE Technical Paper. 2016;(2016-01-0585).

[94] Nicholson L, Fang X, Camm J, Davy M, Richardson D. Comparison of Transient Diesel Spray Break-Up between Two Computational Fluid Dynamics Codes. SAE Technical Paper. 2018;(2018-01-0307):1–13.

[95] Ranz WE, Marshall WR. Evaporation from drops - Part 1; 1952.

[96] Convergent Science. Converge®version 2.4 Methodology; 2017.

[97] El Wakil MM, Uyehara OA, Myers PS. A theoretical investigation of the heating-up period of injected fuel droplets vaporizing in air; 1954.

[98] Xin J, Ricart L, Reitz RD. Computer modeling of diesel spray atomization and combustion. Combustion science and technology. 1998;137(1-6):171–194.

[99] Kastengren A, Ilavsky J, Pablo J, Payri R, Duke DJ, Swantek A, et al. Flow Measurements of droplet size in shear-driven atomization using ultra-small angle x-ray scattering. International Journal of Multiphase Flow. 2017;92:131–139. Available from: http://dx.doi.org/10.1016/j.ijmultiphaseflow.2017.03.005.

[100] Magnotti GM, Genzale CL. Detailed assessment of diesel spray atomization models using visible and X-ray extinction measurements. International Journal of Multiphase Flow. 2017;97:33–45.

[101] Battistoni M, Magnotti GM, Genzale CL, Arienti M, Matusik KE, Duke DJ, et al. Experimental and Computational Investigation of Subcritical Near-Nozzle Spray Structure and Primary Atomization in

the Engine Combustion Network Spray D. SAE Technical Paper. 2018;(2018-01-0277):1–15.

[102] Wang X, Zhao H. Numerical Simulation of the Gasoline Spray with an Outward-Opening Piezoelectric Injector: A Comparative Study of Different Breakup Models. SAE Technical Paper. 2018;(2018-01-0272):1–13.

[103] Levich VG. Physicochemcial Hydrodynamics. New Jersey: Prentice-Hall; 1962.

[104] Wakale AB, Mohamed SY, Naser N, Mubarak Ali MJ, Banerjee R, Im H, et al. An Experimental and Numerical Study of N-Dodecane/Butanol Blends for Compression Ignition Engines. SAE Technical Paper. 2018;(2018-01-0240):1–15.

[105] Desantes JM, Garcia-Oliver JM, Novella R, Perez-Sanchez EJ. Application of an unsteady flamelet model in a RANS framework for spray A simulation. Applied Thermal Engineering. 2017;117:50–64. Available from: `http://dx.doi.org/10.1016/j.applthermaleng.2017.01.101`.

[106] Saha K, Srivastava P, Quan S, Senecal PK, Pomraning E, Som S. Modeling the Dynamic Coupling of Internal Nozzle Flow and Spray Formation for Gasoline Direct Injection Applications. SAE Technical Paper. 2018;(2018-01-0314):1–13.

[107] Pickett LM, Manin J, Payri R, Bardi M, Gimeno J. Transient Rate of Injection Effects on Spray Development. SAE Technical Paper. 2013;(2013-24-0001):15–16. Available from: `http://papers.sae.org/2013-24-0001/`.

[108] Hamzah A, Poursadegh F, Lacey J, Petersen P, Brear MJ, Gordon R, et al. A comparison of diffuse back-illumination (DBI) and Mie-scattering technique for measuring the liquid length of severely flashing spray. 20th Australasian Fluid Mechanics Conference. 2016;(December).

[109] Naber J, Siebers DL. Effects of Gas Density and Vaporization on Penetration and Dispersion of Diesel Sprays. SAE Technical Paper. 1996;(960034). Available from: http://papers.sae.org/960034/.

[110] Lillo PM, Pickett LM, Persson H, Andersson O, Kook S. Diesel Spray Ignition Detection and Spatial/Temporal Correction. SAE International Journal of Engines. 2012;5(3):1330–1346. Available from: http://papers.sae.org/2012-01-1239/.

[111] Donkerbroek AJ, Boot MD, Luijten CCM, Dam NJ, ter Meulen JJ. Flame lift-off length and soot production of oxygenated fuels in relation with ignition delay in a DI heavy-duty diesel engine. Combustion and Flame. 2011;158(3):525–538. Available from: http://dx.doi.org/10.1016/j.combustflame.2010.10.003.

[112] Musculus MP, Dec JE, Tree DR. Effects of fuel parameters and diffusion flame lift-off on soot formation in a heavy-duty di diesel engine. SAE Technical Papers. 2002;(2002-01-0889).

[113] Azimov U, Kim KS, Bae C. Modeling of flame lift-off length in diesel low-temperature combustion with multi dimensional CFD based on the flame surface density and extinction concept. Combustion Theory and Modelling. 2010;14(2):155–175.

[114] Bolla M, Farrace D, Wright YM, Boulouchos K, Mastorakos E. Influence of turbulence-chemistry interaction for n-heptane spray combustion under diesel engine conditions with emphasis on soot formation and oxidation. Combustion Theory and Modelling. 2014;18(2):330–360. Available from: http://dx.doi.org/10.1080/13647830.2014.898795.

[115] CD-adapco. Star-CD®version 4.30 Methodology; 2017.

[116] Liang L, Stevens JG, Farrell JT. A dynamic multi-zone partitioning scheme for solving detailed chemical kinetics in reactive flow computations. Combustion Science and Technology. 2009;181(11):1345–1371.

[117] Westbrook CK. Chemical kinetics of hydrocarbon ignition in practical combustion systems. Proceedings of the Combustion Institute. 2000;28(2):1563–1577.

[118] Theobald MA, Cheng WK. A numerical study of diesel ignition. ASME Paper. 1987;Feb 15.

[119] Yao T, Pei Y, Zhong Bj, Som S, Lu T. A Hybrid Mechanism for n-Dodecane Combustion with Optimized Low-Temperature Chemistry. Fuel. 2017;191(339349).

[120] Wang H, Ra Y, Jia M, Reitz RD. Development of a reduced n-dodecane-PAH mechanism and its application for n-dodecane soot predictions. Fuel. 2014;136:25–36. Available from: `http://dx.doi.org/10.1016/j.fuel.2014.07.028`.

[121] Borghesi G, Krisman A, Lu T, Chen JH. Direct numerical simulation of a temporally evolving air / n-dodecane jet at low-temperature diesel-relevant conditions. Combustion and Flame. 2018;195:183–202.

[122] Ma PC, Wu H, Jaravel T, Bravo L, Ihme M. Large-eddy simulations of transcritical injection and auto-ignition using diffuse-interface method and finite-rate chemistry. Proceedings of the Combustion Institute. 2019;37(3):3303–3310. Available from: `https://doi.org/10.1016/j.proci.2018.05.063`.

[123] Kim N, Jung K, Kim Y. Multi-environment PDF modeling for n-dodecane spray combustion processes using tabulated chemistry. Combustion and Flame. 2018;192:205–220. Available from: `https://doi.org/10.1016/j.combustflame.2018.02.004`.

[124] Chishty MA, Bolla M, Hawkes ER, Pei Y, Kook S. Soot formation modelling for n -dodecane sprays using the transported PDF model. Combustion and Flame. 2018;192:101–119. Available from: https://doi.org/10.1016/j.combustflame.2018.01.028.

[125] Fang X, Ismail R, Davy MH, Camm J. Numerical Studies of Combustion Recession on ECN Diesel Spray A. In: ASME 2018 Internal Combustion Engine Division Fall Technical Conference. San Diego; 2018. p. 1–13.

[126] Fang XL. Numerical Modelling For Diesel Spray Combustion. University of Oxford; 2019.

[127] Fang X, Ismail R, Davy M. A Study on Kinetic Mechanisms of Diesel Fuel Surrogate n-Dodecane for the Simulation of Combustion Recession. SAE Technical Paper. 2019;(2019-01-0202):1–12.

[128] Bhattacharjee S, Haworth DC. Simulations of transient n-heptane and n-dodecane spray flames under engine-relevant conditions using a transported PDF method. Combustion and Flame. 2013;160(10):2083–2102. Available from: http://dx.doi.org/10.1016/j.combustflame.2013.05.003.

[129] Kim S, Jarrahbashi D, Genzale C. The Role of Turbulent-Chemistry Interaction in Simulating End-of-Injection Combustion Transients in Diesel Sprays. SAE Technical Paper. 2017;(2017-01-0838).

[130] Jarrahbashi D, Kim S, Knox BW, Genzale CL. Computational analysis of end-of-injection transients and combustion recession. International Journal of Engine Research. 2017;8(10).

[131] Pickett LM, Abraham J. Computed and measured fuel vapor distribution in a diesel spray. Atomization and Sprays. 2010;20(3):241–250.

[132] Nsikane DM, Vogiatzaki K, Morgan RE. Predictive Engine Simulations based on a novel DoE / RANS approach with coefficient tabulation. Fuel Systems: Engines. 2018;Dec(1).

[133] Nsikane D, Vogiatzaki K, Morgan R, Mustafa K. Predictive CFD Auto-Tuning Approach for an In-Cylinder EU6 LDD DI Engine. SAE Technical Paper. 2019;(2019-24-0033).

[134] Hiroyasu H, Kadota T. Models for combustion and formation of nitric oxide and soot in direct injection diesel engines. SAE Transactions. 1976;p. 513–526.

[135] Raj A, Celnik M, Shirley R, Sander M, Patterson R, West R, et al. A statistical approach to develop a detailed soot growth model using PAH characteristics. Combustion and Flame. 2009;156(4):896–913. Available from: http://dx.doi.org/10.1016/j.combustflame.2009.01.005.

[136] Willman C, Scott B, Stone R, Richardson D. Quantitative metrics for comparison of in-cylinder velocity fields using Particle Image Velocimetry. Experiments in Fluids. 2019;p. 1–16.

[137] Dec JE. A Conceptual Model of DI Diesel Combustion Based on Laser-Sheet Imaging*. SAE Technical Paper. 1997;(970873). Available from: http://papers.sae.org/970873/.

[138] Camm J, Davy M, Fang X, Doherty L, McGilvray M, Foerster F. The Oxford Cold Driven Shock Tube (CDST) for Fuel Spray and Chemical Kinetics. SAE Technical Paper. 2018;(2018-01-0222).